Development of aluminium nitride based materials and application to the fabrication of ultraviolet light emitting diodes

Aly Zaiter

Développement de matériaux à base de nitrures d'aluminium et application à la réalisation de diodes électroluminescentes ultraviolettes

Aly ZAITER

Centre de Recherche sur l'Hétéroépitaxie et ses Applications (CRHEA), CNRS

Présentée en vue de l'obtention du grade de docteur en Physique **de l'**Université Côte d'Azur

Dirigée par :
Julien Brault, Directeur de recherche, CNRS-CRHEA

Soutenue le : 13/12/2023

Devant le jury, composé de :
Abdallah Ougazzaden, Prof, Georgia Tech Europe
Jean-Paul Salvestrini, Prof, Georgia Tech Europe
Christophe Durand, Mcf, Univ. Grenoble Alpes
Guillaume Cassabois, Prof, L2C, Univ. Montpellier
Sylvie Contreras, CR, L2C, Univ. Montpellier
Mohamed Al Khalfioui, Mcf, Univ. Côte d'Azur

PROJET FINANCÉ PAR L'ANR - PROJECT FUNDED BY THE ANR

Développement de matériaux à base de nitrures d'aluminium et application à la réalisation de diodes électroluminescentes ultraviolettes

Jury :

Président :

Jean-Paul Salvestrini, Professeur, GeorgiaTech-Europe, Metz, France

Rapporteurs :

Jean-Paul Salvestrini, Professeur, GeorgiaTech-Europe, Metz, France

Christophe Durand, Maître de conférences, Université Grenoble Alpes, Grenoble, France

Examinateurs :

Abdallah Ougazzaden, Professeur, Georgia Tech-Europe, Metz, France

Guillaume Cassabois, Professeur, L2C, Université Montpellier, Montpellier, France

Sylvie Contreras, Chargée de recherche, L2C, Université Montpellier, Montpellier, France

Mohamed Al Khalfioui, Maître de conférences, Université Côte d'Azur, Valbonne, France

Résumé

Cette thèse aborde la croissance épitaxiale de l'alliage (Al,Ga)N en utilisant des approches innovantes telles que le recuit à haute température et la croissance sur des matériaux lamellaires dits ''2D'', dans le but d'améliorer la qualité structurales des couches pour la fabrication de diodes électroluminescentes (DEL) efficaces.

Ce travail débute par une analyse approfondie de l'effet de recuit post-croissance à haute température sur les couches fines d'AlN (100 - 200 nm) déposées sur substrats de saphir. Une recette de recuit optimisée a été développée en utilisant un premier procédé sous azote (N_2) et un second sous hydrogène (H_2) et azote (N_2). Des fortes améliorations de la morphologie de surface et des propriétés cristallines ont été obtenues, se traduisant par la réduction des valeurs de largeur à mi-hauteur (FWHM) des pics de diffraction de rayons X pour les plans symétriques et asymétriques, tandis que la morphologie de surface a évolué d'une morphologie de surface dominée par les grains à une morphologie lisse à l'échelle atomique. Ensuite, la croissance de l'AlN sur des tremplins de h-BN sur saphir par épitaxie par jets moléculaires (EJM) et recuit post-croissance a été explorée. Un contrôle de la température est nécessaire afin d'éviter la diffusion du h-BN et la formation d'(Al,B)N qui entravent la possibilité d'exfoliation de la couche d'AlN. Une couche d'AlN épitaxiée sur un tremplin d'AlN / h-BN recuit a montré une amélioration notable de la morphologie de surface et de la structure cristalline.

Ensuite, nous avons étudié la croissance de DELs UV standard par épitaxie en phase vapeur (EPV) sur des tremplins d'AlN recuits, ce qui a conduit à une meilleure qualité structurale et optique des DELs avec des rendements quantiques externes (RQE) d'environ 0,3%, soit dix fois supérieurs aux DELs UV à jonction tunnel (JT) réalisées précédemment à cette étude. Ce travail s'est poursuivi par une analyse comparative de la croissance de DELs UV standard et de DELs UV basées sur des boîtes quantiques (BQs) d'(Al,Ga)N à jonction tunnel par EJM, où l'incorporation de JT a entraîné une amélioration remarquable de la puissance optique. Pour une densité de courant de 10 $A.cm^{-2}$, la puissance optique des DELs standard a atteint 30 µW, tandis que celle des DELs JT a atteint une puissance de 240 µW, ce qui représente une augmentation d'un facteur huit. De plus, une augmentation significative du RQE des DELs UV à JT par rapport au RQE des DELs UV standard, atteignant une valeur maximale de 0,65%, a montré une augmentation huit fois plus élevée du RQE. Suite à ce travail, des structures à BQs $Al_yGa_{1-y}N$ /$Al_xGa_{1-x}N$ émettant dans la gamme UV-C ont été développées sur des tremplins de h-BN/saphir par EJM en utilisant des épaisseurs de h-BN de 3 nm et 6 nm. Les propriétés structurales des couches d'$Al_{0.7}Ga_{0.3}N$ ont été étudiées, montrant l'impact des couches de h-BN sur la croissance de l'(Al,Ga)N pour laquelle la direction de croissance du tremplin est conservée, mais qui peut présenter deux orientations différentes dans le plan de croissance. Des BQs avec une émission dans la gamme UV-C et avec des rapports d'intensité intégrée de photoluminescence (PL) indiquant une différence d'un facteur 10 entre les émissions à température ambiante et à basse température ont été obtenues. Ensuite, la structure de BQs épitaxiée sur h-BN a été exfoliée à l'aide d'un simple ruban adhésif. Les mesures de PL attestent de l'émission dans l'UV-C des BQs exfoliées. Le transfert de la structure exfoliée sur un substrat SiO_2/Si via un second transfert au ruban adhésif a démontré une efficacité de transfert de 50 %.

Enfin, la démonstration d'une DEL à base de BQs $Al_yGa_{1-y}N$ sur un tremplin de h-BN de 1,5 nm sur saphir, émettant également dans la gamme UV-C, a été présentée.

Mots-clés: III-nitrures, AlN, (Al,Ga)N, boites quantiques, épitaxie par jets moléculaires, nitrure de bore hexagonal, jonction tunnel, diodes électroluminescentes, microscopie à force atomique, diffraction de rayons X, électroluminescence.

Abstract

This research project encompasses the epitaxial growth of (Al,Ga)N coupled with innovative approaches such as high-temperature annealing and growth on 2D materials, aimed at improving the quality of heterostructures for efficient light-emitting diodes (LEDs) emitting in the ultra-violet (UV) range.

The investigation commences with an in-depth analysis of face-to-face post-growth high-temperature annealing on physical vapor deposited (PVD) AlN layers on sapphire substrates. Optimal annealing recipe that fosters enhanced crystalline quality and surface morphology involving nitrogen (N_2) and hydrogen (H_2) + nitrogen (N_2) has been developed. Significant improvements in surface morphology and crystalline properties have been achieved. This is evident in the reduction of full width at half maximum (FWHM) values for symmetric and skew symmetric planes, while the surface morphology underwent a transition from a grain-dominated to a smooth atomic step morphology. The exploration extended to the growth of AlN on h-BN through molecular beam epitaxy (MBE) and post-growth annealing, a previously unreported study. Despite the initial rough surface and low crystalline quality, improvements were observed by increasing AlN layer thickness and performing high-temperature annealing. However, a limitation in the used temperature is required to avoid a diffusion of h-BN from the interface with sapphire through the AlN region, forming an (Al,B)N alloy within the AlN layer, which prohibits any possibility of later exfoliation. Yet, a regrown AlN layer on the annealed AlN / h-BN template resulted in an improved layer characterized by a smooth surface morphology and significantly improved crystalline structure.

Next, we have studied the growth of standard UV LEDs by metal organic chemical vapor deposition (MOCVD) on the annealed AlN PVD templates, which resulted in better LEDs structural and optical qualities with external quantum efficiencies (EQE) around 0.3%, which was ten times higher than the EQE obtained for tunnel junction (TJ) UV LEDs done in a previous work by our group. The study continued with the comparative analysis of the growth of standard and TJ (Al,Ga)N QDs-based UV LEDs by MBE, where the incorporation of TJs has resulted in a remarkable enhancement of the optical power. For instance, at a current density of 10 $A.cm^{-2}$, the P_{opt} for a standard p-n LED reaches 30 µW, while for the TJ based LED, it significantly rises to 240 µW, representing an eightfold increase. Furthermore, a significant increase in the EQE for the TJ UV LED compared to the EQE of the standard UV LED was found, with a maximum value of approximately 0.65%, marking an eightfold increase in the EQE. Moreover, $Al_yGa_{1-y}N$ QDs/$Al_xGa_{1-x}N$ emitting in the UV-C range have been grown on h-BN / sapphire templates by MBE using two different h-BN thicknesses of 3 nm and 6 nm. The structural properties of $Al_{0.7}Ga_{0.3}N$ layers have been studied showing an impact of the h-BN layers on the subsequent structures in the form of a growth orientation guidance, leading to the formation of two different orientations in the growth plane. The QDs showed an emission in the UV-C and the integrated PL intensity ratios indicated a 10 times reduction between room and low temperature, respectively. Next, the QDs structure grown on 6 nm h-BN underwent a successful exfoliation by scotch-tape. Photoluminescence measurements attested to the preserved UV-C emission from the exfoliated QDs. Transferring the exfoliated structure to an SiO_2 / Si substrate via dry transfer demonstrated a transfer efficiency of 50%.

Finally, the demonstration of an $Al_yGa_{1-y}N$ QDs-based light emitting diode prototype fabricated on a 1.5 nm h-BN on sapphire template, emitting in the UV-C range, was shown.

Keywords: III-nitrides, AlN, (Al,Ga)N, quantum dots, molecular beam epitaxy, h-BN, tunnel junction, LEDs, atomic force microscopy, X-ray diffraction, electroluminescence.

"They say that the best blaze burns the brightest when circumstances are at their worst"

Howl's Moving Castle

To my father

Table of Contents

Introduction

In the modern era, the consumption of artificial light has surged to unprecedented levels, driven by the continuous expansion of urban centers, industrial activities, and technological advancements. The remarkable progress in human civilization, marked by the transition from agrarian societies to highly urbanized ones, has led to a significant rise in the demand for lighting in various domains. This amplified requirement for illumination is not only emblematic of societal progress but also underscores the need for sustainable and efficient lighting technologies that can not only cater to the escalating demand but also minimize the associated energy consumption and environmental impact. The advent of electric lighting revolutionized human existence, enabling activities to extend well into the night and enhancing productivity, safety, and comfort. However, this convenience came at a cost. Traditional lighting sources, such as incandescent and fluorescent bulbs, are notorious for their high-energy consumption and relatively short lifespans. This not only exerts a substantial economic burden on individuals and industries but also exacerbates the overall energy demand, leading to increased greenhouse gas emissions and environmental degradation.

Figure 1. Satellite image of earth during the night showing the vital dependence of humans on artificial light in the modern world [1].

In this context, light-emitting diodes (LEDs) have emerged as a game-changing technology that has the potential to address the escalating demand for efficient lighting solutions. LEDs represent a quantum leap in lighting technology, offering unparalleled energy efficiency, longer lifespans, and enhanced controllability [2]. Their remarkable characteristics stem from their unique semiconductor-based operation, where electrons recombine with holes within the material to emit photons, producing visible light. This mechanism eliminates the wasteful energy conversion processes inherent in conventional lighting sources, making LEDs significantly more energy-efficient and environmentally friendly.

The initial instance of a light-emitting diode (LED) was documented in 1907 when Henry Round, employed at Marconi labs, applied a 10V voltage to a SiC crystal and observed the emission of a "yellowish" light. However, this discovery remained dormant for about twenty years until Oleg Losev in Soviet Russia revitalized it in 1927 by presenting the first functional theory. He further investigated electroluminescence phenomena in SiC and other semiconductor materials. Subsequent researchers continued to build upon Losev's work, leading to the publication of the first LED patent in 1961 for an infrared LED. The following year, Nick Holonyak from General Electric patented the first visible LED (red) [3]–[5].

In the early 1990s, the landscape of light emission underwent a revolution with the advent of III-V semiconductor materials based on nitrides. III-nitride materials such as GaN, AlN, InN, and their alloys emerged as direct band gap semiconductors, highly suitable for modern optoelectronic and electronic applications like LEDs and lasers, owing to their exceptional properties. Among these properties, the notably wide band gap stands out, ranging from 0.69 eV for InN to 3.4 eV for GaN, and even up to 6.1 eV for AlN, as depicted in figure 2. Utilizing the concept of band gap engineering, as previously applied to conventional III-V semiconductors (arsenides, phosphides), III-nitrides have become a promising material for covering a broad spectral range. This range spans from the near-infrared and visible spectrum through the use of $In_xGa_{1-x}N$ alloys to the ultraviolet spectrum through $Al_xGa_{1-x}N$ alloys.

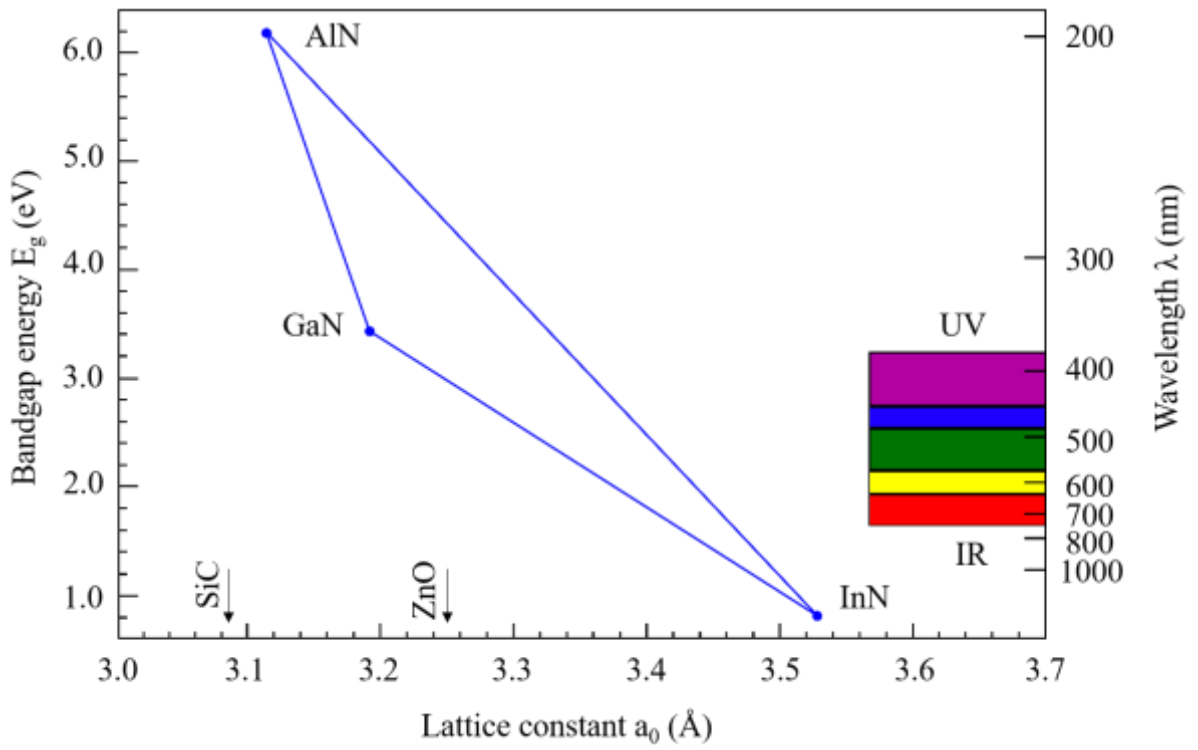

Figure 2. Bandgap energy (E_g) as a function of the lattice constant (a_0) for III-nitride semiconductors at room temperature (300 K) [6].

During the late 1960s, Maruska and Tietjen reported the first instance of single crystalline GaN [7]. However, during this period, the limited crystalline quality and the presence of residual n-type doping posed challenges to the advancement of III-nitride devices. A transformative breakthrough occurred in the mid-1980s with the development of the metal organic vapor phase epitaxy (MOVPE) growth process and the successful production of high-quality GaN materials. Subsequent developments in p-type doping further contributed to these advancements in the early 1990's. These milestones marked the inception of (In, Ga)N blue LEDs, which played a pivotal role in the creation of white LEDs. This groundbreaking invention paved the way for the emergence of energy-efficient, environmentally friendly, and brilliantly luminous light sources, leading to diverse applications. Recognizing these achievements [8]–[10], Isamu Akasaki, Hiroshi Amano, and Shuji Nakamura were awarded the Nobel Prize in Physics in 2014 [11].

Advancements in III-nitride research followed a rapid trajectory: from the initial achievement of high-power blue LEDs in 1994 [12], to attaining remarkably high external quantum efficiencies exceeding 80% fifteen years later [13]. In addition to LEDs, III-nitride materials garnered interest for diverse optoelectronic and electronic devices, encompassing ultraviolet photodetectors [14], laser diodes [15], and high electron mobility transistors

(HEMTs) [16]. The emergence of HEMTs also paved the path for various high-power and radio frequency (RF) applications. Today, III-nitride materials have made their mark across multiple sectors of the semiconductor industry, driven by an array of applications including lighting, RF, power, lasers, data storage, and more.

In recent years, the dawn of a forthcoming industrial revolution has become discernible. In 2010, a pivotal milestone was reached as the count of internet-connected devices surpassed the global human population for the first time [17]. The imminent integration of these devices with 5G technology, a venture set in motion in 2016 [18], will enable seamless data communication among machines. This convergence, known as the "Internet of Things," necessitates innovative paradigms for intelligent devices capable of perceiving and interacting with their surroundings. While the prospect of substantial energy savings has been put forth [19], there might be reservations about this claim, given its frequent repetition. To achieve this vision, a concerted effort in semiconductor sensing technology (including advancements in electronic noses or electronic tongues), device communication (via novel platforms), and application domains (such as novel devices for intelligent lighting) is indispensable. The III-nitride system is poised to play a pivotal role in advancing these applications.

Following the prosperous integration of III-nitride semiconductors as visible emitters and the global drive towards reducing the utilization of mercury-based devices, the path was cleared for the widespread adoption of ultraviolet (UV) LEDs. Furthermore, the emergence of the COVID-19 pandemic triggered substantial expansion in the UV LED market. Nations such as the United States and China embraced this technology for disinfection purposes. Projections indicate that by 2030, the UV LED market is anticipated to achieve a market share of 2.19 billion USD, exhibiting a noteworthy compound annual growth rate (CAGR) of 19.17% [20].

UV LEDs employing (Al,Ga)N alloys demonstrate the capability to span a broad spectrum of UV wavelengths by modulating the band gap emission, ranging from 3.4 eV (for GaN) to 6.1 eV (for AlN) (as illustrated in figure 2). This advantage significantly expands the potential applications of UV LEDs across various UV wavelength ranges. These applications encompass UV curing and 3D printing within the **UV-A range (400 – 320 nm)**, phototherapy and plant growth in the **UV-B range (320 – 280 nm)**, and air purification along with water sterilization in the **UV-C range (< 280 nm)** [21].

Following the transition from (In,Ga)N to (Al,Ga)N-based LEDs (shorter wavelengths < 365 nm), a sharp drop in the external quantum efficiency (EQE) occurs [21]. This is mainly due

to the poor electrical characteristics (due to the low p-doping efficiencies for (Al,Ga)N layers) and the low structural quality of (Al,Ga)N materials (due to the high density of dislocations which act as non-radiative recombination centers). Our strategy to address the challenge of low crystalline quality in (Al,Ga)N buffer layers involves the implementation of a post-growth face-to-face high-temperature annealing process developed by Professor Miyake's research group. This method has shown effectiveness in enhancing the crystalline morphology of AlN templates grown on sapphire substrates. Additionally, to mitigate the impact of reduced crystalline quality on UV LED efficiency, particularly radiative efficiency, we employ three-dimensional (3D) quantum dots (QDs) as the active region in LEDs, in contrast to 2D quantum wells (QWs). By utilizing 3D QDs, carriers are confined within the QDs along all three spatial dimensions, thereby reducing the likelihood of non-radiative recombination with surrounding defects. Furthermore, our study incorporates tunnel junctions (TJs) as another approach to minimize both absorption and electrical losses. TJs utilize quantum mechanical tunneling to enhance hole injection into the active region via non-equilibrium injection, leading to decreased resistance in the p-type contact layer. Moreover, TJs enable the elimination of the absorbing p-GaN contact layer, offering an advantage for deep UV LEDs. Additionally, we explore the potential of Van der Waals epitaxy for growing two-dimensional (2D) materials, such as h-BN, which enables the easy removal of individual layers without damaging the exfoliated layer or the underlying structure. Van der Waals epitaxy, with its unique attributes, presents an appealing avenue for heterogeneous integration. This involves transferring epilayers from their native growth substrate to a dissimilar receiving substrate, tailored to specific functions such as flexibility and/or vertical injection. This approach facilitates the development of flexible devices.

This thesis was part of APOGEE project that focuses on the production of UV-C LEDs prototypes with performance surpassing the current state of the art, i.e., with external quantum efficiencies exceeding 10%. This project involves four academic partners:

- Georgia Tech (Metz), whose activities focus on the growth of hexagonal boron nitride (h-BN) materials by MOVPE and exfoliation technologies.
- LETI (Grenoble), whose activities include the fabrication (deposition) of AlN-based materials (sputtering, pulsed laser ablation) and vertical injection LED technologies.
- L2C (Montpellier), which develops optical spectroscopy characterization of materials in the deep UV (PL, TRPL, µ-PL).

- CRHEA (Valbonne), whose activities center on high-temperature processes for AlN, as well as the development of tunnel junctions, quantum dots and quantum wells for the active zone of LEDs.

This thesis was funded by the ANR project GANEX (Grant Number ANR-11-LABX-0014). GANEX is part of the "Investissements d'Avenir" program, which is publicly funded and managed by the French ANR agency. GANEX is a Labex, a laboratory of excellence. Labex is part of the programs launched in 2011 and 2012 as part of the Investments for the Future initiative. GANEX is a network of French laboratories and companies working on a common theme, III-nitrides (Al,In,GaN), with GaN being the iconic representative. The objective of GANEX is to enhance the position of French academic stakeholders in terms of knowledge and visibility and strengthen that of industrial partners in terms of expertise and market share.

Partial funding and support for this thesis was granted by the PACA (Provence Alpes Côte d'Azur) region, in collaboration with Lumilog / Saint Gobain companies.

This thesis is divided into four chapters and is structured as follows:

- Chapter I will provide an introduction to the fundamental properties of III-nitride materials that serve as the foundation for this study. This section will delve into their crystal and elastic properties, as well as their band structures. Furthermore, the influence of internal electric fields on these materials will be explored. The subsequent segment will encompass an in-depth overview of III-nitride ultraviolet emitters, addressing various technical challenges and proposing different methodologies to enhance their efficiencies. The chapter will conclude by introducing the concept of epitaxial growth, with a specific focus on the molecular beam epitaxy (MBE) technique tailored for nitride materials. Special attention will be given to the unique aspects of quantum dots (QDs) within this context.
- Chapter II will provide an introduction to the face-to-face high temperature annealing technique and its advantage in reducing dislocation densities and improving the crystalline quality in aluminum nitride (AlN) templates grown on sapphire substrates. Furthermore, the annealing of AlN layers grown on sapphire and of AlN layers grown on hexagonal boron nitride (h-BN) on sapphire will be studied.
- Chapter III will provide an overview of the tunneling theory, including the growth of tunnel junction structures and their performances. It will also discuss the metal organic chemical vapor deposition (MOCVD) growth of standard ultraviolet (UV) light emitting

diodes (LEDs) on annealed AlN templates as well as the MBE growth of quantum dots-based standard and tunnel junction UV LEDs.

- Chapter IV will focus on the motivation behind the adoption of van der Waals epitaxy of two-dimensional (2D) materials and the MBE growth of $Al_yGa_{1-y}N$ QDs heterostructures on a 2D material, specifically hexagonal boron nitride (h-BN). Following the growth, the nitride heterostructure exfoliation and transfer on other substrates will be investigated while discussing the structural and optical properties in each step. We will demonstrate the fabrication of an electrically injected $Al_yGa_{1-y}N$ QD-based UV LED prototype grown on h-BN on sapphire emitting in the UV-C range, and discuss its main electro-optical properties.

Finally, a general conclusion and perspectives of this work will be presented.

References:

[1] « Space.com: NASA, Space Exploration and Astronomy News », *Space.com*, 30 août 2023. https://www.space.com (consulté le 30 août 2023).

[2] C. M. Bourget, « An introduction to light-emitting diodes », *HortScience*, vol. 43, nº 7, p. 1944-1946, 2008.

[3] « LED History: Invention of Light Emitting Diode » Electronics Notes ». https://www.electronics-notes.com/articles/history/semiconductors/light-emitting-diode-led-history.php (consulté le 30 août 2023).

[4] O. V. Lossev, « CII. Luminous carborundum detector and detection effect and oscillations with crystals », *The London, Edinburgh, and Dublin Philosophical Magazine and Journal of Science*, vol. 6, nº 39, p. 1024-1044, 1928.

[5] N. Holonyak Jr et S. F. Bevacqua, « Coherent (visible) light emission from Ga (As1− x P x) junctions », *Applied Physics Letters*, vol. 1, nº 4, p. 82-83, 1962.

[6] E. F. Schubert, *Light-Emitting Diodes (2006)*. E. Fred Schubert, 2006.

[7] H. P. Maruska et J. J. Tietjen, « The preparation and properties of vapor-deposited single-crystal-line GaN », *Applied Physics Letters*, vol. 15, nº 10, p. 327-329, 1969.

[8] H. Amano, N. Sawaki, I. Akasaki, et Y. Toyoda, « Metalorganic vapor phase epitaxial growth of a high quality GaN film using an AlN buffer layer », *Applied Physics Letters*, vol. 48, nº 5, p. 353-355, 1986.

[9] H. Amano, M. Kito, K. Hiramatsu, et I. Akasaki, « P-type conduction in Mg-doped GaN treated with low-energy electron beam irradiation (LEEBI) », *Japanese journal of applied physics*, vol. 28, nº 12A, p. L2112, 1989.

[10] S. Nakamura, T. Mukai, M. S. M. Senoh, et N. I. N. Iwasa, « Thermal annealing effects on p-type Mg-doped GaN films », *Japanese Journal of Applied Physics*, vol. 31, nº 2B, p. L139, 1992.

[11] « The Nobel Prize in Physics 2014 », *NobelPrize.org*. https://www.nobelprize.org/prizes/physics/2014/summary/ (consulté le 30 août 2023).

[12] S. Nakamura, T. Mukai, et M. Senoh, « Candela-class high-brightness InGaN/AlGaN double-heterostructure blue-light-emitting diodes », *Applied Physics Letters*, vol. 64, nº 13, p. 1687-1689, 1994.

[13] Y. Narukawa, M. Ichikawa, D. Sanga, M. Sano, et T. Mukai, « White light emitting diodes with super-high luminous efficacy », *Journal of physics D: Applied physics*, vol. 43, nº 35, p. 354002, 2010.

[14] M. Razeghi et A. Rogalski, « Semiconductor ultraviolet detectors », *Journal of Applied Physics*, vol. 79, nº 10, p. 7433-7473, 1996.

[15] S. Nakamura *et al.*, « InGaN multi-quantum-well-structure laser diodes with cleaved mirror cavity facets », *Japanese journal of applied physics*, vol. 35, nº 2B, p. L217, 1996.

[16] M. Asif Khan, J. N. Kuznia, D. T. Olson, W. J. Schaff, J. W. Burm, et M. S. Shur, « Microwave performance of a 0.25 μm gate AlGaN/GaN heterostructure field effect transistor », *Applied Physics Letters*, vol. 65, nº 9, p. 1121-1123, 1994.

[17] O. Stengel, A. Van Looy, et S. Wallaschkowski, *Digitalzeitalter-Digitalgesellschaft: das Ende des Industriezeitalters und der Beginn einer neuen Epoche*. Springer, 2017.

[18] S. Redana *et al.*, « 5G PPP architecture working group: View on 5G architecture », 2019.

[19] J. Karlgren *et al.*, « Socially intelligent interfaces for increased energy awareness in the home », in *The Internet of Things: First International Conference, IOT 2008, Zurich, Switzerland, March 26-28, 2008. Proceedings*, Springer, 2008, p. 263-275.

[20] S. I. LLP, « Global UV LED Market Size, Share To Hit USD 2.19 Billion By 2030 | CAGR 19.17% », *GlobeNewswire News Room*, 19 janvier 2023. https://www.globenewswire.com/news-release/2023/01/19/2592091/0/en/Global-UV-LED-Market-Size-Share-To-Hit-USD-2-19-Billion-By-2030-CAGR-19-17.html (consulté le 22 février 2023).

[21] M. Kneissl, T.-Y. Seong, J. Han, et H. Amano, « The emergence and prospects of deep-ultraviolet light-emitting diode technologies », *nature photonics*, vol. 13, nº 4, p. 233-244, 2019.

Chapter I

Nitrides for ultraviolet light emission

In this chapter, an introduction to III-nitride materials and their fundamental properties, along with a review of the current state of ultraviolet emitter technology and the principles of epitaxial growth will be addressed. Additionally, the specific application of epitaxial growth to the III-nitride system, particularly in relation to quantum dots, will also be discussed. This chapter covers:

- III-nitride materials, their crystal structure and elastic properties.
- Band structure and electronic properties of III-nitrides.
- State of the art and applications of ultraviolet light emitting diodes, specifically (Al,Ga)N based.
- Epitaxial growth techniques for nitride materials, with a particular focus on molecular beam epitaxy.
- Quantum dots growth by molecular beam epitaxy.

I.1 III-nitride materials

I.1.1 Crystal properties

Crystals made from (Al,Ga,In)N can be sorted in three distinct structures: Wurtzite (Wz), zinc blende (ZB) and rock salt. Nevertheless, wurtzite structure is considered for epitaxial growth in this work due to its thermodynamical stability along with a better structural quality compared to the metastable zinc blende and the rock salt phases that require very high pressure growth procedures (>12 GPa) [1] to be induced.

The wurtzite structure has an hexagonal unit cell hence two lattice constants, *c* (unit height) and *a* (unit edge). The unit cell contains six atoms of each type. Furthermore, the wurtzite structure belongs to the space group $P6_3mc$ in the Hermann-Mauguin notation consisting of two hexagonal close-packed (hcp) sublattices offsetting along the c-axis by u (bond length parameter) $u = \frac{3}{8}c$ for the ideal structure (figure 1 (a)). On the other hand, the zinc blende structure has a cubic unit cell containing four metal and four nitrogen (N) elements, respectively. It belongs to the space grouping $F\bar{4}3m$ in the Hermann-Mauguin notation consisting of two interpenetrating face-centered cubic sublattices, offset by $u = a\frac{\sqrt{3}}{4}$ (figure 1 (b)). The rock salt structure belongs to the space grouping $Fm\bar{3}m$ in the Hermann-Mauguin notation. The reason behind its requirement of very high pressures to be induced in (Al,Ga,In)N is caused by the reduction of the lattice dimensions that induces the interionic Coulomb interaction to favor the ionicity over the covalent nature. Therefore, none of the epitaxial growth techniques can produce rock salt III-nitrides.

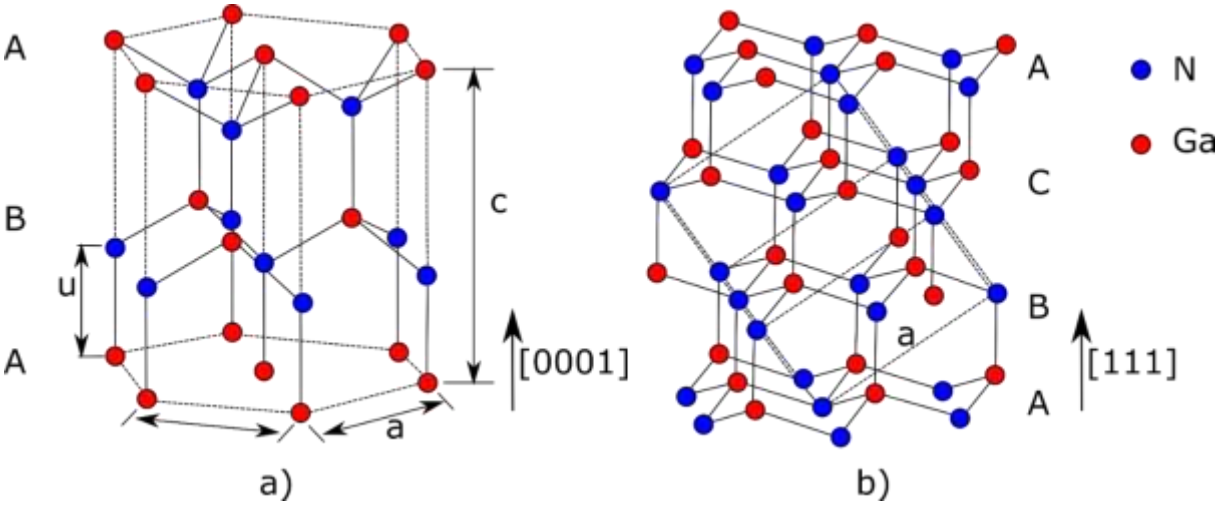

Figure 1. Atomic structures of III-nitride elements. (a) hexagonal unit cell and (b) cubic unit cell [2]. The blue and red spheres indicate nitrogen (N) and Gallium (Ga) atoms, respectively.

In the wurtzite and zinc blende structures, each group III atom is bonded to four nitrogen atoms and each nitrogen atom is bonded to four group III atoms. The major difference between the two structures is that the stacking sequence of the wurtzite structure is AaBbAa along the [0001] axis (figure 2 (a)) whereas it is AaBbCc along the [111] axis for the zinc blende structure (figure 2 (b)).

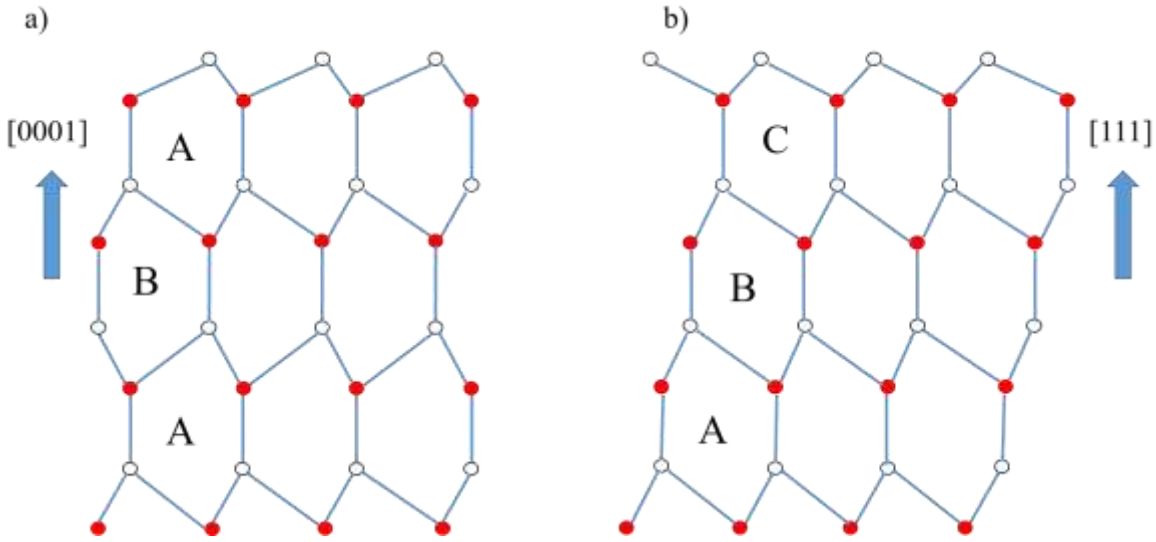

Figure 2. Schematics representing stacking sequences of a) wurtzite (0001) structure (observed along the [11-20] azimuth), and b) zinc blende (111) structure (observed along the [1-10] azimuth).

A set of four integers standing for (h k i l) also known as the Miller-Bravais indices that in turn are related to the vectors $\overrightarrow{a1}$, $\overrightarrow{a2}$, $\overrightarrow{a3}$ and $\vec{c}$, respectively, are usually used for indexing of the lattice points in hexagonal structures. Vectors $\overrightarrow{a1}$, $\overrightarrow{a2}$, $\overrightarrow{a3}$ are rotated by an angle of 120° to each other and their sum should be equal to zero (that is i = - (h+k)) while vector $\vec{c}$ is perpendicular to the hexagonal base as well as representing the [0001] axis (figure 3).

$(h\ k\ i\ l) = (a_1\ a_2\ a_3\ c)$

$i = -(h + k)$

$a_3 = -(a_1 + a_2)$

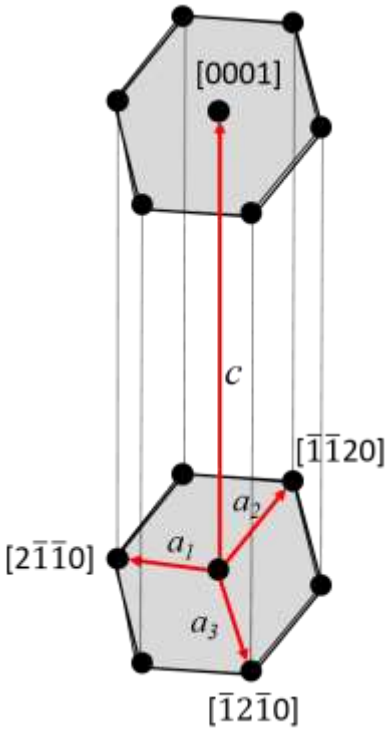

Figure 3. Schematic representation of the crystallographic axes of the wurtzite structure. (h k i l) are the Miller-Bravais indices related to the vectors $\overrightarrow{a1}$, $\overrightarrow{a2}$, $\overrightarrow{a3}$ and $\vec{c}$, respectively.

The lattice parameters *c*, *a* and *u*, respectively, represents the edge, height and bond length units of an hexagonal cell of III-nitride wurtzite structures (figure 1.a). The lattice parameters for AlN, GaN and InN, along with the difference in the *u*/*c* and *c*/*a* ratios for the III-nitride materials, are reported in table I.1. In a perfect wurtzite structure where atoms are considered as hard spheres, the *c/a* and *u/c* ratios are equal to 0.375 and 1.633, respectively. Nevertheless, in nitride materials real crystals, these ratios differ from its ideal values, which leads to a spontaneous polarization field generated from the variation of the ideal lattice parameters together with a deviation from the dipole at the atomic level. These effects at the atomic level will be further discussed in the coming sections.

	***a* (Å)**	***c* (Å)**	***c/a***	***u/c***	**Thermal expansion coefficient (10^{-6} K^{-1})**
AlN	3.112	4.982	1.600	0.382	α_c= 5.3 / α_a= 4.2
GaN	3.189	5.185	1.626	0.377	α_c= 3.17 / α_a= 5.59
InN	3.538	5.703	1.612	0.379	α_c= 2.9 / α_a= 3.8

Table I.1. Lattice parameters for AlN, GaN and InN at 300K [3], [4].

A dependency exists for the lattice parameters on the material temperature; hence, they evolve as a function of the temperature. Thermal expansion coefficients of the three nitride materials are summarized in table I.1. In heteroepitaxy, this dependency induces thermal stresses that have an effect that mainly appears during sample cooling after the growth. It can lead to the creation of defects in form of cracks that complicates the growth of good crystalline quality epilayers in case of GaN growth on sapphire substrates or (Al,Ga)N growth on GaN. This problem has been surpassed by first depositing a thin AlN buffer layer at low temperature [5].

A calculation can be done for the lattice parameters in the case of ternary alloys, for example $Al_xGa_{1-x}N$, by linear interpolation assuming Vegard's law:

$$\boldsymbol{p(Al_xGa_{1-x}N) = xp(AlN) + (1-x)p(GaN)} \quad \text{(Eq. I. 1)}$$

where p is the lattice parameter representing either '*c*' or '*a*' and x is the composition of Al in the $Al_xGa_{1-x}N$ alloy.

The choice of the host substrate for the epitaxy of III-nitrides is a delicate point since the chosen substrate will have an impact on the growth of all subsequent layers, along with their structural, electronic and optical qualities. Therefore, depending on the desired application a compromise is taken between the physical properties, technological considerations, size, price and availability of different substrates. Other factors that are also taken into consideration when choosing the appropriate substrate are the lattice mismatch between the substrate and the ternaries (AlN, GaN and InN) along with the thermal expansion coefficient with these ternaries. For that reason, it can be said that there is no ideal substrate, but rather a suitable substrate to a desired application. Table I.2 summarizes the lattice parameters along with the thermal expansion coefficients for the most available and commonly used substrates for the fabrication of optoelectronic devices.

	6H-SiC (0001)	Si (111)	Al_2O_3 (0001)	AlN	GaN
Lattice parameter *a* (Å)	3.0806	3.84	2.747	3.112	3.189
In-plane lattice mismatch with AlN $(a_{AlN}-a_{sub})/a_{sub}$ (%)	1	-18.9	13	0	2.4
In-plane lattice mismatch with GaN $(a_{AlN}-a_{sub})/a_{sub}$ (%)	3.5	-17	16	-2.4	0
Thermal expansion coefficient (10^{-6} K^{-1})	4.46	3.59	7.3	5.59	4.2
Thermal conductivity ($W.K^{-1}.cm^{-1}$)	3.8	1.5	0.5	3	1.5
Absorption coefficient α (cm^{-1}) in the UV range (at 300 K)	$>10^3$	$>10^6$	$\sim10^2$	$\sim10^4$	$\sim10^5$

Table I.2. Properties of the most common and used substrates for III-nitrides epitaxy [6].

Based on the values provided in table I.2, it appears that SiC is the most suitable substrate for the epitaxy of III-nitride materials since the lattice mismatch with AlN and GaN is smaller compared to Si (111) and sapphire. In addition, its thermal and electrical conductivities are quite good. On the other hand, its absorption coefficient is higher than 10^3 cm^{-1} in the UV range and increases for shorter wavelengths (deep UV) which gives sapphire an advantage in this area. Despite all the advantageous properties, SiC is an expensive substrate with limited size availability and UV light absorption aspect which are considered an important drawbacks.

Si (111) substrate is well known for its low cost and availability in large sizes (up to 12 inches), but it has important lattice mismatch values with AlN and GaN that create plastic relaxation mechanisms and the formation of defects during the growth of III-nitrides leading to poor crystalline quality of the subsequent layers. In addition, the important thermal expansion coefficient mismatch induces strong stress in the layers that can lead to the appearance of cracks.

Sapphire substrate is the most commonly used substrate in the epitaxy of III-nitrides due to its availability, low cost, large size availability (up to 8-inch), high thermal stability, and transparency in the visible and ultraviolet ranges. As the goal of this thesis is the growth of $Al_xGa_{1-x}N$ structures and $Al_xGa_{1-x}N$ based ultraviolet light emitting diodes (UV LEDs), sapphire is the substrate of choice. However, despite the mentioned advantages, some disadvantages are also present such as the high lattice mismatch and the high lattice thermal coefficient mismatch with both AlN and GaN along with a poor thermal conductivity that induce several epitaxial challenges. These disadvantages decrease the crystalline structure quality of the epitaxial layer that suffers from a high defect density ($>10^8 cm^{-2}$).

For the epitaxy of III-nitrides, different crystal planes can be exploited (figure 4) and the epitaxial layers are usually named after the crystal plane used for the growth.

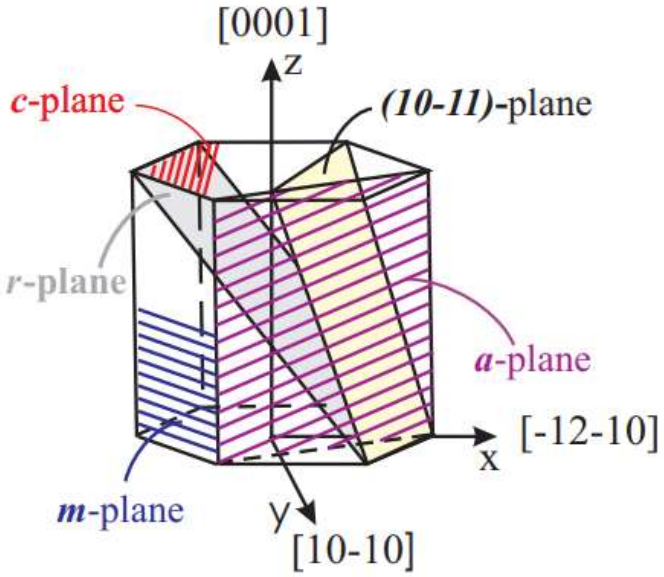

Figure 4. Schematic presentation of the wurtzite crystal structure of III-nitride materials. The most used planes for the epitaxial growth such as the polar *c*-plane (0001), the non-polar *a*-plane ($11\bar{2}0$) and *m*-plane ($1\bar{1}00$) are indicated as hatched areas; and the semi-polar *r*-plane ($10\bar{1}2$) and ($10\bar{1}1$) [7].

Wurtzite III-nitrides are polar crystals along the [0001] direction and the majority is grown on sapphire (0001) *c*-plane. When the single bonds along the *c*-axis are from the group-III atoms toward the N atoms, the polarity is called a group-III polarity with [0001] crystal orientation. On the other hand, opposite to the group-III polarity, the N-polarity with a crystal orientation [$000\bar{1}$] is when it is three bonds away from the group-III atoms toward the N atoms (figure 5). The polarity can be controlled during the growth by modifying the growth conditions and it affects the surface properties together with the optical properties. The group-III polarity layers are considered of a higher quality compared to the N polar ones, specifically concerning the concentration of impurities and the surface roughness [8].

Still, the growth along the [0001] orientation generates built-in electric fields caused by polarization discontinuities at interfaces along the *c*-axis (further discussed later) that has a strong impact on the optoelectronic properties by inducing a red shift of the wavelength emission. For that reason, III-nitrides with non-polar and semi-polar surface orientations has attracted wide interest lately due to the possibility to reduce or avoid the strong built-in electric fields. The two non-polar planes for the wurtzite III-nitrides are ($11\bar{2}0$) *a*-plane, and ($1\bar{1}00$) *m*-plane which are perpendicular to the *c*-plane (see figure 4). Semi-polar planes are the inclined planes at an intermediate angle with the *c*-plane other than 0° (*c*-plane) and 90° (non-polar planes), like ($10\bar{1}2$) and ($10\bar{1}1$) (*r*-plane) planes (see figure 4). In spite of that, non-polar and semi-polar orientations suffer from several important disadvantages compared to the polar c-

plane orientation, which are the small substrate size and its limited availability, the high defect densities, the low crystal quality, and the low carrier mobility.

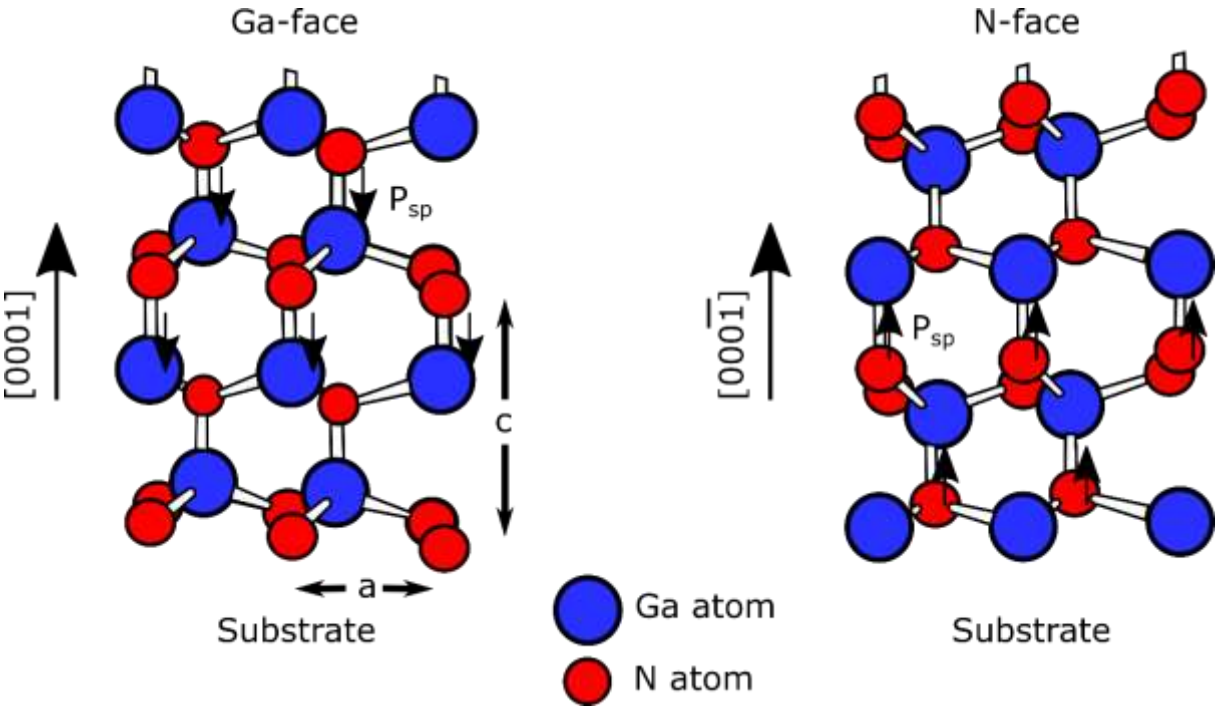

Figure 5. Schematic presentation of the polarity and the polarization direction in a GaN wurtzite structure with metal polarity or N polarity [9].

I.1.2 Elastic properties

- **Strain and stress**

Heteroepitaxial growth of III-nitrides is mainly done on host substrates that present differences in chemical composition, crystal structure, orientation, lattice and/or thermal expansion mismatches and, as mentioned earlier, sapphire is the widely used host substrate. In addition, III-nitride materials also present different lattice parameters and thermal expansion coefficients between each other. The overall differences lead to important stresses and deformations in the epitaxial layers. Mainly, the generated stress is biaxial in the growth plane and it can be either compressive or tensile. In the context of growing III-nitrides on a substrate, the lattice mismatch induces strain in the growing crystal. In the case of a very thin film, for which the thickness of the grown layer did not exceed a certain thickness, called critical thickness, the layer remains in a pseudomorphic strain state: the grown layer undergoes an elastic deformation (either compression or extension) in order to match the lattice of the crystalline substrate, as shown in figure 6 (b). However, in the case of a thicker thin film, i.e. where the thickness exceeds the critical thickness, relaxation of the strain occurs: its process usually occurs through plastic relaxation where the stored strain is released by the formation of

defects. The defects take the form of misfit dislocations at the film-substrate interface, as shown in figure 6 (c), or dislocations within the thin film itself, as shown in figure 6 (d).

Physical fractures or fissures so-called ‘cracks’ can also occur in the context of growing III-nitrides on a substrate. They manifest as separations or discontinuities in the material's structure, resulting in visible gaps or openings. These cracks are primarily caused by the accumulated strain that arises from lattice and thermal mismatch exceeding a critical limit. As the material grows, strain progressively builds up until it reaches a threshold that triggers the material to fracture, giving rise to cracks. The presence of cracks can have adverse effects, such as compromising mechanical strength, reducing electrical conductivity, creating leakage paths, and influencing optical properties. Additionally, cracks can act as stress concentration points, rendering the material more susceptible to further damage or failure.

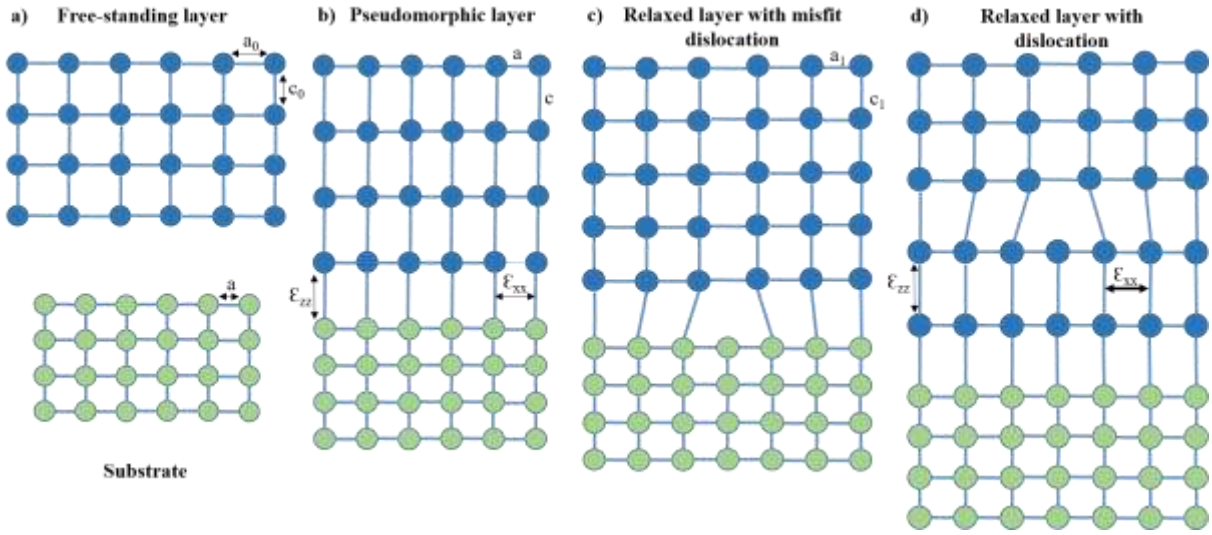

Figure 6. Schematics illustrating different epilayer growth situations on a host substrate: a) fully relaxed or free-standing layer, b) pseudomorphic, defect-free layer, c) relaxed layer with a misfit dislocation at the film-substrate interface, d) relaxed layer with a dislocation within the thin film volume.

As already discussed, the difference in the lattice parameters and the thermal expansion coefficients between the host substrate and the epitaxial layer leads to deformations (Eq. I.2). Note that while the lattice mismatch induces stress due to the lattice adaptation during the growth, the difference in the thermal expansion coefficient imposes a stress during post-growth cooling.

$$\varepsilon_{xx} = \varepsilon_{yy} = \frac{a - a_0}{a_0} \qquad \varepsilon_{zz} = \frac{c - c_0}{c_0} \qquad \text{(Eq. I. 2)}$$

In (Eq. I.2), *a* and *c* are respectively the in-plane and out-of-plane lattice parameters of the epitaxial layer while a_0 and c_0 represent the lattice parameters of the substrate. The parameters describe the strain in the growth plane (ε_{xx}) and along the growth axis (ε_{zz}). The stress (σ) can be determined in function of the strain (ε) and the lattice parameters *a* and *c* by Hooke's law:

$$\sigma_{ij} = \sum_{k,l} C_{ijkl} \cdot \varepsilon_{kl} \qquad \text{(Eq. I. 3)}$$

where σ_{ij} and ε_{kl} are the stress and strain, respectively, and C_{ijkl} is the fourth-order elastic coefficient tensor. For an hexagonal wurtzite structure, Voigt notation [10] enables (Eq. I.3) to be written in the form of a 6 x 6 matrix by replacing the indices {xx, yy, zz, yz, xz, xy} by {1, 2, 3, 4, 5, 6} respectively in order to simplify the notation as shown in Eq. I.4.

$$\begin{pmatrix}\sigma_1\\ \sigma_2\\ \sigma_3\\ \sigma_4\\ \sigma_5\\ \sigma_6\end{pmatrix} = \begin{pmatrix} c_{11} & c_{12} & c_{13} & 0 & 0 & 0 \\ c_{12} & c_{11} & c_{13} & 0 & 0 & 0 \\ c_{13} & c_{13} & c_{33} & 0 & 0 & 0 \\ 0 & 0 & 0 & c_{44} & 0 & 0 \\ 0 & 0 & 0 & 0 & c_{44} & 0 \\ 0 & 0 & 0 & 0 & 0 & c_{66} = \dfrac{c_{11}-c_{12}}{2} \end{pmatrix} \begin{pmatrix}\varepsilon_1\\ \varepsilon_2\\ \varepsilon_3\\ \varepsilon_4\\ \varepsilon_5\\ \varepsilon_6\end{pmatrix} \qquad \text{(Eq. I. 4)}$$

In the case of epitaxial growth, no stress is exerted along the *c*-axis ($\sigma_{zz} = \sigma_3 = 0$) and the layer undergoes a state of biaxial stress in the growth plane. This biaxial stress state renders the in-plane stress components equal ($\sigma_1 = \sigma_2 = \sigma$). Thereby, Eq. I.4 can be simplified to be:

$$\begin{pmatrix}\sigma\\ \sigma\\ 0\end{pmatrix} = \begin{pmatrix} C_{11} & C_{12} & C_{13} \\ C_{12} & C_{11} & C_{13} \\ C_{13} & C_{13} & C_{33} \end{pmatrix} \begin{pmatrix}\varepsilon_1\\ \varepsilon_2\\ \varepsilon_3\end{pmatrix} \qquad \text{(Eq. I. 5)}$$

In addition, an out-of-plane strain ($\varepsilon_3 = \varepsilon_{zz}$) is induced due to the in-plane biaxial strain. Hooke's law provides a relation of the out-of-plane and in-plane strains:

$$\sigma_3 = C_{13}.(\varepsilon_1 + \varepsilon_2) + C_{33}.\varepsilon_3 = 0 \qquad \text{(Eq. I. 6)}$$

since $\varepsilon_1 = \varepsilon_2 = \varepsilon_{xx}$, the equation can be simplified to:

$$\varepsilon_3 = \varepsilon_{zz} = -2\left(\frac{C_{13}}{C_{33}}\right)\varepsilon_{xx} = \frac{\left(C_{sub} - C_{epi}\right)}{C_{epi}} \qquad \text{(Eq. I. 7)}$$

where $2\left(\frac{C_{13}}{C_{33}}\right)$ is the Poisson biaxial ratio, which is referred to as v_c .

Table I.3 gives both the theoretical and experimental values of the elastic coefficients C_{ij} of III-nitride materials extracted from the literature. Due to the different growth techniques of the material and the methods determining its coefficients, a high dispersion of these values exists.

Table I.3. Theoretical and experimental elastic coefficients for AlN and GaN in GPa.

	References	C_{11}	C_{12}	C_{13}	C_{33}	C_{44}	C_{66}
AlN	[11]	396	137	108	373	116	297
	[12]	398	140	127	382	96	
	[13]	345	125	120	395	118	
	[14]	410	140	100	390	120	
	[15]	411	149	99	389	125	
GaN	[11]	367	135	103	405	95	
	[12]	396	144	100	392	91	
	[14]	370	145	110	390	90	
	[16]	390	145	106	398	105	123
	[17]	377	160	114	209	81	
	[18]	374	106	70	379	101	

- **Defects in crystals**

All real crystals contain imperfections that disturb the ordered arrangement of atoms in form of defects. These defects range from point, line (e.g. dislocations), surface (e.g. grain boundaries, twin boundaries, stacking faults) to volume (bubbles, misorientations, precipitates) defects [19]. Their presence can alter the properties (mechanical, electrical and optical) of crystalline solids [19]. Several conditions play a role in the concentration of defects, such as the synthesis conditions of the crystal itself together with the film-substrate interaction in the case of epitaxy, the growth method and the growth conditions. The focus will be on the main and most impactful defects categories in the scope of this thesis, which are point defects, grain boundaries and misorientations.

Two types of point defects labelled intrinsic defects can occur in a pure metal: (1) vacant atomic site or vacancy, where the lattice site exhibit missing atoms; and (2) self-interstitial atom, where an atom is introduced into a non-lattice site causing local distortions of the crystalline lattice. Plastic deformation is one of the causes for vacancies and interstitials in a material. The stable concentration of intrinsic point defects in crystals is subject to, among other aspects, the growth temperature since the energy forming them is positive. In a non-equilibrium process, such as the thin film growth epitaxial process, the defect concentration can be controlled to a certain point by modifying the growth conditions (temperature, flux/mass flow, growth rate etc.).

On the other hand, extrinsic point defects (i.e. impurities) in crystals play an important role in the physical and mechanical properties of a material. They can either be substitutional, i.e. where atoms of the lattice site are replaced by the impurity atoms, or interstitial, i.e. where they

occupy a non-lattice site as mentioned above. The impurity may intentionally be introduced to alter some of the crystal's properties. In semiconductors, doping or the intentional introduction of impurities into a material enables the modification of its structural, electrical and optical properties, for example by introducing additional charge carriers thereby controlling the crystal's electrical properties.

Grains exhibit themselves in a random oriented way and in large numbers in crystalline materials where they are separated by grain boundaries. Grain boundaries can contain the defects mentioned above, they are two-dimensional interface defects as well, changing the direction of the crystalline lattice from one grain to another. Thereby, the rotational angle between two grains defines the nature of the grain boundaries. In polycrystalline films, the rotation angle between two grains is large; therefore, the films exhibit high-angle grain boundaries. Despite the fact that the atomic structure of high angle grain boundaries is periodic in a polycrystal, it is relatively complex [20], [21].

As mentioned earlier, the epitaxial growth of a thin film on a host substrate creates a crystallographic relationship between the two. Misorientations are rotational deviations of the crystallite's lattice with regard to the epitaxial relationship. These rotational deviations can be defined either by a rotational angle around the in-plane axis (referred to as tilt) or by a rotational angle around the out-of-plane axis (referred to as twist) as shown in figure 7. The outcome resulting from the misorientations are grain boundaries, where the misorientation angle defines the density of the threading dislocations needed to compensate the angular mismatch between the grains [19], [20].

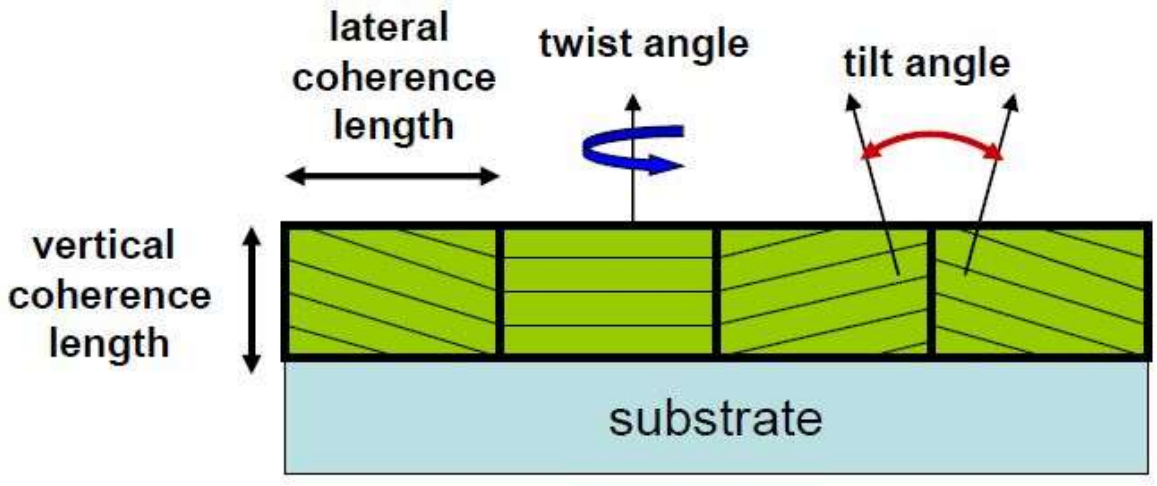

Figure 7. Schematic representations of the tilt and the twist that take place in epitaxial thin film crystals [22].

- **Polarization and Stark effect**

The epitaxial growth of wurtzite III-nitride crystals along the *c*-axis direction (polar plane) results in polarization discontinuities at the hetero-interface inducing strong electric fields, which affect the optoelectronic properties of semiconductor devices. Polarization can be of intrinsic origin, so-called spontaneous polarization, or strain induced, so-called piezoelectric polarization.

The wurtzite structure is not an ideal structure; the four atomic bonds of a tetrahedron are not of an equal length. The III-N bond oriented along the *c*-axis (0001) slightly differs from the other three bonds and the electro-negativity difference between the metal atom and the N-atom leads to a deformation of the electron cloud that creates electron dipoles in the crystal lattice. This leads to the generation of macroscopic polarization called spontaneous polarization (P_{sp}) (Eq. I.8) oriented from the metal polar surface (<0001> axis) towards the N polar surface (<000$\bar{1}$> axis) (figure 8) [23]. The P_{sp} creates a negative polarization value calculated by Zoroddu et al. for III-nitrides and presented in table I.4 for AlN, GaN and InN, respectively [24], [25].

Table I.4. Spontaneous polarization values obtained for binary nitrides [24].

	AlN	GaN	InN
Spontaneous polarization P_{sp} (C.m^{-2})	-0.090	-0.034	-0.042

In the case of ternary alloys, the value of the spontaneous polarization cannot be obtained by simple interpolation [26]. Equation I.8 presents the calculation of the spontaneous polarizations for $Al_xGa_{1-x}N$ alloys in this way:

$$P_{sp}(Al_xGa_{1-x}N) = x.P_{sp}(AlN) + (1-x).P_{sp}(GaN) + b.x(1-x) \qquad \text{(Eq. I. 8)}$$

with b = 0.019 C/m^2 as the bowing parameter for the spontaneous polarization in $Al_xGa_{1-x}N$ [27].

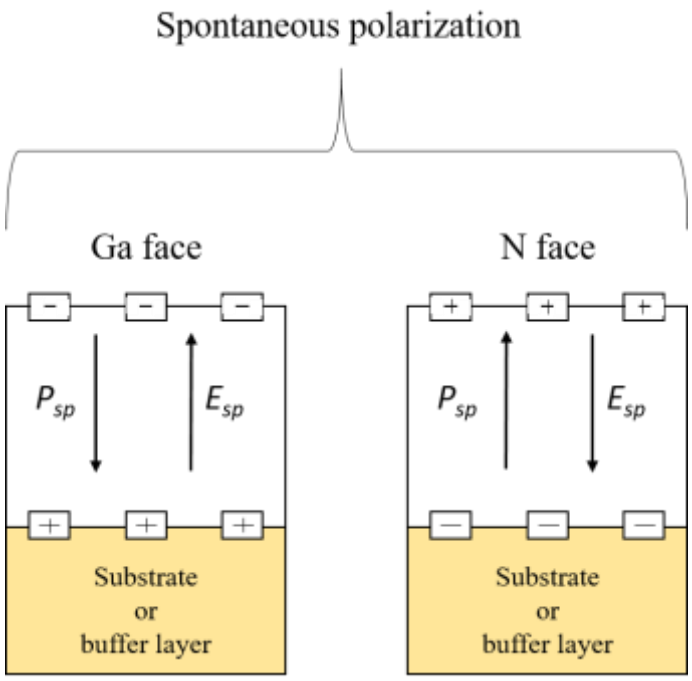

Figure 8. Schematic representation of the direction of the spontaneous polarization (P_{sp}) and electric field (E) in III-nitrides for Ga and N face orientations [28].

Lattice mismatch during heteroepitaxial growth induces crystal deformation that leads to an external type of polarization called piezoelectric polarization (P_{pz}). When the tetrahedrons of the wurtzite structure are deformed, the barycenters of positive and negative charges displace from their regular location, which in turn change the polarization. The direction of the piezoelectric polarization is subject to the type of strain induced. In the case of a compressive strain, the P_{pz} is directed along the <0001> direction whereas for tensile strain, it is directed along the $<000\bar{1}>$ direction (figure 9). Piezoelectric polarization has an important effect in III-nitride nanostructures such as quantum wells or quantum dots GaN/AlGaN or InGaN/GaN [29].

The piezoelectric polarization can be calculated as follows:

$$\vec{P}_{pz} = \begin{pmatrix} 0 & 0 & 0 & 0 & e_{15} & 0 \\ 0 & 0 & 0 & e_{15} & 0 & 0 \\ e_{31} & e_{31} & e_{33} & 0 & 0 & 0 \end{pmatrix} \begin{pmatrix} \varepsilon_{xx} \\ \varepsilon_{yy} \\ \varepsilon_{zz} \\ \varepsilon_{yz} \\ \varepsilon_{xz} \\ \varepsilon_{xy} \end{pmatrix} \qquad \text{(Eq. I. 9)}$$

where ε_{kl} are the strain tensors and e_{ij} are the piezoelectric coefficients [9], [23]. Based on Eq. I.9, the piezoelectric field can either add up or subtract to the spontaneous field following the type of strain. The calculated piezoelectric coefficient values for AlN, GaN and InN are given in table I.5.

Table I.5. Piezoelectric coefficients for AlN, GaN and InN, respectively.

Piezoelectric coefficients ($C.m^{-2}$)	References	AlN	GaN	InN
e_{15}	[9], [30]	-0.48	-0.30	0.65
e_{31}	[23], [31]	-0.60	-0.49	-0.55
e_{33}	[23], [31]	1.46	0.73	1.07

For biaxial (0001) strain, the piezoelectric polarization (P_{pz}) can be expressed as follows:

$$P_{pz} = e_{33}\varepsilon_{zz} + e_{31}(\varepsilon_{xx} + \varepsilon_{yy}) \quad \text{(Eq. I. 10)}$$

and by combining equation (I.7) and equation (I.10), the piezoelectric polarization (P_{pz}) on the *c*-axis in strained layers grown along the same axis can be given by:

$$P_{pz} = 2.\varepsilon_{xx}(e_{31} - e_{33}\frac{C_{13}}{C_{33}}) \quad \text{(Eq. I. 11)}$$

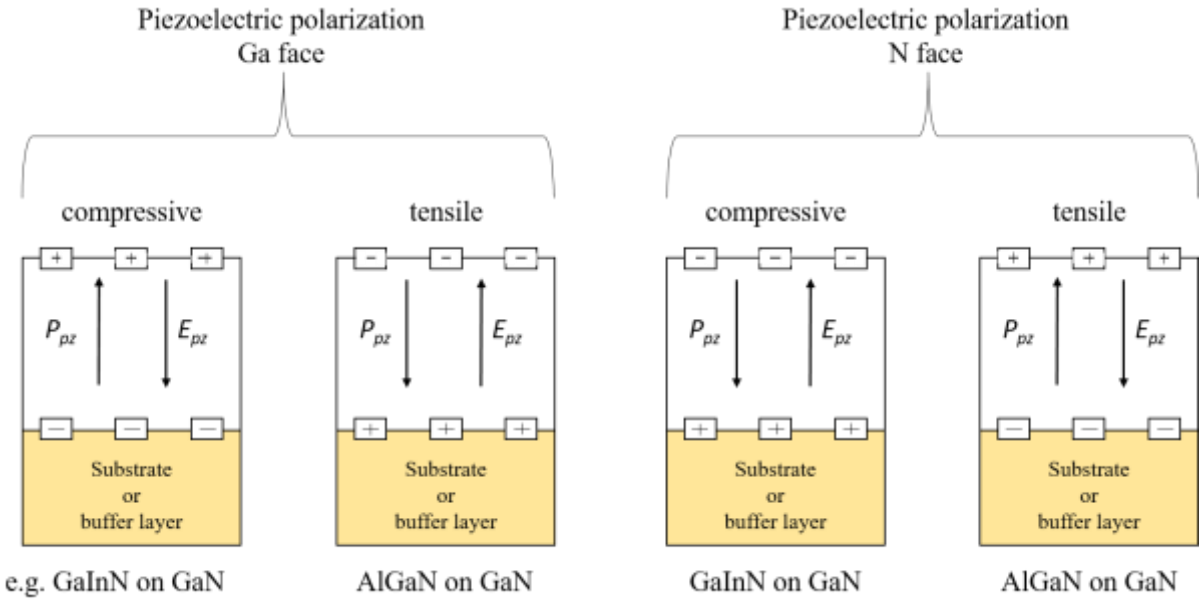

Figure 9. Schematic representation of the direction of the piezoelectric polarization (P_{pz}) and electric field (E) in III-nitrides for Ga and N face orientation [28].

The total polarization (*P*) in a III-nitride wurtzite structure is the sum of the spontaneous and piezoelectric polarizations:

$$\vec{P} = \vec{P}_{sp} + \vec{P}_{pz} \quad \text{(Eq. I. 12)}$$

In heterostructures, such as the case of GaN quantum wells in an AlGaN cladding layer, the total polarization of the two layers is different, which induces polarization discontinuities.

The polarization discontinuities is expressed in the formation of charge densities (-σ and +σ) at each interface which in its turn lead to the generation of an internal electric field in the heterostructure. The charge density (σ) at the interface of the two materials can be expressed as follows:

$$\sigma = P_{AlGaN\ sp} - \left(P_{GaN\ pz} + P_{GaN\ sp}\right) \quad \text{(Eq. I. 13)}$$

with σ the interfacial charge, P_{sp} and P_{pz} the spontaneous and the piezoelectric polarizations, respectively. The internal electric field generated by the surface charge density can then be expressed as:

$$F_{AlGaN} = \frac{\sigma}{2\varepsilon_0\varepsilon_{AlGaN}} \quad ; \quad F_{GaN} = -\frac{\sigma}{2\varepsilon_0\varepsilon_{GaN}} \quad \text{(Eq. I. 14)}$$

where ε_0 stands for the vacuum dielectric permittivity and ε_{AlGaN}, ε_{GaN} are the AlGaN and GaN relative permittivity, respectively.

The electric displacement vector ($\vec{D}$) inside the heterostructure is expressed as:

$$\vec{D} = \varepsilon_0\varepsilon\vec{F} + \vec{P} \quad \text{(Eq. I. 15)}$$

where $\vec{D}$ is conserved for each interface, which then renders it possible to write:

$$\vec{D}_{GaN} = \vec{D}_{AlGaN}$$

and it is possible then to generate the following equation:

$$\varepsilon_0\varepsilon_{GaN}F_{GaN} + P_{GaN} = \varepsilon_0\varepsilon_{AlGaN}F_{AlGaN} + P_{AlGaN} \quad \text{(Eq. I. 16)}$$

It is assumed that the barriers and the QDs have a similar static dielectric constant ($\varepsilon = \varepsilon_{AlGaN} = \varepsilon_{GaN}$), the internal electric field discontinuity (ΔF) in the GaN QD layer (for structures grown on relaxed AlGaN) equals to:

$$\Delta F = \frac{P_{AlGaN} - P_{GaN}}{\varepsilon_0\varepsilon} = \frac{\sigma}{\varepsilon_0\varepsilon} \quad \text{(Eq. I. 17)}$$

The internal electric field (F_{int}) generated distorts the band structure of the heterojunction, spatially separating the electrons and holes wave functions, thereby decreasing the transition energy and the radiative recombination probability, thus the internal quantum efficiency. This common effect in wurtzite *c*-plane structures is called the quantum confined stark effect (QCSE) [25], [32].

By assimilating the QDs to QWs, which means neglecting the lateral confinement effects, the fundamental transition energies for both QDs and QWs are:

$$E_{e1-hh1} = E_g^{QD} + E_{QD} - E_{Ry} - eF_{int}h_{QD} \quad \text{(Eq. I. 18)}$$

$$E_{e1-hh1} = E_g^{QW} + E_{QW} - E_{Ry} - eF_{int}h_{QW} \quad \text{(Eq. I. 19)}$$

where E_g^{QD}, E_g^{QW} refer to the band gap energy of the QD and the QW respectively, E_{QD}, E_{QW} are the quantum confinement energies in the conduction and valence bands of QD and QW, respectively. F_{int} is the internal electric field while h_{QD}, h_{QW} are the QD (average) heights and QW thicknesses, E_{Ry} is the Rydberg energy corresponding to the excitonic binding energy and e is the electronic charge.

I.1.3 Band structure

III-nitrides are direct band gap semiconductors (figure 10), where AlN, GaN, InN and their alloys cover a wide range of the wavelength spectrum ranging from infrared (IR) to ultraviolet (UV) including the visible spectrum. This particular aspect of III-nitrides was one of the main reasons behind the large interest in developing III-V semiconductor devices.

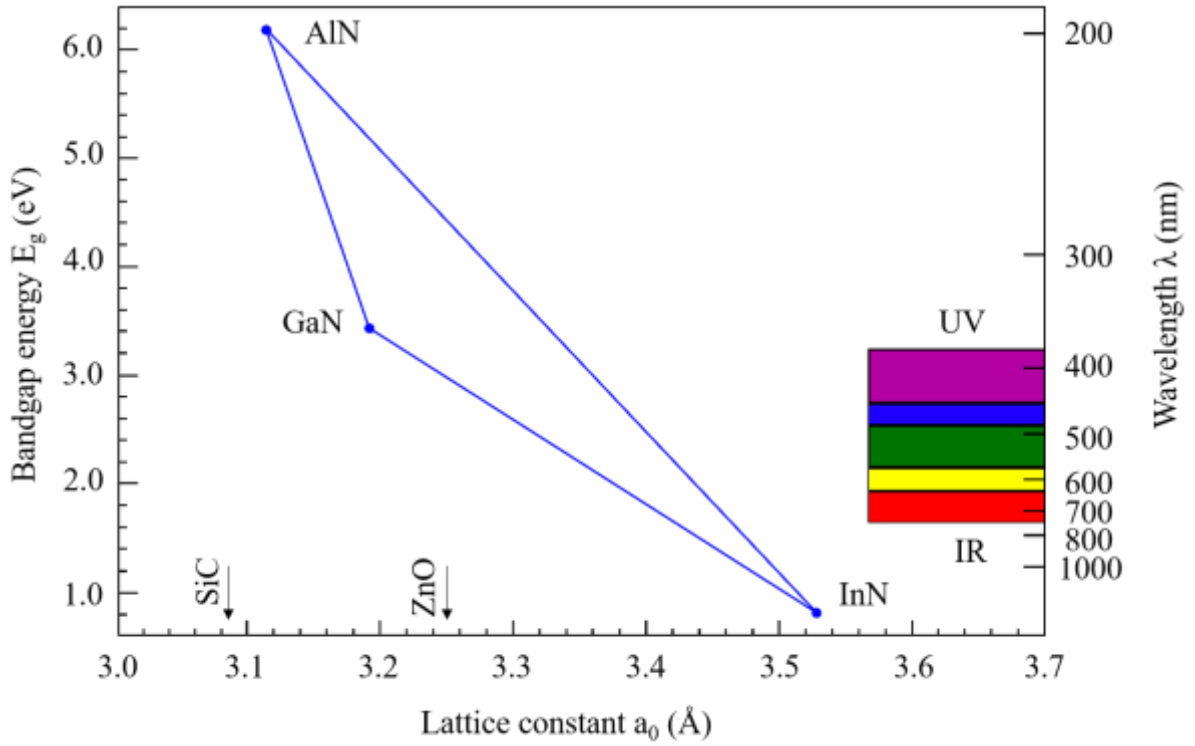

Figure 10. Bandgap energy (E_g) as a function of the lattice constant (a_0) for III-nitride semiconductors at room temperature (300 K) [28].

For a III-nitride direct band gap semiconductor, the minimum of the conduction band and the maximum of the valence band are located at the Γ point (at 0 K). That means the radiative recombination (i.e. the direct band-to-band transition of an electron from the conduction band to the valence band resulting in an emission of a photon) is a first order transition with no phonon involved with a short radiative lifetime. This can result in a large quantum efficiency for semiconductor devices [33]. The electronic band structures of AlN and GaN are shown in figure 11. The hexagonal symmetry of the wurtzite structure (also referred to as the crystal-field splitting or Δ_{cr}) and the spin-orbit interaction (coupling), split the valence band into three subband levels (Γ_7 and Γ_9), which give the possibility for three excitonic transitions (A, B and C) from the valence bands to the conduction band. In addition, the determination of an excitonic transition (A or B or C) is dependent on which valence band the hole originates, for example, the excitonic transition A ($E_c^0 - E_1^0$) is $\Gamma_7^C - \Gamma_7^V$ in AlN, and $\Gamma_7^C - \Gamma_9^V$ in GaN [34].

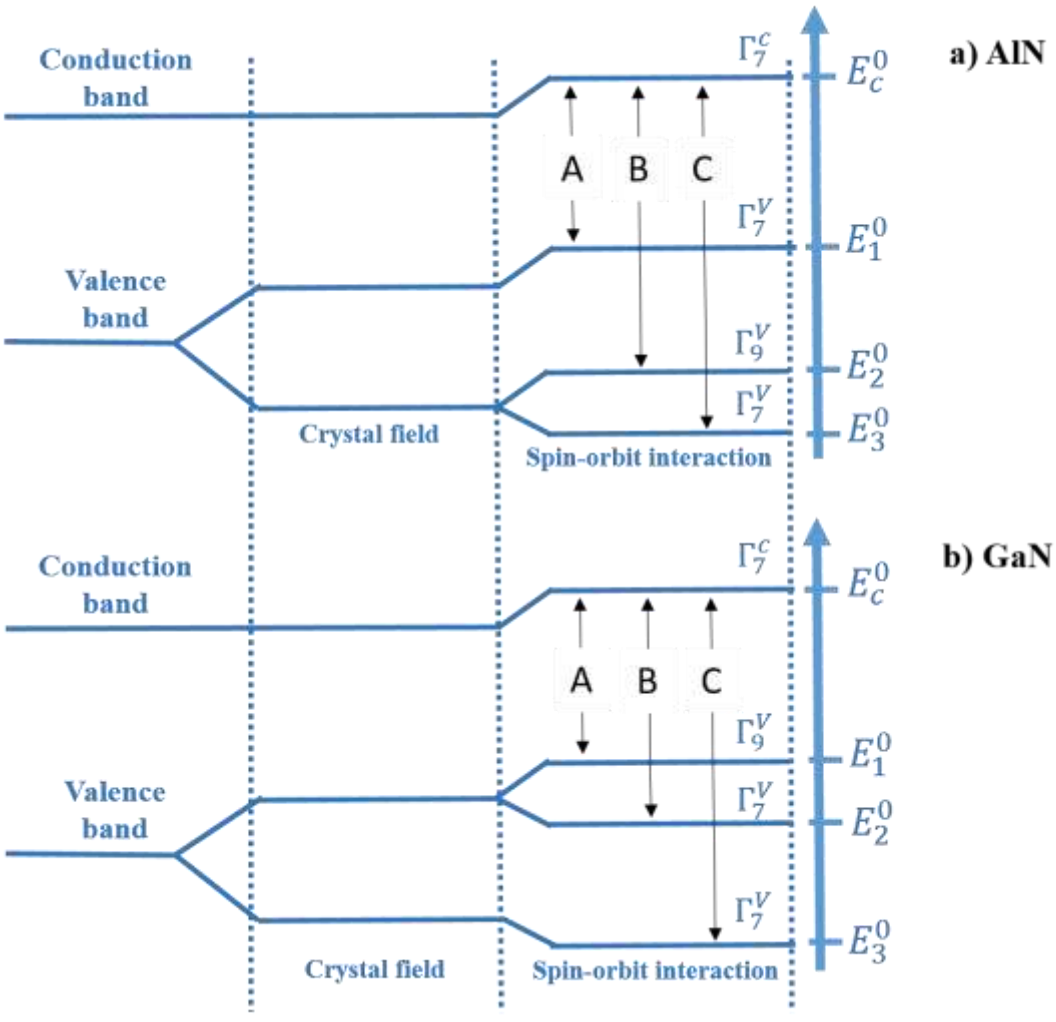

Figure 11. Schematic representation of the band structure for a) AlN and b) GaN [35], [36].

A full valence band and an empty conduction band is defined as the ground state in a semiconductor. In a first excited state, a negatively charged electron in the conduction band undergoes an electrostatic Coulomb force with a positively charged hole in the valence band forming an electron-hole pair (exciton); the transition is referred to as an excitonic transition. The energy of this excitonic transition is lower than the energy of the crystal band gap. It is equal to the band gap energy minus the binding energy of the exciton (Rydberg excitonic) [37] as presented in equation I.20:

$$E_{exc}(K) = E_g + E_n + \frac{\bar{h}^2 K^2}{2M} \; with \; E_n = -\frac{1}{n^2}\frac{\mu}{m_0 \varepsilon_r^2} R_y \qquad \text{(Eq. I. 20)}$$

where E_g stands for the band gap energy, E_n for the binding energy of the exciton, K the exciton wave vector, M and μ are the total effective mass and the reduced mass of the electron-hole pair, respectively. R_y stands for the Rydberg constant of the hydrogen atom, m_0 the electrons effective mass and ε_r the dielectric constant. It has also been reported that the strain in the layers has an influence on the excitonic transition energies [38].

The crystal field splitting (Δ_{cr}) for AlN is strongly negative (Δ_{cr}= - 169 meV [38]) which results in the subbands being splitted into two subbands with the symmetry of the holes situated in the base state Γ_7 (figure 11 (a)). For GaN, Δ_{cr} is slightly positive (Δ_{cr}= 10 meV [39]), which also results in the splitting of the subbands with the symmetry of the holes in the ground state Γ_9 (figure 11 (b)). In $Al_xGa_{1-x}N$ alloys, M. Leroux et al. demonstrated that a gradual increase in the Al composition (starting from $x_{Al} > 0.05$) induces a symmetry inversion of the top of the valence band by changing the hole ground state from Γ_9^V to Γ_7^V [40].

The band gap energy value of a nitride ternary alloy $Al_xGa_{1-x}N$ can be calculated using the following equation:

$$E_g(Al_xGa_{1-x}N) = xE_g(AlN) + (1-x)E_g(GaN) - x(1-x)b(AlGaN) \qquad \text{(Eq. I. 21)}$$

where b is the bowing parameter defined as the coefficient of the parabolic term in the phenomenological expression of alloy energy band gap, i.e. equation I.21. The bowing parameter b for $Al_xGa_{1-x}N$ alloys is estimated to be around 0.9 eV for $x_{Al} \leq 0.3$ [40].

Temperature is one of the parameters affecting the band gap energy, and the variation of the band gap energy as a function of temperature can be described using Varshni's law [41]:

$$E_g(T) = E_g(0) - \frac{\alpha T^2}{\beta + T} \quad \text{(Eq. I. 22)}$$

where $E_g(0)$ stands for the band gap energy at T = 0 K, α and β are fitting parameters. The band gap parameters for AlN, GaN and InN are given at low (0 K) and room temperatures (300 K) in table I.6.

Table I.6. Band gap parameters at low (0 K) and room (300 K) temperatures for AlN, GaN and InN.

	AlN	GaN	InN
E_g at 0 K (eV)	6.12 6.242	3.47 3.492	0.69
E_g at 300 K (eV)	6.026 6.16	3.411 3.426	0.642
α (meV / K)	1.799 0.72	0.59 0.531	0.414
β (K)	1462 500	600 432	454
References	[42] [43]	[44] [45]	[46]

I.2 Ultraviolet light sources

Population expansion, pollution (water, soil, and air), pandemics are some of many current problems facing our societies, demanding sustainable solutions in areas like water sterilization for clean drinkable water, food safety, healthcare, air purification, etc.. One scientific breakthrough offered a solution in the field of health safety and environment. The application of high-energy ultraviolet (UV) light sources has proven to be an effective method in killing bacteria and viruses, replacing the use of chemical treatments instead. A specific spectrum in the UV ranging from 200 to 280 nm (UV-C range) has attracted most interest since it is considered the germicidal range of UV radiation, where the damaging effect on intercellular components (e.g., DNA, RNA, and proteins) of microbes occurs [48], as shown in figure 12.

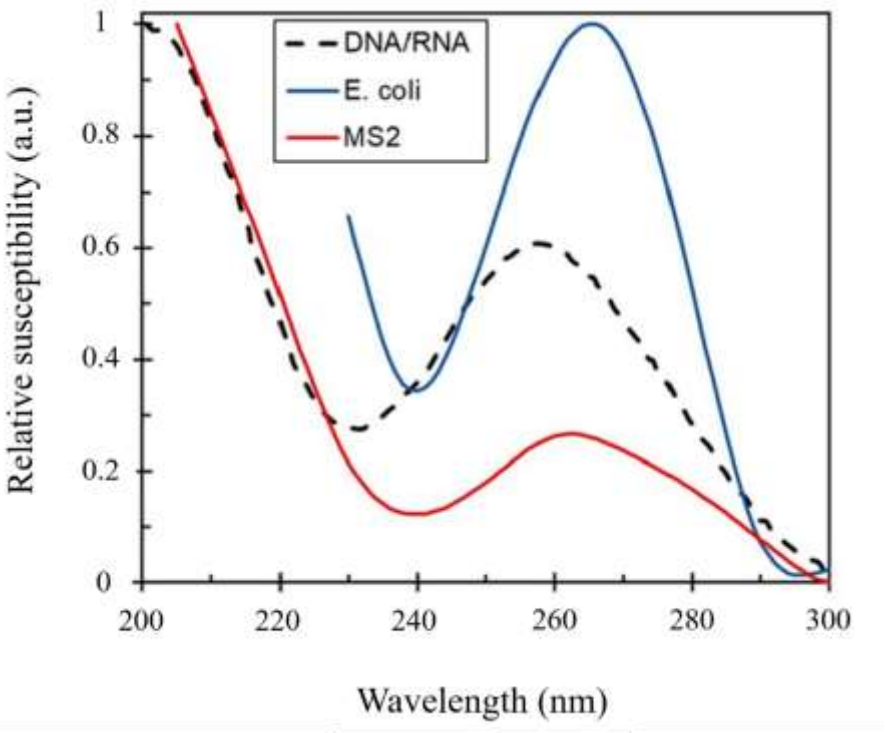

Figure 12. UV susceptibility of a general DNA or RNA, E. coli and MS2 [47].

The absorbed UV radiation damages the genomic system by destroying the adenine-thymine bond and generating a covalent linkage, pyrimidine dimer, between two adenines preventing the replication of the nucleic coding [49], as shown in figure 13.

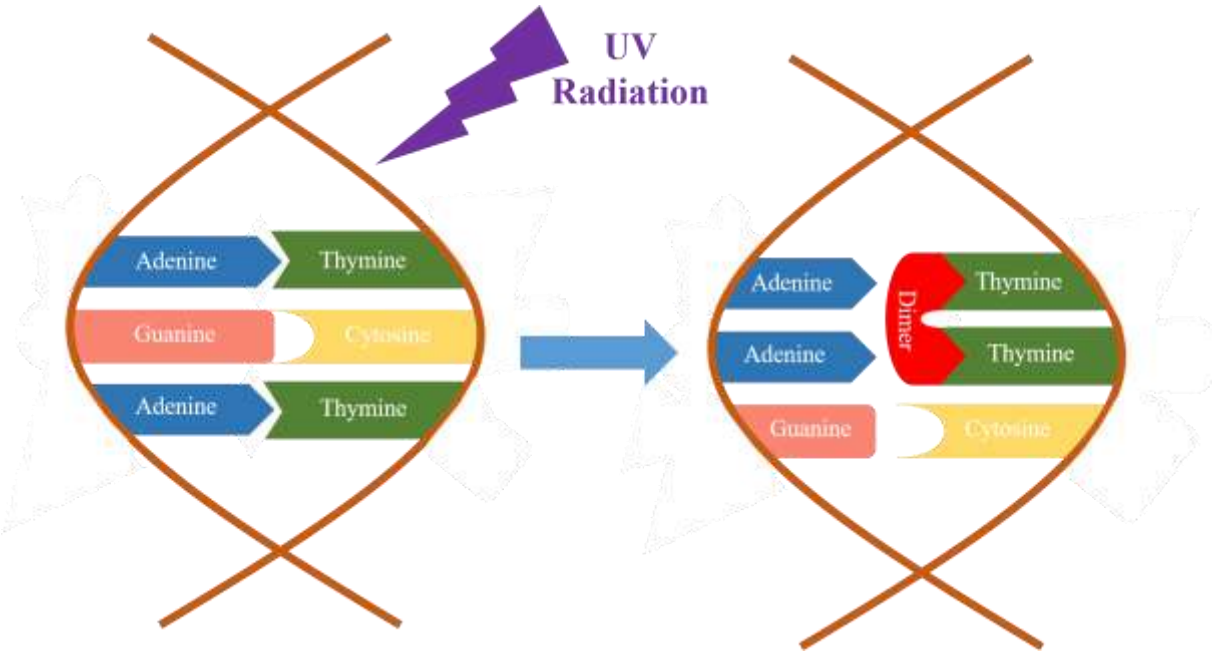

Figure 13. Schematic of a UV exposed double-stranded DNA undergoing a thymine dimerization [47].

The main share in the UV market belongs to UV emitters by gas discharge, with mercury (Hg) based lamps being the most common UV emitting devices with an emission spectrum covering from deep UV to infrared. Mercury (Hg) vapor lamps are divided into three categories: low pressure (LP), amalgam low pressure (ALP), and medium pressure (MP). The operating characteristics of the three types of lamps are presented in table I.7. where the energy conversion efficiency for these devices ranges between 10 and 40%. Despite their high energy conversion efficiency, they suffer from technical disadvantages such as their large sizes, high operating voltage, high operating temperature that decrease the working lifetime resulting in slower on/off switching times [50]. Besides, mercury is a toxic material that damages the environment. For this reason, the Minamata Convention held in Japan on October 10 2013 resulted in an international treaty that focuses on limiting the use of mercury and mercury-based devices, which cleared the way for the development of more efficient clean light sources [51].

Table I.7. Operating characteristics of the commercial Hg lamps [50], [52], [53].

Hg lamp type	Low pressure (LP)	Amalgam low pressure (ALP)	Medium pressure (MP)
Emission (nm)	Monochromatic (185 nm or 254 nm)	Monochromatic (185 nm or 254 nm)	Polychromatic
Conversion efficiency (%)	40	~ 35	15
Output power (W/cm)	< 1.5	< 6	300
Operation temperature (°C)	< 40	< 110	~ 900
Lifetime (kh)	12	> 12	9
Lamp length (cm)	10-150	25-150	5-200
Lamp price ($)	~10-100	~50-500	~500-3000

- ## State of the art of UV LEDs

Scientific development in semiconductors technology together with the international tendency in limiting the use of mercury-based devices paved the way for the mass adoption of UV light emitting diodes (LEDs). UV LEDs are semiconductor devices that emit light in a cleaner, efficient, and less toxic way. The UV spectrum is divided into three regions: UV-A

(from 400 to 320 nm), UV-B (from 320 to 280 nm) and UV-C (< 280 nm). The advantage with UV LEDs is the ability to tune the emission wavelength by adjusting the thickness and the composition of the LED structure rather than emitting at a fixed wavelength like in the case of Hg lamps. (Al,Ga)N based UV LEDs prove this advantage with its ability to cover a wide range of the UV spectrum by tuning the band gap emission from 3.4 eV (for GaN) to 6.1 eV (for AlN) at room temperature (300 K). This advantage broadened the field of application for UV LEDs as a function of the UV wavelength, as shown in figure 14. In addition, with the COVID-19 outbreak, the UV LED market witnessed a significant growth with countries like the United States and China using the technology for disinfection and it is expected to reach a market share of 2.19 billion USD by 2030 with a compound annual growth rate (CAGR) of 19.17% [54].

Following the transition from (In,Ga)N to (Al,Ga)N-based LEDs (shorter wavelengths < 365 nm), a sharp drop in the external quantum efficiency (EQE) occurs [55]. Figure 15 represents the state of the art of EQE in UV LEDs over almost two decades of development.

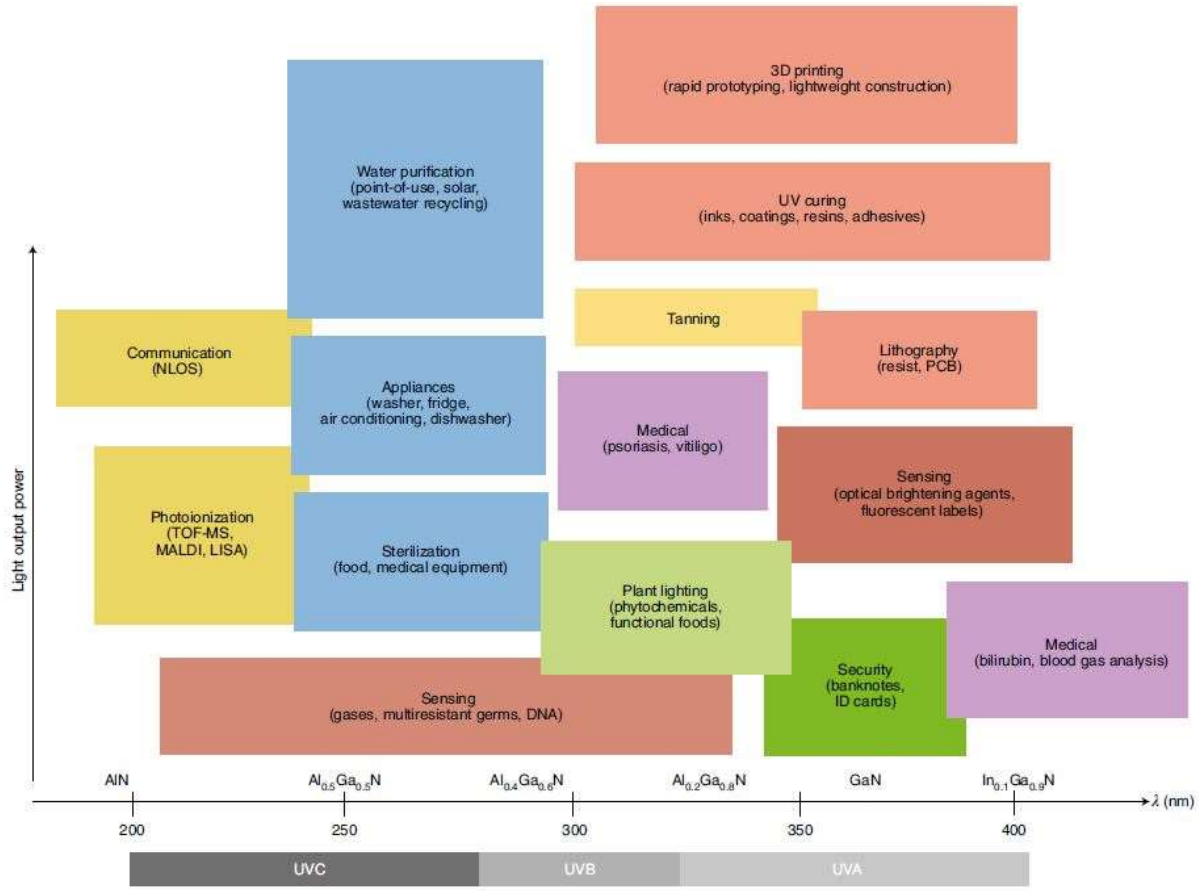

Figure 14. Schematic diagram illustrating various applications of UV-A, UV-B, and UV-C LEDs [55].

Blue LEDs defined by their high performance levels (EQE up to 85%) and InGaN-based near-UV emitters (from 400 to 365 nm) use the same materials and device technology (growing the LED structure on GaN/sapphire templates), which gave InGaN-based LEDs an important advantage for its industrial development. Over the years, near UV LEDs reached performance levels and EQE close to the blue LEDs ones (EQE ≈ 46-76 %) [55], [56]. For (Al,Ga)N based UV LEDs (for $\lambda < 365$ nm), the EQE is mainly in the single digit percentage range. Despite recent progress reporting an increase in the efficiency to around 20 % for UV-C LEDs emitting around 275 nm, the EQE is still low for wavelengths shorter than 350 nm [55], [57], as shown in figure 15. The contributing factors in limiting the performance of UV LEDs, especially deep-UV (DUV) LEDs, are three key parameters that represent the efficiency of different processes in the LED: the internal quantum efficiency (IQE), the injection efficiency (IE), and the light extraction efficiency (LEE). The IQE is defined as the ratio of the number of created photons in the active region to the number of charge carriers (electron-hole pairs) injected in the active region. The IE is defined as the ratio of the number of charge carriers injected in the active region to the total number of injected carriers in the whole device's structure. The LEE is defined as the ratio of the number of extracted photons from the device to the number of the created photons in the active region.

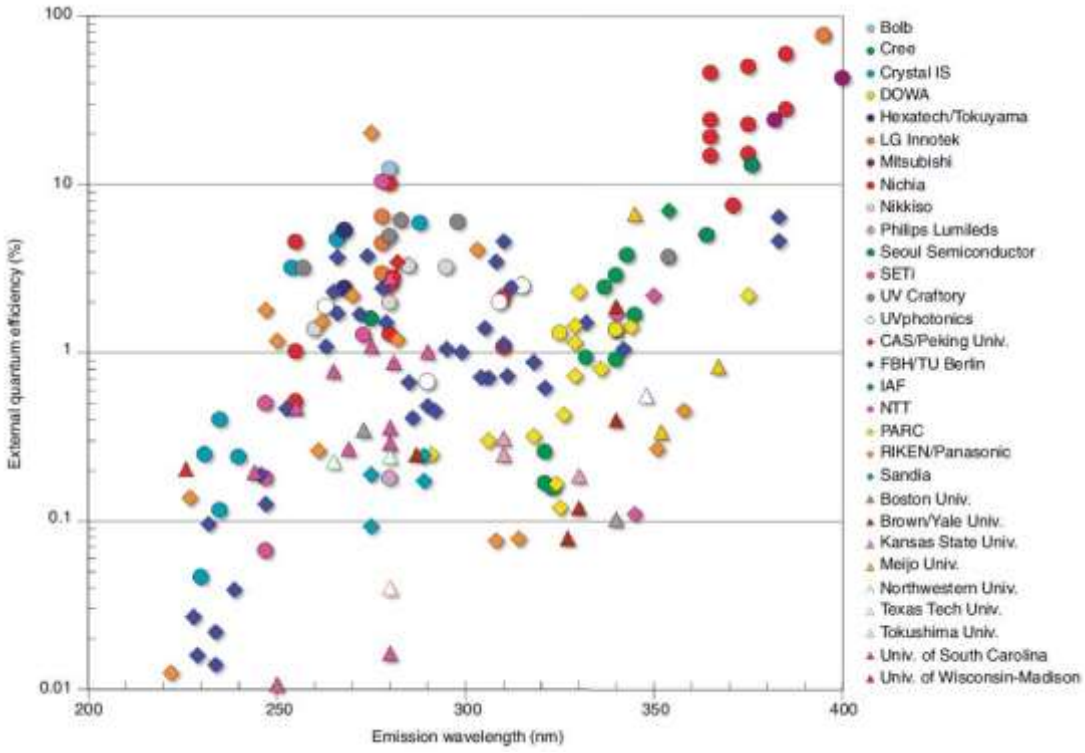

Figure 15. State of the art of external quantum efficiency (EQE) as a function of the wavelength of emission for ultraviolet (UV) LEDs [55].

The EQE can thus be described as the product of three key parameters, the IQE, the IE, and the LEE:

$$\eta_{EQE} = \eta_{IQE} \cdot \eta_{IE} \cdot \eta_{LEE} \quad \text{(Eq. I. 23)}$$

The optical output power (P_{out}) can then be expressed as:

$$P_{out} = \eta_{EQE} \frac{h\omega}{e} I_{op} \quad \text{(Eq. I. 24)}$$

where η_{EQE} is the external quantum efficiency, h is Planck constant, ω the generated photons frequency, e the elementary charge, and I the current.

The power conversion efficiency or the wall plug efficiency (WPE) can then be calculated as the ratio of P_{out} and the injected electric power (P_{inj}):

$$WPE = \frac{P_{out}}{P_{inj}} = \frac{P_{out}}{I_{op}V} = \eta_{EQE} \frac{h\omega}{Ve} \quad \text{(Eq. I. 25)}$$

Figure 16 illustrates a standard (Al,Ga)N based UV LED structure along with the key challenges facing the structure from epitaxial to polarization to electrical challenges.

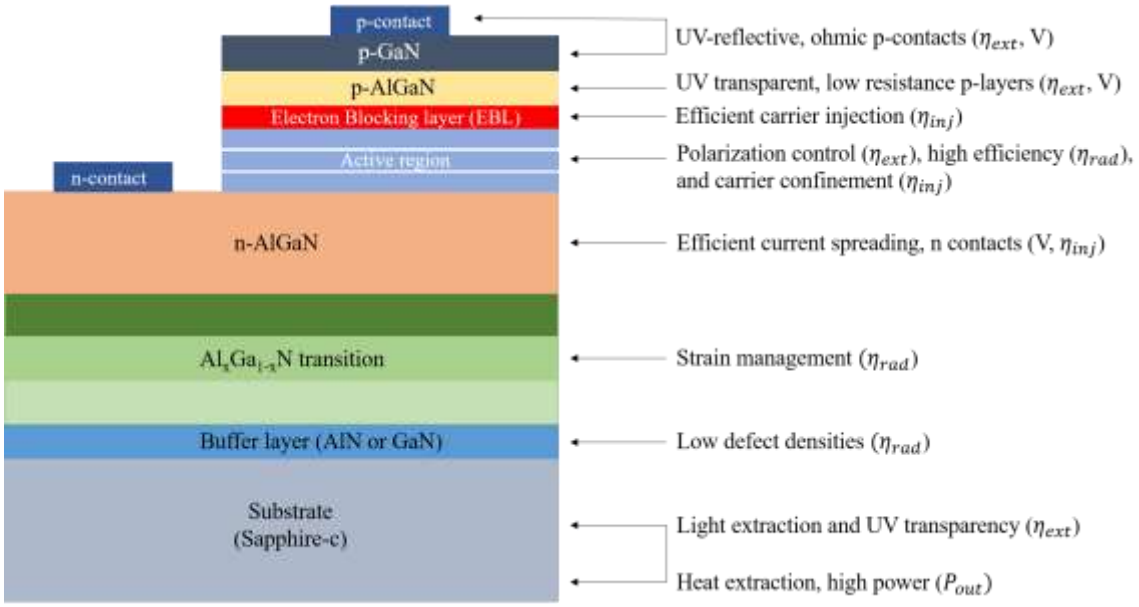

Figure 16. Schematic of a standard (Al,Ga)N UV LED with the key challenges and their impact on the main efficiency terms.

Improvements are required in all sections of the structure in order to increase the injection, radiative (the ratio of the radiative recombinations' rate to the total recombinations' rate), electrical (ratio of the useful electrical output that has been converted into photons to the electrical input required to operate the device) and extraction efficiencies. Most of the key

parameters are interdependent though, and that makes the solutions more complicated to develop. The key challenges affecting the efficiency of the device will be covered in the next three sections, respectively.

I.2.1 Internal quantum efficiency (IQE) challenge

Enhancing the IQE in UV LEDs is a major concern for researchers, including our group, which have made substantial progress in recent years. This progress primarily relies on the improvement of the rate of radiative recombination within the device by reducing structural defects' density in (Al,Ga)N materials, such as dislocations and point defects which serve as non-radiative recombination centers thereby reducing the IQE in UV LEDs. Nitrides' heterostructures are particularly affected by threading dislocations (TDs), which are linear defects within the crystal lattice that propagate through the layers of the structure, extending from the substrate through the epitaxial layers, interrupting the regular arrangements of atoms, as shown in figure 17. They arise from heteroepitaxial growth where the significant lattice mismatch between the epilayers and substrate in (Al,Ga)N alloys cause strain and misalignment between the different layers of the heterostructure. The low Al mobility on the growth surface leads to the formation of high-density, small-area islands, from which TDs are shown to originate at coalescence interfaces, a shown in figure 18. Consequently, TDs density increases with decreasing Al mobility as a function of the Al concentration in (Al,Ga)N, resulting in a strong decrease in the radiative efficiency (i.e. IQE) of the LEDs as soon as the density value exceeds 10^8 cm^{-2}.

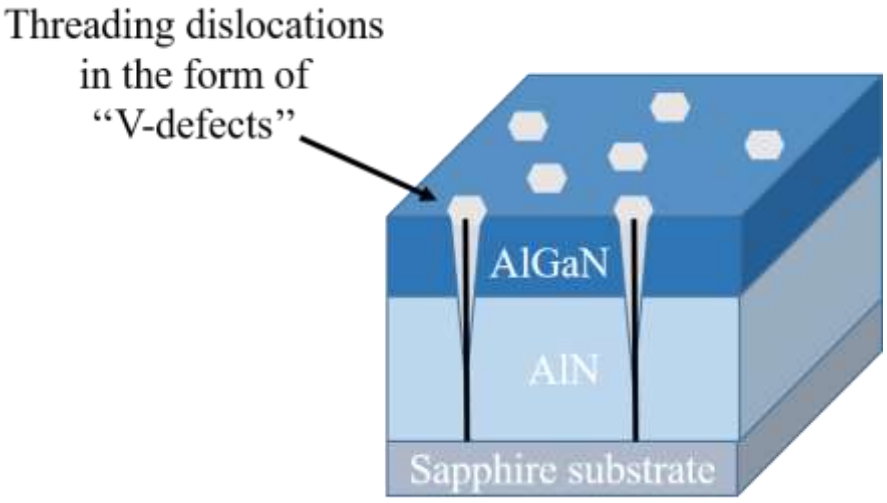

Figure 17. Schematic illustration of threading dislocations (TDs) in an (Al,Ga)N heterostructure.

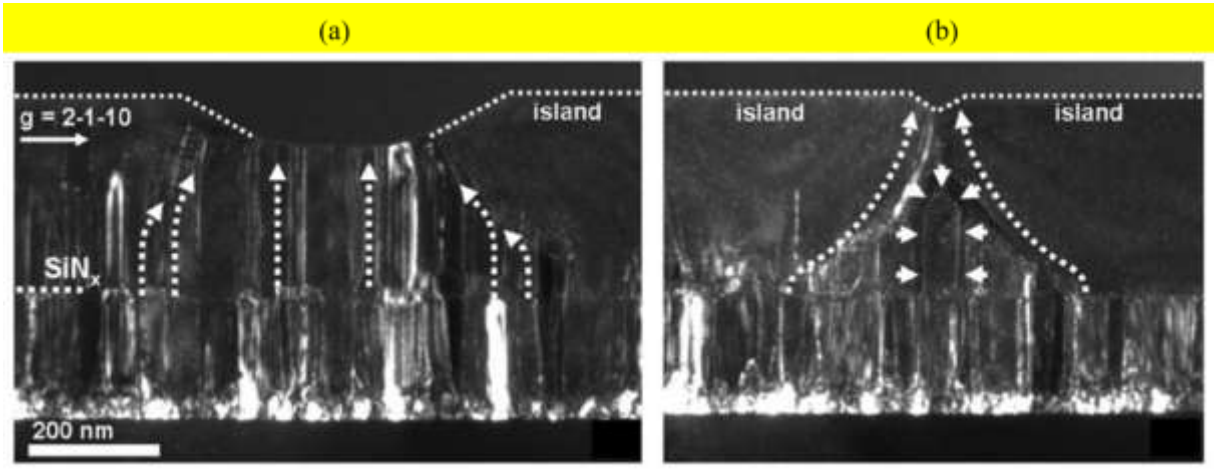

Figure 18. Weak-beam dark-field (WBDF) images between two AlGaN islands. (a) The dashed arrows indicate the general propagation direction of the TDs in the AlGaN overlayer between not coalesced islands where the TDs propagate straight. (b) The coalescence of two AlGaN islands leads to very small areas with TDs at the surface due to the bundling and the formation of dislocation loops (white arrows in b) [58].

Several research groups have conducted investigations and reported the improvement of the IQE in (Al,Ga)N quantum well based UV LEDs as a result of the reduction of the dislocations density (figure 19) [55], [59], [60]. Additionally, (Al,Ga)N structures with high internal electric field discontinuities (up to 9-10 MV / cm for the GaN / AlN system) lead to significant spatial separation of the electron and hole wavefunctions, resulting in a further decrease in the radiative transition rate and a reduction in IQE [61].

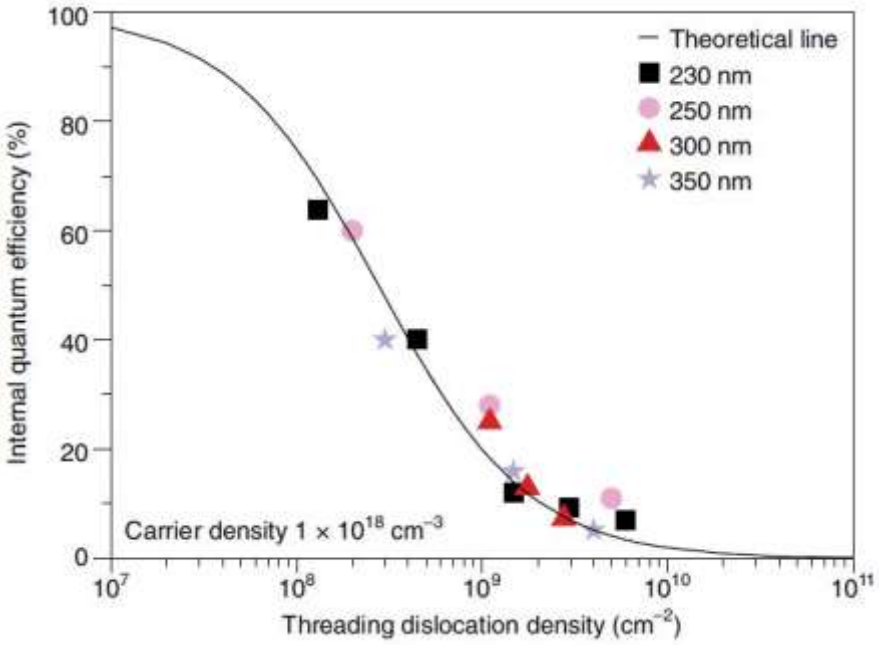

Figure 19. Internal quantum efficiency (IQE) of (Al,Ga)N multiple quantum wells (MQWs) as a function of threading dislocation density (TDD) [55], [59].

Despite offering high crystal quality and low TDs density (< 10^5 cm^{-2}), native AlN bulk substrates are limited by their high cost (~2000 $ for a 2-inch wafer), scarcity, and small sizes (< 2 inches). Therefore, most of the research efforts are directed towards reducing the TDs density in AlN layers grown on foreign substrates such as sapphire and silicon (Si).

Several techniques have been approached to improve the crystalline quality and surface morphology of (Al,Ga)N layers on sapphire substrates such as growing low-defect density AlN templates by migration enhanced epitaxy (MEE). MEE is a crystal growth technique that involves the periodic and alternating supply of the Al and N fluxes to the growing buffer layer. It enhances the migration of the adsorbed atoms, leading to improved crystal quality and low defect densities in the resulting film [62]. Some growth techniques that use MEE are metal organic chemical vapor deposition (MOCVD), lateral epitaxial overgrowth (LEO), and molecular beam epitaxy (MBE).

	X-Ray Diffraction FWHM		Threading Dislocation Densities (TDDs) (cm^{-2})
	Symmetric planes (°)	Asymmetric planes (°)	
MBE	~0.1°	~0.5°	~10^{10}-10^{11}
MOCVD	~0.1°	~0.4°	~10^{9}-10^{10}
ELO	~0.04°	~0.08°	~10^{8}

Table I.8: AlN crystal properties vs. different MEE growth techniques [63, 64, 65, 66].

Another technique is growing a low temperature AlN buffer layer (LT-BL), where Matta et al. reported the improved surface morphology and crystalline quality of AlN layers and AlGaN subsequent layers. [63]. They focused on studying the crystalline and morphological properties of 120 nm thick AlN epilayers grown on c-sapphire substrates using ammonia-assisted MBE. Initially, they examined the impact of the low temperature AlN buffer layer (LT-BL) by varying its thickness (0 to 10 nm) (figure 20) and the growth temperature (390 °C to 580 °C). The results showed that reducing the LT-BL thickness from 10 nm to 3 nm led to an improvement in structural quality, with a significant reduction in mixed and edge threading dislocation (TD) densities by up to 65% [63].

(a)

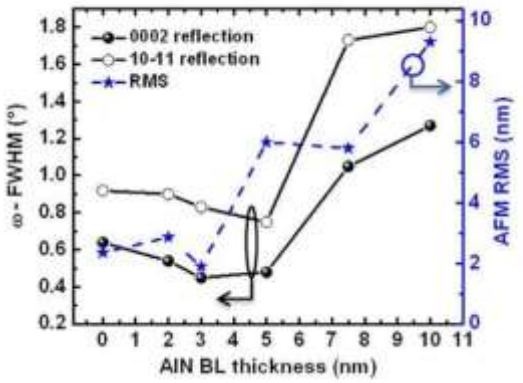

(b)

LT-BL thickness (nm)	(0 0 0 2) (°)	(1 0 −1 1) (°)	RMS (nm)	Mixed TD density (cm^{-2})	Edge TD density (cm^{-2})
0	0.64	0.92	2.40	2.2×10^{10}	7.3×10^{10}
2	0.54	0.90	2.90	1.8×10^{10}	7.1×10^{10}
3	0.45	0.83	1.90	1.5×10^{10}	6.6×10^{10}
5	0.48	0.75	6.00	1.6×10^{10}	5.9×10^{10}
7.5	1.05	1.73	5.80	3.5×10^{10}	1.4×10^{11}
10	1.27	1.8	9.30	4.3×10^{10}	1.4×10^{11}

Figure 20. (a) Variation of the ω-scan FWHM of the (0 0 0 2) and (1 0 −1 1) reflections, and of the RMS roughness as a function of the AlN BL thickness for LT-BL grown at 480°C. The RMS values are measured on (10 × 10) μm^2 atomic force microscopy topographic images. (b) Main crystalline and morphological properties of 120 nm thick AlN epilayers grown on low temperature (480°C) AlN buffer layers with different thicknesses, and measured by X-ray diffraction and atomic force microscopy [63].

The effects of LT-BL growth temperatures were also studied and an optimum range between 480 °C and 520 °C resulted in a reduction of edge TD density by up to 75%, as shown in figure 21 (a).

(a)

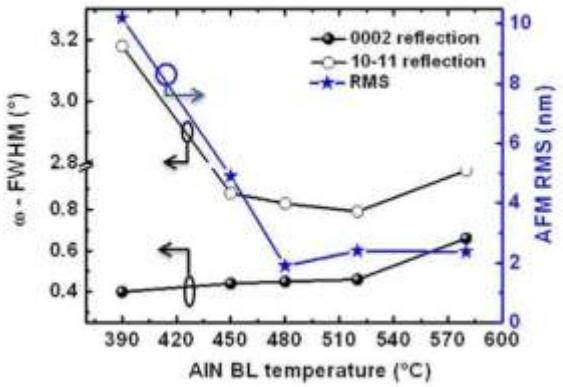

(b)

LT-BL temperature (°C)	(0 0 0 2) (°)	(1 0 −1 1) (°)	RMS (nm)	Mixed TD density (cm^{-2})	Edge TD density (cm^{-2})
390	0.40	3.18	10.2	1.3×10^{10}	2.5×10^{11}
450	0.44	0.88	4.90	1.5×10^{10}	7.0×10^{10}
480	0.45	0.83	1.90	1.5×10^{10}	6.6×10^{10}
520	0.46	0.79	2.40	1.6×10^{10}	6.3×10^{10}
580	0.66	0.99	2.30	2.2×10^{10}	7.8×10^{10}
AlN epilayer grown at 1000°C	0.16	0.73	1.18	5.4×10^{9}	5.8×10^{10}

Figure 21. (a) Variation of the ω-scan FWHM of the (0 0 0 2) and (1 0 −1 1) reflections, and of the RMS roughness as a function of the AlN BL growth temperature. The RMS values are measured on (10 × 10) μm^2 atomic force microscopy topographic images. (b) Main crystalline and morphological properties of 120 nm thick AlN epilayers grown on different AlN buffer layers (with a thickness of 3 nm) using different temperatures. The last sample is an AlN epilayer with a thickness of 120 nm that was grown at higher temperature (~1000 °C) compared to the rest of the samples which were grown at ~940 °C [63].

The optimal conditions were determined to be a 3 nm LT-BL thickness and a growth temperature between 480 °C and 520 °C. The study also examined the growth temperature of the 120 nm AlN epilayer and found further improvements in crystalline quality (observed

through (0 0 0 2) and (1 0 −1 1) reflections with angles of 0.16° and 0.73°, respectively) and morphological properties (with a surface roughness of approximately 1 nm) at higher temperatures (around 1000 °C), as shown in figure 21 (b) [63].

Another approach is by growing AlN/AlGaN superlattices (SLs) where the lattice-mismatch-induced strain between the layers cause the dislocations to bend or terminate at the interface between the layers, effectively blocking their propagation into the upper layers [64]. Multiple research groups have reported improvements in the crystalline quality of the AlGaN layer when AlN/AlGaN SLs are incorporated. X-ray diffraction measurements of symmetric and asymmetric reflections have revealed smaller FWHM values for structures with SLs compared to those without (173 arcsec = 0.05° and 703 arcsec = 0.19° for the (0 0 0 2) and (1 0 −1 5) reflections, respectively), as depicted in Figure 22 (c). Moreover, the SLs have been found to reduce dislocation densities originating from the interface between the AlN buffer layer and sapphire, as shown in Figure 22 (d). The edge dislocation densities for structures with SLs decreased to values of 5-6 x 10^{9} cm^{-2}, while structures without SLs exhibited higher densities of approximately 2-3 x 10^{10} cm^{-2} [64].

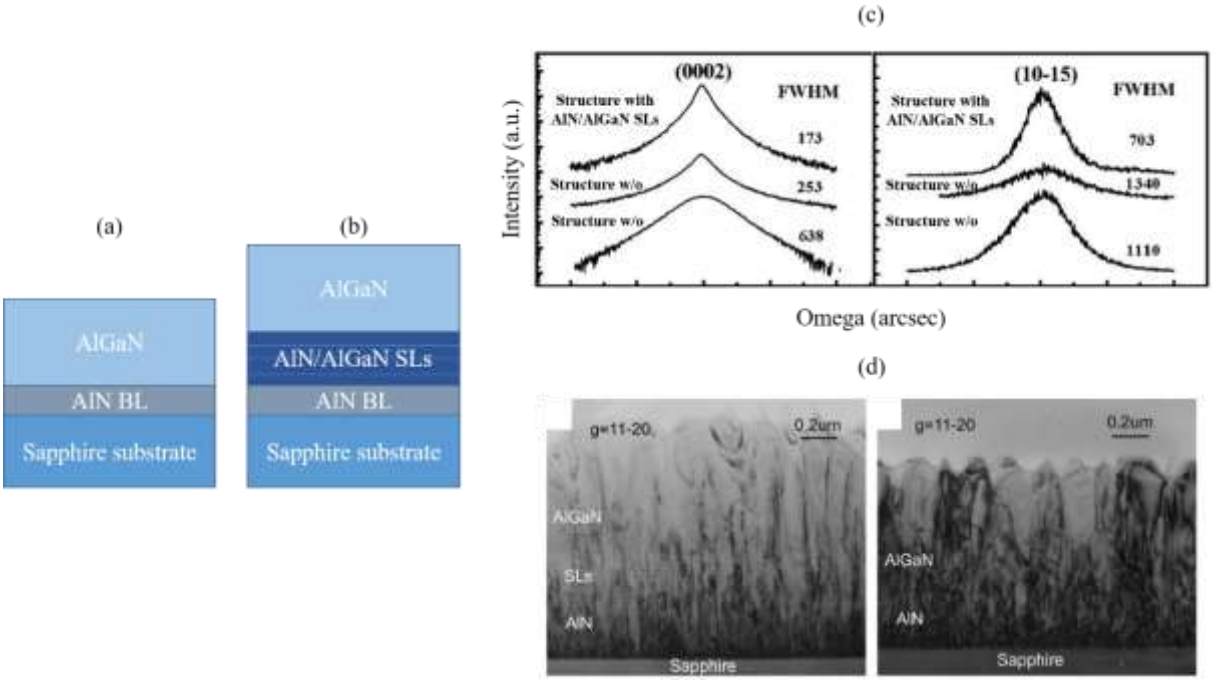

Figure 22. (a) Schematic illustration of an AlGaN structure grown without SLs, (b) AlGaN structure grown with AlN / AlGaN SLs, (c) x-ray rocking curve diffraction measurements of (0 0 0 2) and (1 0 −1 5) symmetric and asymmetric reflections for samples with and without AlN / AlGaN SLs, and (d) two-beam bright field cross-sectional TEM images of a structure with SLs and of a structure without SLs, with diffraction vector g = 1 1 $\bar{2}$ 0 [64].

Post-growth annealing, in particular, face-to-face annealing (FFA) is another solution that helps improve the crystal and morphological properties of AlN templates. The procedure involves placing two AlN substrates in a face-to-face configuration and subjecting them to a high temperature annealing process under a nitrogen atmosphere, as shown in figure 23 (a). This arrangement is crucial for preventing thermal decomposition of the AlN films during annealing. The AlN templates are exposed to temperatures surpassing their recrystallization threshold, enabling the rearrangement and relaxation of the crystal structure. The direct contact between the AlN substrates promotes the diffusion of atoms across the interface, facilitating the repair of defects, reduction of dislocations, and enhancement of the crystal's quality. The elevated temperature enhances the mobility of atoms and vacancies within the crystal lattice, facilitating the migration and elimination of defects at the interface. Consequently, dislocations can glide and annihilate, leading to a decrease in density and an overall improvement in the crystal quality of the AlN templates. This post-growth annealing technique was developed by Miyake et al. on sputtered and MOVPE grown AlN on sapphire and adopted by other research groups where improved crystalline quality and surface morphology of AlN layers were reported [65]–[68].After the thermal annealing process, the AlN films exhibited a reduction in TD density, reaching a minimum value of 4.7 x 10^8 cm^{-2}. Additionally, the surface morphology underwent a transition from nanometer-sized columnar structures with a high density covering the entire surface prior to annealing, to a step and terrace morphology resulting from the coalescence of the columnar structures. This transformation can be observed in figure 23 (b). X-ray measurements further confirmed the improvement in the crystalline quality, as indicated by a significant decrease in the (0 0 0 2) symmetric plane from 532 arcsec (0.15°) to 49 arcsec (0.01°), and in the (1 0 −1 2) asymmetric plane from 6031 arcsec (1.7°) to 287 arcsec (0.08°) [65]. These results are depicted in figure 23 (c).

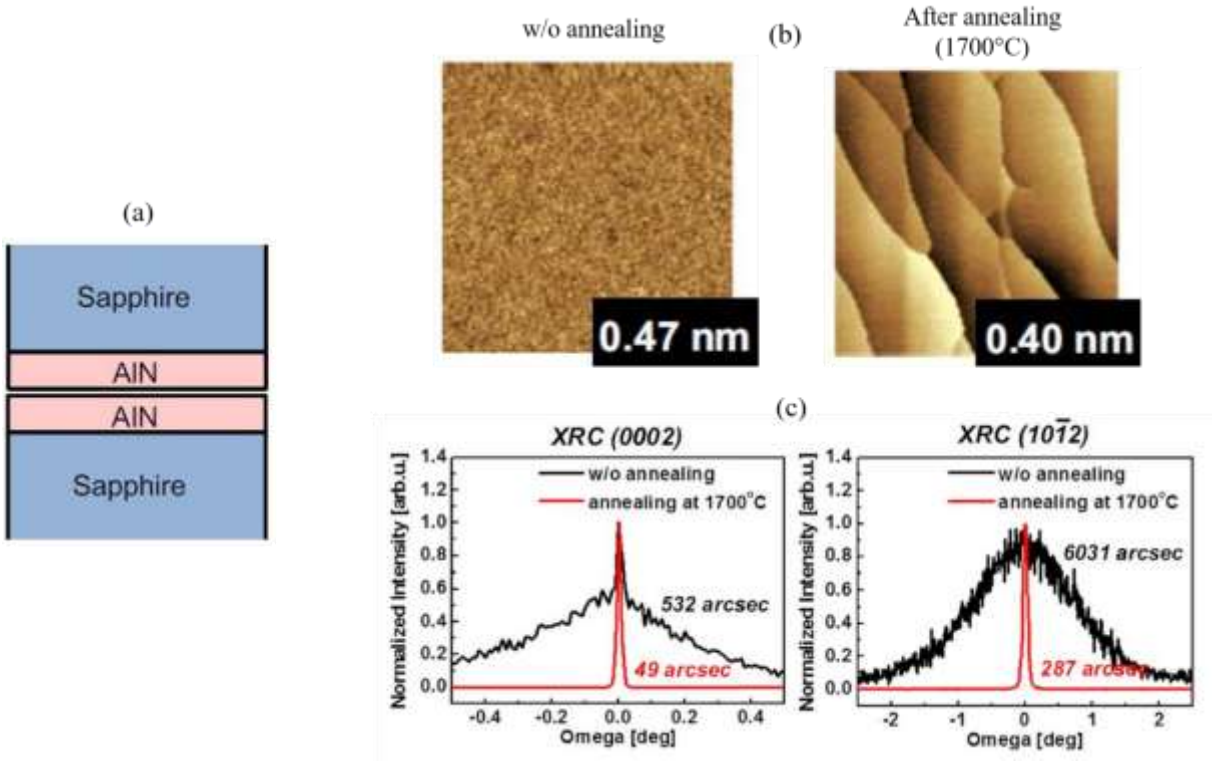

Figure 23. (a) Schematic illustration of two AlN samples placed in a face-to-face position. (b) Atomic force microscopy images of sputtered AlN surface morphology before and after annealing at 1700°C. The scanning area used in the atomic force microscopy was (1 x 1) μm^2. (c) X-ray rocking curve measurements for the (0 0 0 2) and (1 0 −1 2) planes for a sputtered AlN film with and without thermal annealing at 1700°C [65].

Van der Waals epitaxy offers a solution by growing two-dimensional (2D) materials, where the extended crystalline planar structures of the materials are held together by strong in-plane covalent bonds and weak out-of-plane van der Waals forces allowing an easy removal of individual layers without damaging the extracted layer or the remaining structure. In the 1980's, Atsushi Koma's research group in Japan investigated this solution by employing a non-destructive in-depth profiling using low-energy electron loss spectroscopy (LEELS) to analyze a $MoSe_2/MoS_2$ heterostructure grown via van der Waals epitaxy. The interface of the heterostructure was found to be defect-free and as sharp as a single monolayer [69]. Recently, Suresh Sundaram et al. from Georgia Tech Institute in Metz, France, showcased the growth of III-nitride device structures on h-BN in situ, including self-assembled nanoLEDs, enabling smooth, crack-free, and interface damage-free mechanical release of specific pixels from the matrix [70], [71], as shown in figure 24.

By exploiting the unique features of 2D materials, van der Waals epitaxy is an attractive approach for heterogeneous integration, i.e. the transfer of epilayers from their native growth

substrate to a dissimilar receiving substrate and device transfer to suitable substrates thereby facilitating the development of flexible devices.

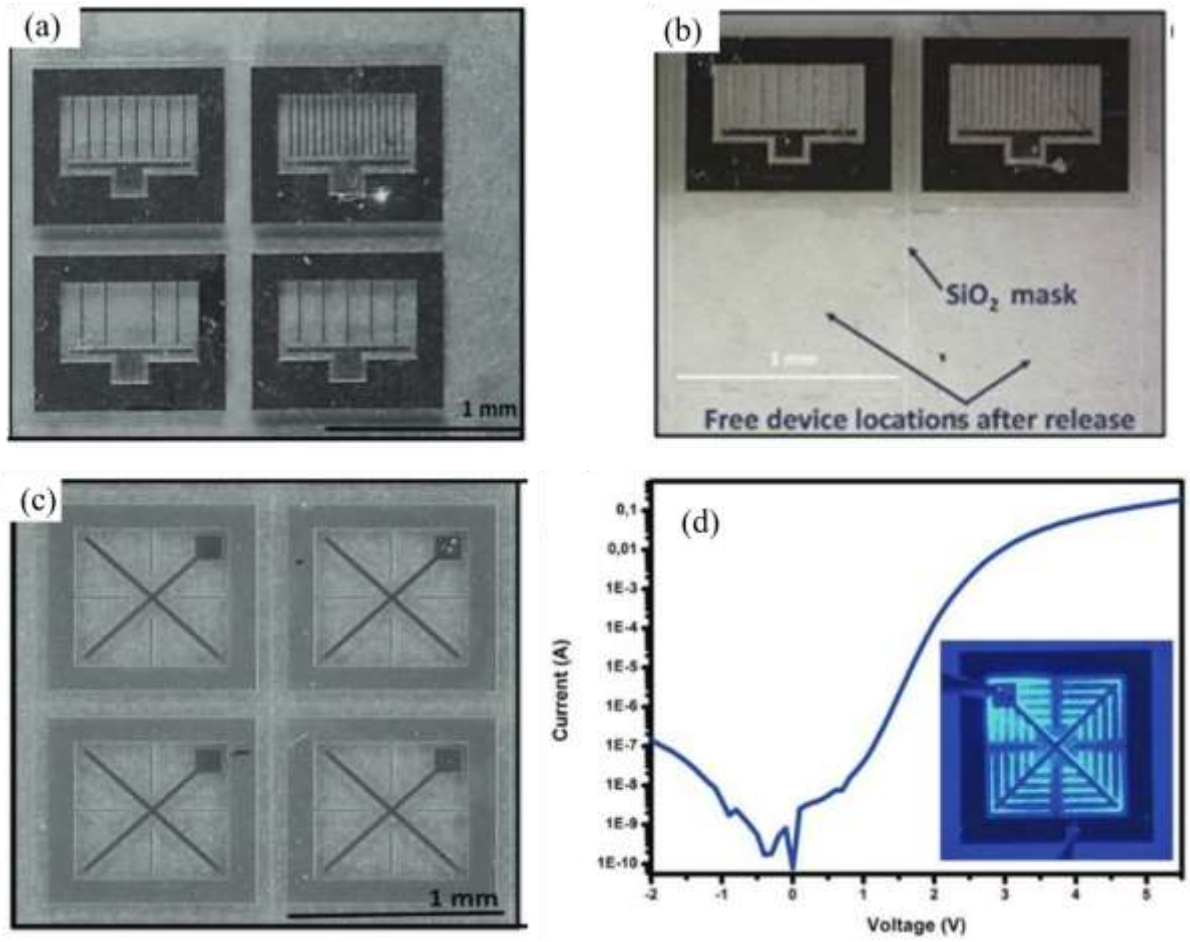

Figure 24. (a) Optical microscope image of devices with a 1 mm^2 contact area of the full front-end processed GaN-based blue LEDs on h-BN grown on patterned sapphire templates. (b) Optical microscope image showing two LEDs with a 1 mm^2 contact area and empty locations of two lifted-off LEDs on h-BN grown on the patterned sapphire, demonstrating patterning induced isolation and specific device lift-off. (c) Optical microscope images of eight devices with 1 mm^2 area and different designs; separated by the SiO_2 mask (white lines around the devices) and ready for pick-and-place. (d) I-V characteristic of a fabricated device emitting blue light shown in the inset [70], [71].

The final example is the promising growth technique of 3D quantum dots (QDs) that provides a significant increase in the IQE over the conventional growth technique of 2D quantum wells (QWs). QDs have a discrete energy spectrum due to their size and shape resulting in discrete electronic transitions instead of a continuous energy spectrum in QWs. Also, QDs have enable for a 3D confinement of carriers vs. a 1D confinement for quantum wells, thanks to their 3D nanometer-size structure, thereby decreasing the probability of non-radiative recombination with TDs which result in weak decrease of the PL integrated intensity as a function of temperature leading to an increase in the IQE, as shown in figure 25(a), (c) and

(d). Several studies reported the growth of (Al,Ga)N QDs and showed their ability in emitting in the UV and deep UV hence covering a large part of the UV range (figure 25 (b)) [25], [72]making them a strong solution in highly efficient UV LED devices.

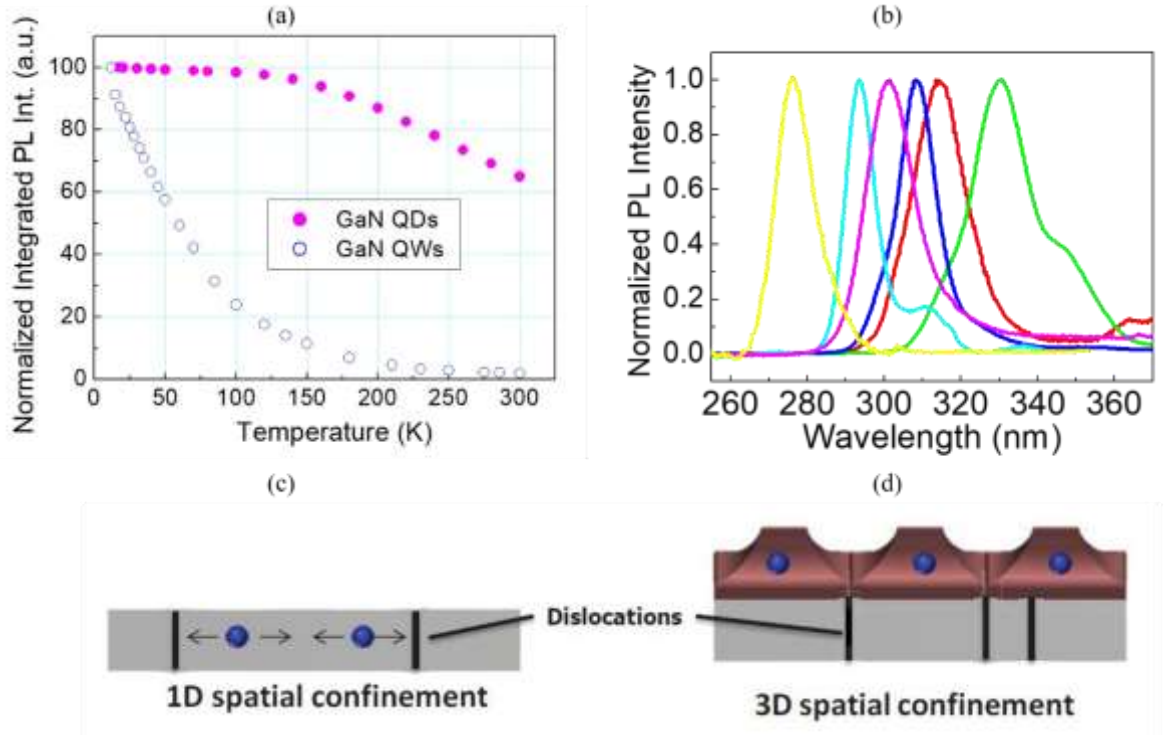

Figure 25. (a) Photoluminescence normalized integrated intensity as a function of temperature for GaN QDs and GaN QWs. (b) Wavelength emission for $Al_yGa_{1-y}N$ QDs with different Al composition. (c) and (d) are schematic illustrations presenting the excitons (blue circles) confinement in a quantum well and quantum dots, respectively [25].

I.2.2 Injection efficiency (IE) challenge

The high performance of UV LEDs strongly depends on efficient carrier injection in the active region that necessitates low resistivity of both n- and p-type layers. Achieving efficient p-type doping in (Al,Ga)N based UV LEDs using magnesium (Mg) has been a challenge due to the presence of deep acceptor levels associated with Mg.

The activation energy (E_a) or the energy required to activate the Mg acceptors is higher in AlN compared to that in GaN, since it is located at a deeper level of 510 meV in AlN and at a shallower depth of 160 meV in GaN [73]. In addition, many studies reported that for $Al_xGa_{1-x}N$ alloys, the increase in the E_a of Mg acceptors is quite steady with the increase in the Al content (figure 26) [74].

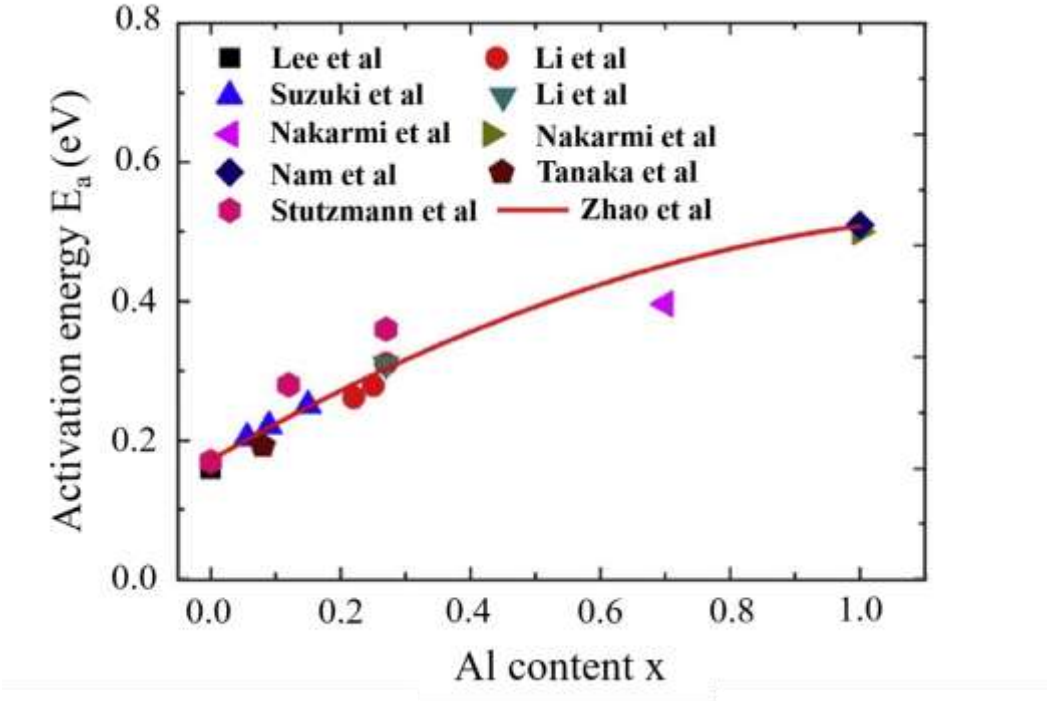

Figure 26. Dependence of the activation energy (E_a) of Mg acceptor in (Al,Ga)N alloys as a function of the Al content [74].

Many solutions have been proposed in order to improve the p-doping efficiency and one of them being the Mg-doped superlattices (SLs) where thin layers of Mg-doped (Al,Ga)N are sandwiched between undoped (Al,Ga)N layers, as shown in figure 27.

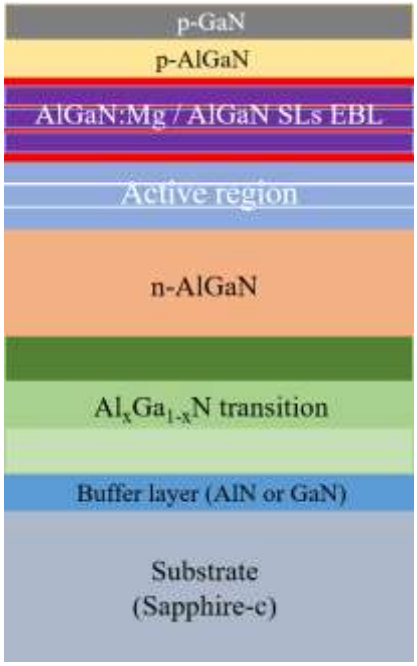

Figure 27. Schematic diagram of an LED structure incorporating Mg-doped AlGaN / AlGaN SLs EBL.

The inherent low doping efficiency of deep acceptors can be partially overcome through the use of a periodic oscillation of the valence band edge. This involves creating a situation where the band edge is far below the Fermi energy, leading to ionization of acceptors, and the resulting holes accumulate where the band edge is close to the Fermi level, forming a confined sheet of carriers. Superlattices play a key role in achieving this valence band edge oscillation by utilizing alloys with different valence band edge positions. In this approach, proposed by Schubert et al., the superlattice structure incorporates materials with different valence band edge positions. As a result, deep acceptors located in the barriers of the superlattice are able to ionize into the valence band of the neighboring narrow band-gap material, rather than ionizing into the deeper valence band of the host material. This mechanism increases the overall hole concentration, and even though the free carriers are separated into parallel sheets, their spatially averaged density becomes much higher than that of a simple bulk film [75]. Figure 28 (a) displays the results of room temperature Hall effect measurements conducted on films without and with a superlattice. The bulk GaN film exhibited a hole concentration of 4.3×10^{17} cm^{-3} with a mobility of 16 cm^2/V s. For $Al_{0.1}Ga_{0.9}N$, the corresponding values were 1.7×10^{17} cm^{-3} for the hole concentration and 13 cm^2/V s for the mobility. In the case of the superlattice based samples, the mobility decreased to approximately 10 cm^2/V s, likely due to increased scattering caused by heterointerfaces. As the dimension L of the superlattice was increased, the measured hole concentration showed a rapid rise to around 2.5×10^{18} cm^{-3}, which is more than ten times higher than the value obtained in the bulk alloy [76]. Figure 28 (b) displays the resistivity of the samples as a function of temperature. With an increase in the superlattice dimension L, the temperature dependence decreases significantly. For superlattice based samples having L of approximately 70 Å or longer, the resistivity remains nearly constant across different temperatures. In these films, the presence of band bending resulting from the polarization effect is sufficient to facilitate the ionization of acceptors and the formation of a hole sheet. On the other hand, in bulk films, the ionization of acceptors is highly dependent on temperature [76].

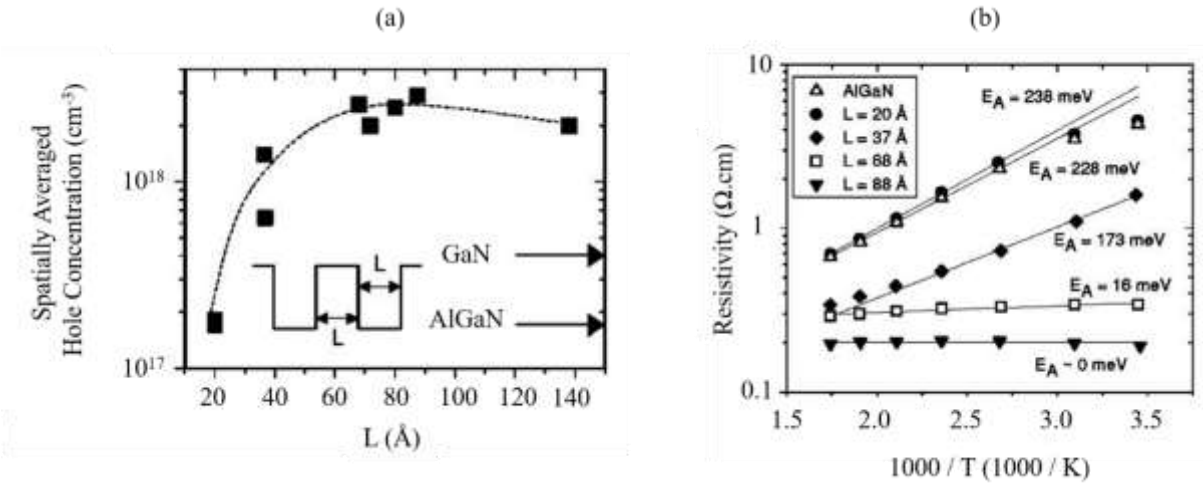

Figure 28. (a) Room temperature Hall effect measurements conducted on superlattice based samples. The arrows indicate values obtained from bulk films of Mg-doped GaN and $Al_{0.1}Ga_{0.9}N$ for comparison. The dashed line serves as a visual guide to help interpret the data. (b) Temperature-dependent resistivity measurements. Values obtained on bulk film of Mg-doped $Al_{0.1}Ga_{0.9}N$ are included for comparison [76].

By employing different superlattices' structures with varying valence band edge positions, this technique provides a way to enhance the concentration of holes and improve the doping efficiency in (Al,Ga)N-based materials.

Another approach is Mg doping with hexagonal Boron nitride (h-BN) as a substitute for p-AlGaN layers and potentially paving the way for high efficient performances. Traditional p-type AlGaN layers doped with Mg suffer from deep acceptor levels, which limit efficient carrier injection in the active region of the device. In contrast, h-BN does not exhibit such deep acceptor levels, potentially leading to improved carrier injection efficiency. In addition, shallower acceptor levels in the valence band in h-BN enable a larger number of Mg dopants to act as effective acceptors, leading to a higher concentration of free holes. Furthermore, Mg-doped h-BN has lower optical absorption compared to p-AlGaN, leading to improved light extraction efficiency and reduced self-absorption losses in the LED structure. A study conducted by R. Dahal et al. revealed that Mg-doped h-BN can offers a significantly lower acceptor activation energy and higher hole concentration compared to conventional p-$Al_xGa_{1-x}N$ layers [77]. As displayed in figure 29 (a), the Mg acceptor level (E_A) in $Al_xGa_{1-x}N$ increases with the Al content (x), ranging from approximately 170 meV in GaN (x = 0, with Eg ~ 3.4 eV) to 510 meV in AlN (x=1, with Eg ~ 6.1 eV). The free hole concentration (p) is inversely related to the acceptor activation energy and can be expressed as $p \sim \exp(-E_A / kT)$, where k is Boltzmann's constant and T is the temperature. With an E_A value of around 500 meV, there

would be only one free hole for approximately every 2 x 10^9 incorporated Mg impurities at room temperature, resulting in highly resistive p-layers. On the other hand, Mg-doped h-BN (h-BN:Mg) exhibits a much lower p-type resistivity of around 12 Ω cm at 300 K. The estimated E_A value in h-BN:Mg is approximately 31 meV based on temperature-dependent resistivity measurements (figure 29 (b)). With a Mg-doping concentration of 1 x 10^{19} cm^{-3}, the expected fraction of acceptor activation and the corresponding p value at 300 K would be about 30% and 3 x 10^{18} cm^{-3}, respectively [77].

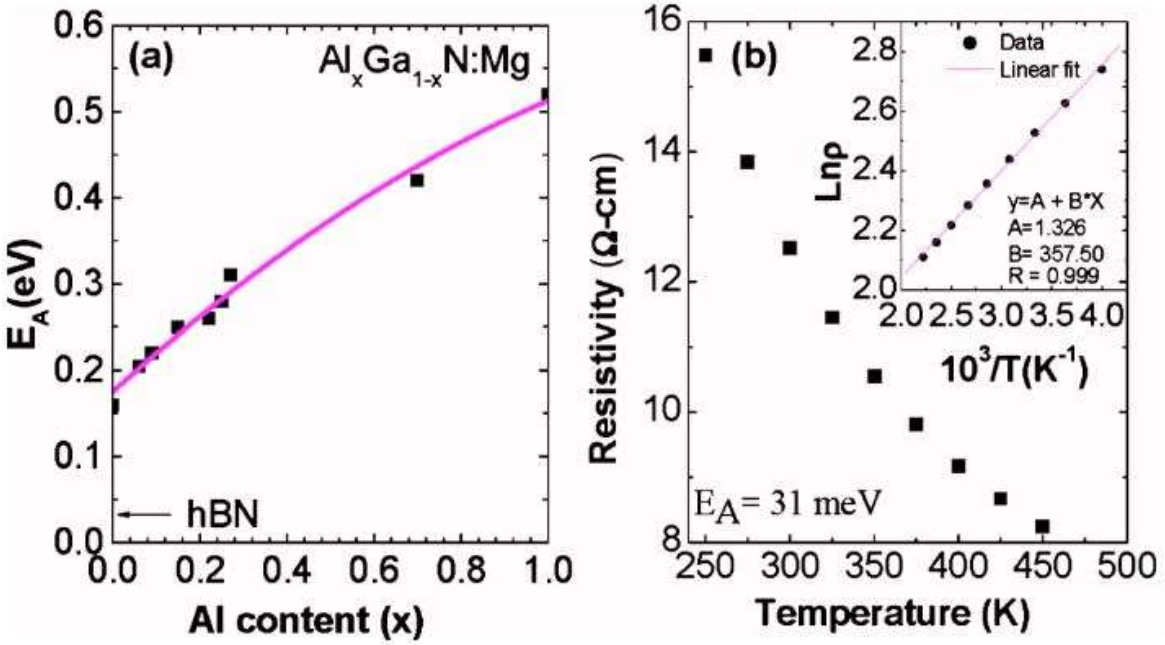

Figure 29. (a) Mg acceptor level (E_A) as a function of Al content (x) measurements in $Al_xGa_{1-x}N$ and the arrow indicates the E_A for h-BN:Mg. (b) Temperature-dependent p-type resistivity measurements of h-BN:Mg [77].

Furthermore, the implementation of multiple quantum barriers (MQBs) electron blocking layer (EBL) (figure 30 (a)) instead of the single EBL proved to be efficient in suppressing the electron overflow and reducing the electric field effects. The MQB structure causes multi-reflection effects in the wave-functions of the confined carriers (electrons or holes). As these carriers encounter the potential barriers and wells in the MQB, they experience multiple reflections at each interface. These reflections can enhance or interfere with the carrier wave-functions, leading to unique energy levels and optical properties in the material. Studies have shown that the effective electron barrier height in a MQB structure is significantly higher compared to a bulk potential barrier. The use of MQB has increased the effective electron barrier height by approximately 30% for GaAs/AlAs MQBs and up to 50% for GaInAs/InP

MQBs. Hideki Hirayama et al. have demonstrated the advantages of using a MQB instead of a single EBL for AlGaN-based deep UV LEDs [78]. In Figure 30 (b) and (c), a significant increase in output power and EQE was observed when the single EBL was replaced by the MQB. For the 250 nm AlGaN MQW LED with a 5-layer MQB ($Al_{0.95}Ga_{0.05}N$;Mg 4nm / $Al_{0.77}Ga_{0.23}N$;Mg 2nm), the maximum output powers were 4.8 mW at an injection current of 135 mA, compared to 2.2 mW at 300 mA for the single EBL structure. The maximum EQE values for the MQB-structured LED and the single EBL LED were 1.18% and 0.43%, respectively. Thus, the EQE of the 250 nm LED increased by 2.7 times with the introduction of the MQB. In Figure 30 (d), the wavelength dependence of EQE for 230 – 280 nm AlGaN-based DUV LEDs with either a single EBL or an MQB was measured under room temperature continuous wave (RT cw) operation. The EQE values of the 250 – 260 nm-band AlGaN-based LEDs were increased by a factor greater than 2.5 with the use of an MQB-EBL. The increase in EQE with the introduction of an MQB is believed to be due to an improvement in electron injection efficiency (EIE), resulting from the suppression of electron overflow, which is blocked by the enhanced "effective" barrier height when using an MQB [78].

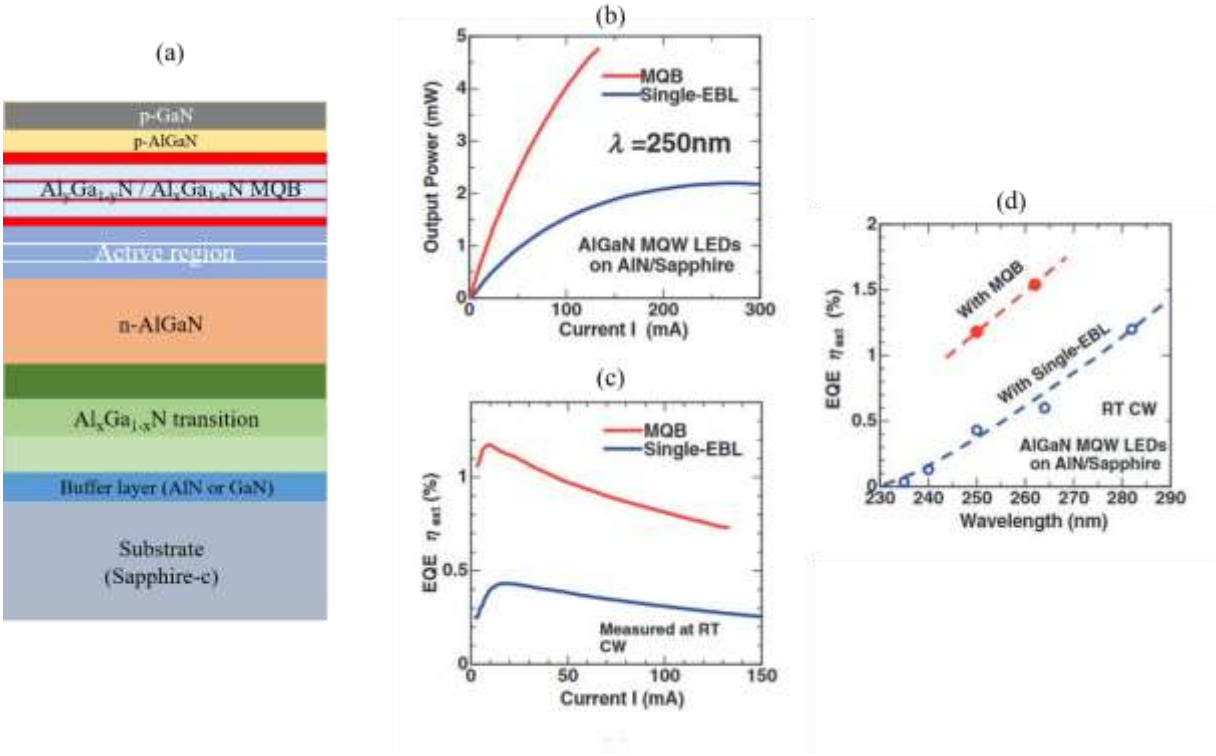

Figure 30: (a) A schematic representation of a UV LED structure with MQB EBL. (b) The output power and (c) EQE plotted against the current for 250 nm AlGaN MQW LEDs with an MQB and a single EBL, both measured under room temperature continuous wave (RT CW) operation. (d) The wavelength dependence of the EQE for 230 – 280 nm-band AlGaN-based deep ultraviolet (DUV) LEDs with a single EBL and with an MQB, measured under RT CW operation [78].

In order to minimize the absorption losses from the UV-absorbing p-GaN top layer, a promising approach consists on replacing it with a UV-transparent p-AlGaN layer in combination with Ni / Al electrode allowing an efficient extraction of light generated within the active region, as illustrated in figure 31 (a). On the other hand, UV-transparent p-AlGaN layers suffer from high sheet resistance, which can result in high contact resistance together with the degradation coming from the presence of the Ni / Al electrode, leading to a decrease in device performance and lifetime. Noritoshi Maeda and Hideki Hirayama demonstrated the successful implementation of high-efficiency deep-UV LEDs using a transparent p-AlGaN contact layer. However, replacing the conventional p-GaN top layer with a p-AlGaN layer comes with certain challenges [79]. In figure 31 (b), current density-EQE characteristics are compared between conventional p-GaN+Ni/Au and p-AlGaN+Ni/Al structures. While the LEE showed an increase of about 1.6 times by introducing the transparent p-AlGaN contact layer and Ni/Al reflective electrode, the EQE only increased by 1.3 times. This significant reduction in EQE is attributed to the decrease in EIE resulting from the reduction in hole concentration when using high-Al-composition p-AlGaN. Furthermore, the EQE loss is also influenced by the Ni/Al electrode, which experiences degradation due to the surface roughness of the samples. The very thin Ni layer (1 nm) in the Ni/Al electrode is highly sensitive to the sample's surface roughness, leading to an uneven distribution of hole density in the p-AlGaN surface and an overall reduction in hole density, thus impacting the injection efficiency of the LED [79].

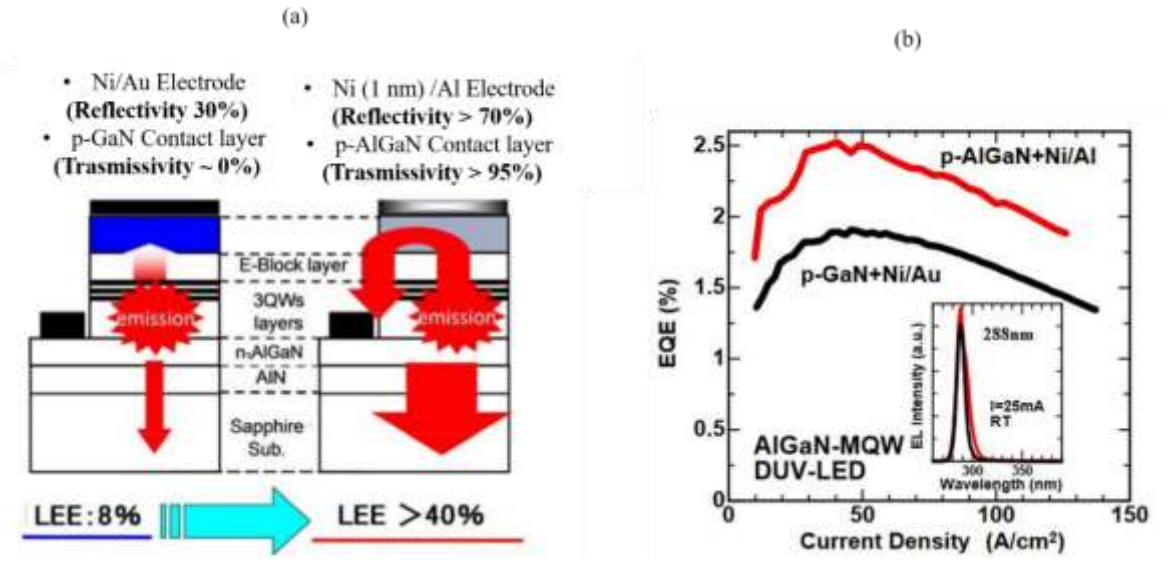

Figure 31: (a) Schematic representation of LEE improvement using p-AlGaN transparent contact layer and highly-reflective Ni/Al p-type electrode instead of an conventional p-GaN contact layer and a Ni/Au electrode. (b) Current density-EQE characteristics for 288 nm wavelength emission UV LEDs comparing between 275 nm p-AlGaN contact layer +Ni/Al electrode (red line) and a conventional p-GaN contact layer + Ni/Au electrode (black line) [79].

I.2.3 Light extraction efficiency (LEE) challenge

A solution adopted to improve the carrier injection efficiency in UV LEDs, the p-GaN contact layer, is actually causing one of the main issues in achieving efficient light extraction. One solution is to replace the UV-absorbing p-GaN contact layer with a UV-transparent p-AlGaN layer. However, this can lead to a reduction in carrier injection efficiency as discussed in the previous section. On the other hand, adopting advanced UV-reflective metals and encapsulation technologies can significantly improve the LEE such as high-reflectance metals, reflective photonic crystals (PCs), die encapsulation, patterned sapphire substrates, micro-lens arrays and excimer laser-based lift-off method (LLO).

Another challenge facing the LEE is its strong dependency on the optical polarization of the emitted light. The emission pattern for transverse magnetic (TM, $E \parallel c$) polarized light is confined to the plane of the device, resulting in much lower light extraction compared to transverse electric (TE, $E \perp c$) polarized light from a (0 0 0 1) device [80]. In the $Al_xGa_{1-x}N$ system, the topmost valence band splits into three closely spaced subbands with different symmetry, influenced by spin-orbit and crystal field interactions, as shown in figure 32.

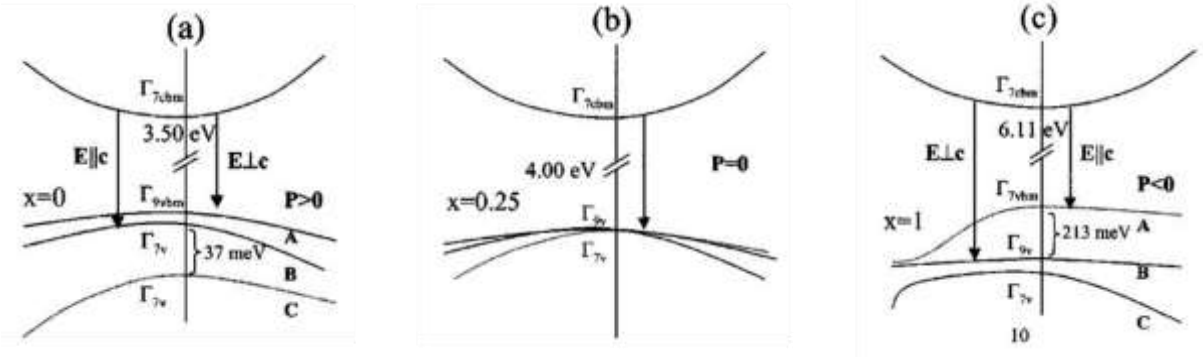

Figure 32. $Al_xGa_{1-x}N$ alloys band structures near the Γ point for different Al composition. (a) x = 0, (b) x = 0.25, and (c) x = 1 [81].

The radiative transition of an electron from the Γ_7 conduction band to a valence band depends on the symmetry of the corresponding valence subband. The significant difference in crystal field energy sign and value between GaN (12.3 meV) and AlN (-221 meV) causes a change in the valence band order and light polarization from TE polarization (GaN) to TM polarization (AlN) as the aluminum mole fraction increases in the MQW for shorter emission wavelengths, as illustrated in figure 33. Consequently, the light extraction efficiency and, therefore, the EQE are polarization-dependent and notably reduced for shorter wavelengths [82].

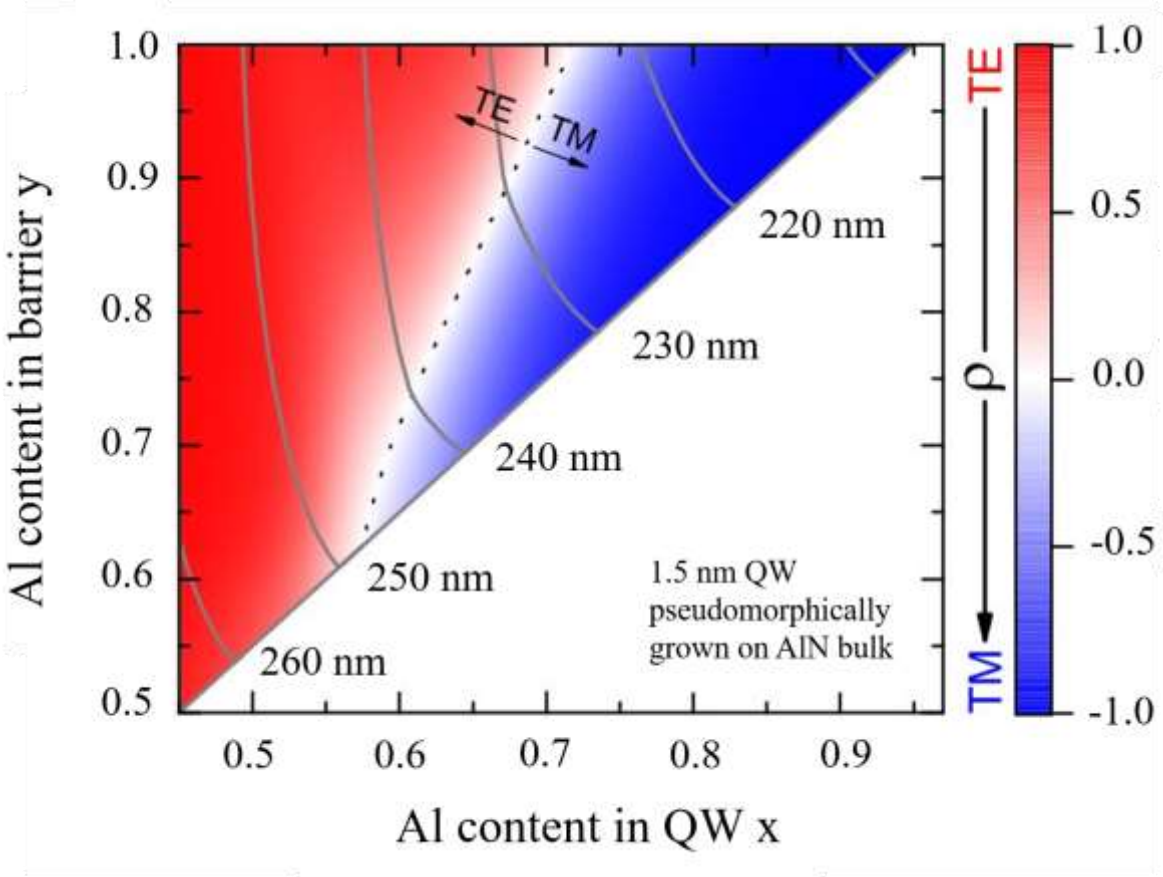

Figure 33. Dependence of the degree of polarization ρ on the emission from AlGaN-based QWs pseudomorphically grown on bulk AlN obtained from **k·p**-perturbation theory [82].

The focus by several research groups is to strike an optimal balance between the IQE, the IE and LEE, which implies compromises between the three key parameters. One promising approach that can reduces both the absorption and the electrical loss is tunnel junctions (TJs). TJs exploit quantum mechanical tunneling to enable electron transport through the insulating layer and overcome the potential barrier (figure 34), leading to a highly efficient electron transport process. In addition, TJs improve hole injection into the active region through non-equilibrium injection, i.e. when holes are injected across a barrier with high energy (higher than the thermal energy at the given temperature) and low hole concentration. The tunneling process allows holes to "tunnel" through the barrier even when they do not have sufficient thermal energy to overcome the barrier by classical means, which also leads to a reduction in the resistance of the p-type contact layer. Furthermore, TJs allow the removal of the absorbing p-GaN contact layer that can offer an advantage for deep UV LEDs.

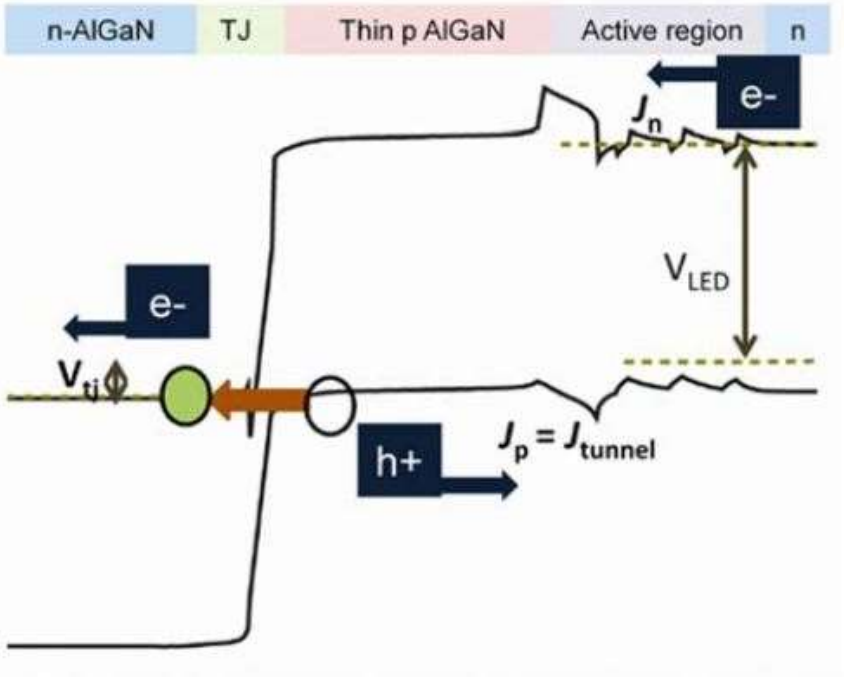

Figure 34. Schematic energy band diagram of a tunnel junction UV LED operating under forward bias [83].

Figure 35 (a) illustrates the I-V characteristics of a tunnel-injected UVA LED operating at 327 nm. The LED demonstrates remarkable performance with low resistance and high current operation, evidenced by a series resistance of less than 5.6×10^{-4} Ω cm^2. This efficiency is facilitated by the implementation of a transparent n-(Al,Ga)N top contact layer (figure 35 (c)), enabling effective light extraction from the active region through the device's top surface. Remarkably, the LED achieves an output power of 0.58 mW at an operating current of 20 mA (figure 35 (b)). The n-(Al,Ga)N top contact layer's high conductivity also plays a vital role in ensuring uniform light emission across the entire device mesa, even with only a small section of the device covered by the top metal contact, as depicted in figure 35 (b). This exceptional performance is attributed to the successful high-density hole injection into the active region, leading to enhanced LED efficiency and light emission [83].

In conclusion, achieving a significant improvement in UV LEDs device performance is a complex task that requires addressing multiple factors that contribute to the overall external quantum efficiency (EQE) and wall-plug efficiency (WPE). Rather than a single revolutionary breakthrough, it is more likely that a series of incremental improvements will be needed in each of the key areas (IQE, IE, LEE) in order to achieve the desired performance enhancements.

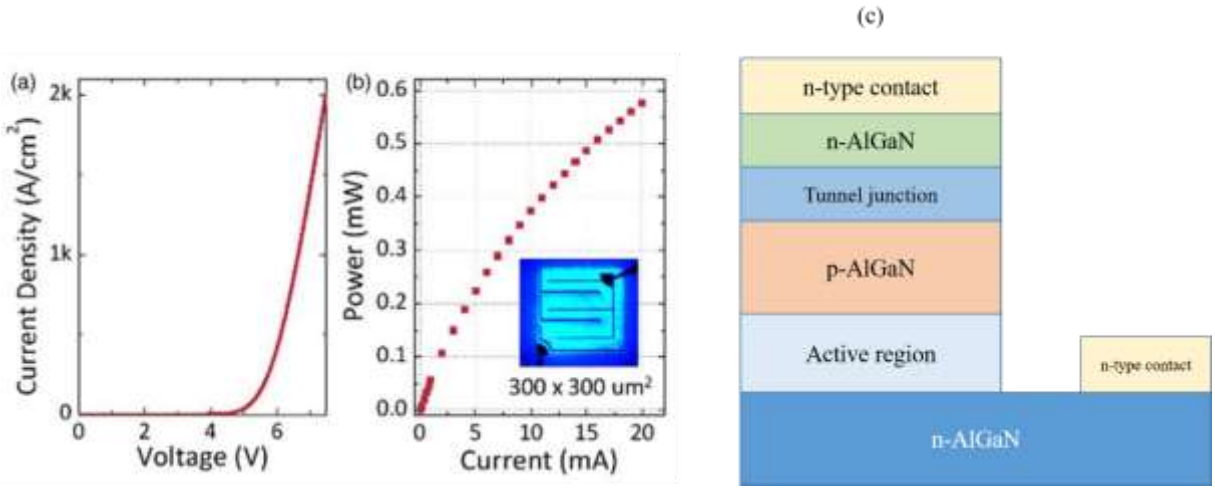

Figure 35. (a) I-V characteristics and output power (b) of a tunnel junction UV LED [84]. The inset to (b) is a microscope image of a top emitting UV LED device (300 x 300) μm^2. (c) Schematic illustration of a TJ (Al,Ga)N UV LED structure.

I.3 Epitaxial thin film growth

A thin film is defined as a condensed layer of solid material ranging from fractions of a nanometer to several micrometers in thickness, deposited on a bulk material considered as a substrate. Thin films can be differentiated amid several classifications, for instance by their material properties, composition or by their microstructure that can be classified under three main groups: Amorphous, polycrystalline, and single crystalline (epitaxial) thin films, as presented in figure 36. An amorphous thin film is defined as a random dense packing of atoms with only short-range order, while single crystalline or epitaxial thin films show a highly ordered atomic arrangement (fully crystalline) displaying one definite orientation following the crystalline substrate. Polycrystalline state comes in between consisting of crystallites (or grains) with random grain shape, size, separated by grain boundaries and random oriental packing on the substrate. The material deposition forming the crystal layers, hence the crystalline thin film, is referred to as the *growth* technique. Two main categories of epitaxy exist: homoepitaxy and heteroepitaxy. In homoepitaxy, the thin film and the substrate are made of the same material and therefore have identical chemical natures. In contrast, heteroepitaxy involves growing a thin film on a substrate made of a different material, resulting in a difference in crystal structure and/or lattice parameter between the two.

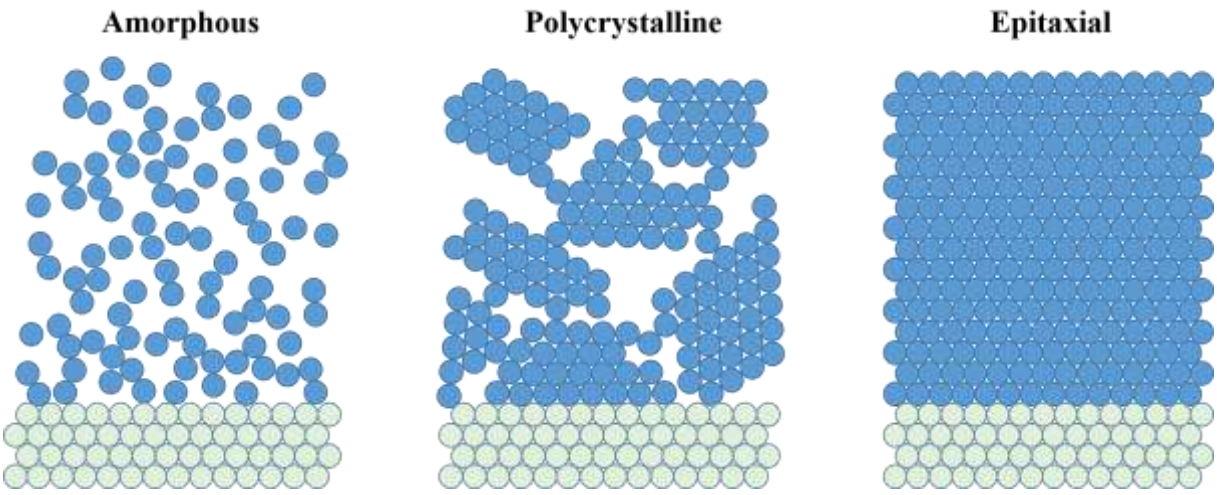

Figure 36. Schematics illustrating different thin film microstructures: amorphous, polycrystalline and epitaxial.

The main epitaxial growth techniques used to grow III-nitrides include metal-organic hydride vapor phase epitaxy (HVPE), ammonothermal growth (growth on native seeds), chemical vapor deposition (MOCVD), and molecular beam epitaxy (MBE). HVPE involves the reaction of metal chloride or metal hydride vapors with hydrogen gas and the deposition of the resulting compound on a heated substrate. The metal chloride or metal hydride gases react with hydrogen gas near the heated substrate's surface. This reaction leads to the formation of volatile metal hydride species where next they decompose near the substrate surface, releasing the desired metal atoms and hydrogen gas. HVPE is defined by its high growth rates (> 100 µm / h), and high quality materials growth, therefore, it is used for growing thick or bulk substrates like GaN bulk substrates. Ammonothermal growth method enables the growth of large diameter crystals of high crystalline quality. MOCVD is a process where volatile metal-organic precursor gases react with a reactive gas, such as hydrogen (H) or ammonia (NH_3), resulting in the deposition of a compound on a heated substrate. Inside the growth chamber, the metal-organic precursors decompose near the heated substrate's surface, releasing metal atoms and organic byproducts. These metal atoms then react with the reactive gas near the substrate's surface, leading to the formation of the desired compound. For instance, in the case of Ga and NH_3, GaN is produced. MOCVD is the most adopted choice in the epitaxy industry having a good equilibrium between growing good crystalline quality thin films at an acceptable growth rate (3 to 4 µm / h). MBE can also grow good quality thin films but it has a much lower growth rate (typically below 1 µm/h). However, it stands out from the other methods by having important advantages. MBE enables the use of *in-situ* surface characterization technique like the reflection high-energy diffraction (RHEED) method which enables growth monitoring together with the

ability to grow at low rate (< Angstrom / s), ultra-high vacuum and at low temperature [85]. In this thesis, we are interested in developing and growing AlGaN-based heterostructures and UV LEDs by molecular beam epitaxy (MBE).

I.3.1 Molecular beam epitaxy (MBE)

Molecular beam epitaxy (MBE) is a highly adaptable method for fabricating epitaxial films of a wide range of materials, including semiconductors, metals, and insulators. It is known for its ultra-high vacuum (UHV) conditions (~ 10^{-10} Torr for the residual pressure) providing a low concentration of impurities, thus minimizing collision probability with the molecular beam. It has Knudsen effusion cells that contain, heat and evaporate different III-nitride materials (Al,Ga,In) existing in the cells in a solid form with high chemical purity (typically 4N, i.e. 99.99%). Shutters exist to stop or allow the transfer of the flux from a cell to the growth chamber. Thanks to the UHV conditions mentioned above, the elements are sent to the substrate's surface in form of a molecular beam or fluxes of atoms/molecules that is due to the mean free path of atoms being longer than the source-substrate distance. The substrate is held on a molybdenum support that rotates to ensure a homogenous deposition. Both the substrate surface temperature and the growth rate can influence the kinetic energy of the adsorbed atoms. Heating the substrate further increases the kinetic energy of the adsorbed atoms reaching its surface, enabling them to grow in the perfect position. In addition, the growth rate control enables limiting or enhancing the surface diffusion (diffusion length) of the adsorbing species, which refers to how far the atoms or molecules can diffuse across the substrate's surface before they become incorporated into the growing crystal structure. This controlled diffusion helps to ensure that the atoms or molecules are deposited in a precise and ordered manner, forming a well-defined monolayer-by-monolayer growth mode. An MBE growth reactor is illustrated in figure 37.

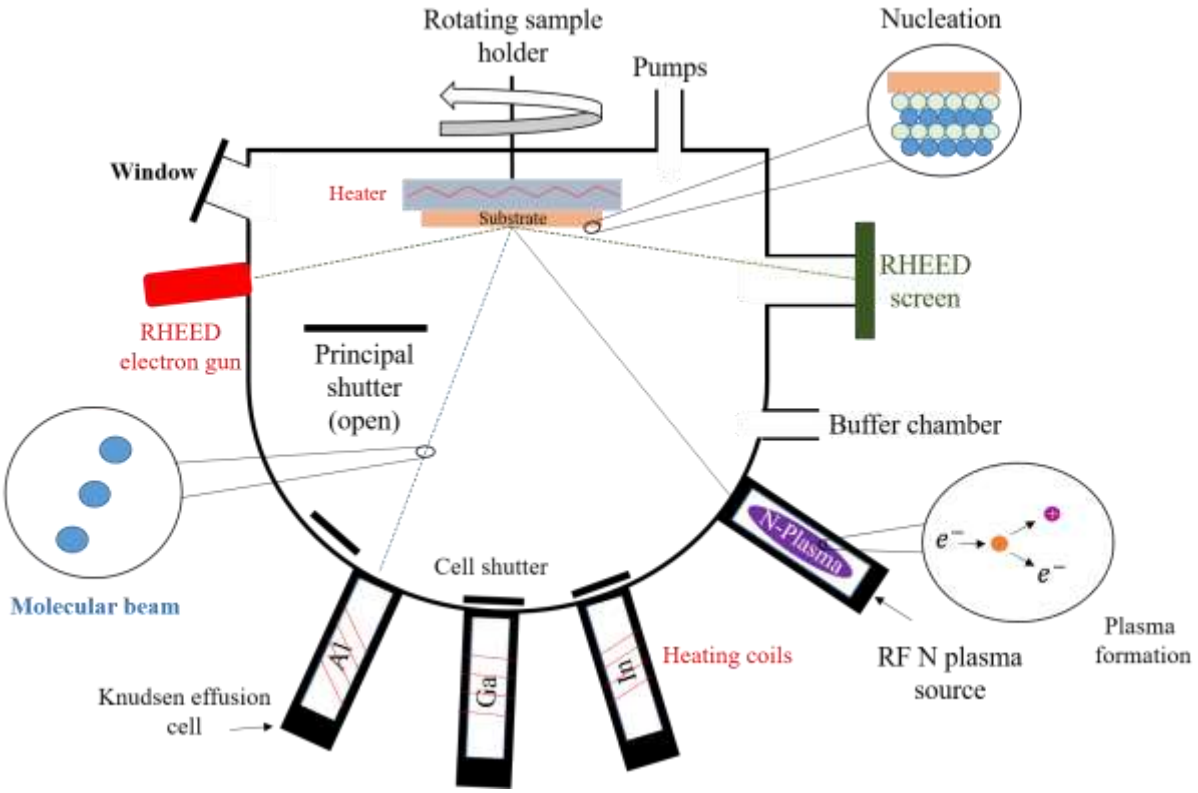

Figure 37. Schematic illustration of an MBE growth reactor.

UHV conditions enable the use of several *in-situ* characterization techniques where RHEED is the most used technique during MBE growth. It gives access to various *in-situ* information such as real time characterization of the crystallinity, surface morphology as well as growth monitoring and providing information regarding the surface reconstruction, i.e. the rearrangement of surface atoms on the crystal lattice to achieve a more stable or lower energy configuration. All these advantages make RHEED a powerful technique during growth, allowing MBE to be a useful technique for the growth of high quality epitaxial structures.

- **Ammonia (NH_3) and plasma assisted molecular beam epitaxy (PAMBE)**

The fluxes of elements III (Al,Ga, and In) and the doping elements (Mg,Si, and Ge) are generated by effusion cells that heat the high purity solid sources resulting in an evaporation of the atoms / molecules from the solid sources. However, it is difficult to break nitrogen molecules to incorporate it into elements III since the 9.5 eV N-N energy bond is a very strong chemical bond. Therefore, two methods exist to obtain element V. The first is ammonia assisted MBE (NH_3-MBE), which utilizes ammonia (NH_3) as a precursor. In this process, the nitrogen atom is obtained by the pyrolytic decomposition of the NH_3 molecule on the substrate's surface

due to the weak bond between nitrogen and hydrogen atoms while the H atoms desorb from the surface as H_2 gas. Hence, the general reaction equation for the surface decomposition of ammonia (NH_3) to produce the III-N alloy using molecular beam epitaxy (MBE) can be written as:

$$III + NH_3 \longrightarrow III\text{–}N + \frac{3}{2}H_2 \qquad \text{(Eq. I. 26)}$$

where III represents the element III of the III-N alloy, such as Al, In or Ga, and H_2 is hydrogen gas. The second method is plasma assisted MBE (PAMBE), which employs a plasma source such as electron-cyclotron resonance (ECR) or radio frequency (RF) to obtain the nitrogen atom directly from ultra-pure N_2 gas. The ultra-pure N_2 gas is introduced into the plasma source chamber, where it is exposed to high-energy electrons or radio frequency electromagnetic fields. These energetic particles collide with the N_2 molecules, providing sufficient energy to break the N_2 bond. As a result of the collisions, some N_2 molecules undergo dissociation, splitting into individual N atoms and other fragments. The generated N atoms are then transported from the plasma source chamber to the main growth chamber, where the epitaxial growth takes place. The N atoms are directed towards the substrate surface and are incorporated into the growing crystal structure, as depicted in figure 37.

PAMBE offers certain advantages such as the ability to grow at lower temperatures (100-200°C lower than NH_3-MBE) and without hydrogen (H_2) on the growing surface, which is useful for effective p-doping. Indeed, H_2 is typically used as a carrier gas for MOCVD, and it is also present on the growing surface during the growth process. Hydrogen can passivate dopant impurities in the material, making it challenging to achieve efficient p-doping. On the other hand, in PAMBE, the N atoms are obtained directly from ultra-pure N_2 gas without the need for hydrogen. This hydrogen-free growth environment prevents passivation of dopant atoms, making it easier to achieve effective p-doping. However, growing at low temperatures can result in low quality layers due to a decreased surface mobility of atoms. NH_3-MBE, on the other hand, allows for a higher growth rate (>1 µm / hour) at higher V / III ratios and temperatures.

Sequential growth using NH_3-MBE and PAMBE can be advantageous as it allows for the benefits of both methods to be utilized in the same structure and in one growth run. This hybrid growth mode is studied and will be presented in this thesis.

- **Reflection high energy electron diffraction (RHEED)**

Reflection high energy electron diffraction or RHEED is an *in-situ* characterization technique developed by Nishikawa and Kikuchi in 1928 [86]. It is used in MBE growth to characterize the surface morphology and crystallinity of the growing layer. Since its first application in the late sixties [87], it has been developed and adopted as an essential growth monitoring measurement tool during MBE growth.

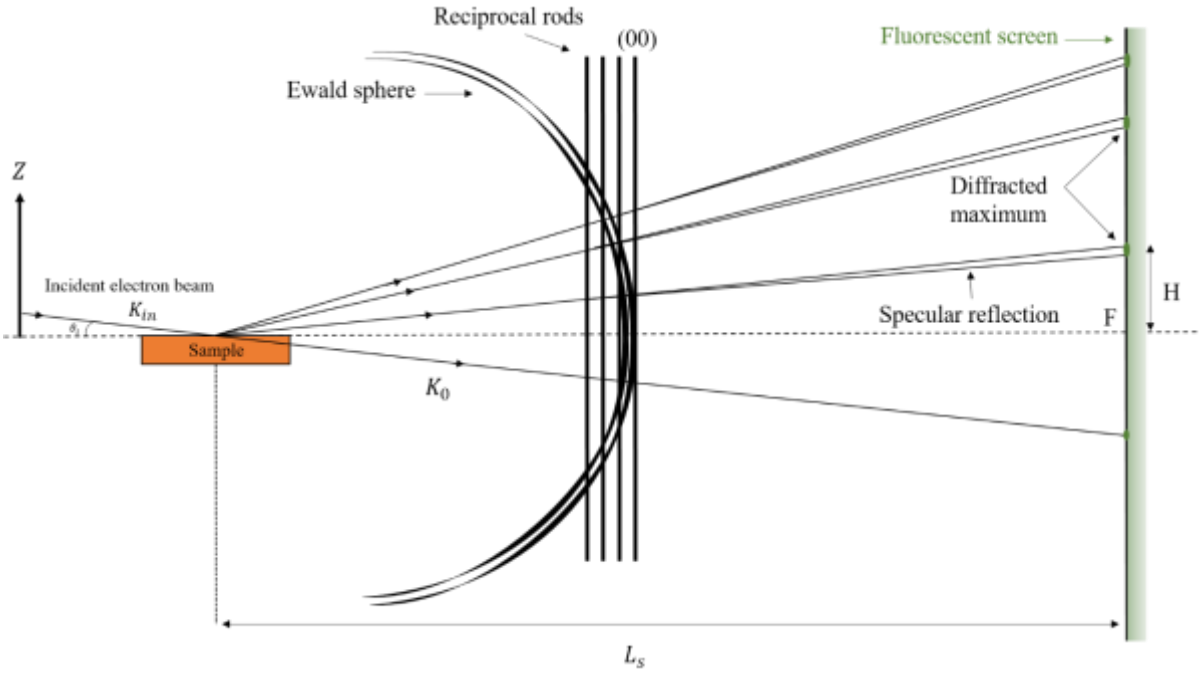

Figure 38. Schematic representation of the diffraction conditions for a RHEED measurement.

The RHEED technique consists in using an electron gun that sends high-energy electron beam (10 – 30 KeV) to the substrate's surface at a very low incidence angle ($0 < \theta < 2°$) that leads to a diffraction from only a few atomic planes below the substrate's surface. A 2D diffraction pattern is then formed and observed on a fluorescent screen. This pattern resulting from a constructive interference between the scattered electrons and the periodic arrangement of atoms in the crystal lattice is a representation of the reciprocal space of the crystal surface, and is characterized by diffraction rods (elongated spots) rather than discrete points due to the 2D diffraction geometry. The intersection of the diffraction rods with the Ewald sphere is where the diffraction occurs and is detected by the fluorescent screen, as seen in figure 38.

The De Broglie wavelength (λ) of the electrons is related to the wave vector ($\boldsymbol{k_{in}}$) of the incident electrons by the following equation: $\lambda = 2\pi / k_{in}$. The Ewald sphere's size is

determined by the wave vector $\boldsymbol{k_{in}}$ magnitude, which can be calculated by incorporating the electrons De Broglie wavelength:

$$\lambda = \frac{h}{\sqrt{2m_0E + E^2c^2}} \qquad \text{(Eq. I. 27)}$$

where h is Planck constant, m_0 the electron mass, E the kinetic energy of the electrons, c the speed of light.

The shape of the pattern observed on the fluorescent screen can vary depending on the growth mode occurring on the sample's surface. If the growth mode is 2D, a series of parallel elongated thin lines will be observed and referred to as a streaky pattern. However, if the growth mode is 3D and the associated surface morphology is rough, the pattern will be in the form of series of dots and referred to as a spotty pattern, as shown in figure 39.

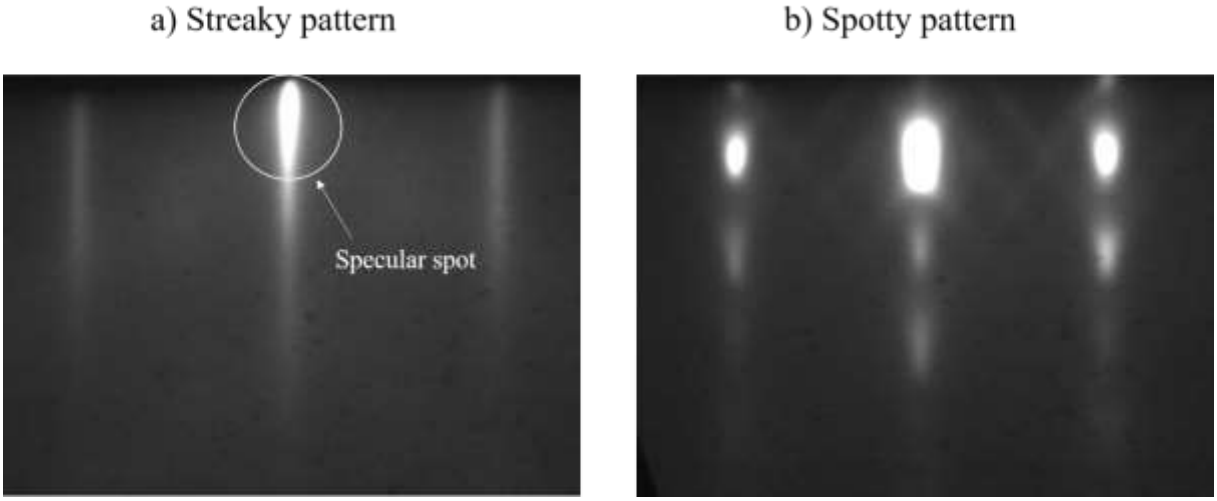

Figure 39. Reflection high energy electron diffraction (RHEED) images for a) 2D and b) 3D surface morphologies.

During the growth, monatomic islands are formed on the surface and gradually coalesce to form a continuous layer. The surface roughness varies with the coverage rate, which is determined by the time required to deposit a monolayer (ML) with 1 ML equal to the half of the *c* lattice parameter. The intensity of the specular spot, which arises from the beam reflected on the surface, depends on the roughness of the surface due to the diffusion of part of the beam. Thus, the growth rate of a 2D layer can be determined by measuring the rate of oscillation of the intensity of the specular spot. This technique is often used to calibrate the deposition rate of Al and Ga during the growth.

I.3.2 Growth modes

Crystal growth modes depend on the balance between the surface energy (energy required to create a unit area of the surface of a crystal) and the adhesion energy (energy required to maintain the contact between the substrate and the growing film), and are observed in a wide range of material systems. In epitaxial growth, the surface energies that have the main impact on the growth mode are the surface energy of the substrate (γ_{sub}), the surface energy of the film (γ_{film}), and the surface energy of the interface ($\gamma_{interface}$).

Considering the surface energy cost ($\Delta\gamma$) between a 2D film totally covering the substrate ($\gamma^{2D} = \gamma_{film} + \gamma_{interface}$) and a 3D islands morphology covering half of the substrate ($\gamma^{3D} = \frac{1}{2}(\gamma_{sub} + \gamma_{film} + \gamma_{interface})$), the following equation can be written:

$$\Delta\gamma = \gamma^{3D} - \gamma^{2D} \approx \frac{1}{2}(\gamma_{sub} - \gamma_{interface} - \gamma_{film}) \quad \text{(Eq. I. 28)}$$

Thereby, it is the difference $\gamma_{sub} - \gamma_{interface} - \gamma_{film}$ that will condition the growth mode from the initial growth stages.

Three principal growth modes exist and are schematically represented in figure 40:

a) The Frank-Van der Merwe (FM) growth mode (figure 40.a), is a layer-by-layer growth mode (2D growth) where the layers surface morphology is a flat smooth surface. In this growth mode, the energy cost is positive ($\Delta\gamma > 0$) where the substrate surface energy is higher than both the film and the interface surface energies: $\gamma^{3D} > \gamma^{2D}$ ($\gamma_{sub} > \gamma_{film} + \gamma_{interface}$).
b) The Volmer-Weber (VW) growth mode (figure 40.b), is an island growth mode (3D growth) where the surface morphology is defined as a non-uniform, rough surface with poor interface quality between the islands and the substrate. In this growth mode, the deposited atoms first form small islands on the substrate surface, which grow independently until they coalesce into a continuous film. In this growth mode, the energy cost is negative ($\Delta\gamma < 0$) where the substrate surface energy is lower than both the film and the interface surface energies: $\gamma^{3D} < \gamma^{2D}$ ($\gamma_{sub} < \gamma_{film} + \gamma_{interface}$).
c) The Stranski-Krastanov (SK) growth mode (figure 40.c), is a 2D-3D transition growth mode where the first layer growth starts as a 2D-FM growth mode and after a certain thickness called critical thickness, the transition occurs and 3D islands form. The lattice mismatch between the substrate and the epitaxial layer induces strain in the growing

layers. The strain energy (elastic energy) increases with the increasing film thickness until it reaches a critical thickness where the elastic stress is too high and must be relaxed. The layer can either elastically relax by forming 3D islands at the surface, leading to a Stranski-Krastanov transition or plastically relax by forming misfit dislocations and remaining as a 2D layer. Misfit dislocations can also take place in a 3D layer in Stranski-Krastanov growth mode, as shown in figure 41.

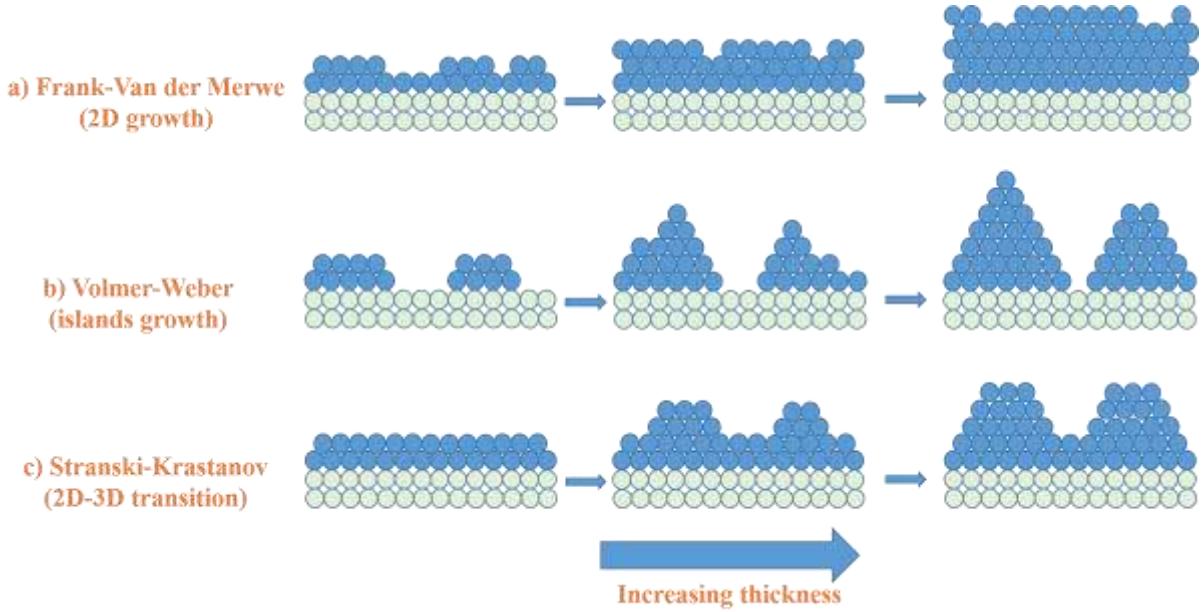

Figure 40. Schematic illustration of the three main growth modes: a) the Frank-Van der Merwe (2D growth), b) the Volmer-Weber (3D growth), and c) the Stranski-Krastanov (2D-3D transition).

The film's free energy per unit area, $E = E_{strained\ epilayer} + E_{surface}$, can be written as a function of the film thickness h (h > 1 ML) for the four growth modes as follow [88]:

$$E_{2D}(h) = M(\Delta a/a)^2 h + \gamma_{film} \quad \text{(Eq. I. 29)}$$

$$E_{SK}(h) = (1-\alpha)M(\Delta a/a)^2 h + \gamma_{film} + \Delta\gamma \quad \text{(Eq. I. 30)}$$

$$E_{2D-MD}(h,d) = (1-d_0/d)^2 M(\Delta a/a)^2 h + 2\,E_{MD}(h)/d + \gamma_{film} \quad \text{(Eq. I. 31)}$$

$$E_{SK-MD}(h,d) = (1-\alpha)(1-d_0/d)^2 M(\Delta a/a)^2 h + 2\,E_{MD}(h)/d + \gamma_{film} + \Delta\gamma \quad \text{(Eq. I. 32)}$$

where M is the film biaxial modulus, $\Delta a/a$ the lattice mismatch between the epilayer and the substrate, γ_{film} the film's surface energy, α the elastic energy gain in accommodating film's strain through the formation of partly relaxed SK islands, $\Delta\gamma$ the surface energy cost to create facets, d the average distance between misfit dislocations (MDs) at the film-substrate interface,

d_0 the distance for a fully relaxed epilayer, d_0/d the plastic energy gain in accommodating misfit with MDs, and E_{MD} the energy cost per unit length in forming MDs.

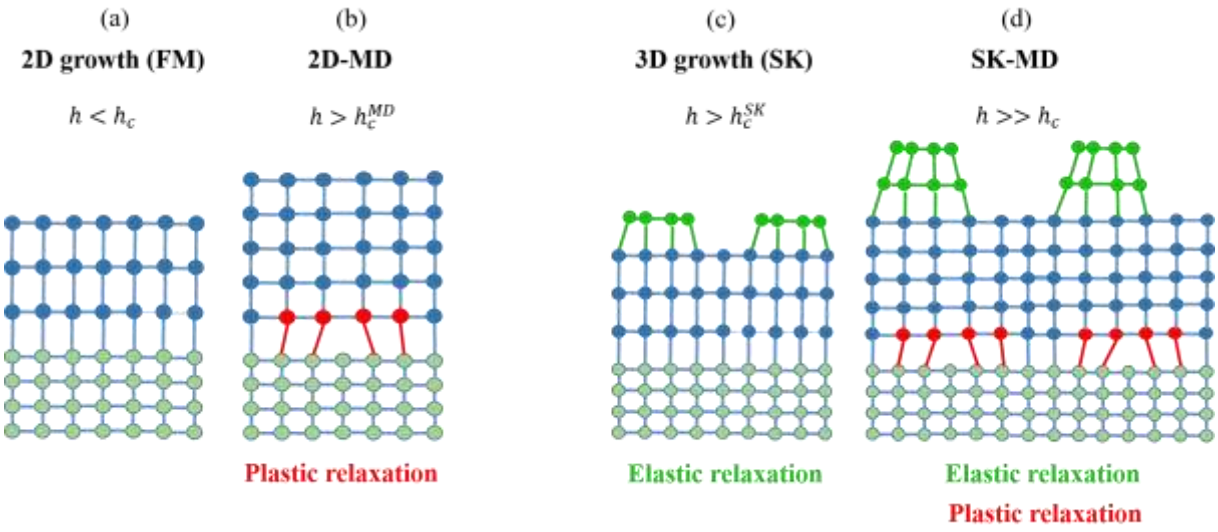

Figure 41. Schematic illustration of different growth modes: (a) the Frank-Van der Merwe (FM) 2D growth mode, (b) the FM 2D with plastic relaxation in form of misfit dislocations (MD), (c) the Stranski-Krastanov (SK) 3D growth mode with elastic relaxation, and (d) the SK 3D with both elastic and plastic relaxations. h_c is the critical thickness where the elastic stress accumulated in the 2D layer is relaxed, h_c^{MD} is the critical thickness from which plastic relaxation occur in the layer forming misfit dislocations, and h_c^{SK} is the critical thickness where a 3D growth mode can occur.

The energy gain and energy cost to elastically relax the stress owing to the SK growth mode were formalized by Tersoff and Tromp [89] followed after it by Tersoff and LeGoues [90]. They considered, for an SK island, the energy balance (ΔE) between the surface energy cost ($\Delta E_{surface} = \Delta\gamma = \gamma^{3D} - \gamma^{2D} > 0$) to form islands and the elastic energy gain ($\Delta E_{elastic} = E_{elastic}^{SK} - E_{elastic}^{2D} < 0$) from the relaxation of a part of the epitaxial stress [89], [90]:

$$\Delta E(in\ Joules) = \Delta E_{surface} + \Delta E_{elastic} \qquad \text{(Eq. I. 33)}$$

The transition from 2D to 3D growth is typically not favorable when ΔE is positive. This is particularly true at the beginning of the growth process, when the deposited material amount is low and the surface-to-volume ratio is high, which prevents the accumulation of sufficient elastic energy $E_{elastic}$ (proportional to the thickness h) to induce the 2D-3D transition. However, as ΔE becomes negative, the Stranski-Krastanov (SK) transition becomes favorable. In this case, transitioning from a 2D strained layer to a 3D relaxed one reduces the total energy of the layer.

In equation (I.30), α is defined as the elastic energy gain in accommodating film's strain through the formation of partly relaxed SK islands, where the islands induce a surface energy cost ($\Delta E_{surface} = \Delta\gamma = \gamma^{3D} - \gamma^{2D}$). With this, it becomes possible to determine the critical thickness h_c^{SK} from which the 2D-3D transition occurs. This transition occurs when the relaxed elastic energy $\alpha M(\Delta a/a)^2 h$ (>0) exceeds the additional surface energy cost ($\Delta E_{surface} = \Delta\gamma$):

$$h_c^{SK} = \frac{\Delta\gamma}{\alpha M(\Delta a/a)^2} \quad \text{(Eq. I. 34)}$$

A critical thickness can be calculated using equation (I.31) to determine when the 2D-MD growth mode is more favorable to occur than the 2D coherent mode. This critical thickness, denoted as h_c^{MD} is defined by the point where the plastically relaxed elastic energy, given by $(2d_0/d)\, M(\Delta a/a)^2 h$, exceeds the energy cost of creating a network of dislocations at the interface, given by $2\, E_{MD}(h)/d$:

$$h_c^{MD} = \frac{E_{MD}(h_c^{MD})}{d_0 M(\Delta a/a)^2} \quad \text{(Eq. I. 35)}$$

The ratio η between the two critical thicknesses, h_c^{SK} and h_c^{MD}, in equation (I.36), plays a key role in determining the dominant growth mode, as illustrated in Figure 42.

$$\eta = \frac{h_c^{MD}}{h_c^{SK}} \quad \text{(Eq. I. 36)}$$

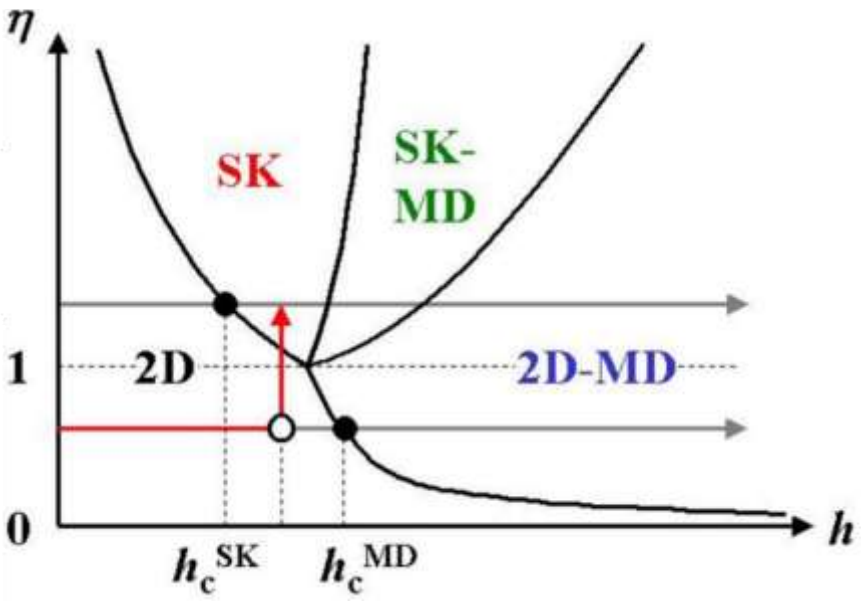

Figure 42. Schematic diagram of the 4 growth modes as a function of the thickness (h) and the ratio η between the two critical thicknesses h_c^{SK} and h_c^{MD} [91].

According to the schematic diagram in figure 42, plastic relaxation occurs when $\eta < 1$, which corresponds to the condition where $h_c^{MD} < h_c^{SK}$. On the other hand, if $\eta > 1$, meaning that $h_c^{MD} > h_c^{SK}$, the SK transition takes place before the plastic relaxation. When the surface energy changes, the transition from the 2D mode to the SK mode occurs and are indicated by the red arrow in the diagram. The two grey horizontal arrows correspond to the sequence of the growth morphologies where a constant η reflects growth without significant changes in the growth conditions (i.e., in Δγ since all other parameters related to the materials are fixed).

I.3.3 Quantum dots growth by MBE

$Al_xGa_{1-x}N$ UV LEDs suffer from high dislocation densities (> 10^9 cm^{-2}) that act as non-radiative recombination centers inducing a decrease in the IQE and the EQE. Moreover, the drop in the EQE becomes more pronounced with shorter wavelengths (figure 15). The growth of 3D quantum dots as the active region instead of 2D quantum wells can help reduce the effect of excitons non-radiative recombination with surrounding TDs thus increasing the IQE, as shown in figure 43.

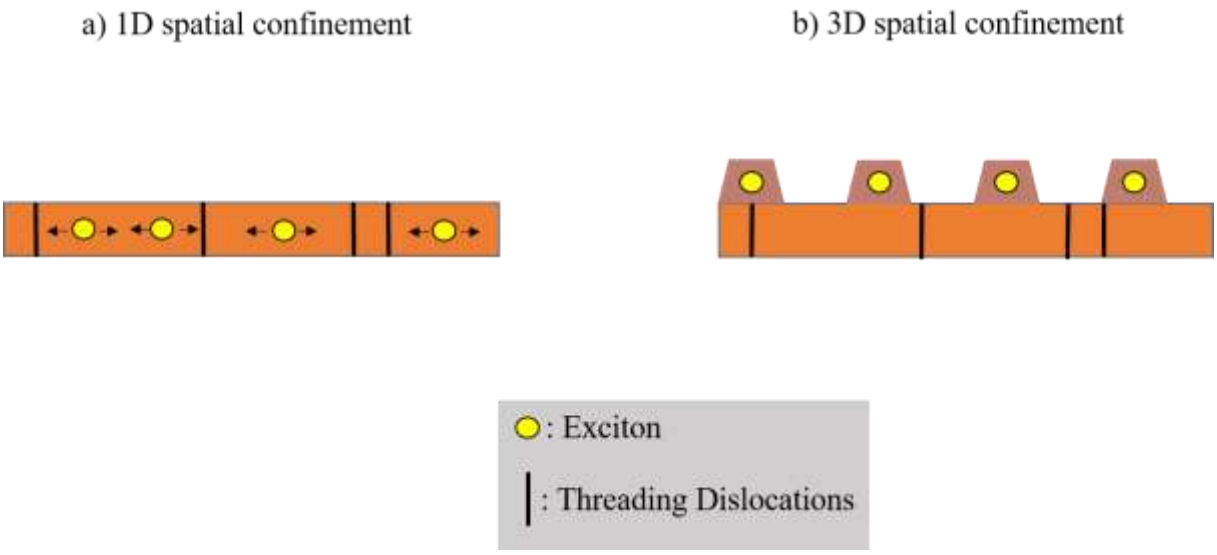

Figure 43. Schematic illustration of the exciton confinement in a) quantum well and b) quantum dots.

QDs have a better carrier confinement due to their three-dimensional confinement potential resulting in a higher probability of radiative recombination, leading to a higher IQE compared to quantum wells (figure 25 (a)). In addition, QDs offer the possibility of tuning the emission wavelength that can be controlled by adjusting the size and composition of the dots during growth.

The SK 2D-3D transition growth mode can trigger the formation of quantum dots (QDs) by increasing the film surface energy (γ_{film}) in favor of minimizing $\Delta\gamma$ and relaxing the stress by forming QDs with facets, as shown in figure 44. Those facets have a surface energy γ_{facet}, and the equation describing the relation between γ_{facet}, γ_{film}, and $\Delta\gamma$ is as follows [89]:

$$\Delta\gamma = A\left(\frac{\gamma_{facet}}{sin\,\theta} - \frac{\gamma_{film}}{tan\,\theta}\right) \quad \text{(Eq. I. 37)}$$

where A is a coefficient that depends on both the 3D islands sizes and density, and θ is the angle between the facets and the (0001) plane.

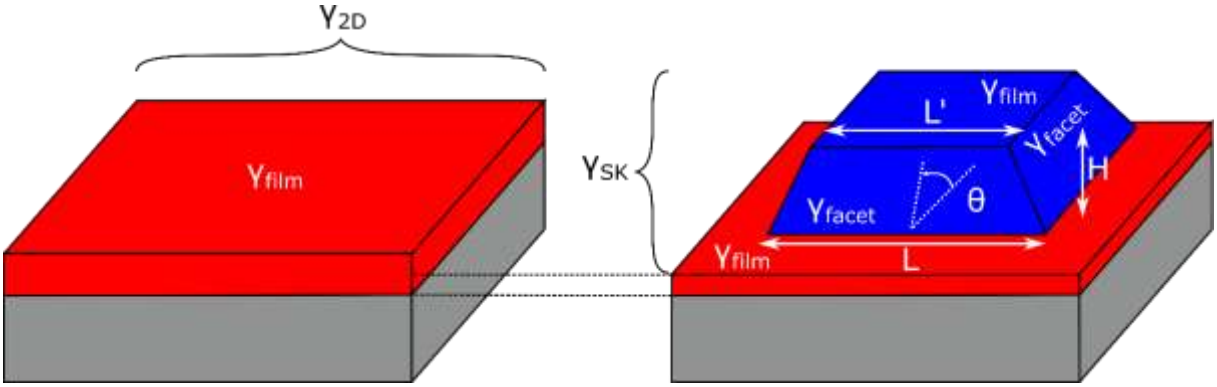

Figure 44. Schematic illustration of the different surface energies and parameters between a regular 2D film and a truncated pyramid after a SK 2D-3D transition [91].

By adjusting the growth conditions, it is possible to increase the value of γ_{film} without significantly affecting γ_{facet}. As γ_{film} increases, the surface energy cost ($\Delta\gamma$) decreases until it reaches a point where the gain in elastic energy ($\Delta E_{elastic}$) becomes greater than $\Delta\gamma$ ($|\Delta E_{elastic}| > |\Delta\gamma|$). This condition triggers the formation of QDs through the SK 2D-3D transition growth mode.

There are two methods to enhance the film surface energy (γ_{film}) of (Al,Ga)N QDs. One approach involves growing the QDs under nitrogen-rich conditions, which has been supported by theoretical calculations indicating an increase in the surface energy (γ_{0001}) of GaN (0001) under such conditions [92]. The other method is to perform a growth interruption under vacuum, which also leads to an increase in the (0001) surface energy [88], [93]. The growth of (Al,Ga)N QDs can be achieved using either an NH_3 source or an N_2 plasma source, but the process differs between the two sources. Notably, when using NH_3 under nitrogen-rich conditions, the transition from 2D to 3D growth does not occur during QD formation.

- **Quantum dots growth with ammonia source**

Under N-rich conditions, it is possible to achieve a 2D growth mode using NH_3 with a high V / III ratio of 4, in the case of GaN [94]. However, growing under NH_3 flux can have certain effects on the QD growth process since the presence of ammonia prevents the SK 2D-3D transition from occurring, regardless of the thickness of the deposited GaN layer. Under NH_3 flux, the surface is hydrogenated with a large number of N-H bonds that decrease the (0001) surface energy (γ_{film}) resulting in a higher surface energy cost ($\Delta\gamma$) to form the islands than the elastic energy gain ($|\Delta\gamma| > |\Delta E_{elastic}|$), which prevents the formation of QDs. For instance, it is possible to observe 2D-3D SK transition in the case of GaN / AlN using a nitrogen plasma source but it is not possible under NH_3 flux. According to a study by B. Damilano et al., in order to induce the formation of GaN QDs, a growth interruption of the GaN layer is necessary by turning off the NH_3 flux and proceeding under vacuum conditions [95], as shown in figure 45. Under vacuum, the $\gamma_{film}/\gamma_{facet}$ ratio increases and the surface energy cost is reduced ($|\Delta E_{elastic}| > |\Delta\gamma|$) permitting a 2D-3D transition and favoring a (0001) surface covered by elastically relaxed faceted islands, as shown in figure 44. Using a non-hydrogen source such as N_2 can directly trigger the 2D-3D transition since the gain in $\Delta E_{elastic}$ becomes dominant, as will be discussed in the next section.

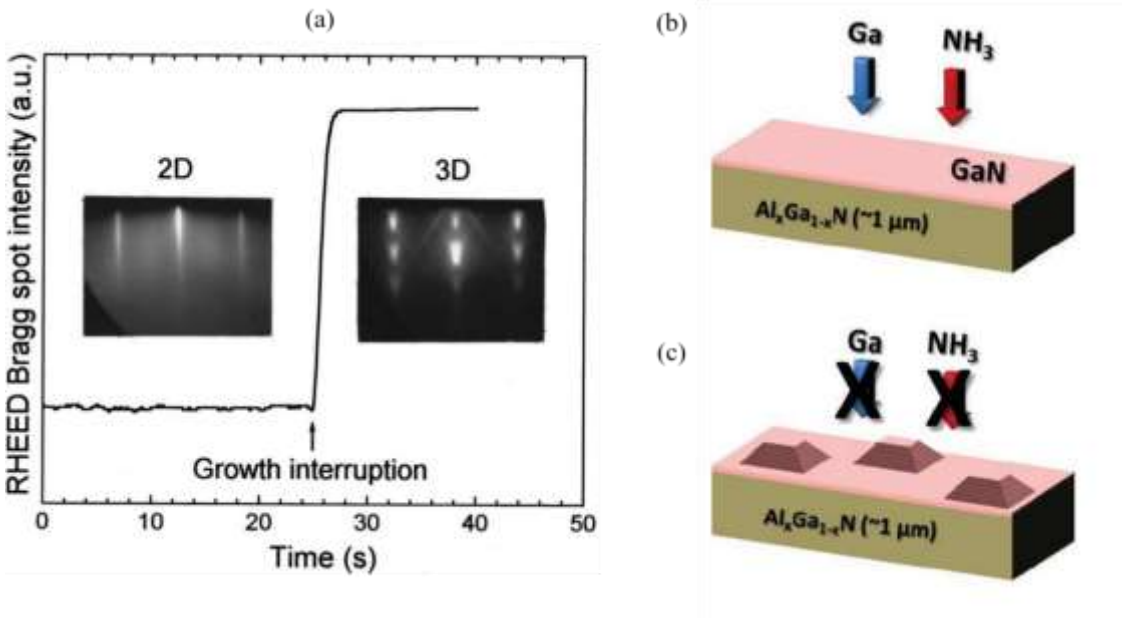

Figure 45. (a) Variation of the RHEED Bragg spots intensity during the growth of GaN and subsequent growth interruption. The inset presents the RHEED figures for a 2D GaN layer and 3D GaN islands. The strong increase of the intensity is due to the formation of 3D islands. (b) and (c) are schematic illustrations of the deposition of a 2D GaN layer and QDs formation under vacuum (growth interruption) [95].

It should be also mentioned that, for the 2D-3D transition to occur, it is not sufficient to only conduct the growth interruption under vacuum but also the deposited amount should exceed the SK critical thickness (h_c^{SK}), which is 3 MLs in the case of the GaN / AlN system [95]. The transition from a 2D surface to a 3D surface and the formation of QD facets can be observed in real-time by monitoring the intensity of RHEED during the growth process. Initially, a streaky pattern is observed indicating a 2D surface, which eventually changes to Bragg spots indicating the 3D surface, as illustrated in figure 45 (a). The facets of the QDs can be observed to form an angle of approximately 30° with respect to the (0001) surface.

- ## Quantum dots growth with a plasma source

In contrast to the growth of QDs using an NH_3 source (carried out under N-rich coniditons), which requires a growth interruption by switching off the NH_3 flux and proceeding under vacuum conditions to decrease the surface energy cost, plasma-assisted growth using N_2 source allows the 2D-3D transition to occur during the growth in a classical Stranski-Krastanov mode. This is made possible by the N-rich conditions (III/V < 1) created by the plasma N_2 source, which increase the (0001) surface energy (γ_{film}) (figure 46) [92], promoting the formation of 3D faceted structures. The increase in the surface energy is accompanied by a reduction in the surface energy cost ($|\Delta\gamma|$), which becomes smaller than the elastic energy gain ($|\Delta E_{elastic}| > |\Delta\gamma|$), resulting in a transition from a 2D to a 3D growth mode.

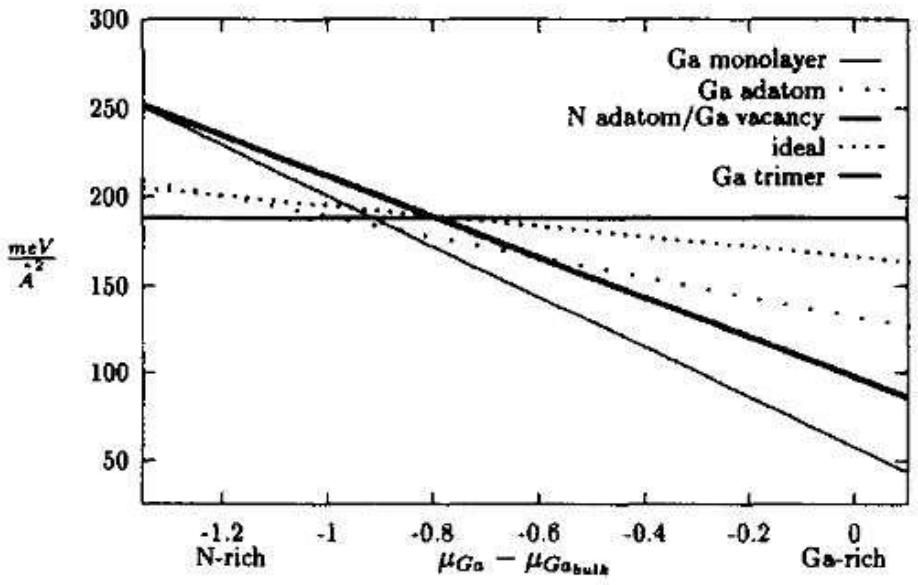

Figure 46. Surface energies in meV/Å^2 of Ga and N covered GaN (0 0 0 1) surfaces plotted vs $\mu_{Ga} - \mu_{Ga\,bulk}$. The parts on the left and on the right of the diagram correspond to N and Ga rich growth conditions, respectively. The diagram explains phase transitions observed during MBE growth [92].

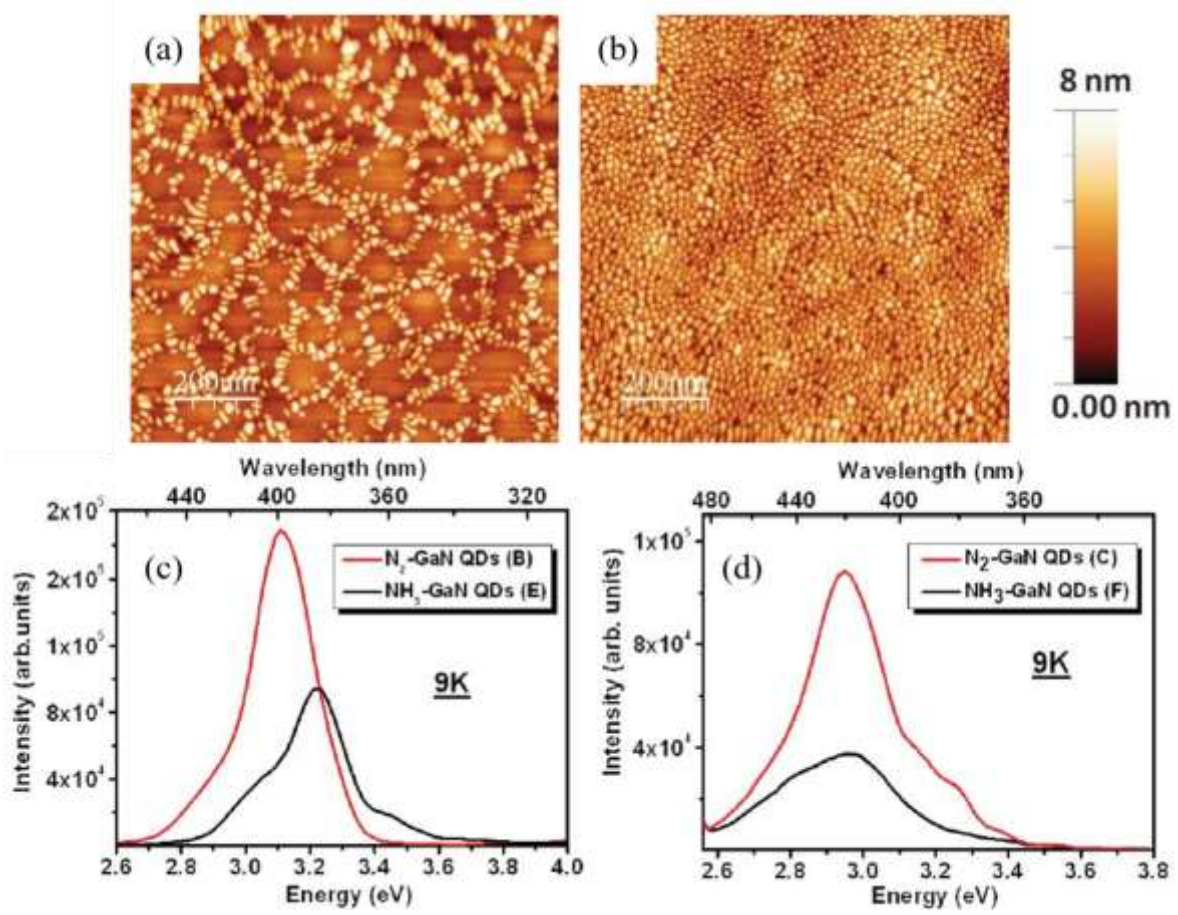

Figure 47. (a), (b) Atomic force microscopy images of GaN QDs grown on $Al_{0.7}Ga_{0.3}N$ by NH_3-MBE and PAMBE, respectively. (c), (d) PL comparison at low temperature between PAMBE grown GaN QDs and NH_3-MBE grown GaN QDs in $Al_{0.6}Ga_{0.4}N$ (0 0 0 1) and $Al_{0.7}Ga_{0.3}N$ (0 0 0 1) matrices, respectively [25].

Furthermore, the role of kinetics in QD formation has been highlighted by Samuel Matta et al. They demonstrated that using a plasma N_2 source for GaN QD growth can result in higher QD densities compared to using an NH_3 source, which is attributed to surface diffusion and the impact of hydrogen on surface energy [25]. Their findings demonstrated that PAMBE-grown GaN QDs exhibited a more homogeneous distribution on (Al,Ga)N with a higher density (3 x 10^{11} cm^{-2}) compared to NH_3-MBE-grown GaN QDs (1.2 x 10^{11} cm^{-2}), as depicted in Figure 47(a) and (b). This advantage can be attributed to the nitrogen source used, as the QD formation mechanism is highly influenced by it. When a plasma N_2 source is employed, the 2D-3D transition process begins during growth in a classical Stranski-Krastanov growth mode. Conversely, with an NH_3 source, the 2D-3D transition occurs only during a growth interruption under vacuum after the 2D layer-by-layer deposition. This distinction is associated with the surface energy contribution, which significantly differs when using NH_3 or N_2 gas sources for QD fabrication. In the case of NH_3 growth, the 2D-3D transition is connected to the desorption

of NH_x species during the growth interruption and vacuum annealing steps. The PL intensity was found to be 2 to 3 times higher for QDs grown using an N_2 source, as shown in Figure 47(c) and (d). This could be partially attributed to the higher QD density observed in PAMBE. Moreover, the PL full width at half maximum for NH_3-MBE-grown QDs (240 meV for sample E and 388 meV for sample F) was larger compared to PAMBE-grown QDs (227 meV for sample B and 267 meV for sample C), indicating better height homogeneity for PAMBE-grown QDs [25].

I.4 Conclusion

In summary, this chapter provided a comprehensive overview of III nitrides and their crystal properties, including elastic properties, defects, polarization, Stark effect, and band structure. The historical challenge of finding suitable substrates led researchers to venture into diverse options, considering cost and availability along with the intended application. We delved into the properties of sapphire, the substrate chosen for this thesis, and its epitaxial relations with (Al,Ga)N. We explored the state-of-the-art in UV light sources, with a focus on UV LEDs, and identified the key challenges facing internal quantum efficiency (IQE), injection efficiency (IE), and light extraction efficiency (LEE) in these devices. Furthermore, we delved into the epitaxial thin film growth techniques, particularly molecular beam epitaxy (MBE), ammonia (NH_3) assisted MBE, and plasma-assisted MBE (PAMBE). Through the exploration of these growth methods, we discussed the unique growth modes and conditions that enable the fabrication of QDs. By understanding the growth processes and the impact of different sources on QD formation, we gained valuable insights into enhancing the structural and optical properties of III nitride-based QDs. These insights have implications for achieving higher efficiency and performance in UV LED devices.

References:

[1] H. Morkoç, *Handbook of Nitride Semiconductors and Devices, Materials Properties, Physics and Growth*. John Wiley & Sons, 2009.

[2] J.-C. Moreno, P. Lorenzini, P. Muralt, R. Epfl, L. Buchaillot, et J. Fompeyrine, « Discipline : Physique présentée et soutenue publiquement par Etude de la croissance et des propriétés de films minces d'AlN épitaxiés par jets moléculaires sur substrat silicium : application aux résonateurs acoustiques et perspectives d'hétérostructures intégrées sur silicium Thèse dirigée par Fabrice SEMOND et Jean MASSIES Jury », 2009.

[3] H. Morkoç, S. Strite, G. B. Gao, M. E. Lin, B. Sverdlov, et M. Burns, « Large-band-gap SiC, III-V nitride, and II-VI ZnSe-based semiconductor device technologies », *Journal of Applied Physics*, vol. 76, n° 3, p. 1363-1398, 1994, doi: 10.1063/1.358463.

[4] S. C. Jain, M. Willander, J. Narayan, et R. Van Overstraeten, « III-nitrides: Growth, characterization, and properties », *Journal of Applied Physics*, vol. 87, n° 3, p. 965-1006, 2000, doi: 10.1063/1.371971.

[5] T. Kashima *et al.*, « Microscopic Investigation of $Al_{0.43}Ga_{0.57}N$ on Sapphire », *Japanese Journal of Applied Physics*, vol. 38, n° 12B, p. L1515, déc. 1999, doi: 10.1143/JJAP.38.L1515.

[6] « NSM Archive - Physical Properties of Semiconductors ». http://www.ioffe.ru/SVA/NSM/Semicond/ (consulté le 18 août 2023).

[7] M. Xie et kemi och biologi L. universitet I. för fysik, *Structural and elastic properties of InN and InAlN with different surface orientations and doping*. Department of Physics, Chemistry and Biology (IFM), Linköping University, 2012.

[8] S. K. Davidsson, J. F. Fälth, X. Y. Liu, H. Zirath, et T. G. Andersson, « Effect of AlN nucleation layer on the structural properties of bulk GaN grown on sapphire by molecular-beam epitaxy », *Journal of Applied Physics*, vol. 98, n° 1, p. 016109, juill. 2005, doi: 10.1063/1.1977189.

[9] O. Ambacher *et al.*, « Two dimensional electron gases induced by spontaneous and piezoelectric polarization in undoped and doped AlGaN/GaN heterostructures », *Journal of Applied Physics*, vol. 87, n° 1, p. 334-344, janv. 2000, doi: 10.1063/1.371866.

[10] J. F. Nye, *Physical Properties of Crystals: Their Representation by Tensors and Matrices*. in Oxford science publications. Clarendon Press, 1985. [En ligne]. Disponible sur: https://books.google.fr/books?id=ugwql-uVB44C

[11] A. F. Wright, « Elastic properties of zinc-blende and wurtzite AlN, GaN, and InN », *Journal of Applied Physics*, vol. 82, n° 6, p. 2833-2839, sept. 1997, doi: 10.1063/1.366114.

[12] K. Kim, W. R. L. Lambrecht, et B. Segall, « Elastic constants and related properties of tetrahedrally bonded BN, AlN, GaN, and InN », *Physical Review B*, vol. 53, n° 24, p. 16310-16326, juin 1996, doi: 10.1103/PhysRevB.53.16310.

[13] K. Tsubouchi, K. Sugai, et N. Mikoshiba, « AlN Material Constants Evaluation and SAW Properties on AlN/Al<inf>2</inf>O<inf>3</inf>and AlN/Si », in *1981 Ultrasonics Symposium*, IEEE, 1981, p. 375-380. doi: 10.1109/ULTSYM.1981.197646.

[14] C. Deger *et al.*, « Sound velocity of AlxGa1−xN thin films obtained by surface acoustic-wave measurements », *Applied Physics Letters*, vol. 72, n° 19, p. 2400-2402, mai 1998, doi: 10.1063/1.121368.

[15] L. E. McNeil, M. Grimsditch, et R. H. French, « Vibrational Spectroscopy of Aluminum Nitride », *Journal of the American Ceramic Society*, vol. 76, n° 5, p. 1132-1136, mai 1993, doi: 10.1111/j.1151-2916.1993.tb03730.x.

[16] A. Polian, M. Grimsditch, et I. Grzegory, « Elastic constants of gallium nitride », *Journal of Applied Physics*, vol. 79, n° 6, p. 3343-3344, mars 1996, doi: 10.1063/1.361236.

[17] H. P. Maruska et J. J. Tietjen, « THE PREPARATION AND PROPERTIES OF VAPOR-DEPOSITED SINGLE-CRYSTAL-LINE GaN », *Applied Physics Letters*, vol. 15, n° 10, p. 327-329, nov. 1969, doi: 10.1063/1.1652845.

[18] Y. Takagi, M. Ahart, T. Azuhata, T. Sota, K. Suzuki, et S. Nakamura, « Brillouin scattering study in the GaN epitaxial layer », *Physica B: Condensed Matter*, vol. 219-220, p. 547-549, avr. 1996, doi: 10.1016/0921-4526(95)00807-1.
[19] D. Hull et D. J. Bacon, *Introduction to dislocations*, vol. 37. Elsevier, 2011.
[20] P. M. John, « MBE-growth and characterization of Zn3N2 and Mg3N2: from epitaxy to materials science », Université Côte d'Azur, 2021.
[21] L. Priester, *Joints de Grains, Les*. Ed. Techniques Ingénieur, 2006.
[22] M. N. Crhea, « Structural characterization I X-ray diffraction ».
[23] F. Bernardini, V. Fiorentini, et D. Vanderbilt, « Spontaneous polarization and piezoelectric constants of III-V nitrides », *Physical Review B*, vol. 56, n° 16, p. R10024, 1997.
[24] A. Zoroddu, F. Bernardini, P. Ruggerone, et V. Fiorentini, « First-principles prediction of structure, energetics, formation enthalpy, elastic constants, polarization, and piezoelectric constants of AlN, GaN, and InN: Comparison of local and gradient-corrected density-functional theory », *Physical Review B*, vol. 64, n° 4, p. 045208, 2001.
[25] S. Matta, « AlGaN quantum dots grown by molecular beam epitaxy for ultraviolet light emitting diodes », Université Montpellier, 2018.
[26] F. Bernardini et V. Fiorentini, « Nonlinear macroscopic polarization in III-V nitride alloys », *Physical Review B*, vol. 64, n° 8, p. 085207, 2001.
[27] V. Fiorentini, F. Bernardini, et O. Ambacher, « Evidence for nonlinear macroscopic polarization in III–V nitride alloy heterostructures », *Applied physics letters*, vol. 80, n° 7, p. 1204-1206, 2002.
[28] E. F. Schubert, *Light-Emitting Diodes (2006)*. E. Fred Schubert, 2006.
[29] B. Damilano, « Nanostructures (Ga, In, Al) N: croissance par épitaxie sous jets moléculaires, propriétés optiques, applications aux diodes électroluminescentes », Nice, 2001.
[30] K. Shimada, « First-principles determination of piezoelectric stress and strain constants of wurtzite III–V nitrides », *Japanese journal of applied physics*, vol. 45, n° 4L, p. L358, 2006.
[31] A. Hangleiter, F. Hitzel, S. Lahmann, et U. Rossow, « Composition dependence of polarization fields in GaInN/GaN quantum wells », *Applied physics letters*, vol. 83, n° 6, p. 1169-1171, 2003.
[32] M. Leroux *et al.*, « Quantum confined Stark effect due to built-in internal polarization fields in (Al, Ga) N/GaN quantum wells », *Physical Review B*, vol. 58, n° 20, p. R13371, 1998.
[33] B. Gil, « Physics of Wurtzite Nitrides and Oxides », *Passport to Devices*, 2014.
[34] Y. Taniyasu, M. Kasu, et T. Makimoto, « Radiation and polarization properties of free-exciton emission from AlN (0001) surface », *Applied physics letters*, vol. 90, n° 26, p. 261911, 2007.
[35] R. Dingle, D. D. Sell, S. E. Stokowski, et M. Ilegems, « Absorption, reflectance, and luminescence of GaN epitaxial layers », *Physical Review B*, vol. 4, n° 4, p. 1211, 1971.
[36] T. Onuma *et al.*, « Exciton spectra of an AlN epitaxial film on (0001) sapphire substrate grown by low-pressure metalorganic vapor phase epitaxy », *Applied Physics Letters*, vol. 81, n° 4, p. 652-654, 2002.
[37] M. Leroux, « Matériaux semi-conducteurs III-V, II-VI et nitrures pour l'optoélectronique », *Hermes publications, Paris*, 2003.
[38] B. Gil, O. Briot, et R.-L. Aulombard, « Valence-band physics and the optical properties of GaN epilayers grown onto sapphire with wurtzite symmetry », *Physical Review B*, vol. 52, n° 24, p. R17028, 1995.
[39] I. Vurgaftman et J. n Meyer, « Band parameters for nitrogen-containing semiconductors », *Journal of Applied Physics*, vol. 94, n° 6, p. 3675-3696, 2003.
[40] M. Leroux *et al.*, « Optical Characterization of AlxGa1—xN Alloys (x< 0.7) Grown on Sapphire or Silicon », *physica status solidi (b)*, vol. 234, n° 3, p. 887-891, 2002.
[41] Y. P. Varshni, « Temperature dependence of the energy gap in semiconductors », *physica*, vol. 34, n° 1, p. 149-154, 1967.
[42] Q. G. Q. Guo et A. Y. A. Yoshida, « Temperature dependence of band gap change in InN and AlN », *Japanese Journal of Applied Physics*, vol. 33, n° 5R, p. 2453, 1994.
[43] T. Wethkamp *et al.*, « Dielectric function of hexagonal AlN films determined by spectroscopic ellipsometry in the vacuum-uv spectral range », *Physical Review B*, vol. 59, n° 3, p. 1845, 1999.

[44] Y. Li *et al.*, « Temperature dependence of energy gap in GaN thin film studied by thermomodulation », *Applied physics letters*, vol. 70, n° 18, p. 2458-2460, 1997.
[45] S. Tripathy *et al.*, « Optical properties of GaN layers grown on C-, A-, R-, and M-plane sapphire substrates by gas source molecular beam epitaxy », *Journal of applied physics*, vol. 85, n° 12, p. 8386-8399, 1999.
[46] J. Wu *et al.*, « Temperature dependence of the fundamental band gap of InN », *Journal of Applied Physics*, vol. 94, n° 7, p. 4457-4460, 2003.
[47] M. Raeiszadeh et B. Adeli, « A critical review on ultraviolet disinfection systems against COVID-19 outbreak: applicability, validation, and safety considerations », *Acs Photonics*, vol. 7, n° 11, p. 2941-2951, 2020.
[48] J. R. Bolton et C. A. Cotton, *The ultraviolet disinfection handbook*. American Water Works Association, 2011.
[49] M. Norval, « The effect of ultraviolet radiation on human viral infections », *Photochemistry and photobiology*, vol. 82, n° 6, p. 1495-1504, 2006.
[50] « Helios-Quartz_UV-LAMPS_eng.pdf ». Consulté le: 21 février 2023. [En ligne]. Disponible sur: http://www.heliosquartz.com/wp-content/uploads/2016/01/Helios-Quartz_UV-LAMPS_eng.pdf
[51] « Homepage | Minamata Convention on Mercury ». https://www.mercuryconvention.org/en (consulté le 24 février 2023).
[52] uvo3master, « Difference Between Low & Medium Pressure UV Lamps | UVO3 », 25 novembre 2011. https://www.uvo3.co.uk/low-vs-medium-pressure-uv-lamps/ (consulté le 21 février 2023).
[53] « Heraeus Group ». https://www.heraeus.com/en/group/home/home.html (consulté le 18 juillet 2023).
[54] S. I. LLP, « Global UV LED Market Size, Share To Hit USD 2.19 Billion By 2030 | CAGR 19.17% », *GlobeNewswire News Room*, 19 janvier 2023. https://www.globenewswire.com/news-release/2023/01/19/2592091/0/en/Global-UV-LED-Market-Size-Share-To-Hit-USD-2-19-Billion-By-2030-CAGR-19-17.html (consulté le 22 février 2023).
[55] M. Kneissl, T.-Y. Seong, J. Han, et H. Amano, « The emergence and prospects of deep-ultraviolet light-emitting diode technologies », *nature photonics*, vol. 13, n° 4, p. 233-244, 2019.
[56] Y. Narukawa, M. Ichikawa, D. Sanga, M. Sano, et T. Mukai, « White light emitting diodes with super-high luminous efficacy », *Journal of physics D: Applied physics*, vol. 43, n° 35, p. 354002, 2010.
[57] T. Takano, T. Mino, J. Sakai, N. Noguchi, K. Tsubaki, et H. Hirayama, « Deep-ultraviolet light-emitting diodes with external quantum efficiency higher than 20% at 275 nm achieved by improving light-extraction efficiency », *Applied Physics Express*, vol. 10, n° 3, p. 031002, 2017.
[58] O. Klein, J. Biskupek, K. Forghani, F. Scholz, et U. Kaiser, « TEM investigations on growth interrupted samples for the correlation of the dislocation propagation and growth mode variations in AlGaN deposited on SiNx interlayers », *Journal of Crystal Growth*, vol. 324, n° 1, p. 63-72, juin 2011, doi: 10.1016/j.jcrysgro.2011.03.050.
[59] K. Ban *et al.*, « Internal quantum efficiency of whole-composition-range AlGaN multiquantum wells », *Applied physics express*, vol. 4, n° 5, p. 052101, 2011.
[60] M. Shatalov *et al.*, « AlGaN deep-ultraviolet light-emitting diodes with external quantum efficiency above 10% », *Applied Physics Express*, vol. 5, n° 8, p. 082101, 2012.
[61] M. Leroux *et al.*, « Stark effect in ensembles of polar (0001) Al0. 5Ga0. 5N/GaN quantum dots and comparison with semipolar (11− 22) ones », *Journal of Applied Physics*, vol. 116, n° 3, p. 034308, 2014.
[62] Y. Horikoshi, « Advanced epitaxial growth techniques: atomic layer epitaxy and migration-enhanced epitaxy », *Journal of crystal growth*, vol. 201, p. 150-158, 1999.
[63] S. Matta *et al.*, « Properties of AlN layers grown on c-sapphire substrate using ammonia assisted MBE », *Journal of Crystal Growth*, vol. 499, p. 40-46, oct. 2018, doi: 10.1016/j.jcrysgro.2018.07.023.
[64] M. Z. Peng *et al.*, « Reducing dislocations of Al-rich AlGaN by combining AlN buffer and AlN/Al0. 8Ga0. 2N superlattices », *Journal of crystal growth*, vol. 310, n° 6, p. 1088-1092, 2008.

[65] H. Miyake, C. H. Lin, K. Tokoro, et K. Hiramatsu, « Preparation of high-quality AlN on sapphire by high-temperature face-to-face annealing », *Journal of Crystal Growth*, vol. 456, p. 155-159, déc. 2016, doi: 10.1016/j.jcrysgro.2016.08.028.
[66] H. Miyake *et al.*, « Annealing of an AlN buffer layer in N_2 –CO for growth of a high-quality AlN film on sapphire », *Appl. Phys. Express*, vol. 9, nº 2, p. 025501, févr. 2016, doi: 10.7567/APEX.9.025501.
[67] M. Nemoz, R. Dagher, S. Matta, A. Michon, P. Vennéguès, et J. Brault, « Dislocation densities reduction in MBE-grown AlN thin films by high-temperature annealing », *Journal of Crystal Growth*, vol. 461, p. 10-15, mars 2017, doi: 10.1016/j.jcrysgro.2016.12.089.
[68] A. Zaiter *et al.*, « Crystalline Quality and Surface Morphology Improvement of Face-to-Face Annealed MBE-Grown AlN on h-BN », *Materials*, vol. 15, nº 23, p. 8602, 2022.
[69] A. Koma et K. Yoshimura, « Ultrasharp interfaces grown with Van der Waals epitaxy », *Surface Science*, vol. 174, nº 1, p. 556-560, août 1986, doi: 10.1016/0039-6028(86)90471-1.
[70] T. Ayari *et al.*, « Novel scalable transfer approach for discrete III-nitride devices using wafer-scale patterned H-BN/sapphire substrate for pick-and-place applications », *Advanced Materials Technologies*, vol. 4, nº 10, p. 1900164, 2019.
[71] S. Sundaram *et al.*, « MOVPE of GaN-based mixed dimensional heterostructures on wafer-scale layered 2D hexagonal boron nitride—A key enabler of III-nitride flexible optoelectronics », *APL Materials*, vol. 9, nº 6, p. 061101, 2021.
[72] J. Brault *et al.*, « Polar and semipolar GaN/Al0. 5Ga0. 5N nanostructures for UV light emitters », *Semiconductor Science and Technology*, vol. 29, nº 8, p. 084001, 2014.
[73] K. B. Nam, M. L. Nakarmi, J. Li, J. Y. Lin, et H. X. Jiang, « Mg acceptor level in AlN probed by deep ultraviolet photoluminescence », *Appl. Phys. Lett.*, vol. 83, nº 5, p. 878-880, août 2003, doi: 10.1063/1.1594833.
[74] C.-Z. Zhao, T. Wei, L.-Y. Chen, S.-S. Wang, et J. Wang, « The activation energy for Mg acceptor in AlxGa1-xN alloys in the whole composition range », *Superlattices and Microstructures*, vol. 109, p. 758-762, sept. 2017, doi: 10.1016/j.spmi.2017.06.006.
[75] E. F. Schubert, W. Grieshaber, et I. D. Goepfert, « Enhancement of deep acceptor activation in semiconductors by superlattice doping », *Applied physics letters*, vol. 69, nº 24, p. 3737-3739, 1996.
[76] P. Kozodoy, M. Hansen, S. P. DenBaars, et U. K. Mishra, « Enhanced Mg doping efficiency in Al 0.2 Ga 0.8 N/GaN superlattices », *Applied Physics Letters*, vol. 74, nº 24, p. 3681-3683, 1999.
[77] R. Dahal *et al.*, « Epitaxially grown semiconducting hexagonal boron nitride as a deep ultraviolet photonic material », *Appl. Phys. Lett.*, vol. 98, nº 21, p. 211110, mai 2011, doi: 10.1063/1.3593958.
[78] H. Hirayama, Y. Tsukada, T. Maeda, et N. Kamata, « Marked Enhancement in the Efficiency of Deep-Ultraviolet AlGaN Light-Emitting Diodes by Using a Multiquantum-Barrier Electron Blocking Layer », *Appl. Phys. Express*, vol. 3, nº 3, p. 031002, févr. 2010, doi: 10.1143/APEX.3.031002.
[79] N. Maeda et H. Hirayama, « Realization of high-efficiency deep-UV LEDs using transparent p-AlGaN contact layer », *physica status solidi c*, vol. 10, nº 11, p. 1521-1524, 2013, doi: 10.1002/pssc.201300278.
[80] H.-Y. Ryu, I.-G. Choi, H.-S. Choi, et J.-I. Shim, « Investigation of light extraction efficiency in AlGaN deep-ultraviolet light-emitting diodes », *Applied Physics Express*, vol. 6, nº 6, p. 062101, 2013.
[81] K. B. Nam, J. Li, M. L. Nakarmi, J. Y. Lin, et H. X. Jiang, « Unique optical properties of AlGaN alloys and related ultraviolet emitters », *Applied physics letters*, vol. 84, nº 25, p. 5264-5266, 2004.
[82] C. Reich *et al.*, « Strongly transverse-electric-polarized emission from deep ultraviolet AlGaN quantum well light emitting diodes », *Applied Physics Letters*, vol. 107, nº 14, p. 142101, 2015.
[83] Y. Zhang, Z. Jamal-Eddine, et S. Rajan, « Recent progress of tunnel junction-based ultra-violet light emitting diodes », *Japanese Journal of Applied Physics*, vol. 58, nº SC, p. SC0805, 2019.
[84] Y. Zhang *et al.*, « Interband tunneling for hole injection in III-nitride ultraviolet emitters », *Applied Physics Letters*, vol. 106, nº 14, p. 141103, 2015.

[85] T. Foxon, « History of MBE », *Molecular Beam Epitaxy: Materials and Applications for Electronics and Optoelectronics*, p. 1, 2019.
[86] S. Nishikawa et S. Kikuchi, « Diffraction of cathode rays by calcite », *Nature*, vol. 122, n° 3080, p. 726-726, 1928.
[87] J. R. Arthur et J. J. LePore, « GaAs, GaP, and GaAs x P 1− x Epitaxial Films Grown by Molecular Beam Deposition », *Journal of Vacuum Science and Technology*, vol. 6, n° 4, p. 545-548, 1969.
[88] H. Mariette, « Formation of self-assembled quantum dots induced by the Stranski–Krastanow transition: a comparison of various semiconductor systems », *Comptes Rendus Physique*, vol. 6, n° 1, p. 23-32, 2005.
[89] J. Tersoff et R. M. Tromp, « Shape transition in growth of strained islands: Spontaneous formation of quantum wires », *Physical review letters*, vol. 70, n° 18, p. 2782, 1993.
[90] J. Tersoff et F. K. LeGoues, « Competing relaxation mechanisms in strained layers », *Physical review letters*, vol. 72, n° 22, p. 3570, 1994.
[91] F. Tinjod, « Mécanismes de formation des boîtes quantiques semiconductrices, application aux nanostructures II-VI et étude de leurs propriétés optiques », Université Joseph-Fourier-Grenoble I, 2003.
[92] J. Elsner, M. Haugk, G. Jungnickel, et T. Frauenheim, « Theory of Ga, N and H terminated GaN (0 0 0 1)(0 0 0 1) surfaces », *Solid state communications*, vol. 106, n° 11, p. 739-743, 1998.
[93] B. Damilano, J. Brault, et J. Massies, « Formation of GaN quantum dots by molecular beam epitaxy using NH3 as nitrogen source », *Journal of Applied Physics*, vol. 118, n° 2, juill. 2015, doi: 10.1063/1.4923425.
[94] N. Grandjean, M. Leroux, J. Massies, M. Mesrine, et M. Laügt, « Molecular beam epitaxy of GaN under N-rich conditions using NH3 », *Japanese journal of applied physics*, vol. 38, n° 2R, p. 618, 1999.
[95] B. Damilano, N. Grandjean, F. Semond, J. Massies, et M. Leroux, « From visible to white light emission by GaN quantum dots on Si (111) substrate », *Applied physics letters*, vol. 75, n° 7, p. 962-964, 1999.

Chapter 2

Post-growth high temperature annealing

In this chapter, an introduction to the face-to-face high temperature annealing technique and its advantage in reducing dislocation densities and improving the crystalline quality in aluminum nitride (AlN) templates is given. Furthermore, the annealing of AlN layers grown on sapphire and of AlN layers grown on hexagonal boron nitride (h-BN) is investigated and discussed. This chapter covers:

- The development of face-to-face high temperature annealing method.
- The annealing of AlN templates grown by physical vapor deposition (PVD) growth method.
- The annealing of AlN layers grown by molecular beam epitaxy (MBE) on h-BN / sapphire templates.
- The surface and structural characterization using diffraction techniques, from X-Ray diffraction (XRD) via reflection high-energy electron diffraction (RHEED) and atomic force microscopy (AFM) to transmission electron microscopy (TEM).

II.1. Face-to-face high temperature annealing

II.1.1. Introduction

Aluminum nitride (AlN) based materials have drawn significant interest for aluminum gallium nitride (AlGaN) based UV LEDs due to its wide direct bandgap of 6.1 eV, high chemical and thermal stability, high thermal conductivity, high surface acoustic wave velocity, low thermal expansion coefficient and high breakdown dielectric strength [1], [2]. Regarding the importance of the substrate in epitaxial growth, on one hand, native AlN bulk substrates present unique features with their high crystal quality and remarkably low TDDs ($<10^5$ cm^{-2}), but they are expensive, scarce and come in small sizes (typically below 2-inch). On the other hand, sapphire is mostly used as a substrate of choice for the growth of AlN for its low cost, transparency in the UV range and large size availability (up to 8-inch). However, despite these advantages, some drawbacks are also present: a high lattice mismatch (~13% for AlN for the basal plane lattice parameter, a_{AlN} = 3.112 Å) along with a lattice thermal coefficient mismatch (~43% for the basal plane) that induce several epitaxial challenges. Indeed, these mismatches decrease the crystalline structural quality of the epitaxial layer and increase the TDDs that act as non-radiative recombination centers thereby limiting the efficiency of LEDs.

Post-growth annealing or high temperature annealing is a method used to enhance the crystalline quality of AlN layers grown on sapphire substrates by reducing the threading dislocation densities (TDDs) in the layers. Pr. Hideto Miyake and his research group developed the use of face-to-face high temperature annealing (FFA) technique in nitrogen ambience on sputtered and metal organic vapor phase epitaxy (MOVPE) grown AlN on sapphire, i.e. so-called AlN template in the following. They were able to reduce the TDDs, modifying the surface morphology from a columnar aspect to a step and terrace one, all along while improving the crystalline structural quality [3]. The surface cover up of an AlN template with another AlN template or with a sapphire wafer is done to suppress the thermal decomposition of the AlN films, as shown in figure 1 [4].

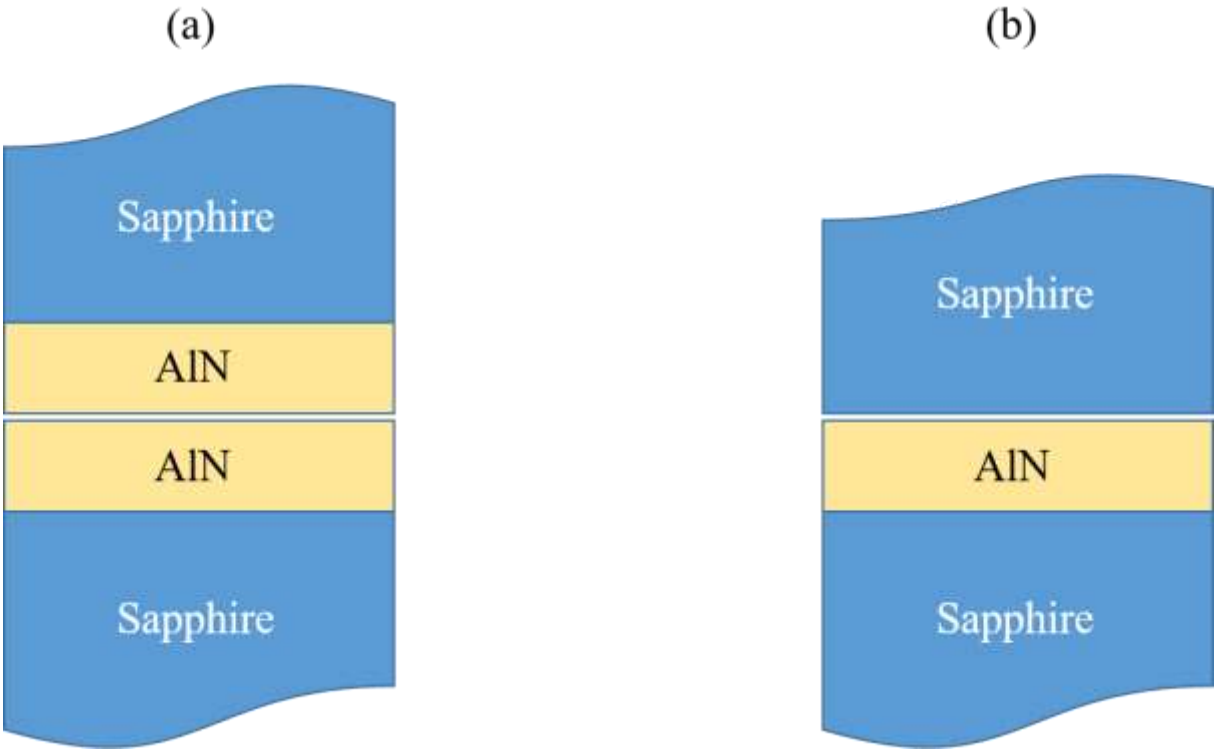

Figure 1. Schematic illustration of sample setup. (a) two AlN templates on sapphire were overlapped face-to-face. (b) AlN template covered with a sapphire wafer.

II.1.2. Annealing of PVD-grown AlN templates

The growth of both smooth surface and high crystalline quality AlN templates is important in order to fabricate efficient (Al,Ga)N based UV LEDs. Our research group in CRHEA was interested in conducting an annealing study on AlN films deposited on sapphire by sputtering technique provided by EVATEC AG Company based in Switzerland. The study focused on performing different annealing recipes that differ by both time duration and temperature while investigating the annealing effect and diffusion mechanism on the AlN layers in order to assess the best annealing recipe with the most efficient thermal budget.

a) PVD-grown AlN templates

Physical vapor deposition (PVD) is a thin film deposition technique that involves the deposition of atoms or molecules onto a substrate surface in a vacuum environment. The process involves heating a source material (metal or semiconductor) to a high temperature, which causes it to vaporize and form a plasma. The plasma is then directed towards the substrate, where it condenses and forms a thin film. There are several methods of PVD, including evaporation, sputtering, and ion plating. In evaporation, the source material is heated until it reaches its boiling point and vaporizes, while in sputtering, energetic ions are used to

eject atoms from the source material. Ion plating involves the use of an ion beam to sputter the source material and simultaneously bombard the substrate with ions, which can improve film adhesion and densification. In our case, the AlN templates provided are grown by sputtering technique. This technique involves bombarding the target source with high-energy ions originated from a rare gas discharge (such as argon) in a vacuum chamber, which causes atoms or molecules to be ejected from the target surface. The ejected particles then travel in straight lines and are deposited onto the substrate, forming a thin film, as shown in figure 2. The generation of the high-energy ions is done according to the following ionization process:

$$Ar + e^- \rightarrow Ar^+ + e^- + e^- \qquad \text{(Eq. II. 1)}$$

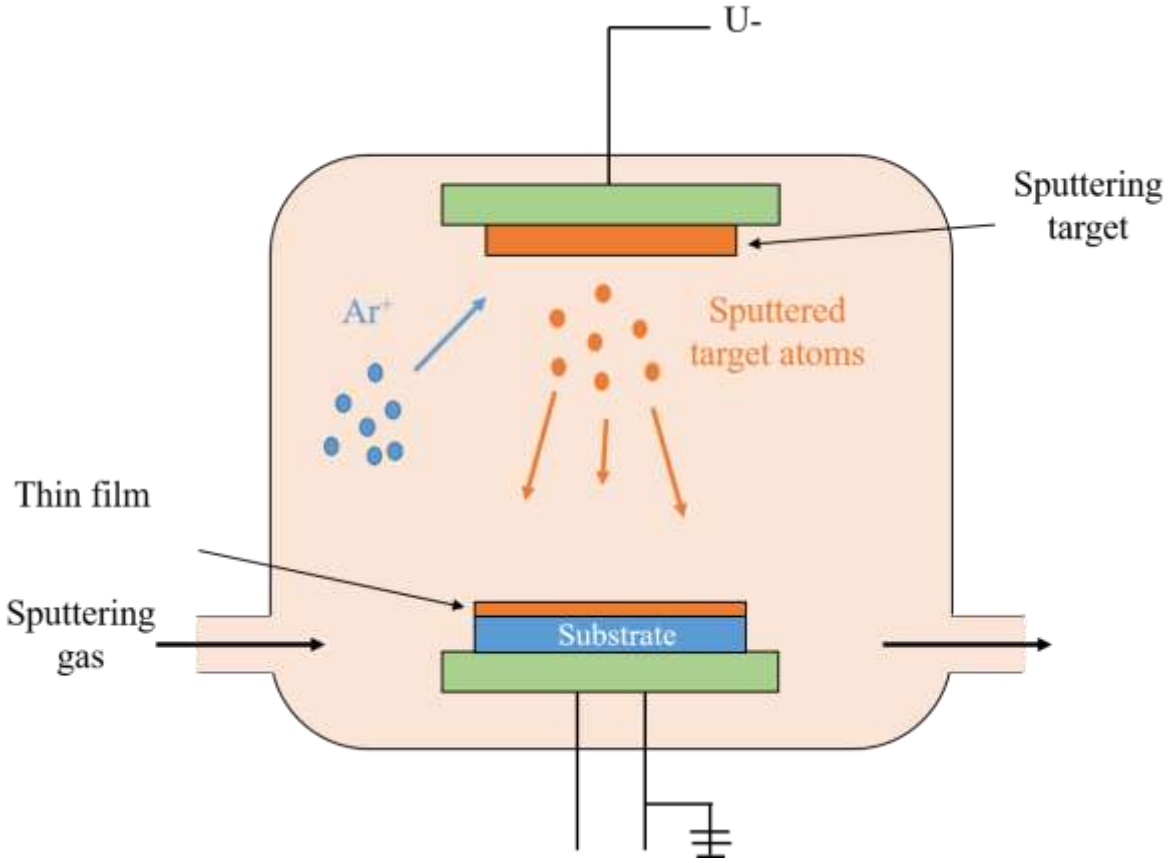

Figure 2. Schematic illustration of a typical physical vapor deposition (PVD) system.

- ## Structural and morphological properties

The sputtered AlN templates were studied by both reflection high-energy electron diffraction (RHEED) and atomic force microscopy (AFM) EDGE-DIMENSION (BRUKER, Billerica, MA, USA), operating in tapping-mode. The AFM data were processed using WSxM software (version number 4.0 Beta 9.1) [5] in order to investigate the surface morphology. In

addition, X-ray diffraction (XRD) measurements were performed using a PANalytical X'Pert PRO MDR four-circle diffractometer (Malvern Panalytical, Malvern, United Kingdom) in order to study the crystalline quality of the AlN layers. The RHEED surface reconstruction measurement shown in figure 3 conducted on the 100 nm AlN PVD template indicates a three dimensional (3D) surface with spots attributed to the presence of islands (i.e., 3D-like structure) on the surface.

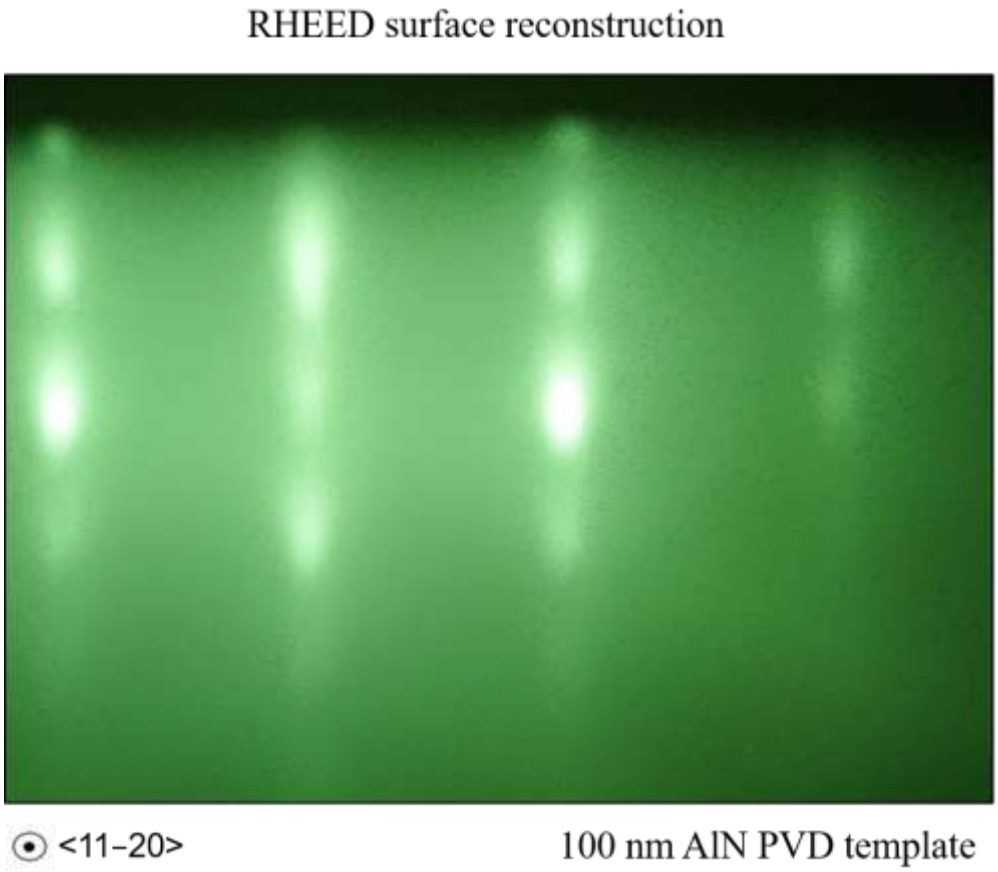

Figure 3. Reflection high-energy electron diffraction (RHEED) image along the $< 1\,1 - 2\,0 >$ azimuth of the surface. The spots were attributed to the presence of islands (i.e., 3D-like structures) on the surface.

AFM measurements confirmed the surface observed by RHEED, indicating a surface dominated by AlN grains. The surface roughness determined by the surface root-mean-square (RMS) is equal to 1 nm with AlN grains' average height of 3 nm ($\pm$ 1.5 nm) and average diameter of 30 nm ($\pm$ 10 nm), as shown by surface profile images given in figure 4. This type of morphology was found for both types of AlN samples studied during this work (i.e. using 100 nm and 200 nm thick AlN layers).

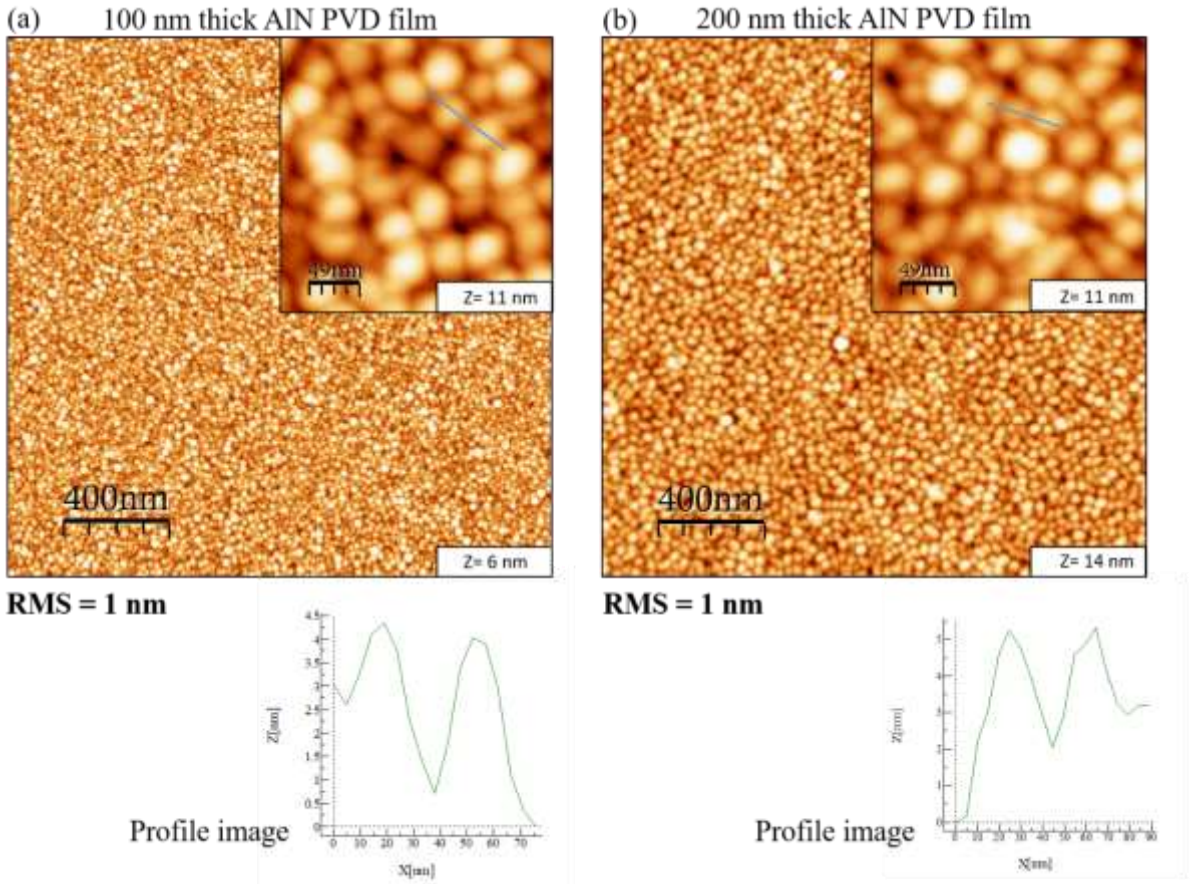

Figure 4. Atomic force microscopy images of (2 x 2) µm^2 of: (a) a 100 nm thick AlN PVD film, and (b) a 200 nm thick AlN PVD film. The insets show (250 x 250 nm^2) scan images. The term Z represents the vertical scale and the variation in height in the AFM images, and its value is reported at the bottom right hand side of the image. In the bottom of each image is a profile measurement of a specific marked zone indicated by a blue line in the (250 x 250 nm^2) scan images.

Regarding the structural quality, the XRD Omega-scan performed on the 100 nm sputtered AlN template had a full width at half maximum (FWHM) value equal to 0.23° (828 arcsec) for the (0 0 0 6) symmetric plane and a high value of 1.3° (4684 arcsec) for the asymmetric plane (1 0 −1 1). The omega-scans FWHM are impacted by many factors such as the wafer curvature, the instrumental width, the coherence length, the lattice strain and the lattice rotation due to dislocations (tilt and twist misorientations – see Chapter I). Nonetheless, for films with high TDDs as in our case here, the lattice rotations due to dislocations have the most important influence [6], [7]. Therefore, the tilt defined as out-of-plane misorientation and the twist defined as in-plane misorientation can be evaluated from the symmetric and skew symmetric reflections. By coupling the XRD measurements with the Dunn and Koch equation [8], it is possible then to correlate mixed and edge TDDs with the FWHM of the symmetric and skew symmetric reflections [9]. It is critical to mention that the screw TDDs are neglected as they are present in very low proportion (~1%) in nitrides [10]. For the AlN template with the 100 nm

thickness, the dislocation densities values were estimated at $1.13x10^{11}$ cm^{-2} for the edge-type dislocations and $1.17x10^{10}$ cm^{-2} for the mixed-type dislocations. For the AlN template with the 200 nm thickness, the FWHM values were found to be 0.22° (792 arcsec) and 0.89° (3197 arcsec) for the (0 0 0 6) symmetric plane and (1 0 −1 1) asymmetric plane, respectively. The estimated dislocation densities were $6x10^{10}$ cm^{-2} and $6.6x10^{9}$ cm^{-2} for edge-type and mixed-type dislocations, respectively. The values estimated for both samples indicate that the crystalline quality is in need for an improvement in order to decrease the value of different type of dislocations. This fact was behind our motivation to conduct an annealing study to improve and prepare ready-to-grow annealed templates defined by both low dislocation densities value and smooth surface morphology for the subsequent growth of heterostructures with improved structural properties and high efficiency UV LEDs.

b) PVD-grown AlN templates face-to-face annealing

Two full wafer (2 inches) AlN sputtered films with two different thicknesses (100 nm and 200 nm) were put in a face-to-face position in a home-made resistively heated horizontal hot wall chemical vapor deposition (CVD) reactor with a graphite chamber for high temperature annealing, as shown in figure 5.

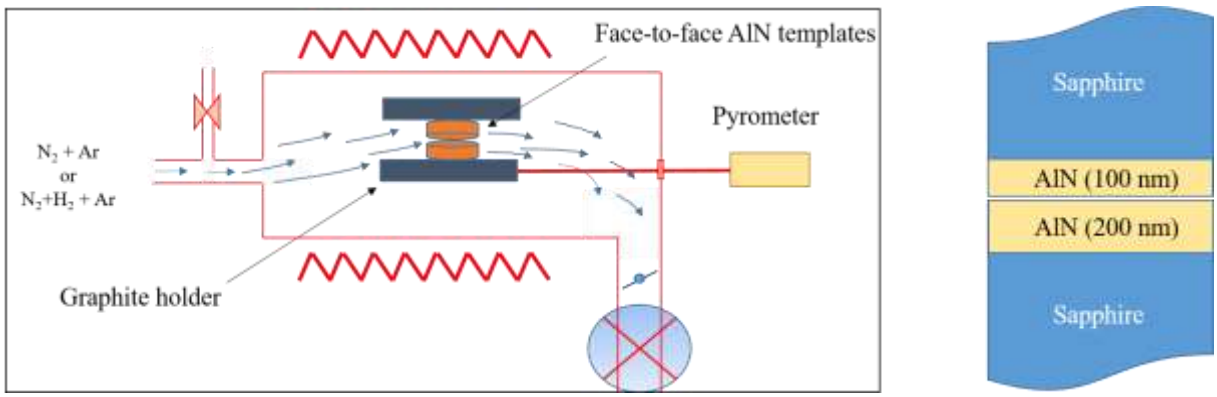

Figure 5. On the left is a schematic illustration of the CVD reactor used for high temperature annealing and on the right is the face-to-face AlN PVD films used for annealing.

Wafers were positioned in a face to face arrangement, held in place by four screws to maintain alignment with two identical graphite holders. Temperature measurement was facilitated by a pyrometer focused on the side of the lower graphite holder. Calibration of the temperature at the center of the holders was achieved using silicon melting. The annealing steps were conducted in two annealing phases under different gas mixture. The first phase consisted of two annealing steps for 15 minutes each at a temperature T_{N2} under a constant nitrogen (N_2) laminar flow of 6 slm and a total pressure of 800 mbars in order to improve the crystalline structural

quality. The second phase consisted of three annealing steps for 10 minutes each at a temperature T_{H2+N2} under a 50% (3 slm) hydrogen (H_2) + 50% (3 slm) nitrogen (N_2) flow and a total pressure of 800 mbars in order to improve the surface morphology and smoothen it. At each annealing step, when the heating was terminated, the samples were left to cool down to room temperature under the carrier gas (at an initial cooling rate of 3°C/s).

c) Steps of HTA investigated / developed

We investigated both the annealing temperature and time under N_2 in order to find the temperature and time that can improve the sample's structure the most. We started investigating the annealing temperature for the first annealing phase T_{N2}: the range has been set to be between 1550°C and 1650°C at 800 mbar under 6 slm (standard liters per minute) N_2 for 15 minutes each. Figure 6(a) shows the XRD FWHM variation for both the symmetric (0 0 0 6) and asymmetric (1 0 −1 1) planes as function of the annealing temperature for both the 100 nm and the 200 nm AlN PVD templates. It can be seen in figure 6(a) that right from the first annealing at 1550°C, a strong improvement in the crystalline quality occurred in the form of a reduction of the FWHM values for both templates. Then, it further continued decreasing after the second and third successive annealing on the same wafers at 1600°C and 1650°C, respectively. For the 100 nm AlN PVD template, the FWHM value decreased from 0.23° (830 arcsec) to 0.09° (330 arcsec) and from 1.3° (4684 arcsec) to 0.23° (1000 arcsec) for the symmetric (0 0 0 6) and asymmetric (1 0 −1 1) planes, respectively. Furthermore, for the 200 nm AlN PVD template, the FWHM value decreased from 0.22° (792 arcsec) to 0.08° (299 arcsec) and from 0.89° (3214 arcsec) to 0.19° (680 arcsec) for the symmetric (0 0 0 6) and asymmetric (1 0 −1 1) planes, respectively.

Screw dislocations, characterized by a Burgers vector c = <0 0 0 1>, primarily impact the tilt value of thin films, while edge dislocations, with a Burgers vector a = 1/3 <1 1 −2 0>, primarily influence the twist value. Mixed dislocations, characterized by a Burgers vector a+c = 1/3 <1 1 −2 3>, affect both the tilt and twist values. We focused on distinguishing between edge and mixed threading dislocations since screw threading dislocations constitute a very small proportion, approximately 1%, of all threading dislocations in nitride materials [10]. The edge threading dislocation densities was then estimated by coupling the XRD measurements with the Dunn and Koch equation [8]:

$$\rho = \frac{\alpha^2}{4.35 \text{ x } b^2}$$

where α represents the twist value corresponding to the skew symmetric FWHM value in radians and b is the Burgers vector of the edge dislocation. Assuming that the tilt is only due to mixed TDs (due to the very low proportion of pure screw dislocations) mixed TDDs can be calculated from the tilt using the same formula.

For the 100 nm thick AlN PVD template, the edge dislocation density decreased from an initial value of 1.14 x 10^{11} cm^{-2} before the annealing to 6.3 x 10^{9} cm^{-2} after the annealings and for the mixed dislocation density, it decreased from 1.17 x 10^{10} cm^{-2} before the annealing to 8.4 x 10^{8} cm^{-2} after the annealings, as shown in figure 6(b). Regarding the 200 nm thick AlN PVD template, the edge dislocation density decreased from an initial value of 6.2 x 10^{10} cm^{-2} before the annealing to 3.4 x 10^{9} cm^{-2} after the annealings, while for the mixed dislocation density, it decreased from 6.7 x 10^{9} cm^{-2} before the annealing to 4.7 x 10^{8} cm^{-2} after the annealings, as shown in figure 6(b). Based on these results, we were able to conclude that the best values under N_2 were obtained at 1650°C, thus adopting this temperature under N_2 for our annealing recipe.

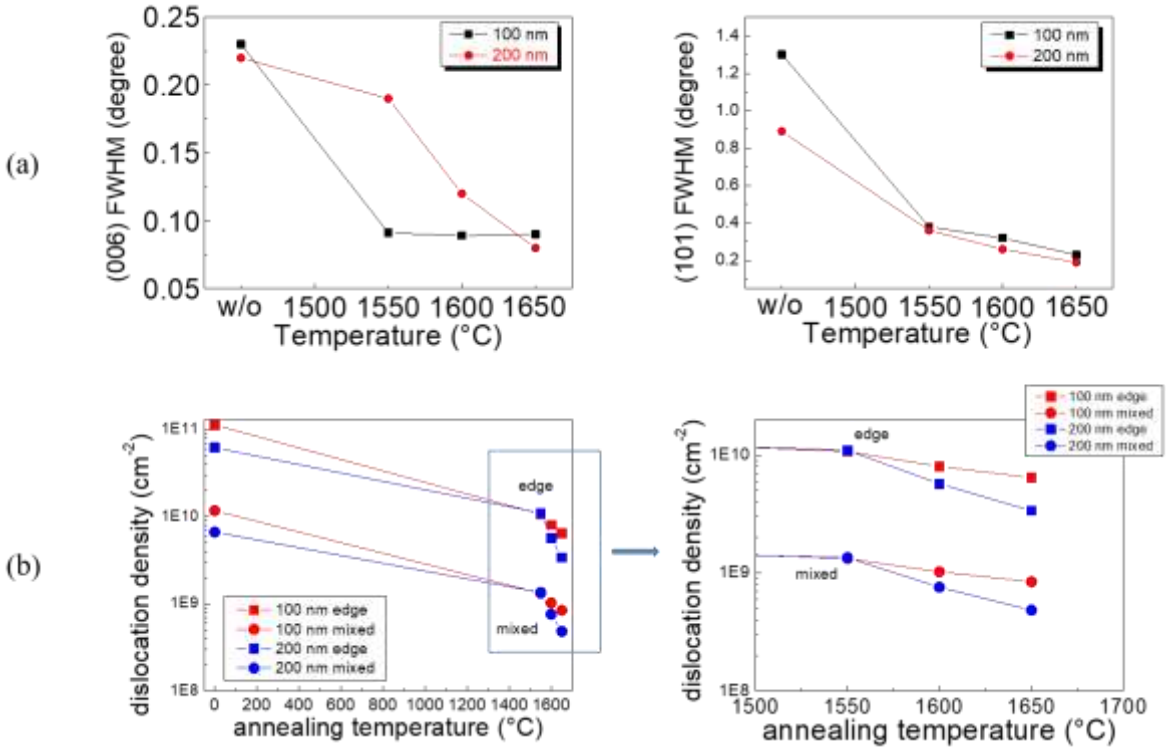

Figure 6. (a) Variation of the XRD-RC FWHM as a function of the annealing temperatures for the 100 nm and the 200 nm thick AlN PVD templates. (b) Edge and mixed dislocation densities of the 100 nm and the 200 nm thick AlN PVD templates estimated from the tilt and twist values as a function of the annealing temperatures.

The second step was to investigate the optimum annealing time under N_2 at 1650°C. For that, a successive annealing cycle of 15 minutes followed by XRD measurements was repeated three times for both templates. Figures 7(a) and (b) show the variation of the XRD-RC FWHM for both templates for the symmetric (0 0 0 6) and asymmetric (1 0 −1 1) planes.

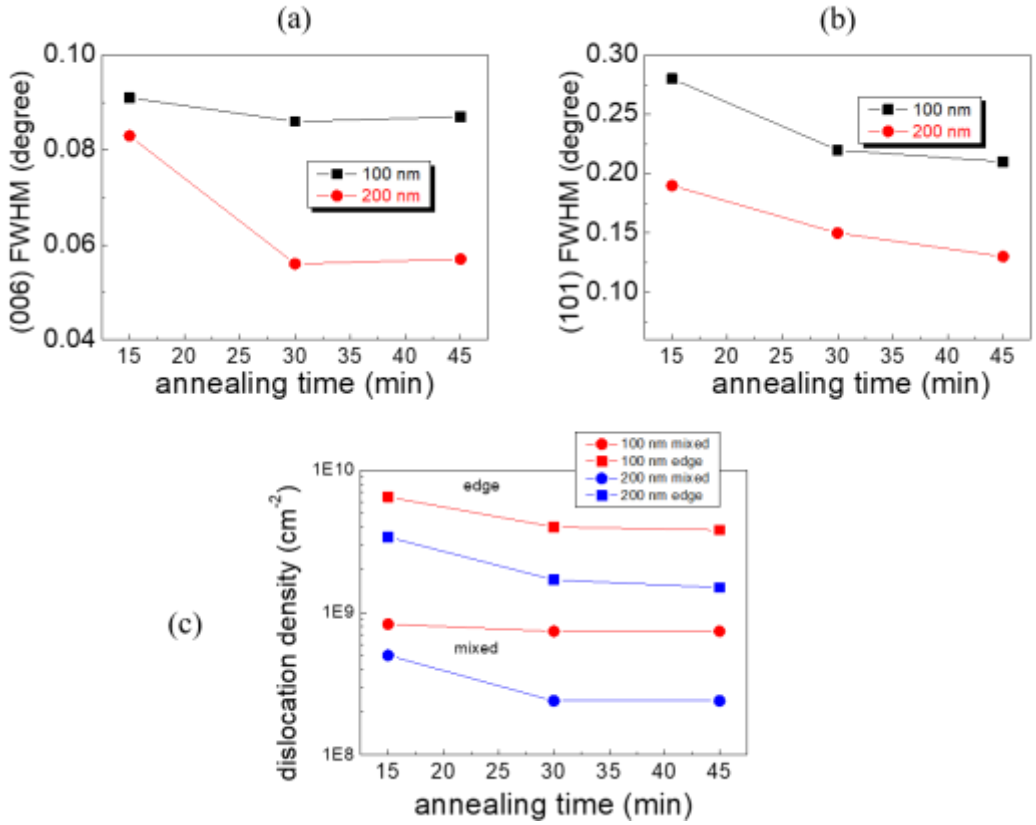

Figure 7. (a) Variation of the XRD-RC FWHM values of the (0 0 0 6) symmetric plane as a function of the annealing time for the 100 nm and the 200 nm thick AlN PVD templates. (b) Variation of the XRD-RC FWHM values of the (1 0 −1 1) asymmetric plane as a function of the annealing time for the 100 nm and the 200 nm thick AlN PVD templates. (c) Edge and mixed dislocation densities of the 100 nm and the 200 nm AlN thick PVD templates estimated from the tilt and twist values as a function of the annealing time.

For the 100 nm thick template, the 15 minutes annealing time under N_2 resulted in a FWHM value for the symmetric (0 0 0 6) plane to be 0.091° (328 arcsec) and it decreased to 0.086° (310 arcsec) after 15 more minutes (total 30 minutes). After an additional 15 minutes, which made the total annealing time of 45 minutes, the FWHM value remained fairly stable at 0.087° (315 arcsec). On the other hand, the asymmetric (1 0 −1 1) plane FWHM values were found to be 0.28° (1006 arcsec) after a 15 minutes annealing time and it decreased to 0.22° (790 arcsec) after 15 additional minutes. It continued to slowly decrease to reach 0.21° (772 arcsec) after a total of 45 minutes. The estimated value of the edge dislocation density was 6.52 x 10^9 cm^{-2} for 15 minutes annealing and decreased to 4 x 10^9 cm^{-2} after 30 minutes where it slightly decreased

to 3.75 x 10^9 cm^{-2} after a total of 45 minutes, as shown in figure 7(c). In addition, the estimated value of the mixed dislocation density was 8.3 x 10^8 cm^{-2} for 15 minutes annealing, decreased to 7.3 x 10^8 cm^{-2} after 30 minutes, and stayed at the same value of 7.3 x 10^8 cm^{-2} after a total of 45 minutes (figure 7(c)).

Regarding the 200 nm thick template, the 15 minutes annealing time under N_2 resulted in a FWHM value for the symmetric (0 0 0 6) plane to be 0.083° (299 arcsec) and it decreased to 0.056° (204 arcsec) after 15 more minutes (total 30 minutes). After an additional 15 minutes, which made the total annealing time 45 minutes, the FWHM value remained fairly stable at 0.057° (206 arcsec). On the other hand, the asymmetric (1 0 −1 1) plane FWHM values were found to be 0.19° (684 arcsec) after a 15 minutes annealing time and it decreased to 0.15° (542 arcsec) after 15 additional minutes. It continued to decrease to reach 0.13° (487 arcsec) after a total of 45 minutes. The estimated value of the edge dislocation density was 3.41 x 10^9 cm^{-2} for 15 minutes annealing and decreased to 1.7 x 10^9 cm^{-2} after 30 minutes where it slightly decreased to 1.5 x 10^9 cm^{-2} after a total of 45 minutes. In addition, the estimated value of the mixed dislocation density was 4.9 x 10^8 cm^{-2} for 15 minutes annealing, decreased to 2.4 x 10^8 cm^{-2} after 30 minutes, and stayed at the same value of 2.4 x 10^8 cm^{-2} after a total of 45 minutes.

The results obtained for both templates under 6 slm N_2 at 1650°C led to the adoption of an annealing time of 30 minutes. It is under this annealing duration that the best results were obtained in terms of the FWHM values for the symmetric and asymmetric planes and for the edge and mixed dislocation density values while maintaining an efficient annealing thermal budget. The annealing recipe includes an N_2 annealing at 1650°C for 30 minutes for crystalline quality improvement. Despite the improved results in terms of crystalline quality obtained by annealing under N_2, the surface morphology of both templates did not improve much or neither at all for both templates, as shown in figure 8.

As a result, and in order to not further increase the recipe's thermal budget that is limited by the CVD reactor operating specifications, we decided to modify the recipe by including an additional annealing step under a 50% (3 slm) hydrogen (H_2) + 50% (3 slm) nitrogen (N_2) flow. This process aimed at improving the surface morphology of AlN templates and was in use at CRHEA since it enabled to obtain smooth surfaces on AlN templates by annealing under 50% (3 slm) hydrogen (H_2) + 50% (3 slm) nitrogen (N_2) flow [11].

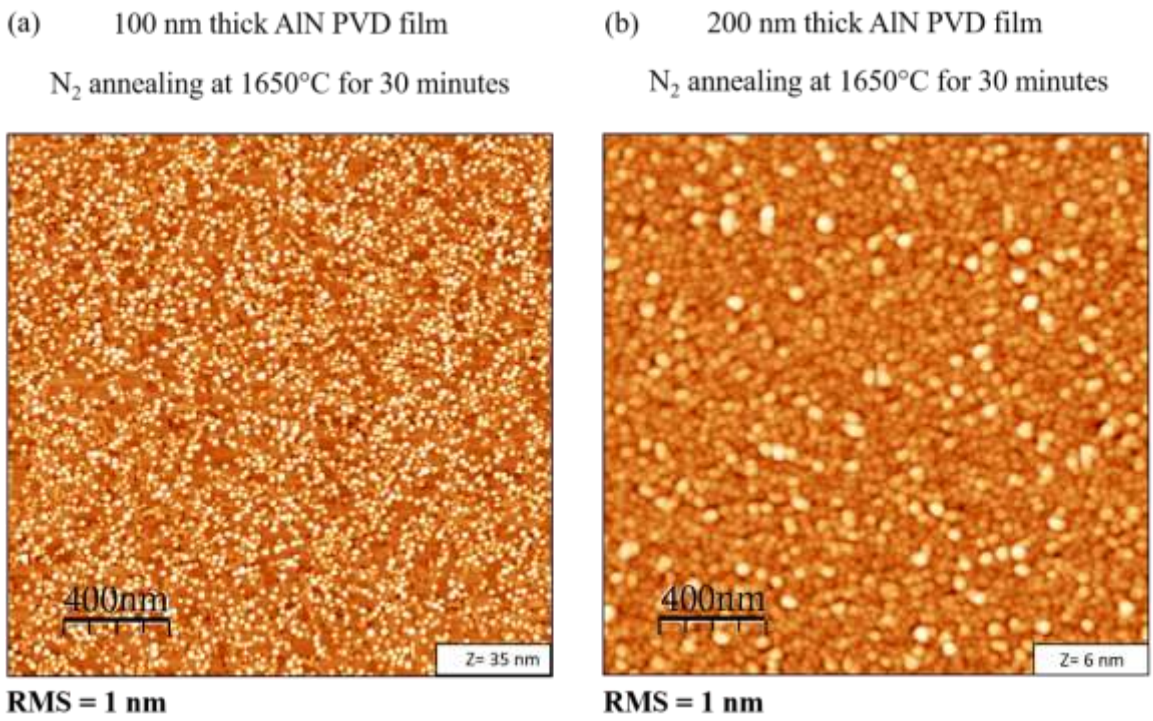

Figure 8. Atomic force microscopy images of (2 x 2) μm^2 of: (a) a 100 nm thick AlN PVD film, and (b) a 200 nm thick AlN PVD film, both annealed under N_2 at 1650°C for 30 minutes. The term Z represents the vertical scale and the variation in height in the AFM images, and its value is reported at the bottom right hand side of the image.

II.1.3. Surface morphology characterization by AFM

After a two-step annealing of 15 minutes (i.e. a total duration of 30 minutes) each at 1650°C under a constant nitrogen (N_2) laminar flow, the annealed 100 nm and 200 nm AlN samples' surfaces underwent a surface characterization by AFM in order to investigate the morphology, as shown in figure 9 (a). We observed that the surface morphology did not change and that the surface RMS roughness stayed equal to 1 nm for both templates. The annealing time duration (30 minutes combined) was not enough to initiate the surface improvement. Therefore, we further annealed it with H_2 since it plays an essential role in the surface transition from a rough to a smooth surface morphology [12]. After an annealing under 50% H_2 + 50% N_2 at 1550°C for 10 minutes, the surface started to get smoother in the case of the annealed 100 nm thick AlN film with a surface roughness RMS = 0.4 nm (figure 9 (b)). The grain average height decreased from 3.5 nm to 2 nm ($\pm$ 1 nm) and the grain average diameter increased to 80 nm ($\pm$ 20 nm). The increase in the grain diameter is due to the surface morphology transition from a grain-dominated surface to a surface morphology where the 3D-like structures are starting to coalesce to progressively form a 2D smooth surface. The coalescence between the grains can explain the increase in the diameter and the decrease in the grain height. On the other

hand, for the 200 nm thick annealed AlN film, the surface roughness increased with a surface roughness RMS = 3.2 nm (figure 9 (b)). In this case, the grains average height increased from 3 nm to 10 nm (± 4 nm) and the grains average diameter increased from 30 nm to 100 nm (± 25 nm). After a second annealing step under 50% H_2 + 50% N_2 at 1550°C for 10 minutes, a significant modification of the surface morphology was found and a reduction of the surface roughness occurred on both the 100 nm and the 200 nm thick annealed templates. For the 100 nm AlN thick template, the surface greatly improved and its morphology changed from a grain-dominated surface to a 2D (i.e. made of smooth terraces and steps) morphology, involving a complete disappearance of the grains (figure 9 (c)) and a surface roughness RMS = 0.3 nm. In comparison, the 200 nm AlN thick template underwent a similar morphological transition to a smooth surface (figure 9 (c)), with a surface roughness RMS = 0.4 nm. Furthermore, by adding the third annealing step under 50% H_2 + 50% N_2 at 1550°C for 10 minutes, we observed a further reduction of the surface roughness and improvement of the surface morphology. More precisely, the morphology of the 100 nm AlN thick template improved to a morphology made of wide terraces (with an average width of 250 nm ± 50 nm separated by atomic steps (figure 9 (d)). The surface roughness RMS was reduced to 0.2 nm. Similarly, the morphology of the 200 nm AlN thick template also showed a morphology made of wide terraces (with an average width of 550 nm ± 110 nm) separated by atomic steps (figure 9 (d)). The surface roughness RMS was also found to be equal to 0.2 nm.

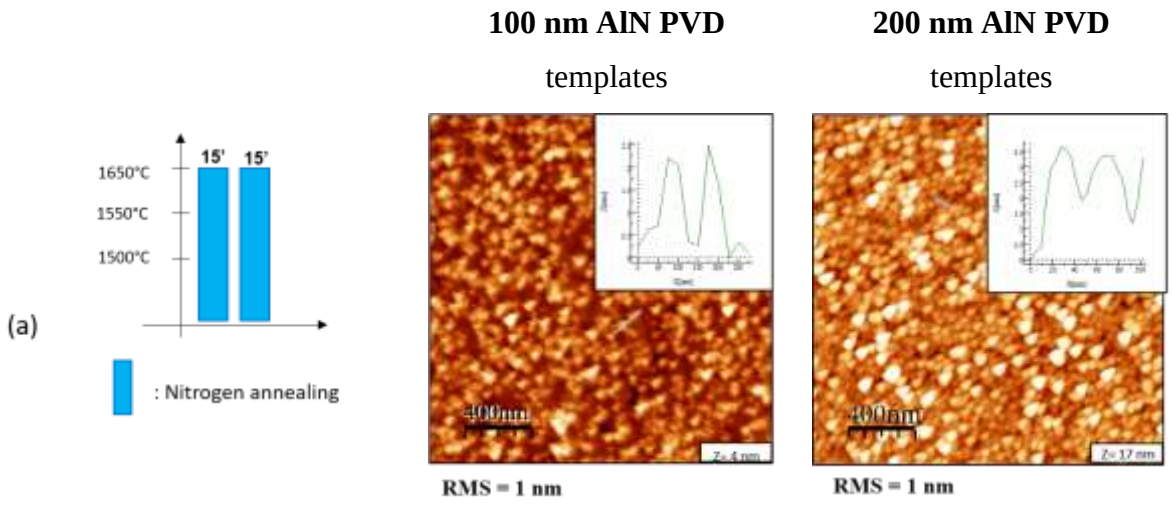

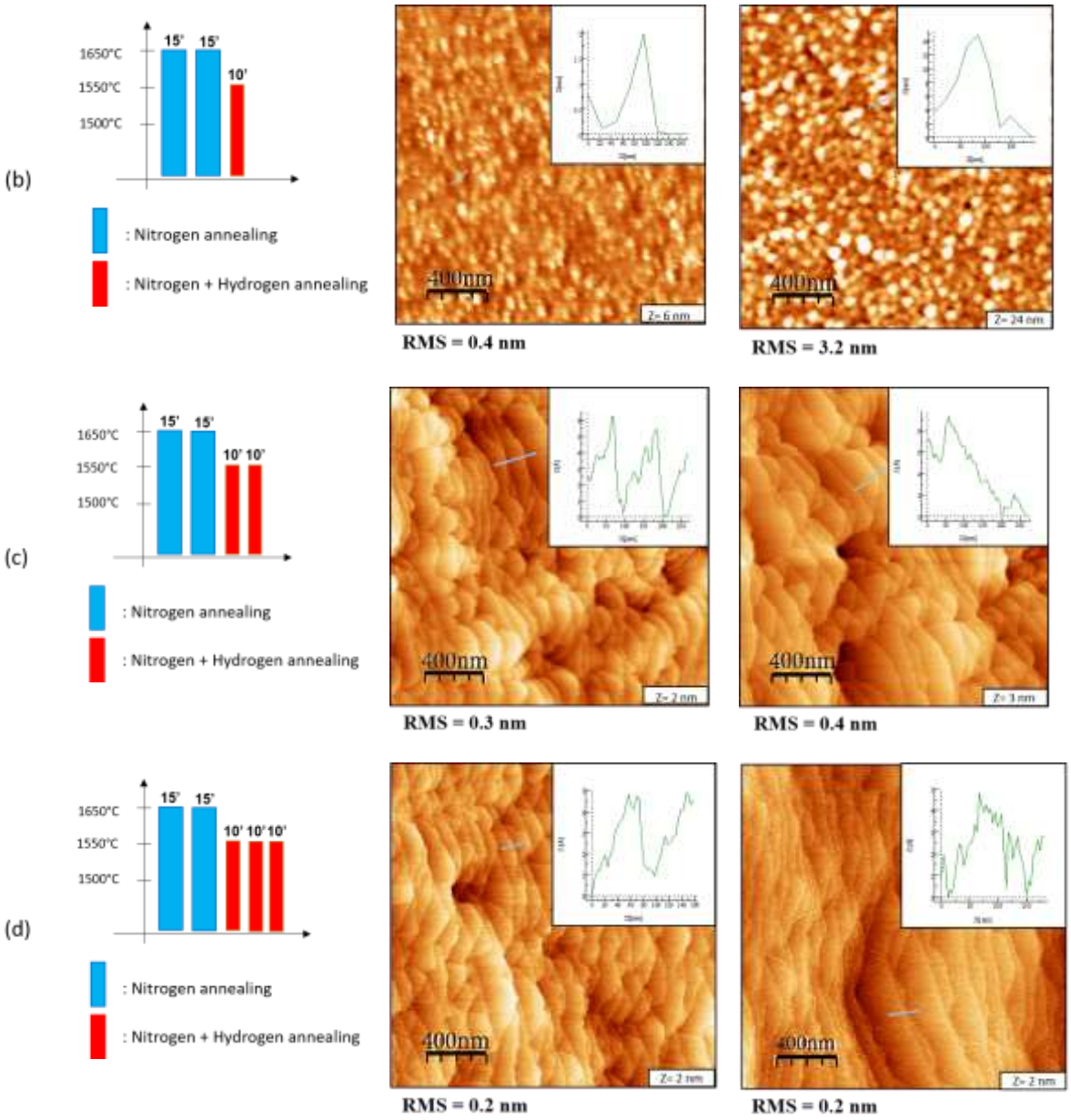

Figure 9. Atomic force microscopy images of (2 x 2) µm^2 of 100 nm and 200 nm AlN thick PVD templates. The AlN surface morphology is presented for: (a) a first annealing under N_2 for a total duration of 30 min, (b) a second annealing under 50% H_2 + 50% N_2 for 10 min, (c) a third annealing under 50% H_2 + 50% N_2 for 10 min, and (d) a fourth annealing under 50% H_2 + 50% N_2 for 10 min. The insets show profile measurements of specific marked zones indicated by a blue line in the (2 x 2) µm^2 scan images.

The effect of H_2 on the surface morphology has clearly been observed. It leads to a smoothening of the AlN surface morphology, which involved a clearing of the 3D-like structures on the surface. The 50% H_2 + 50% N_2 annealing after an N_2 annealing has proved to be a complementary annealing where the surface morphology can be strongly improved. It avoids the use of very long annealing times, typically of several hours [13], required with the use of N_2 only, thereby significantly reducing the thermal budget of the annealing recipes.

II.1.4. Crystalline structure characterization by XRD

We studied the evolution of the crystalline quality after the different annealing steps by performing XRD-RC measurements on the symmetric (0 0 0 6) and asymmetric (1 0 −1 1) planes. Both templates underwent a significant amelioration of their crystalline quality in the form of a decrease in their FWHM values. For the 100 nm AlN thick template, the (0 0 0 6) symmetric plane decreased from an initial value of 0.23° (829 arcsec) (i.e. before the annealings) to 0.09° (329 arcsec) after the complete annealing procedure. Regarding the (1 0 −1 1) asymmetric plane, the FWHM value decreased from an initial value (i.e. before the annealings) of 1.30° (4684 arcsec) to 0.22° (792 arcsec) after the complete annealing procedure. The 200 nm AlN thick template also improved and its FWHM value for the symmetric (0 0 0 6) plane decreased from an initial value of 0.22° (792 arcsec) (i.e. before the annealings), to 0.06° (216 arcsec) after the complete annealing procedure. The (1 0 −1 1) asymmetric plane FWHM value decreased from an initial value of 0.89° (3204 arcsec) to 0.14° (504 arcsec) after the complete annealing procedure. The values obtained indicate a strong improvement of the crystalline quality for both templates combined with a smooth surface morphology thus showing the success of the annealing recipe adopted and the impact of the proposed high temperature annealing process.

II.1.5. TEM characterization before the annealing

Philippe Vennégues from CRHEA (CNRS) did the sample preparation and most of the observations. In addition, D. Cooper from CEA LETI performed the STEM HR imaging. Cross-sectional TEM characterizations on the 100 nm thick AlN PVD template were performed in order to study its initial structure before performing any annealing. Figure 10 (a) shows the images taken from the sample along the <1 0 −1 0> and the <1 1 −2 0> zone axes. The surface morphology confirms the AlN grain-dominated morphology observed by AFM: the observed surface is a corrugated surface showing the grains in a wave-like form. In addition, we investigated the lattice defects, in particular their type and spatial arrangement. It has been confirmed that the type of dislocations that dominate the structure are majorly type a (edge) dislocations, which are out-of-contrast in the <0 0 0 2> dark field but in contrast in the <1 1 −2 0> dark field, as shown in figure 10 (b).

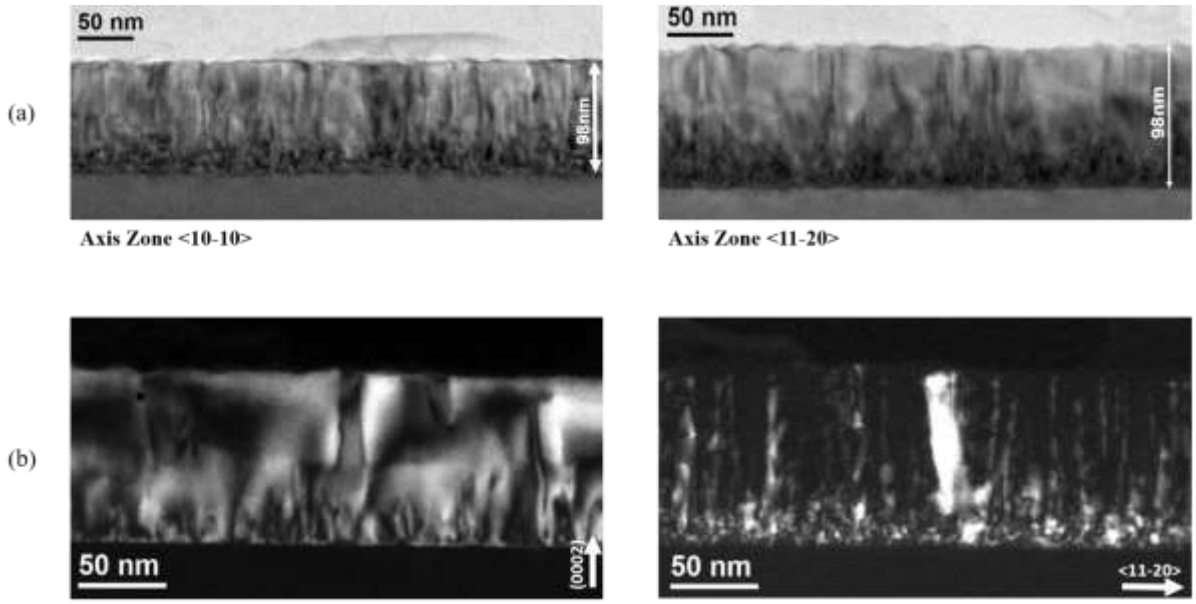

Figure 10. Multibeam cross-sectional TEM images of the 100 nm AlN thick PVD template taken (a) along the <1 0 −1 0> (left) and <1 1 −2 0> (right) AlN zone axes. (b) The type a (edge) dislocations are out-of-contrast in the <0 0 0 2> dark field and in contrast in the <1 1 −2 0> dark field.

We proceeded to perform high-angle annular dark-field scanning transmission electron microscopy (HAADF-STEM) along the <1 1 −2 0> zone axis in order to determine the polarity of the layers. Figure 11 shows the image acquired where the Al atoms (high light intensity) can be distinguished from the N atoms (low light intensity), thus indicating an Al polarity of the layers.

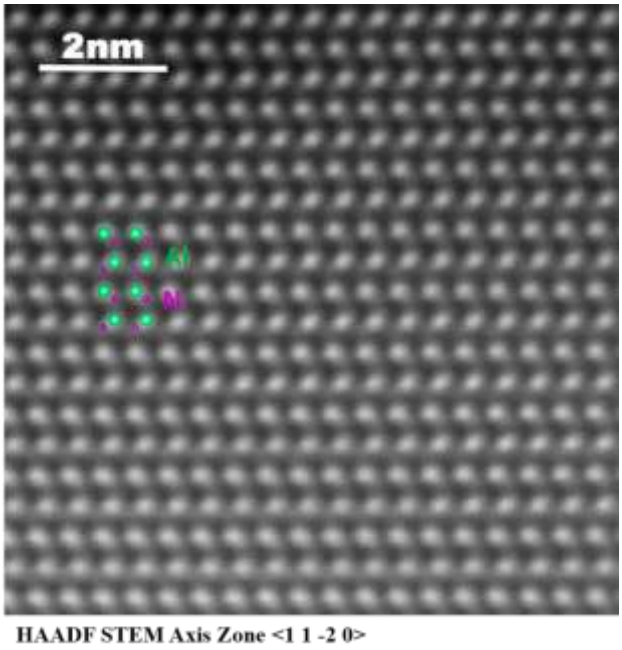

Figure 11. HAADF-STEM along the <1 1 −2 0> zone axis where the AlN layer has an Al polarity.

Furthermore, a plane view TEM mapping has been done where dislocations and some closed domains, probably resulting from prismatic stacking faults (PSF), have been observed, as shown in figure 12. The measurements of closed domains have been done on seven different zones where the closed domains have been estimated to represent 8% of the total surface of the layer and the dislocation density to be around 1.8 x 10^{11} cm^{-2} in close accordance with the XRD estimated values previously estimated of 1.2 x 10^{11} cm^{-2}.

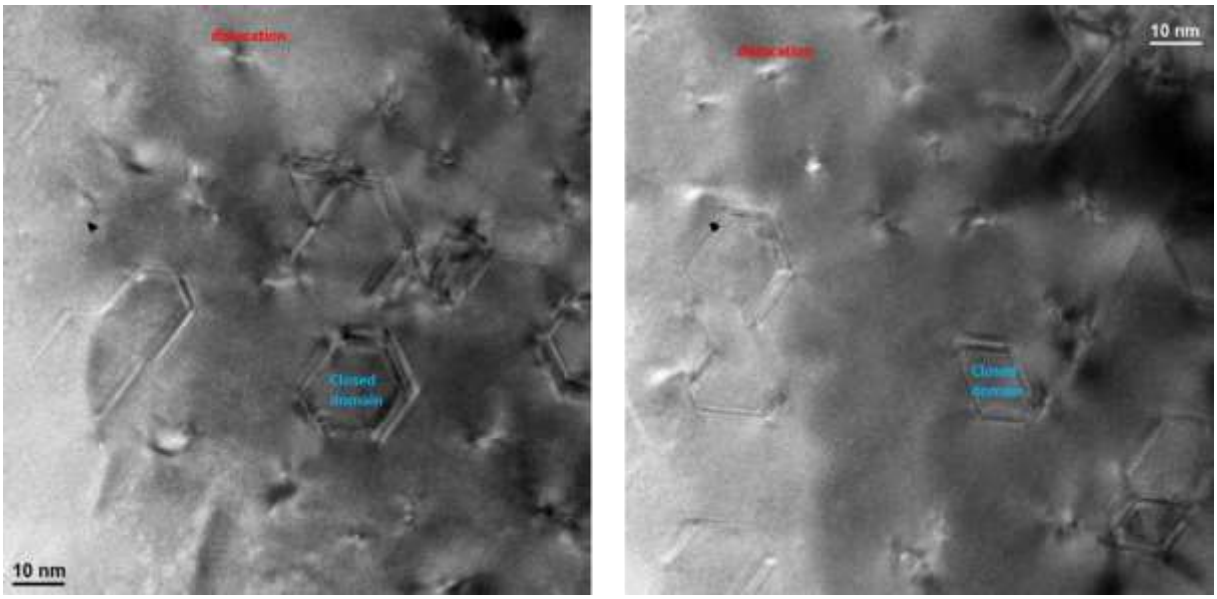

Figure 12. Plan view TEM images showing dislocations and closed domains.

A cross-section TEM image along the axis zone <1 0 −1 0> shows almost vertical planar defects (figure 13 (a)) marked by blue arrows, which stop in the AlN layer at a position marked by a red arrow (figure 13 (a)). In high resolution (HR) (figure 13 (b)), we do not see any vertical or horizontal displacement at the level of these defects. It is coherent with the prismatic stacking faults (PSF) of vector displacement ½ <1 0 −1 1> in the defect plane. Furthermore, in a dark field <1 0 −1 0> close to the zone axis <1 1 −2 0>, we see the vertical defects prismatic stacking faults marked by blue arrows (figure 13 (c)), which are created from horizontal defects basal stacking faults (BSF) marked by red arrows (figure 13 (c)). This set of defects can form closed domains.

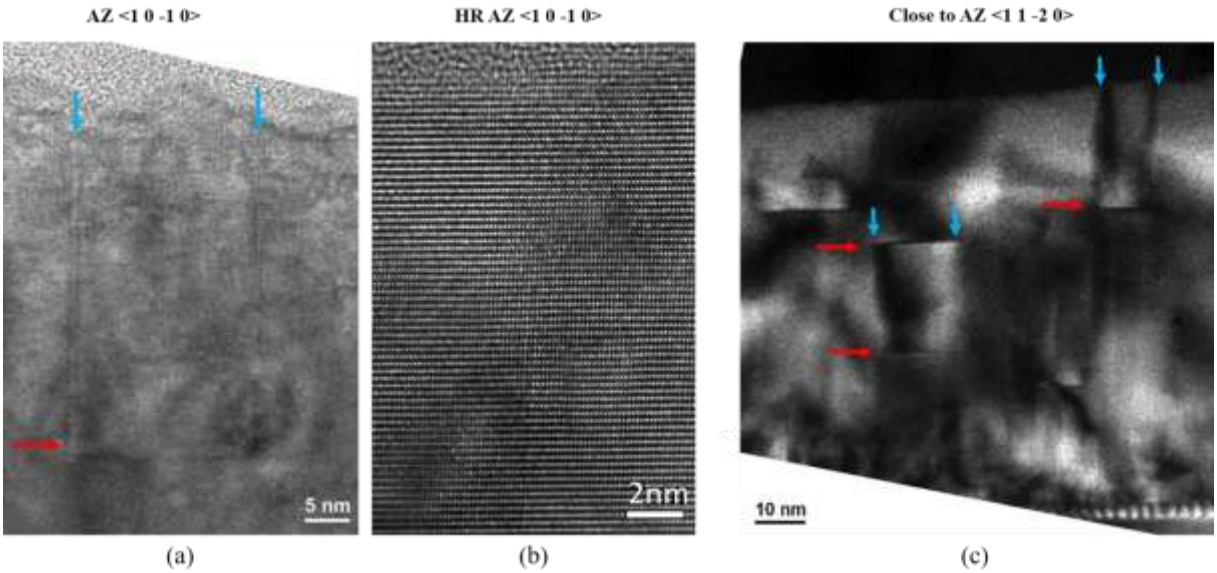

Figure 13. Cross-sectional TEM images of AlN PVD (100 nm thick) template along the <1 0 −1 0> and <1 1 −2 0> AlN zone axes. (a) Low-resolution image of vertical planar defects (blue arrows) which terminate on a basal stacking fault in AlN (red arrow). (b) High-resolution image where no vertical or horizontal displacement at the level of these defects could be observed. (c) Dark field <1 0 −1 0> image taken close to the axis zone <1 1 −2 0> where the vertical defects PSF can be seen marked by blue arrows. They are created from horizontal defects BSF marked by red arrows.

II.1.6. TEM characterization after the annealing

After the template underwent face-to-face annealings at 1650°C under N_2 for a total duration of thirty minutes, we performed a TEM study in order to investigate the annealing's effect and its impact on both the surface morphology and the crystalline structure of the AlN layer. In figure 14 (a), a cross-sectional image is taken of the sample along the <1 0 −1 0> zone axis. Contrary to the initial (non-annealed) AlN layer, the surface morphology observed is not a corrugated surface anymore. It indicates that the AlN morphology has started to transform from a wave-like form observed before the annealing to a flatter one. In addition, in figures 14 (b) and (c), the type a (edge) dislocations that cannot be seen along the <0 0 0 2> zone axis but are in contrast along the <1 1 −2 0> zone axis, have significantly decreased compared to the images taken before the annealing. Once again, these results confirm the improved FHWM value obtained by XRD and presented above. This indicates that the high temperature annealings under N_2 have improved the crystalline quality, which is mainly characterized in terms of reducing the dominant type a (edge) dislocation density. On the other hand, it had a limited effect on transforming the wave-like morphology of the layers into a flatter one, as observed with the AFM measurements performed and discussed above, showing that the AlN grain-like morphology still dominates after these annealings despite the decrease in the grains average sizes (figure 9 (a)).

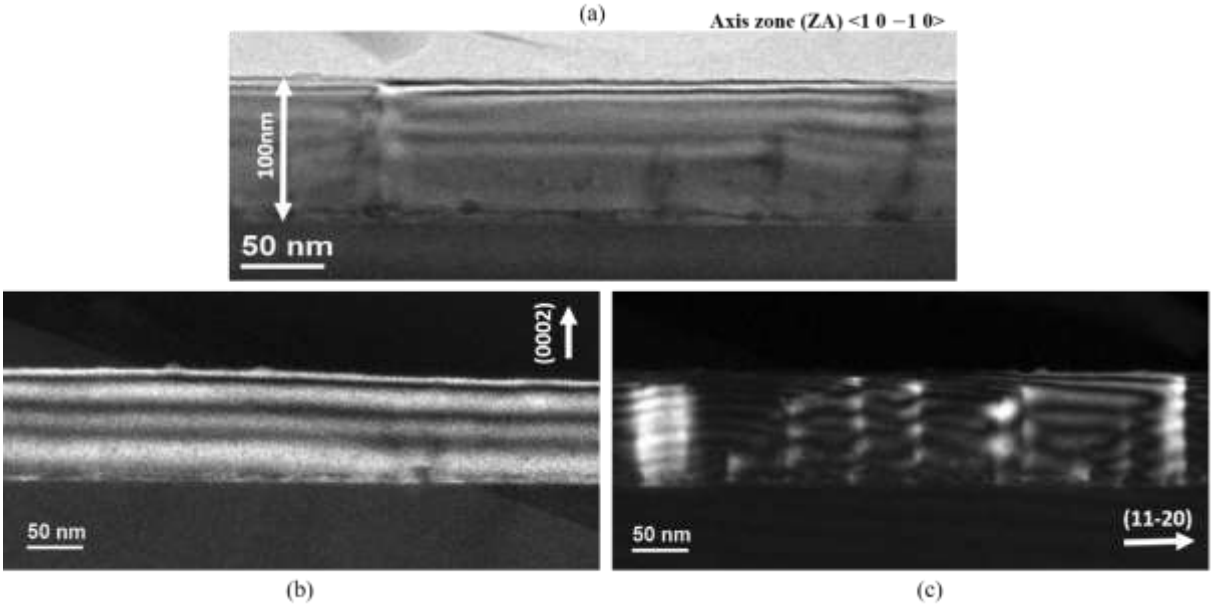

Figure 14. Cross-sectional TEM images of annealed AlN PVD (100 nm thick) template: (a) Multibeam image, (b) <0 0 0 2> dark field and (c) <1 1 −2 0> dark field.

Furthermore, two specific layer structures have also been observed, one close to the AlN/sapphire interface and one on the top of it, separated by a polarity inversion domain boundary, as shown in figure 15 (a). In addition, truncated pyramid-like cavities have also been observed in the AlN zone. The black horizontal line contrast observed near the interface was a polarity inversion domain boundary (IDB) from N-polar to Al-polar along the growth direction. Figure 15 (b) is a HR image of the IDB confirming the Al-polar domain on top of the domain boundary and the N-polar one below. Many research groups reported the observation of hexagonal voids and polarity inversion from N-polar to Al-polar on their annealed templates [3], [14]–[17]. They proposed that the truncated pyramid-like cavities (or hexagonal voids) are a result of the condensation of point defects [17]. Furthermore, the diffusion of oxygen atoms from the sapphire zone during the annealing and its concentration at the polarity inversion boundary has led to the formation of aluminum oxynitride ($Al_xO_yN_z$), which causes the polarity inversion from N-polar to Al-polar [14], [15], [17], [18].

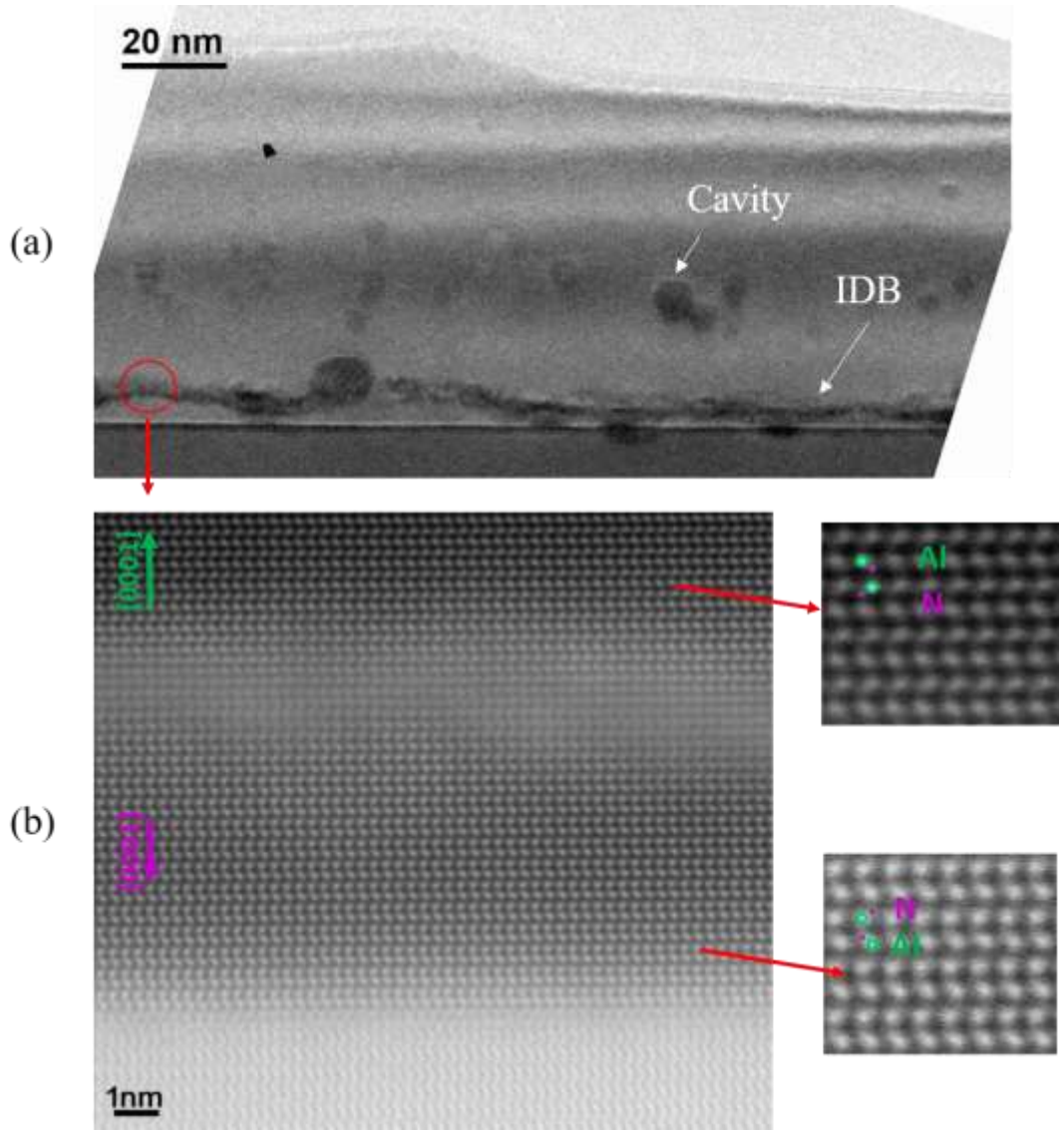

Figure 15. (a) HR-STEM cross-section image of the annealed template. (b) A magnified HR image of a specific zone from the polarity inversion domain boundary. The two magnified zones observed on the right show the polarity inversion.

After the samples were undergoing successive face-to-face annealings under $H_2 + N_2$ at 1550°C with a total duration of twenty minutes, TEM characterization were further performed. We observed some defects close to the surface, as shown in figure 16 (a). These defects have a contrast with fringes (figure 16 (b)), characteristic of planar defects. We also observed nano-domains, some having a triangular shape (figure 16 (b)): the ones in the Al-polar zone are facing downwards, as indicated by a red arrow, and the ones in the N-polar zone are facing upwards, as also indicated by a red arrow. The planar defects were IDB with an Al-polarity on the top and an N-polarity underneath. Furthermore, they have moved through the layers to reach around 70 nm from the surface, as shown in figures 16 (a). This diffusion created a polarity alternation on the surface where some areas became N-polar and other areas remained Al-polar. This has

been confirmed by HR images (figure 16 (c)) from a marked zone of the IDB where both the Al-polarity and the N-polarity were confirmed. This IDB movement is probably due to the continuation of the oxygen diffusion during the successive annealings performed under N_2 + H_2 (i.e. it consisted in a total of three annealings with duration of 5 minutes, 5 minutes, and 10 minutes per annealing, respectively. That oxygen diffusion led to the IDB movement through the AlN, thus reaching the surface. In addition, the IDB movement from the interface with the sapphire substrate through the AlN layer has been accelerated by the presence of H_2 during the successive annealings, as compared to the previous annealings performed under N_2 only.

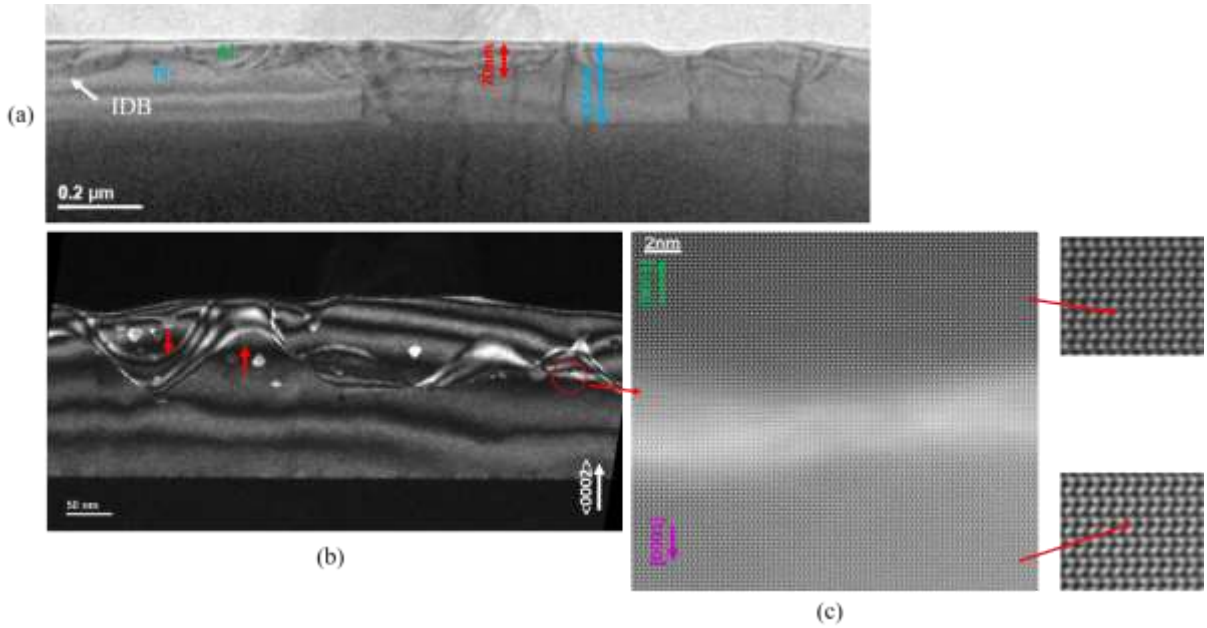

Figure 16. (a) Low resolution cross-section image of the 200 nm thick AlN template after successive N_2 + H_2 annealings. (b) <0 0 0 2> dark field image of planar defects where on top of it is the Al-polar zone, and beneath it the N-polar zone. Nano-domains with a triangular shape can also be observed. (c) A magnified HR image of a specific zone from (b) of the polarity inversion domain boundary. The two magnified zones observed on the right show the polarity inversion.

Plan view TEM images showed a low density of type a (edge) dislocations and a high density of nano-defects, a form of 3D defects with facets along the <1 0 −1 1> and <0 0 0 1> zone axes. It was complicated to estimate the density of dislocations at low magnification since it was hard to differentiate them from the nano-defects, as shown in figure 17 (a). In figure 17 (b), we see a magnification of a part of figure 17 (a) where the nano-defects are marked by a red arrow and the dislocations are marked by blue arrows. The estimation was around 3 x 10^9 cm^{-2}, a significant decrease from the initial values measured on the AlN layer, i.e. before the whole annealings process, that were in the 10^{11} cm^{-2}.

II.1.7. Conclusion

In summary, a TEM study on AlN PVD templates before annealing showed a structure made of a high density of type a (edge) dislocations along with prismatic stacking faults (PSF) and basal stacking faults (BSF), resulting in the formation of closed domains. The first annealing procedure at 1650°C under N_2 improved the crystalline structure by reducing the density of dislocations and eliminating stacking faults. However, it was witnessed the formation of polarity inversion domain boundaries at the interface of sapphire and AlN due to oxygen diffusion from the sapphire substrate. This IDB had Al-polar zone above it and N-polar zone beneath it. In addition, hexagonal cavities appeared that were located on and above the IDB in the AlN layer. After the successive annealings under $N_2 + H_2$ at 1550°C, the structure witnessed a further reduction in the edge dislocation densities but also witnessed the movement of the IDB in the AlN layer: at this stage, the IDB arrived close to the surface (around 70 nm below) which may be linked to the continuous diffusion of oxygen throughout the annealing. Al-polar and N-polar zones were also found to be present on the surface with hexagonal cavities pointing downwards in the Al-polar zones and upwards in the N-polar zones. These 3D nano-defects have facets along the <1 0 −1 1> and <0 0 0 1> zone axes. A schematic summary is represented in figure 18.

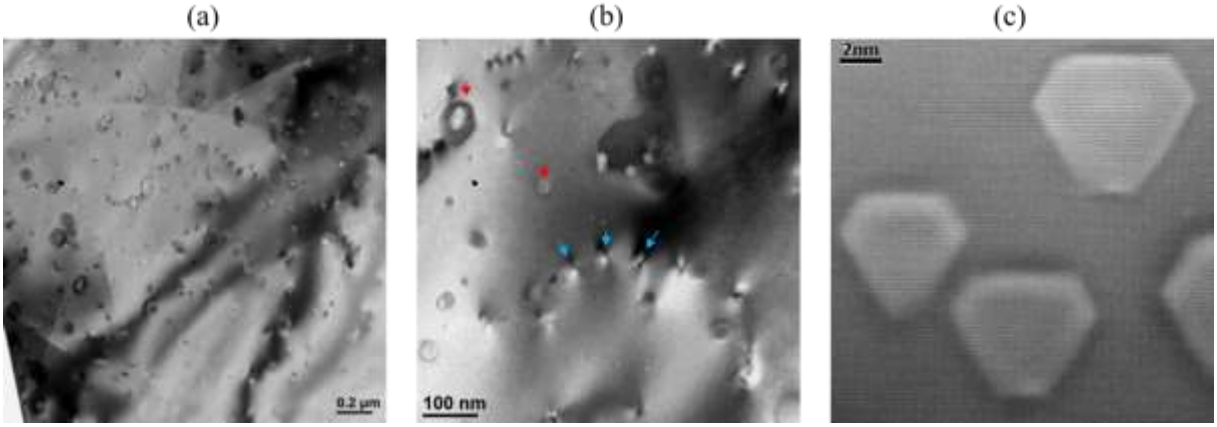

Figure 17. (a) Plan view image showing nano-defects and dislocations. (b) A magnified image of a part of (a) showing a better view of the nano-defects (marked by a red arrow) and edge dislocations (marked by blue arrows). (c) Cross section HR image of the nano-defects showing <1 0 −1 1> and <0 0 0 1> facets.

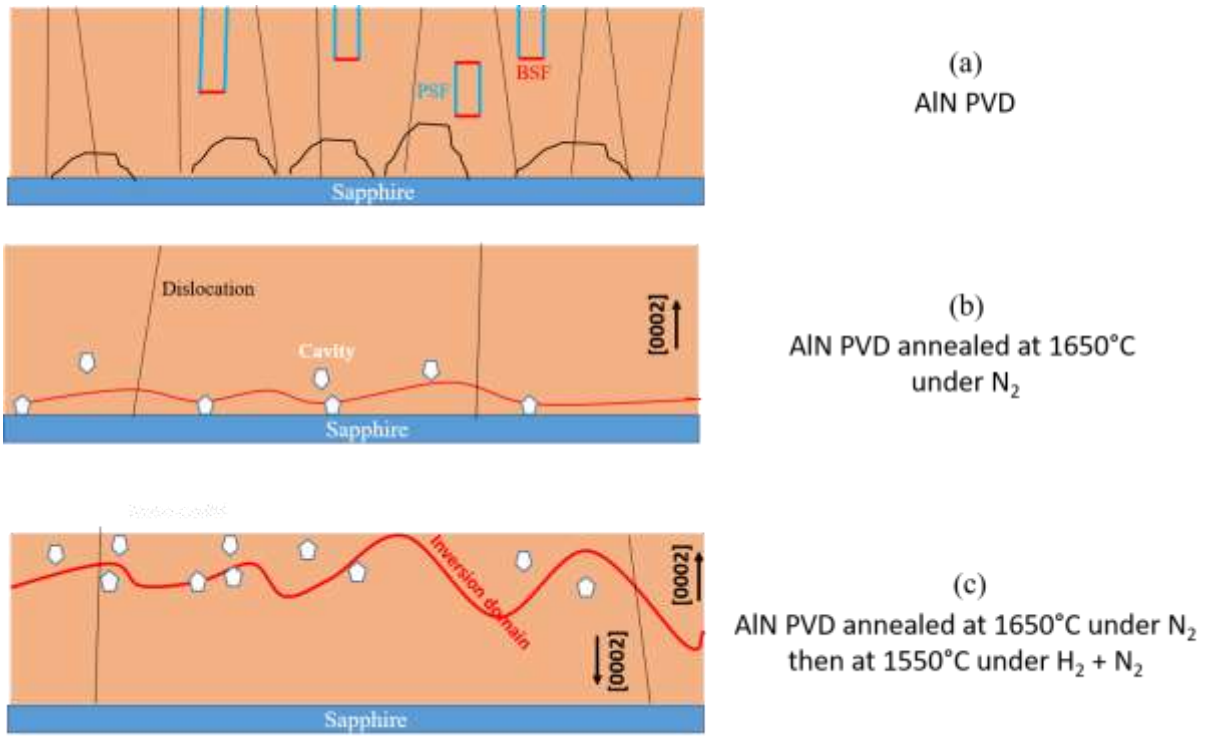

Figure 18. Schematic representation of the 100 nm thick AlN PVD template: (a) before any annealing, (b) after the annealing process at 1650°C under N_2, and (c) after the annealing process at 1550°C under $H_2 + N_2$.

II.2. Post-growth annealing of MBE-grown AlN on h-BN / sapphire templates

In this study, which involves a collaboration with the group of Prof. Abdallah Ougazzaden from Georgia Tech-Europe in Metz, AlN epilayers were grown by ammonia-assisted molecular beam epitaxy on 3 nm h-BN grown on c-sapphire substrates. Their structural properties were investigated by comparing as-grown and post-growth annealed layers. The role of the high temperature annealings on the crystalline quality and surface morphology was studied as a function of the AlN thickness and the annealing duration and temperature.

II.2.1. Introduction

As pointed out at the beginning of this chapter, the growth of AlN on sapphire has important advantages like the low cost of the sapphire wafer, its transparency in the UV range and its large size availability (up to 8-inch). Nevertheless, it also presents some drawbacks mainly in the form of a high lattice mismatch along with a lattice thermal coefficient mismatch. Their influence on the AlN epitaxial growth is typically a decrease of the crystalline structural quality and an increase of the TDDs that act as non-radiative recombination centers, thereby limiting the efficiency of AlN-based LEDs.

Post-growth annealing is one of the solutions as has been already described and studied in the section above, but there is another solution that has attracted wide interest to circumvent the lattice mismatch issue: it is the use of two-dimensional (2D) materials [19]. Their extended crystalline planar structures, which are held together by strong in-plane covalent bonds and weak out-of-plane van der Waals forces, make it possible for their individual layers to be easily removed by breaking the van der Waals bonds with little damage either to the extracted layer or to the remaining structure [20]. Therefore, van der Waals epitaxy enables these special features of 2D materials to be exploited to significantly reduce the lattice matching problem faced in the conventional growing methods of heterostructures [19]. Although many 2D materials could be potentially used, hexagonal boron nitride (h-BN) seems to be among the best suited due to its chemical compatibility with AlN- or AlGaN- based epitaxial layers. In addition, h-BN templates can serve as mechanical release layers for III-nitride devices, such as LEDs [21], [22], to be transferred to adequate substrates, therefore creating flexible devices [21]. However, the growth of high-quality III-nitride films is not straightforward as the lack of dangling bonds at the surface complicates the nucleation step as in the case of gallium nitride (GaN) growth on h-BN, which can result in the formation of randomly oriented, polycrystalline,

and isolated islands [21]. Meanwhile, due to the lower mobility and higher sticking coefficient of Al adatoms, AlN could serve as a better nucleation layer on h-BN.

Limited studies exist regarding the improvement of AlN quality on h-BN, and most of these studies used MOVPE. Dipankar Chugh et al. improved the morphology and crystal quality of AlN grown on h-BN by MOVPE by adopting a modified multilayer process involving pulsed ammonia flow for depositing smooth AlN layers on h-BN/sapphire templates [23]. Qingqing Wu et al. reported the growth of monolayer h-BN by low-pressure chemical vapor deposition (CVD) on copper (Cu) foil substrate and then transferred it on a sapphire substrate for the growth of AlN and DUV LEDs [24]. The same group also reported crack-free crystalline AlN and DUV LEDs with an emission at 281 nm on MOVPE- grown multilayer h-BN, thus showing the advantage of multilayer MOVPE-grown h-BN to obtain good-quality epilayers and devices on large surfaces [22]. On the other hand, the growth of AlN on h-BN by MBE has not yet been reported and will be investigated in this study. The fabrication of AlN layers by MBE on h-BN/sapphire was carried out and we also studied the effects of post-growth face-to-face annealing (FFA) on the surface morphology and crystalline quality of the AlN epitaxial layers.

- ## Samples structure and methods

The growth of 3 nm thick h-BN was performed in Georgia Tech-Europe, Metz, in an Aixtron MOVPE close-coupled showerhead (CCS) reactor (AIXTRON Company, Cambridge, UK). It was done on (0001) sapphire substrates at 1280°C and 90 mbar pressure. Triethylboron (TEB) and ammonia (NH_3) were used as B and N precursors, respectively. Detailed growth conditions of h-BN are reported elsewhere [25]. The AlN template layers were then grown on h-BN by ammonia-assisted MBE using conventional Al effusion cell, NH_3 as a nitrogen precursor, and a graphite furnace designed for high temperatures in a RIBER 32P reactor (RIBER S.A, Bezons, France). The procedure used for the growth of AlN samples is as follows. An AlN buffer layer of 5 nm was first grown at 950°C with an ammonia flow rate of 50 sccm. Next, AlN growth was performed at 1050°C with an ammonia flow rate of 50 sccm and at a growth rate of 100 nm/h. We considered two templates with different AlN layer thicknesses: sample A (50 nm) and sample B (100 nm), as depicted in figure 19.

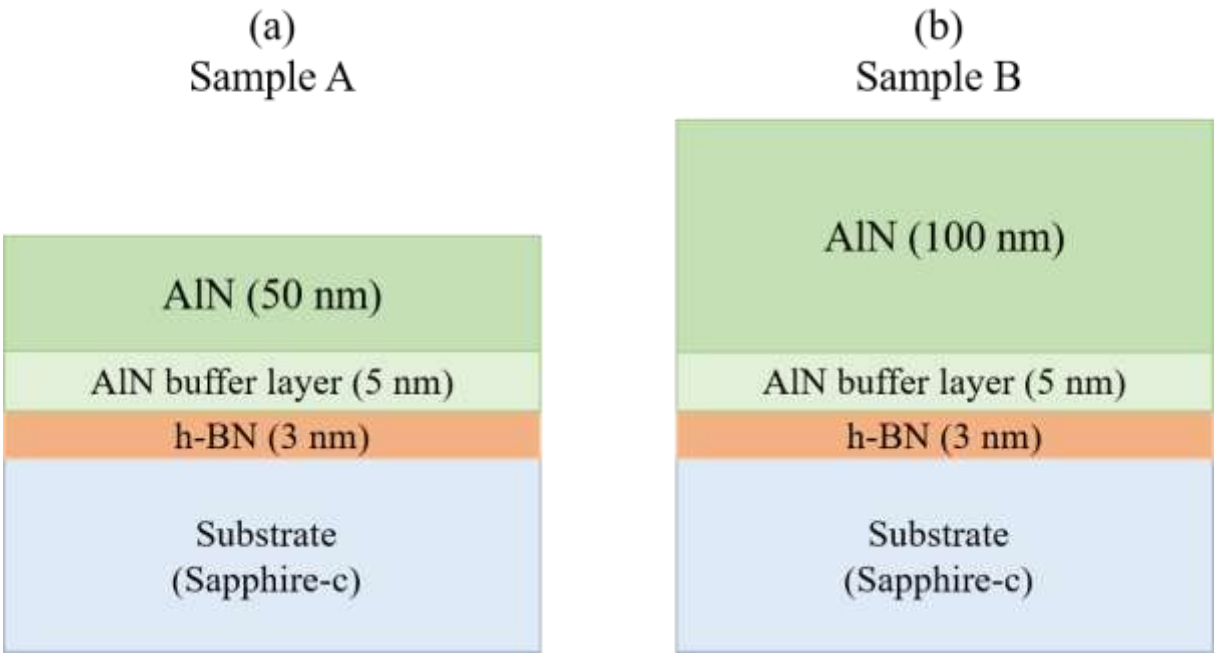

Figure 19. Schematics of the two AlN structures grown on h-BN / sapphire templates. (a) 50 nm AlN structure grown on 3 nm h-BN on sapphire (sample A). (b) 100 nm AlN structure grown on 3 nm h-BN on sapphire (sample B).

For the annealing process, the surface of sample B was covered with the surface of sample A in a face-to-face (FTF) configuration to suppress the thermal decomposition of the AlN films during annealing. They were placed in the same CVD reactor described in section I.2.c. The annealing steps were conducted at temperatures ranging from 1450°C to 1650°C under a constant N_2 laminar flow of 6 slm (standard liters per minute) and a total pressure of 800 mbars. After the temperature rise and its stabilization, the samples were left under N_2 carrier gas for a duration of 15 min for each annealing. An annealing procedure involving a total of four annealing steps was investigated. When the heating was terminated, the samples were left to cool down to room temperature under the carrier gas (at an initial cooling rate of 3 ◦C/s). Atomic force microscopy (AFM) operating in tapping mode was used to investigate the surface morphology. In addition, in order to study the crystalline quality of the AlN layers and to investigate the influence of annealing, X-ray diffraction (XRD) measurements were performed. Omega scans of both the symmetric (0 0 0 2) and skew symmetric (1 0 -1 1) plane reflections were measured. Cross-sectional transmission electron microscopy (TEM) (Thermos Fisher Company, Massachusetts, United States) was also performed on sample A after all the annealing steps. Specimens for transmission electron microscopy (TEM) were prepared using a conventional technique involving mechanical thinning followed by ion milling using Ar+ at

0.5–4.5 keV. The samples were observed using a Titan 80-300 microscope (CP2M, Marseille, France).

Finally, in order to assess whether annealing could be used to fabricate layers of AlN as ready-to-grow templates for the fabrication of AlN-based structures, a regrowth step by MBE of a 220 nm thick AlN at 1100°C (sample C) on sample B (annealed 100 nm thick AlN template) was carried out. To assess this growth process, AFM and XRD measurements were followed to study the surface morphology and the crystalline structure.

II.2.2. Growth of AlN by MBE

a) Characterization of h-BN Templates before Growth

As a first step, the two 3 nm thick h-BN layers on sapphire samples were characterized to investigate their surface morphology. AFM topographic images of (10 x 10) μm^2 and (1 x 1) μm^2 together with their root mean square (RMS) values are reported in Figure 20(a, b). Figure 20(a) shows the h-BN layer that covers the entire wafer surface with a measured surface RMS roughness of 0.7 nm. Figure 20(b) presents a (1 x 1) μm^2 AFM scan that shows small holes (with a density of 1.9 x 10^8 cm^{-2}) covering the entire surface. These holes can be described as pits of hexagonal shape with a depth of 2.5 $\pm$ 0.5 nm (Figure 20c). The surface RMS roughness was measured as 0.5 nm. The presence of wrinkles (white segments in the AFM image) is typical for 2D materials in general. In the case of h-BN, it is due to the thermal expansion coefficient (TEC) difference between h-BN and sapphire substrates, which induces a compressive strain in the layer during the cooling process. The wrinkling instability releases the energy, which creates the roughness in the sample [25]–[27]. The observation of wrinkles is an indicator of the VDW epitaxy of the layered h-BN.

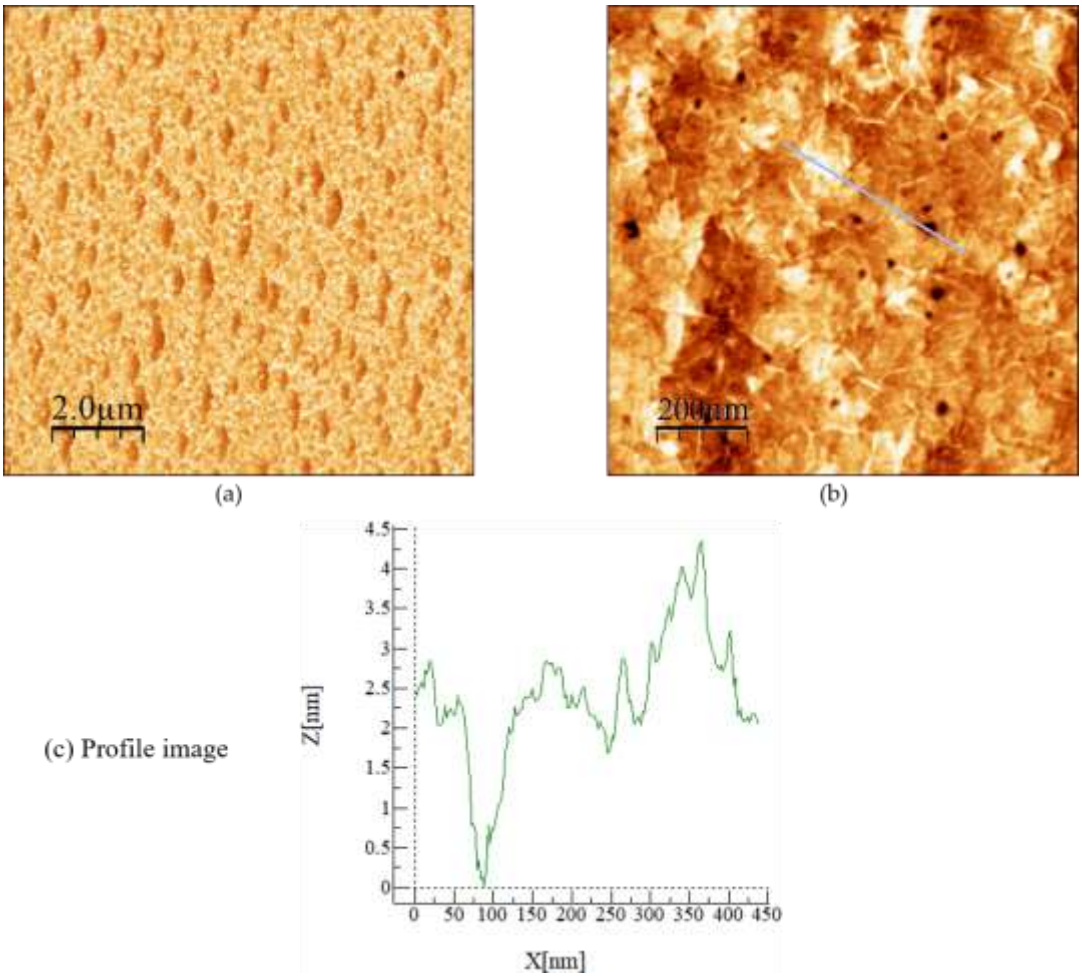

Figure 20. Atomic force microscopy images of a 3 nm h-BN epilayer grown on sapphire c-plane substrate. (a) (10 × 10) µm^2 image with a surface roughness RMS = 0.7 nm, (b) (1 × 1) µm^2 image with a surface roughness RMS = 0.5 nm, and (c) profile measurement of a specific marked zone indicated by a blue line in (b).

b) Growth of AlN on h-BN / sapphire templates by MBE

We proceeded to grow AlN on both h-BN samples by MBE. Figure 21(a) shows RHEED images of the h-BN surface before growth along the <1 1 −2 0> (left) and <1 −1 0 0> (right) azimuths. Charge effects due to the insulating nature of the h-BN surface caused the dim and broadened patterns observed. Figure 21(b) shows the diffraction pattern on sample B (100 nm thick AlN) after growth. The smooth vertical lines observed were an indication of the smoothness of the surface morphology. Moreover, the spots were attributed to the presence of islands (i.e., 3D-like structures) on the surface. Studying the surface reconstruction by RHEED can be a way to determine the polarity of the AlN layers. After finishing the growth of AlN and decreasing the surface temperature under NH_3 flux, it was possible to observe a transition from a (1 x 1) to a (2 x 2) surface reconstruction when the temperature went below 600°C. For NH_3-

assisted MBE, it is a characteristic feature of the metal polarity of the nitride layer [6], [28]. Figure 21(c) displays the diffraction patterns of the AlN surface after growth at low temperature (<550°C) and the (2 x 2) reconstruction under NH_3, which confirmed the Al polarity of the layer.

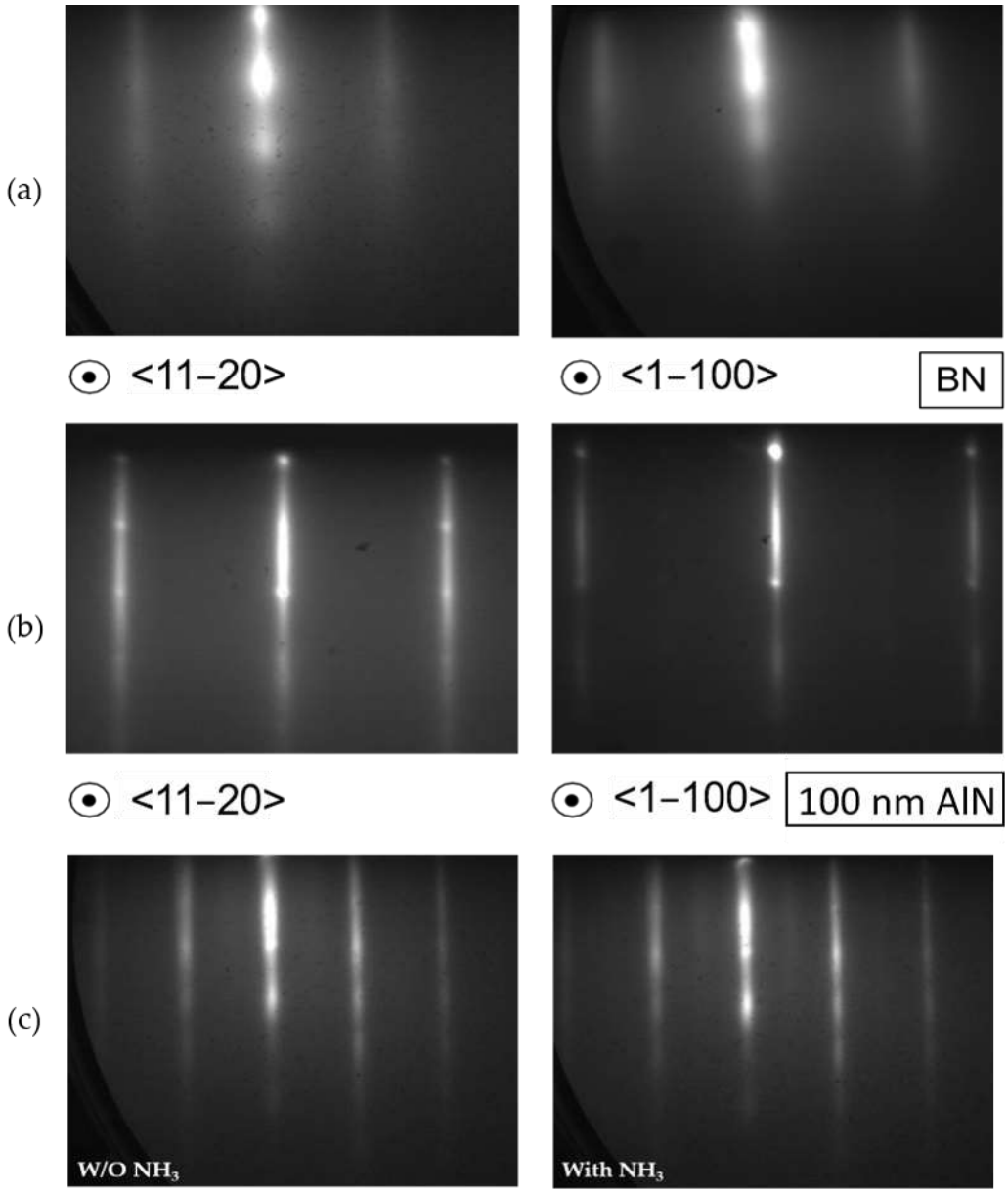

Figure 21. Reflection high-energy electron diffraction (RHEED) images along the ⟨1 1 −2 0⟩ and ⟨1 −1 0 0⟩ azimuths of the surface. (a) For the h-BN layer, (b) for the AlN layer at the end of the growth. The spots were attributed to the presence of islands (i.e., 3D-like structures) on the surface, while the dim and broadened patterns were caused by charge effects due to the insulating nature of the h-BN and AlN surfaces. (c) Images of the diffraction of the AlN surface after the cooling down process without NH_3 (left) and under NH_3 (right) (for a substrate temperature <550°C). The (2 × 2) reconstruction (fig. 21(c) on the right) confirmed the Al polarity of the layer.

II.2.3. Post-growth high temperature annealing

Figure 22 shows the AFM images ((10 x 10) and (2 x 2) μm^2) for samples A (left) and B (right) before and after FFA. In Figure 22 (a) for sample A, a rough surface (RMS = 5.2 nm) defined by islands (density around 3.3 x 10^8 cm^{-2}, height ~50 $\pm$ 15 nm, width ~170 $\pm$ 27 nm) was observed. Figure 22 (b–e) shows AFM images after FFA (images on the left side for sample A). First, the image after annealing at 1450°C is shown in Figure 22 (b), followed by the second annealing at 1550°C in Figure 22 (c), and then the third and fourth annealing steps at 1650°C in Figure 22 (d, e), respectively. As can be seen, after the first FFA, the surface got smoother with a decrease in the island height (~25 $\pm$ 4 nm) and width (~100 $\pm$ 12 nm) with an RMS roughness of 2 nm. However, the density of the islands remained constant (at around 3 x 10^8 cm^{-2}). For the second annealing at 1550°C, as can be observed from Figure 22 (c), the islands' density decreased significantly down to a density of 1.2 x 10^8 cm^{-2}, and the RMS roughness decreased to 1.5 nm. In addition, holes could be clearly observed and appeared to be larger as the annealing temperature increased. They were actually already present after the AlN growth, but their characteristics were difficult to be determined due to the surface roughness. Figure 22 (d) shows AFM images after the third annealing at 1650°C, where the surface roughness RMS had increased from 1.5 to 2.5 nm. As shown in Figure 22 (e), after the fourth annealing at 1650°C, an additional material was clearly observed on the surface. In fact, its presence could already be observed after the third annealing, as shown in the inset of Figure 22 (d). Compared to the previous annealing, the surface roughness RMS had decreased to 2.1 nm.

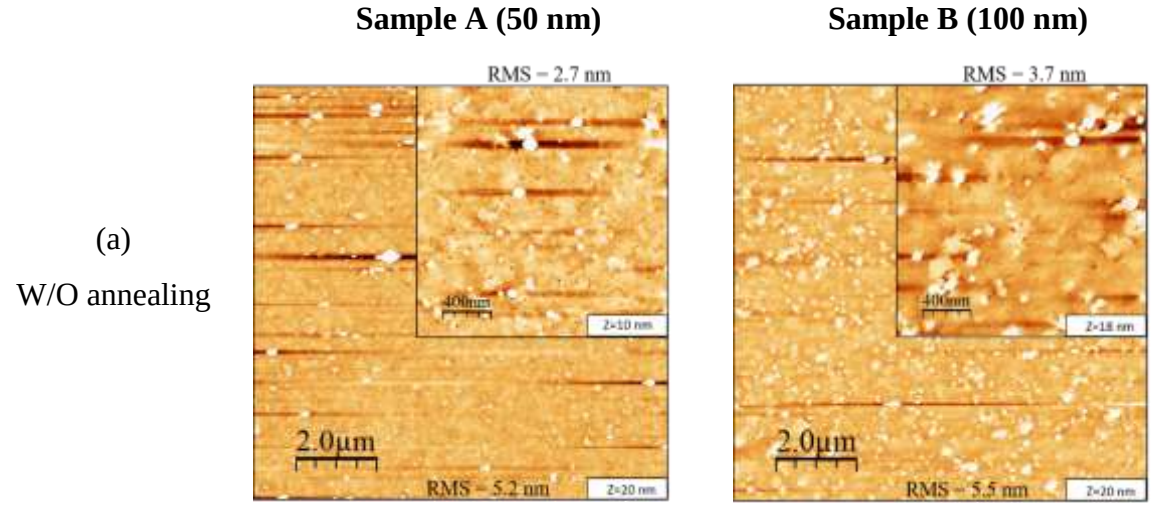

(b)
First FFA at
1450°C; 800
mbar; 15 min

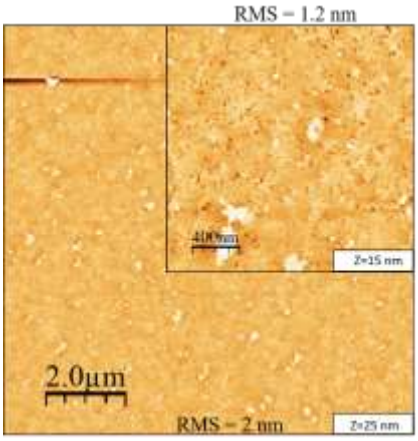

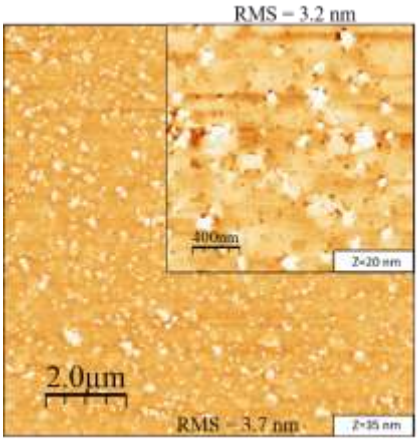

(c)
Second FFA at
1550°C; 800
mbar; 15 min

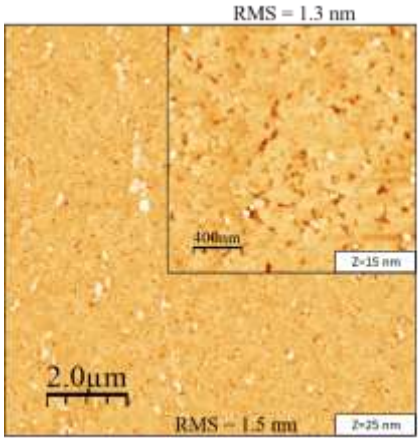

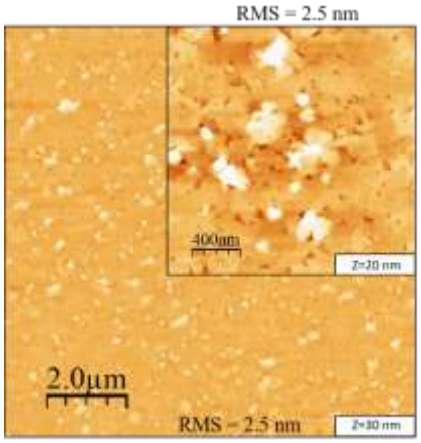

(d)
Third FFA at
1650°C; 800
mbar; 15 min

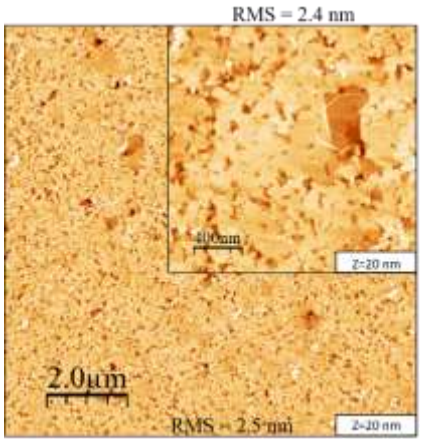

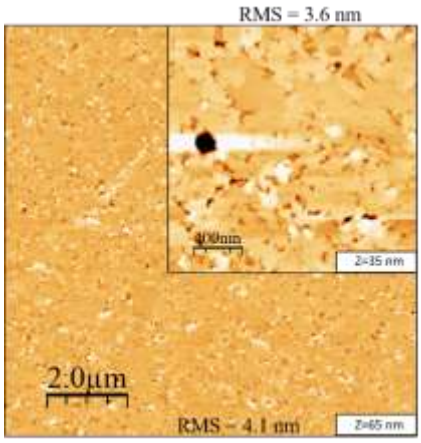

(e) Fourth FFA at 1650°C; 800 mbar; 15 min

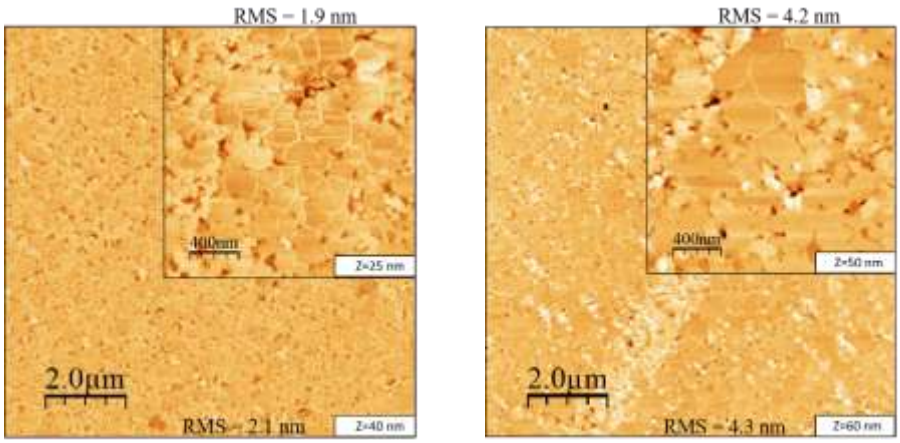

Figure 22. Atomic force microscopy images of (10 × 10) µm^2 of samples A and B, i.e., 50 and 100 nm of AlN grown on 3 nm h-BN, respectively: (a) without post-growth annealing, (b) with a first annealing at 1450°C, (c) with a second annealing at 1550°C, (d) with a third annealing at 1650°C, and (e) with a fourth annealing at 1650°C. The insets show (2 × 2) µm^2 scan images. The term Z represents the vertical scale and the variation in height in the AFM images, and its value is reported at the bottom right hand side of each image.

As shown in Figure 22 (a), for sample B before FFA, a rough surface defined by a high density of 3D islands with a density of about 6.9 x 10^8 cm^{-2} could be seen. The RMS roughness was 5.5 nm; the average island height was 53 $\pm$ 11 nm, which was somewhat similar to the islands height of sample A; and the average width was 120 $\pm$ 19 nm. Figure 22 (b–e) shows AFM images after FFA. After the first FFA, as can be observed, the surface got smoother with a decrease in the island density down to 5.5 x 10^8 cm^{-2}. The size also decreased, with the height being around 37 $\pm$ 4 nm and the width around 100 $\pm$ 20 nm. Consequently, the RMS roughness was found to decrease with a value of 3.7 nm. For the second annealing at 1550°C, as can be observed from Figure 22 (c), the island density and size continued to decrease, with the density going down to 3.8 x 10^8 cm^{-2} and the height decreasing to ~15 $\pm$ 4 nm. Accordingly, the RMS also decreased to 2.5 nm. At this stage, holes started to have a clearer appearance on the surface after the reduction of the presence of islands, similar to sample A. Figure 22 (d) shows the third annealing at 1650°C, where the 3D islands have mostly disappeared. However, the surface got rougher, with the RMS roughness increasing from 2.5 to 4.1 nm. As can be seen in Figure 22 (e), the fourth annealing at 1650°C increased the roughness of the surface up to an RMS value of 4.3 nm. Similar to the case of sample A, an additional material was observed in small regions of the sample's surface. Notably, its presence was more significant on sample A, as can be observed in the inset of Figure 22 (d) after the third annealing. This difference between samples A and B was attributed to the difference in thickness of the AlN layer.

Figure 23 illustrates the RMS roughness variation of samples A and B before and after each FFA stage. As can be observed, the FFA positively affected the RMS roughness of the AlN surface of both samples by initially decreasing and eliminating the 3D island structures. However, after the third annealing at 1650°C, an increase in the RMS roughness was evidenced, which was related to the presence of holes and the formation of an additional material at the surface of the AlN layer.

The omega scan FWHM are impacted by many factors, such as the wafer curvature, instrument width, coherence length, lattice strain, and lattice rotation due to dislocations (tilt and twist misorientations). For films with high TDDs, as in our case here, the lattice rotations due to dislocations have the most important influence [6], [7]. Therefore, the tilt, defined as out-of-plane misorientation, and the twist, defined as in-plane misorientation, can be evaluated from the symmetric and skew symmetric reflections. XRD rocking curve FWHM of symmetric (0 0 0 2) and skew symmetric (1 0 −1 1) diffractions for both samples were studied. By coupling the XRD measurements with the Dunn and Koch equation [8], it was then possible to correlate mixed and edge TDDs with the FWHM of the symmetric and skew symmetric reflections [8], [9]. It is critical to mention that the screw TDDs were neglected as they are present in very low proportion (~1%) in nitrides [10].

The estimation of mixed and edge TDDs for samples A and B are shown in Figure 24 (a, b), respectively. For sample A, the mixed TD density before the FFA was in the 4×10^{10} cm^{-2} range, and it decreased by a factor of 8, down to 5×10^{9} cm^{-2} after the complete FFA process. Regarding the edge TD density, a very high density of 3×10^{12} cm^{-2} was estimated before the FFA, which then decreased by a factor of 3, down to 9×10^{11} cm^{-2} after FFA. For sample B, the mixed TD density before the FFA was 5×10^{10} cm^{-2}, and it decreased to 4×10^{9} cm^{-2} after the FFA, corresponding to an improvement by a factor of 10. At the same time, the edge TD density went from 4×10^{12} cm^{-2} before the FFA down by a factor of 5 to 8×10^{11} cm^{-2} after annealing. These results indicated an improvement of the structural quality of the AlN film due to reduction in the tilt and twist components from the epitaxial AlN films by FTF high-temperature annealing.

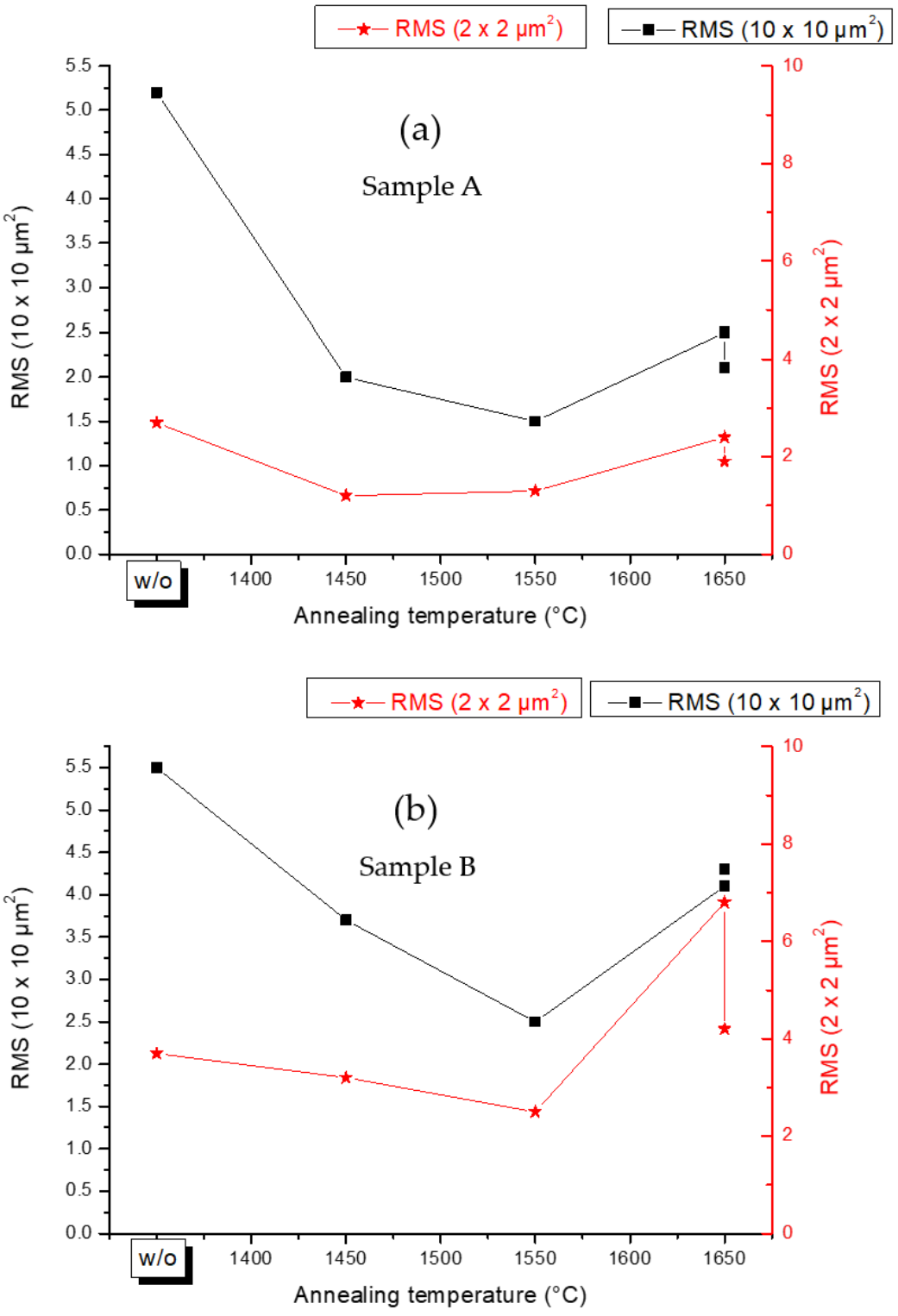

Figure 23. Variation of the RMS roughness as a function of the annealing temperatures for (a) sample A and (b) sample B. The RMS values are measured on (10 × 10) μm^2 atomic force microscopy topographic images.

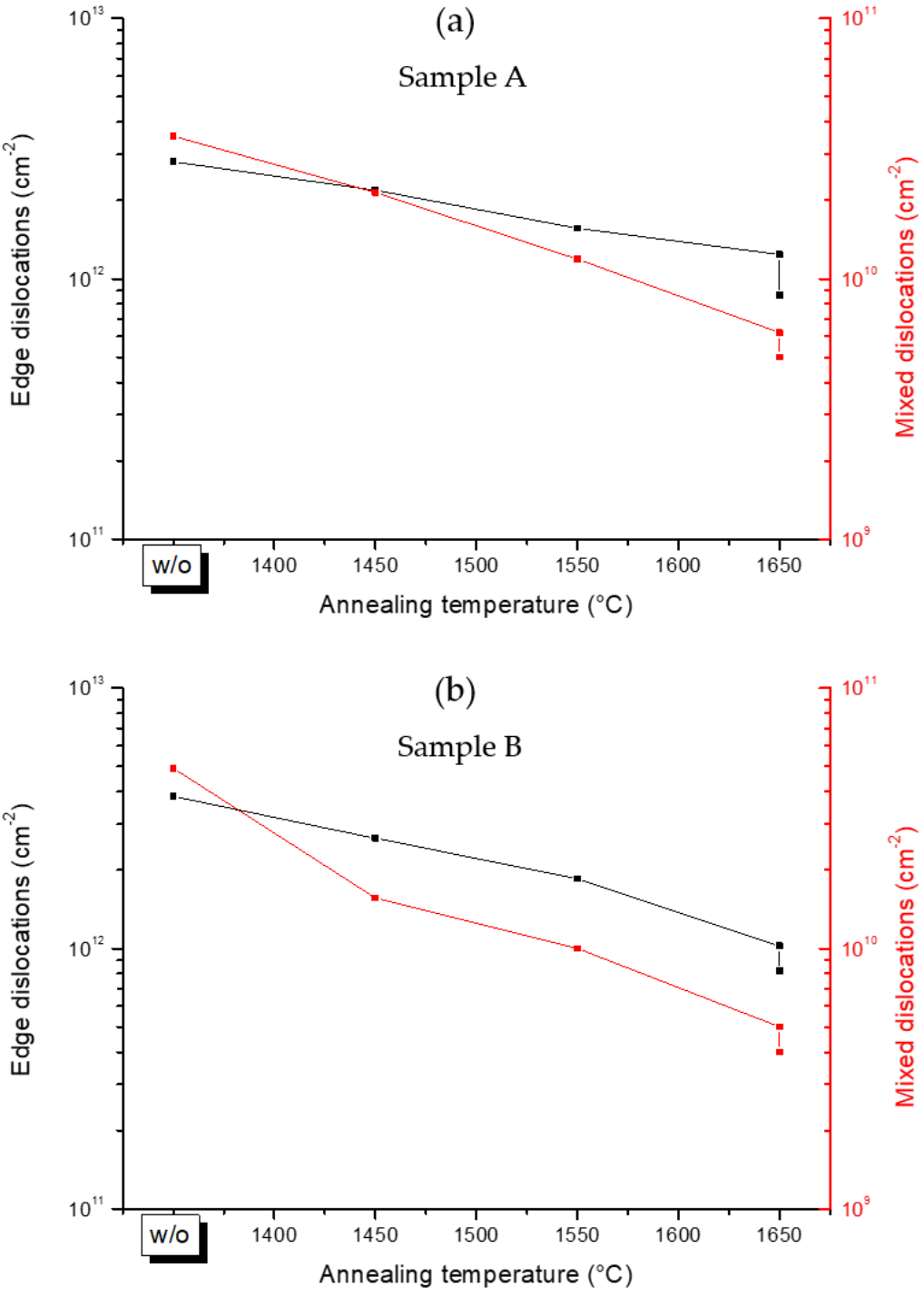

Figure 24. Mixed and edge dislocation densities of (a) sample A and (b) sample B estimated from tilt and twist values as a function of the annealing temperatures.

II.2.4. AlN regrowth by MBE

We then proceeded to regrow a 220 nm thick AlN layer (sample C) on sample B (annealed 100 nm thick AlN) to investigate the influence of the annealed template on the crystalline quality and the surface morphology of the regrown AlN layer. Once again, the growth was performed using MBE with ammonia (NH_3) as the nitrogen source. Figure 25 shows the AFM images of sample C, which indicate a smoother surface morphology compared to samples A and B. The surface was made of large terraces with the presence of atomic steps and nm-high steps separating each terrace. For the (10 x 10) μm^2 surface image, an RMS roughness of 1.7 nm was formed. The morphology was made of terraces with an average terrace length of 920 ± 110 nm and separated by steps with an average height of 3.5 ± 0.5 nm, i.e., corresponding roughly to 14 monolayers of AlN.

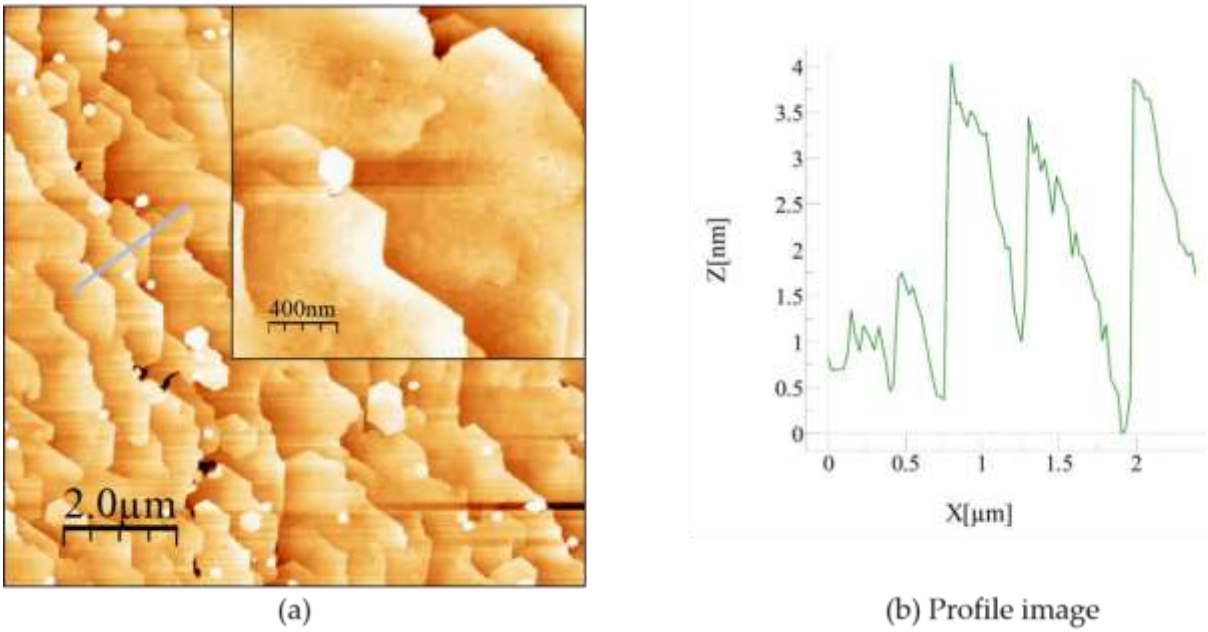

Figure 25. Atomic force microscopy images of sample C, a 220 nm thick AlN epilayer grown on annealed sample B. (a) (10 × 10) μm^2 image with an RMS = 1.7 nm, the inset showing (2 × 2) μm^2 scan image with an RMS = 1 nm. (b) Profile measurement of a specific marked zone of the (10 × 10) μm^2 image indicated by a blue line.

In addition, for the (2 x 2) μm^2 surface image, the RMS roughness was reduced to 1 nm. The AFM results clearly showed how the annealing recipe ameliorated the surface morphology of the AlN layer by developing large terraces with smooth atomic step morphology. Furthermore, for both the symmetric plane (0 0 0 2) and the skew symmetric plane (1 0 −1 1), the crystalline structure study of the regrown 220 nm-thick AlN layer by X-ray measurements revealed an enhanced crystalline quality of the regrown AlN layer. The FWHM value of the symmetric (0 0 0 2) plane was 0.31° and 2.89° for the (1 0 −1 1) skew symmetric plane similar

to the improved FHWM values obtained for sample B after the annealings, as shown in Table I . The improvement in surface morphology and crystalline quality of the regrown AlN layer (sample C) on the annealed AlN surface (sample B) can be attributed to the high annealing temperature that promoted diffusion and rearrangement of atoms, which helped reducing defects and dislocations present in the as-grown layer. This process led to the elimination or reduction of defects that have initially contributed to the poor crystalline quality and surface roughness in sample B. The improved surface morphology and crystalline quality of the annealed AlN layer (sample B) provided a better template for nucleation during the regrowth process. The smoother and more ordered surface led to a more uniform and controlled nucleation that resulted in an improved crystal growth for sample C. The edge and mixed TDDs values were estimated to show a total reduction from 4 x 10^{12} cm^{-2} to 7 x 10^{11} cm^{-2} and from 5 x 10^{10} cm^{-2} to 4 x 10^{9} cm^{-2} between the initial AlN layer and the final one obtained after both the HTA process and AlN regrowth, respectively. This clearly shows that such annealed MBE-grown AlN templates can be used as "ready-to-grow" templates for the fabrication of AlN-based structures with better surface morphology.

The evolution of the (0 0 0 2) RC FWHM as a function of the annealing steps for samples A and B is illustrated in figure 26(a) and (b). Furthermore, the estimated edge and mixed TDDs are summarized in Table 1 along with the values of the RMS roughness and the FWHM of the symmetric and skew symmetric planes. We observed that the FFA annealing process played a significant role in reducing both the edge and mixed TD densities for samples A and B, thus improving the crystalline qualities of the layers. Sample A's mixed TD density decreased by 85% in total, while the edge TD density was reduced by a total of 70%. Sample B's mixed TD density had a total reduction of 92%, while its edge TD density decreased by 80%.

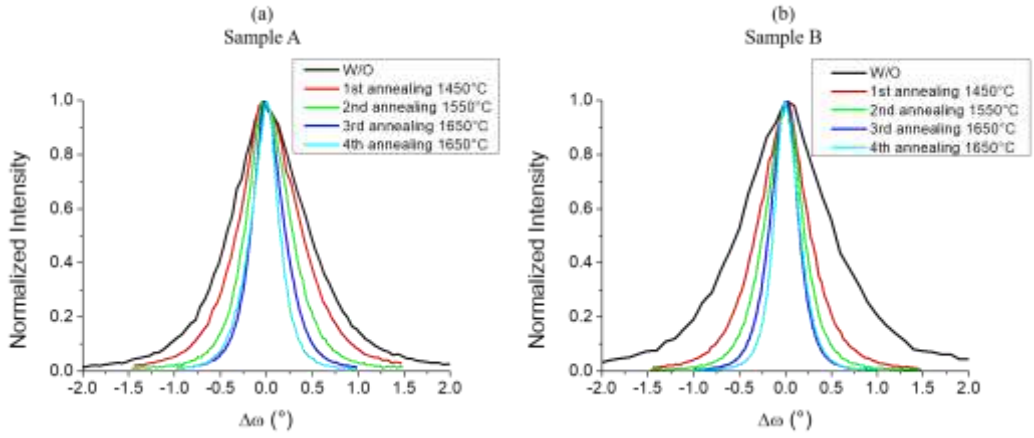

Figure 26. X-ray RC ω-scan of the symmetric (0 0 0 2) plane of AlN before and after FFA: a) for sample A, b) for sample B.

	Annealing temperature (°C)	RMS (nm) (10 x 10) μm^2	(0 0 0 2) (°)	(1 0 −1 1) (°)	Estimated Mixed TDD (cm^{-2})	Estimated Edge TDD (cm^{-2})
Sample A (AlN 50 nm)	W/O	5.2	0.93	5.67	4.0×10^{10}	3.0×10^{12}
	1450	2.0	0.73	5.50	2.1×10^{10}	2.2×10^{12}
	1550	1.5	0.54	4.60	1.2×10^{10}	1.6×10^{12}
	1650	2.5	0.39	3.77	6.2×10^{9}	1.2×10^{12}
	1650	2.1	0.35	3.14	5.0×10^{9}	9.0×10^{11}
Sample B (AlN 100 nm)	W/O	5.5	1.10	6.62	5.0×10^{10}	4.0×10^{12}
	1450	3.7	0.62	5.01	1.6×10^{10}	2.6×10^{12}
	1550	2.5	0.48	4.22	1.1×10^{10}	1.8×10^{12}
	1650	4.1	0.35	3.42	5.1×10^{9}	1.1×10^{12}
	1650	4.3	0.31	3.06	4.0×10^{9}	8.0×10^{11}
Sample C (AlN 220 nm)	-	1.7	0.31	2.89	4.0×10^{9}	7.0×10^{11}

Table 1. Table summarizing the main crystalline and morphological properties of samples A, B, and C measured by atomic force microscopy and X-ray diffraction before and after FFA and after an AlN regrowth step.

II.2.5. TEM characterization of sample A

The growth of AlN on h-BN/sapphire templates by MBE led to the fabrication of Al-polar layers with mainly 2D surfaces perturbed by the presence of 3D islands. In order to investigate the surface morphology and crystalline quality, which was characterized by a high degree of mosaicity, a TEM investigation of sample A (50 nm thick AlN) was performed in the cross section after the whole series of annealing processes were carried out. Figure 27 presents the TEM images along the <1 0 −1 0> and <1 1 −2 0> AlN zone axes. At first, an interface was observed close to the interface between the sapphire and AlN/h-BN (around 10 nm from the interface), which should correspond to an inversion domain boundary between a bottom N-polar and a top Al-polar region, as always reported for face-to-face annealing of AlN on sapphire [16], [29]. Moreover, a truncated pyramid-like cavity was found. Figure 27 (b) shows the truncated pyramid-like cavity, shown in Figure 27 (a), at high resolution. This cavity revealed an unexpected process, with a BN inclusion being found in the sapphire substrate (with an in-depth thickness penetration of around 4.2 nm). The formation of this inclusion was due to the high-temperature annealing. Another consequence of the annealing processes is shown

in Figure 27 (c). As can be seen, no h-BN was found in between the sapphire and AlN layer, i.e., B had diffused into the AlN layer. In fact, similar observations were found in most of the interface between the nitride layers and the sapphire substrate, and h-BN was found only around cavities, as shown in Figure 27 (b). In addition, the polarity inversion boundary, indicated in Figure 27 (a), could be clearly seen with the N-polar AlN underneath it (i.e., at the interface with the sapphire substrate) and the Al-polar AlN above it towards the surface.

There is almost no more h-BN left at the interface with the sapphire. Boron has diffused towards the sample surface, forming h-BN on the surface in a few places. We observed both diffusion and segregation: h-BN tends to be rejected at the surface. When h-BN was found to remain at the interface with the sapphire, it was almost exclusively under cavities. In other words, this h-BN was found beneath the sapphire surface.

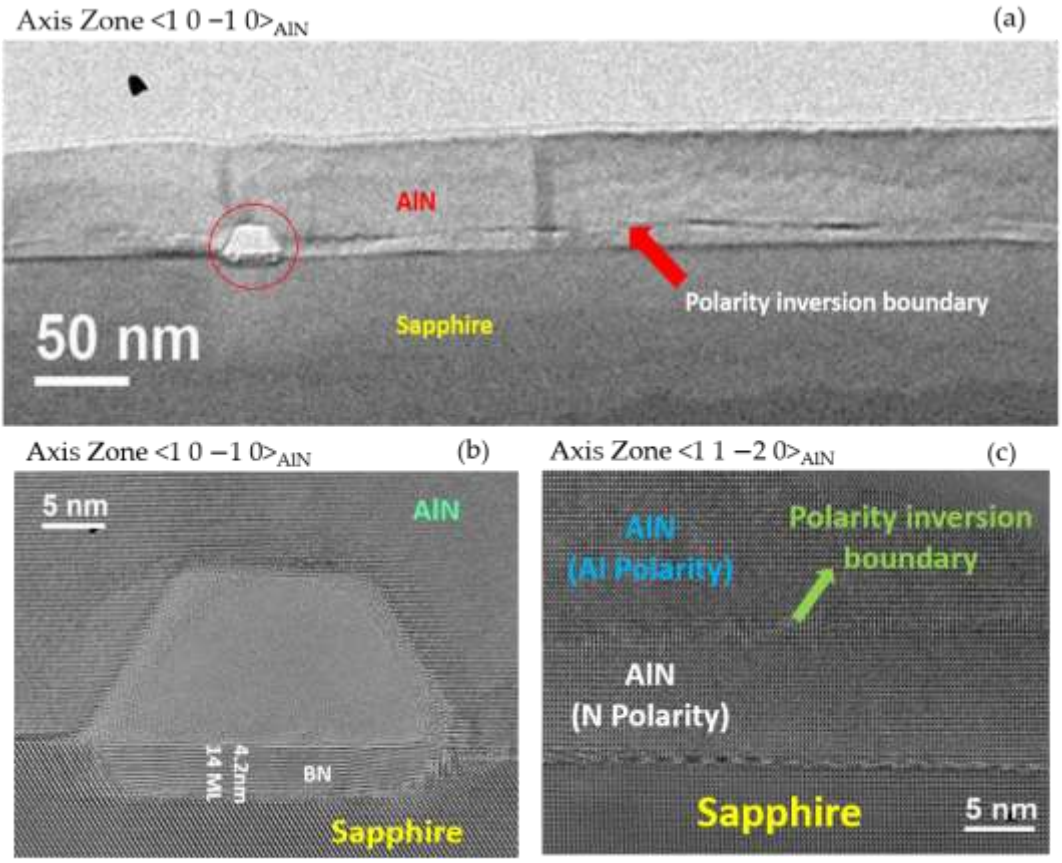

Figure 27. Multibeam cross-sectional TEM images of sample A (50 nm thick AlN) along the <1 0 −1 0> and <1 1 −2 0> AlN zone axes. (a) Low-resolution image of AlN on h-BN showing a cavity at the interface with the sapphire substrate. In addition, a polarity inversion boundary is shown close to the interface (~10 nm above it). (b) High-resolution image of the cavity observed in (a), where h-BN inclusion in the sapphire zone can be observed. (c) High-resolution image of the interface between sapphire and AlN, where h-BN has completely disappeared from the interface with sapphire. In addition, the polarity inversion boundary can be observed with N-polar AlN underneath it and Al-polar AlN above it.

Figure 28 (a) shows an AlN truncated pyramid-like structure at the surface, which confirms that the 3D islands observed by AFM before and during the annealings were AlN islands. Furthermore, the additional material observed by AFM on the surface of both samples after the whole annealing process was found to be BN as its morphology has the characteristic morphology of h-BN. This demonstrated that B had diffused from the interface with sapphire up to the surface of the AlN layer and had recrystallized to form h-BN islands (yellow arrow). This was also confirmed by performing AFM phase imaging on both samples (Figure 29). The zone marked by a red arrow is therefore supposed to be a region made of (Al,B)N, which was formed due to the diffusion of B into the AlN layer during annealing. Figure 28 (b, c) are high-resolution images of specific features present at the surface, namely, the AlN truncated pyramid-like structure and the recrystallized h-BN, respectively.

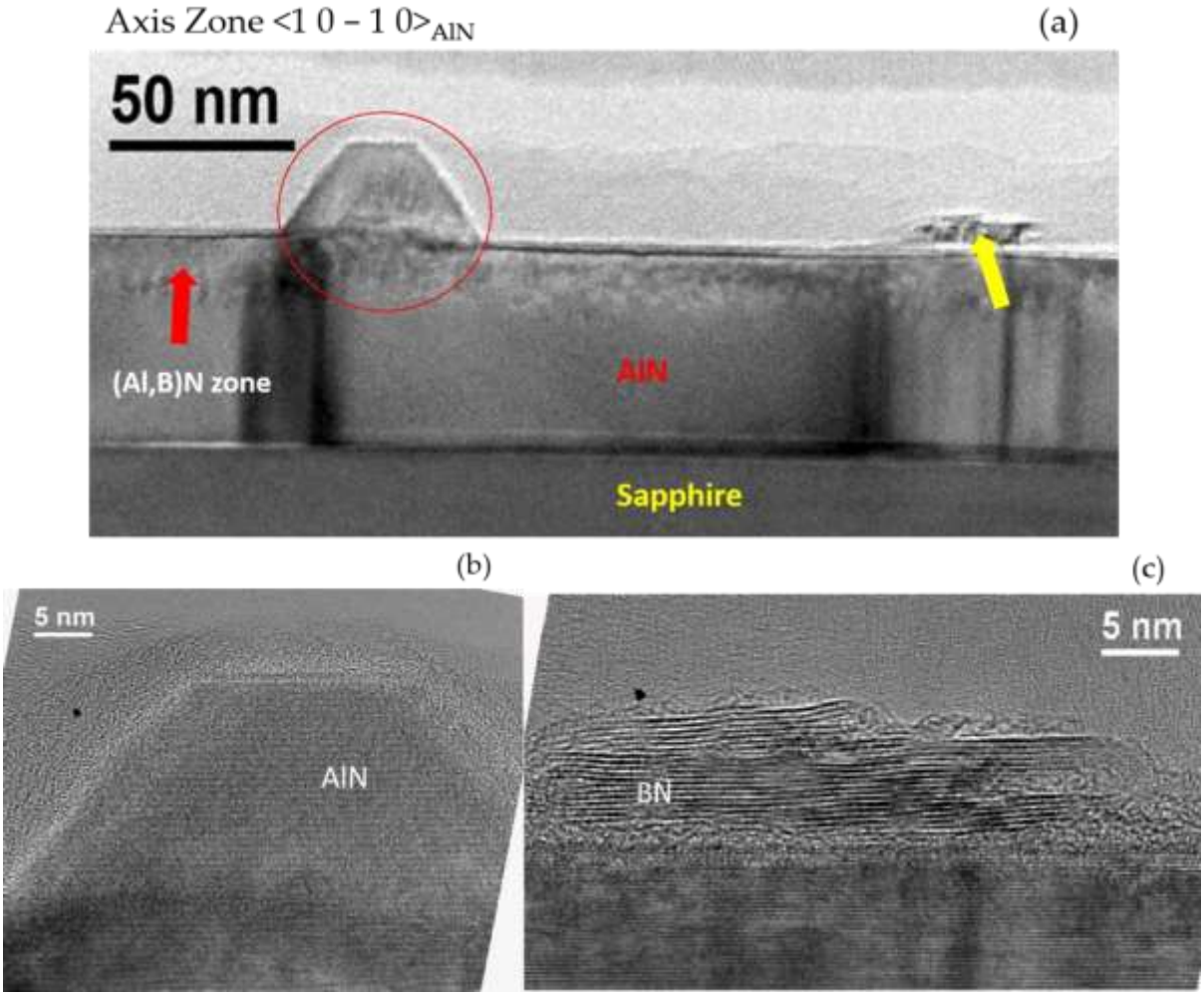

Figure 28. (a) AlN truncated pyramid-like structure at the surface (red circle). The yellow arrow points to a region made of h-BN due to the diffusion of B into the AlN layer, which reached the surface and recrystallized after annealing. The red arrow shows a specific contrasted region underneath the surface, which can be attributed to the presence of B in the AlN layer forming an (Al,B)N material. (b, c) High-resolution images of AlN truncated pyramid-like structure and recrystallized h-BN region, respectively.

During high-temperature annealing processes, solid-phase reactions occurred that improved the crystalline quality of the structure, similar to what has been previously reported [3]. It should be mentioned that for the third and fourth annealing steps at 1650°C, for both samples (A and B), the FWHMs for both the symmetric (0 0 0 2) and skew symmetric (1 0 −1 1) planes hardly decreased (especially for sample B). This can be explained by the study conducted by Prof. Miyake's group on FFA of AlN films, which showed that the XRD peak FWHM values were similar for annealing processes carried out at 1600 and 1650°C. In fact, the XRD peak FWHM values only significantly decreased for annealing at the higher temperature of 1700 ◦C [3]. This feature was attributed to the columnar structure of AlN. The alignment of the AlN columns composing the AlN layer requires high energy to enable coalescence, which then results in annihilation of the domain boundaries and thus improves the crystalline quality of the AlN films [3]. However, in our case, the surface became thermally unstable for an annealing temperature above 1550°C. This feature can be explained by the diffusion of B in the AlN layer, which led to the formation of h-BN regions at the surface of the AlN layer. This also clarifies the origin of the increase in the surface roughness RMS values after the third annealing and sets a limit for the maximum annealing temperature that can be used.

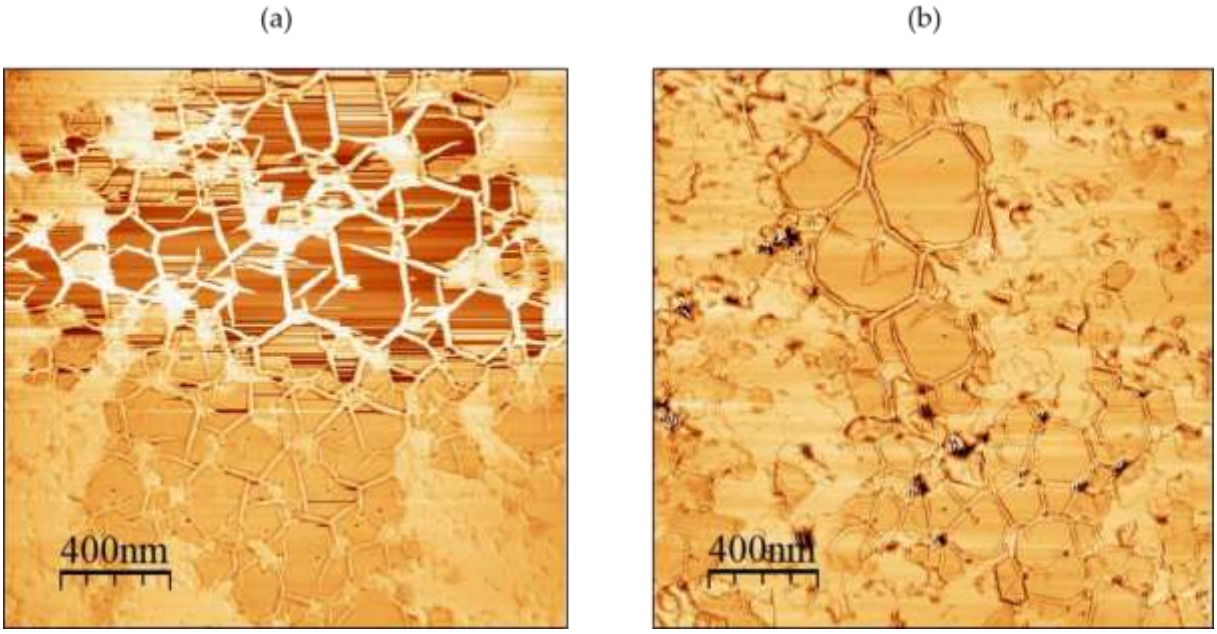

Figure 29. Atomic force microscopy phase images of (2 × 2) μm^2 showing h-BN regions resulting from the diffusion of h-BN through the AlN layer up to the surface for (a) sample A (50 nm AlN) and (b) sample B (100 nm AlN).

II.2.6. Conclusion

AlN epitaxial layers (50 nm and 100 nm thick) were grown on 3 nm thick h-BN/sapphire templates by MBE, and their main structural properties were characterized by AFM and XRD. The h-BN, with a thickness of 3 nm, was directly grown on 2-inch sapphire substrates by MOVPE. The influence of post-growth FFA high-temperature annealing on h-BN and AlN structures was studied as a function of the annealing conditions. The temperature was varied from 1450 to 1650°C, and different annealing time durations were used. The surface roughness (RMS) was determined by AFM, and a significant decrease in AlN thickness was found after the first two annealing steps at 1450 and 1550°C. Some modifications were observed at the AlN surface, including a decrease in the 3D island structures that were initially present after MBE growth as well as surface smoothening, with the RMS roughness varying from 5.2 down to 2.1 nm. However, an observable increase in the RMS roughness after the third and fourth annealing steps at 1650°C was found. For the (0 0 0 2) and the (1 0 −1 1) reflections, the omega scan FWHM significantly decreased as the annealing temperature increased, indicating the crystalline quality improvement of the AlN layers. Edge and mixed TDDs were estimated and showed a reduction for each annealing step. TEM observations performed after the whole annealing cycle showed that B had diffused from the sapphire interface through the AlN layer. In some regions, the h-BN even diffused up to the surface, where it had recrystallized on top of the AlN layer. In other zones along the interface with sapphire, h-BN was also found to exist inside the sapphire substrate. These unexpected diffusion mechanisms indicate that annealing conditions should be carefully controlled in order to remain below the thermal instability of h-BN. Finally, an AlN layer was regrown by MBE on the thermally annealed 100 nm thick layer, showing a step bunching morphology with µm-wide terraces. In addition, better structural quality with a reduction in mixed and edge TDDs compared to the initial AlN layers was observed. This study indicates that annealed MBE-grown AlN layers on h-BN could potentially be used as templates for AlN-based heterostructures with improved structural quality by adequately adjusting the annealing temperature and time duration. Furthermore, high-temperature annealing could also open the possibility of (Al,B)N alloy fabrication by B diffusion in AlN.

References:

[1] Y. Taniyasu, M. Kasu, et T. Makimoto, « An aluminium nitride light-emitting diode with a wavelength of 210 nanometres », *Nature*, vol. 441, nº 7091, p. 325-328, mai 2006, doi: 10.1038/nature04760.

[2] N. Faleev, H. Lu, et W. J. Schaff, « Low density of threading dislocations in AlN grown on sapphire », in *Journal of Applied Physics*, 2007. doi: 10.1063/1.2728755.

[3] H. Miyake, C. H. Lin, K. Tokoro, et K. Hiramatsu, « Preparation of high-quality AlN on sapphire by high-temperature face-to-face annealing », *Journal of Crystal Growth*, vol. 456, p. 155-159, déc. 2016, doi: 10.1016/j.jcrysgro.2016.08.028.

[4] K. Hamanaka, T. Tachiki, et T. Uchida, « Face-to-Face Annealing of Bi2Sr2CaCu2O8+ δ/MgO Precursor Films Fabricated by Metal–Organic Decomposition », *Japanese Journal of Applied Physics*, vol. 48, nº 12R, p. 125502, 2009.

[5] I. Horcas, R. Fernández, J. M. Gómez-Rodríguez, J. Colchero, J. Gómez-Herrero, et A. M. Baro, « WSXM : A software for scanning probe microscopy and a tool for nanotechnology », *Review of Scientific Instruments*, vol. 78, nº 1, p. 013705, janv. 2007, doi: 10.1063/1.2432410.

[6] Y. Xia *et al.*, « Growth of Ga- and N-polar GaN layers on O face ZnO substrates by molecular beam epitaxy », *Journal of Crystal Growth*, vol. 388, p. 35-41, févr. 2014, doi: 10.1016/j.jcrysgro.2013.11.017.

[7] T. A. Lafford, B. K. Tanner, et P. J. Parbrook, « Direct measurement of twist mosaic in GaN epitaxial films as a function of growth temperature », *J. Phys. D: Appl. Phys.*, vol. 36, nº 10A, p. A245-A248, mai 2003, doi: 10.1088/0022-3727/36/10A/351.

[8] C. G. Dunn et E. F. Kogh, « Comparison of dislocation densities of primary and secondary recrystallization grains of Si-Fe », *Acta Metallurgica*, vol. 5, nº 10, p. 548-554, oct. 1957, doi: 10.1016/0001-6160(57)90122-0.

[9] M. Nemoz, R. Dagher, S. Matta, A. Michon, P. Vennéguès, et J. Brault, « Dislocation densities reduction in MBE-grown AlN thin films by high-temperature annealing », *Journal of Crystal Growth*, vol. 461, p. 10-15, mars 2017, doi: 10.1016/j.jcrysgro.2016.12.089.

[10] D. M. Follstaedt, N. A. Missert, D. D. Koleske, C. C. Mitchell, et K. C. Cross, « Plan-view image contrast of dislocations in GaN », *Applied Physics Letters*, vol. 83, nº 23, p. 4797-4799, déc. 2003, doi: 10.1063/1.1632540.

[11] R. Dagher *et al.*, « High temperature annealing and CVD growth of few-layer graphene on bulk AlN and AlN templates », *physica status solidi (a)*, vol. 214, nº 4, p. 1600436, 2017.

[12] F. Owman, C. Hallin, P. Mårtensson, et E. Janzen, « Removal of polishing-induced damage from 6H-SiC (0001) substrates by hydrogen etching », *Journal of crystal growth*, vol. 167, nº 1-2, p. 391-395, 1996.

[13] S. Kuboya, K. Uesugi, K. Shojiki, Y. Tezen, K. Norimatsu, et H. Miyake, « Crystalline quality improvement of face-to-face annealed MOVPE-grown AlN on vicinal sapphire substrate with sputtered nucleation layer », *Journal of Crystal Growth*, vol. 545, p. 125722, 2020.

[14] S. Xiao, R. Suzuki, H. Miyake, S. Harada, et T. Ujihara, « Improvement mechanism of sputtered AlN films by high-temperature annealing », *Journal of Crystal Growth*, vol. 502, p. 41-44, nov. 2018, doi: 10.1016/j.jcrysgro.2018.09.002.

[15] T. Akiyma, M. Uchino, K. Nakamura, T. Ito, S. Xiao, et H. Miyake, « Structural analysis of polarity inversion boundary in sputtered AlN films annealed under high temperatures », *Japanese Journal of Applied Physics*, vol. 58, nº SC, p. SCCB30, 2019.

[16] S. Hagedorn *et al.*, « Stabilization of sputtered AlN/sapphire templates during high temperature annealing », *Journal of Crystal Growth*, vol. 512, p. 142-146, avr. 2019, doi: 10.1016/j.jcrysgro.2019.02.024.

[17] L. Cancellara *et al.*, « Role of oxygen diffusion in the dislocation reduction of epitaxial AlN on sapphire during high-temperature annealing », *Journal of Applied Physics*, vol. 130, nº 20, p. 203101, nov. 2021, doi: 10.1063/5.0065935.

[18] S. Mohn *et al.*, « Polarity control in group-III nitrides beyond pragmatism », *Physical Review Applied*, vol. 5, nº 5, p. 054004, 2016.

[19] A. Koma et K. Yoshimura, « Ultrasharp interfaces grown with Van der Waals epitaxy », *Surface Science*, vol. 174, nº 1, p. 556-560, août 1986, doi: 10.1016/0039-6028(86)90471-1.

[20] P. Ajayan, P. Kim, et K. Banerjee, « Two-dimensional van der Waals materials », *Physics Today*, vol. 69, nº 9, p. 38-44, sept. 2016, doi: 10.1063/PT.3.3297.
[21] Y. Kobayashi, K. Kumakura, T. Akasaka, et T. Makimoto, « Layered boron nitride as a release layer for mechanical transfer of GaN-based devices », *Nature*, vol. 484, nº 7393, Art. nº 7393, avr. 2012, doi: 10.1038/nature10970.
[22] Q. Wu *et al.*, « Exfoliation of AlN film using two-dimensional multilayer hexagonal BN for deep-ultraviolet light-emitting diodes », *Appl. Phys. Express*, vol. 12, nº 1, p. 015505, janv. 2019, doi: 10.7567/1882-0786/aaeede.
[23] D. Chugh, S. Adhikari, J. Wong-Leung, M. Lysevych, C. Jagadish, et H. H. Tan, « Improving the Morphology and Crystal Quality of AlN Grown on Two-Dimensional hBN », *Crystal Growth and Design*, vol. 20, nº 3, p. 1811-1819, mars 2020, doi: 10.1021/acs.cgd.9b01543.
[24] Q. Wu *et al.*, « Growth mechanism of AlN on hexagonal BN/sapphire substrate by metal-organic chemical vapor deposition », *CrystEngComm*, vol. 19, nº 39, p. 5849-5856, 2017, doi: 10.1039/c7ce01064h.
[25] X. Li *et al.*, « Large-area two-dimensional layered hexagonal boron nitride grown on sapphire by metalorganic vapor phase epitaxy », *Crystal Growth and Design*, vol. 16, nº 6, p. 3409-3415, juin 2016, doi: 10.1021/acs.cgd.6b00398.
[26] S. Saha *et al.*, « Comprehensive characterization and analysis of hexagonal boron nitride on sapphire », *AIP Advances*, vol. 11, nº 5, mai 2021, doi: 10.1063/5.0048578.
[27] P. Vuong *et al.*, « Influence of Sapphire Substrate Orientation on the van der Waals Epitaxy of III-Nitrides on 2D Hexagonal Boron Nitride: Implication for Optoelectronic Devices », *ACS Applied Nano Materials*, vol. 5, nº 1, p. 791-800, janv. 2022, doi: 10.1021/acsanm.1c03481.
[28] A. R. Smith *et al.*, « Determination of wurtzite GaN lattice polarity based on surface reconstruction », *Applied Physics Letters*, vol. 72, nº 17, p. 2114-2116, 1998, doi: 10.1063/1.121293.
[29] J. Kaur *et al.*, « Electron microscopy analysis of microstructure of postannealed aluminum nitride template », *Applied Physics Express*, vol. 9, nº 6, juin 2016, doi: 10.7567/APEX.9.065502.

Chapter 3

Standard and Tunnel Junction UV LEDs

This chapter provides an overview of the tunneling theory, including the growth of tunnel junction structures and their performance. It also explores previous research conducted on tunnel junctions and compares the recent advancements and improvements made in this thesis to the existing results. This chapter covers:

- Historical overview of MBE and MOCVD growth of tunnel junction UV LEDs.
- Summary of previous results on tunnel junction LEDs.
- MOCVD growth of standard UV LEDs on annealed PVD templates.
- MBE growth of quantum dots-based standard and tunnel junction UV LEDs.

III.1. Tunnel junctions

III.1.1. Overview of historical background

The investigation of electron tunneling in non-metallic materials under a strong electric field dates back to 1934 with Zener's pioneering studies [1]. In 1957, Chynoweth and McKay conducted measurements on reverse-biased p-n diodes, which were interpreted as Zener tunneling [2]. The discovery of interband tunneling in semiconductors came later, in a report by Leo Esaki, who worked with forward-biased Ge degenerately doped p-n junctions [3]. The intriguing negative resistance behavior exhibited by these junctions, combined with the opportunity to study degenerate semiconductors like Ge and Si, spurred rapid advancements in both theoretical [4]–[6] and experimental research [7]–[11] on the tunnel effect. This led to the development of the first III-V tunnel diode by Nick Holonyak in 1960, utilizing GaAs [12]. Subsequently, tunnel junctions found applications in various areas. For instance, in 1979, Harris et al. proposed connecting solar cells with tunnel junctions to enhance conversion efficiencies, while in 1982, van der Ziel et al. suggested employing GaAs tunnel junctions to connect three double heterostructures for the production of monolithic GaAs laser diodes [13].

The adoption of n-doped upper epilayers and tunnel junctions (TJs) instead of the conventional p-doped cladding, which has been the standard stacking order, originated in 1993 with the development of the first AlGaAs quantum well laser diode featuring a GaAs/InGaAs tunnel contact [14]. Subsequent advancements in tunnel junctions further optimized AlGaAs laser diodes for improved performance [15], [16]. In 1997, Wierer et al. proposed the use of TJs as intracavity contacts for vertical cavity surface emitting lasers (VCSELs), enabling hole injection to the p-type material through lateral electron currents [15], [17]. The integration of TJs in III-N VCSEL systems significantly enhanced the threshold current density and differential efficiency of the diodes [18]–[20].

In terms of LEDs, the first patent for an LED with tunnel junctions was filed by Olson et al. in 1992. The GaAs tunnel junction served as a means to connect different active regions in LEDs, enabling simultaneous emission of light at multiple wavelengths [21]. This invention was subsequently adapted for InGaN/GaN quantum well LEDs [22], [23] and the production of monolithic white LEDs using quantum wells of various colors [24], [25]. Another application of tunnel junctions in LEDs is the connection of LEDs emitting at the same wavelength to address the droop issue. Instead of increasing the current density, the device operates at a higher bias (sum of biases on all stages) with a moderate current, resulting in high power density and

mitigated droop. This concept was initially proposed by Guo et al. [26]–[28] and has been further optimized by several research groups [29]–[31].

The first demonstration of a nitride LED with a tunnel junction (TJ) was conducted by Jeon et al. in 2001. The TJ offers dual advantages in these devices, addressing two main issues. Firstly, it enhances the lateral current uniformity in LEDs that are not strictly vertical and suffer from reduced p conductivity. The significantly higher n conductivity facilitates improved current spreading from the contact pads. Secondly, replacing the highly resistive ohmic p-contact with a low resistivity n-contact reduces the overall resistivity of the diode [32].

The idea of using tunnel junctions in UV LEDs was initially proposed by Simon et al. in 2009 [33] and later by Schubert in 2010 [34], [35]. These suggestions were motivated by various factors that remain relevant. In (Al, Ga)N materials, the activation energy of Mg-acceptors increases substantially from around 200 meV to over 600 meV in AlN, while the donors (from Si or Ge) remain shallow until higher Al contents (i.e. up to [Al] ≈80%) in AlGaN alloys [36]. To address this issue, a p-GaN current spreading layer is typically deposited on top of the structure, but this compromises extraction efficiency as GaN absorbs UV light. Therefore, replacing the top p-contact layer with a tunnel contact (i.e., a highly n-doped layer) has the potential to significantly enhance hole injection in the active region without introducing additional absorption losses.

A tunnel junction facilitates the transfer of electrons from the valence band of the p-type material to the conduction band of the n-type material through inter-band tunneling. Simultaneously, holes from the valence band of the p-type material are injected into the active region. This process leads to a higher concentration of non-equilibrium carriers within the active region, which significantly enhances radiation recombination.

Despite the many advantages that TJs can offer, there are still challenges associated with the use of it, and the road for an optimal and definitive tunnel junction UV LED is under construction.

III.1.2. High-doping for tunnel junctions

The presence of degenerate doping, although not mandatory, can be advantageous in tunnel junctions LEDs by reducing the tunneling width, i.e. the effective distance that carriers need to tunnel through. This leads to an increase in the tunneling probability of carriers from one side of the junction to the other, which contributes to an enhanced current flow. The effects

of high Mg doping and the sources of donors commonly used in nitride tunnel junctions, namely Si and Ge will be discussed.

III.1.2.1. Mg doping

The p-doping of III-nitrides poses significant challenges, which becomes even more crucial when considering tunnel junctions that rely on high doping levels for efficient tunneling. It may seem counterintuitive considering that the ionization energy of Mg acceptors decreases steeply with higher acceptor concentrations N_A [37] as depicted in figure 1. Furthermore, the apparent dependence of the ionization energy with the Mg-acceptor concentration can be described by an acceptor level distribution, instead of a discrete energy level, which depends on the acceptor concentration. The formation of this broad band is the consequence of electrostatic interaction screening by impurities. The apparent acceptor ionization energy Ea decreases with the increase of the band width, i.e., with the increase of the acceptor concentration N_A [38].

This suggests the possibility of achieving p++ doping levels in tunnel junctions due to the reduced acceptor ionization energy. However, in reality, N_A struggles to surpass certain limits due to the high ionization energy of Mg acceptors in GaN and particularly in (Al,Ga)N. As a result, achieving significantly higher doping levels remains a challenge.

To enhance the concentration of free holes, one might consider increasing the level of Mg doping ($> 10^{20}$ cm^{-3}). However, heavy doping of GaN and (Al,Ga)N with Mg brings about several challenges. Firstly, the solubility of Mg in GaN is relatively low, reaching a maximum of $3x10^{20}$ cm^{-3} at a very low growth temperature of 550°C [39]. At higher temperatures commonly used for GaN growth, the solubility decreases, potentially leading to the formation of Mg precipitates [39]. Additionally, high levels of Mg doping have been found to cause polarity inversion in NH_3-MBE GaN:Mg [40] and pyramidal inversion domains in MOCVD GaN:Mg [41]. These defects cause a compensation of the p-type doping. Moreover, high concentrations of Mg decrease the formation energy of donor-like nitrogen vacancies, which in turn passivates the acceptors and reduces the concentration of free holes. Collectively, these issues further complicate the utilization of high Mg doping levels [42], [43].

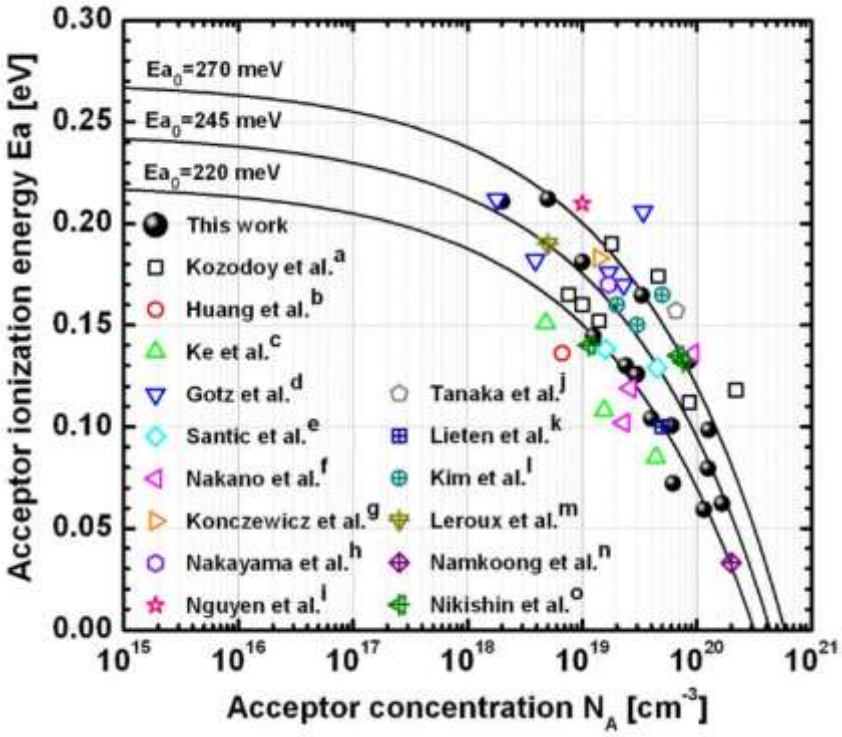

Figure 1: Relationship between acceptor ionization energy and acceptor concentration N_A extracted from Brochen et al. [37].

The difficulty of efficient p-type doping in GaN:Mg results in relatively high resistivity layers, and this is especially worse in (Al,Ga)N alloys, which negatively impact the injection efficiency. However, when using TJs, where both the top and bottom contacts are of n-type (figure 2), the electrical characteristics of the device are expected to be improved.

Figure 2: (Al,Ga)N TJ based LED structure.

III.1.2.2. Si doping

The most common n-type dopant for GaN is Si. N-doping poses fewer challenges compared to p-doping. Si acts as a shallow donor in GaN with an energy level of approximately 17 meV [43], [44], and its solubility in GaN is considered relatively high, reaching levels on the order of 10^{20} cm^{-3} [45]. Si has been employed as a source of donors in nitride materials, leading to high carrier densities of around 2 x 10^{20} cm^{-3} and to mobilities of around 70 cm^2/Vs at this carrier density. Moreover, the use of Si as a dopant has demonstrated low compensation levels, typically below 5%, resulting in resistivities as low as 3.5 x 10^{-4} Ωcm^{-2} [46].

Si is widely used as the standard dopant in the industry and in most research groups working on GaN and (Al,Ga)N. However, there are certain limitations associated with Si doping. In the case of (Al,Ga)N alloys, Si acts as a shallow donor for Al contents up to approximately 80%. Beyond this point, there is evidence from literature indicating a significant increase in the activation energy of Si donors (figure 3), which may be attributed to the formation of DX centers. These DX centers act as deep acceptors, compensating for the donors and reducing the concentration of free carriers. Their presence can be particularly detrimental to tunnel junctions, especially for shorter wavelength applications such as UV-C [45], [47].

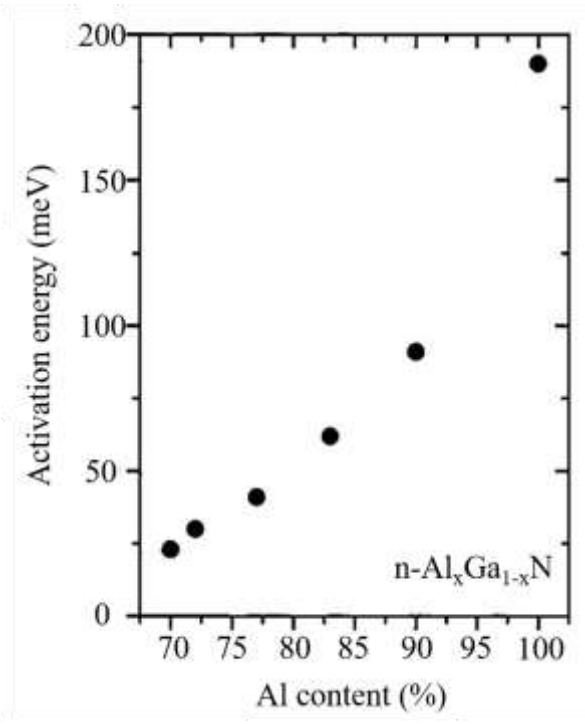

Figure 3: Si donor activation energy as a function of the Al content *x* in $Al_xGa_{1-x}N$ alloys [48].

Moreover, it has been observed that high Si doping levels (>$10^{19}cm^{-3}$) can induce tensile strain in the lattice, which becomes more pronounced as the doping level increases. This strain

negatively impacts the crystalline quality of the material and imposes limitations on the maximum thickness of highly doped Si layers [49]. The introduction of Si atoms, which are smaller than Ga, at high concentrations leads to a tensile strain in the lattice. Dadgar et al. have proposed that high Si doping levels also promote dislocation climb by the formation of SiN at the dislocation core. This process enhances vacancy formation, as Ga atoms can no longer be attached to these points in the lattice, a phenomenon known as involuntary SiN masking [50]. Moram et al. suggest that Si atoms hinder dislocation movement, creating "impurity atmospheres" that pin the dislocations and prevent them from relieving the in-plane biaxial stress by moving through the crystal lattice. In the absence of other stress relief mechanisms, this can ultimately lead to the cracking of epitaxial films once they exceed a critical thickness [51]. In order to achieve higher doping levels while maintaining structural quality, several research groups have explored alternative n-dopants such as Germanium (Ge).

III.1.2.3. Ge doping

Germanium (Ge) serves as an alternative n-dopant to silicon in GaN due to its shallow donor characteristics (with an ionization energy of 31 meV). One advantage of Ge is its closer atomic size to Ga compared to Si. This closer match suggests that Ge can occupy Ga sites in the lattice with less distortion to the network than Si. Even in samples with high densities of edge-type dislocations, Ge does not contribute to the dislocation climb effect, thereby avoiding the introduction of tensile strain to the lattice [50], [52].

MOCVD growth has demonstrated the capability to achieve high Ge incorporation levels up to 2 x 10^{20} cm^{-3} without compromising crystal quality. By utilizing high Ge molar flows during the growth process, the incorporation of Ge in GaN is effective and does not result in crystal degradation [53], [54].

It was demonstrated that the resistivity of highly Ge-doped GaN layers can be as low as 1.7 x 10^{-4} $\Omega.cm^2$ [55]. However, it should be noted that thicker layers (> 50 nm) of NH_3-MBE n+ GaN:Ge have exhibited rougher surfaces. The change in surface kinetics observed in these cases could be attributed to Ge segregation as the incorporation saturates or the formation of a surface Ge_XN_Y phase. Nevertheless, it is important to mention that TJ layers are typically much thinner, often not exceeding 20 nm. As a result, this change in growth kinetics is not expected to significantly impact the interface between the n+ and p+ layers, including the interlayers [56].

The research on highly Ge-doped (Al,Ga)N has been relatively limited compared to GaN. This disparity in research activity may be attributed to calculations made by different research groups which suggest that the formation of DX centers in Ge-doped (Al,Ga)N occurs at aluminum contents higher than 40% [57], [58]. This indicates that the formation of DX centers in Ge-doped (Al,Ga)N occurs at much lower aluminum contents compared to Si-doped (Al,Ga)N.

Furthermore, the inclusion of Ge in (Al,Ga)N with higher aluminum contents leads to the segregation of Ge and the formation of Ge clusters. This occurs due to the shorter bond length between Al and N in comparison to Ge-N and Ga-N bonds, causing Ge to be excluded in favor of forming AlN bonds. Although Ge concentrations as high as 10^{21} cm^{-3} can be achieved, the free carrier concentration significantly decreases with increased aluminum content, reaching 10^{18} cm^{-3} at an Al content of 65% [59], as depicted in figure 4. Despite the decrease in free carrier concentration with increased aluminum content, the tunability of dopant concentrations and profiles in Ge or Si-doped (Al,Ga)N materials allows for tailoring the conductivity of the tunnel junction to suit the intended application, making them viable options for n-type doping in tunnel junctions, especially when considering specific device design considerations and desired performance outcomes.

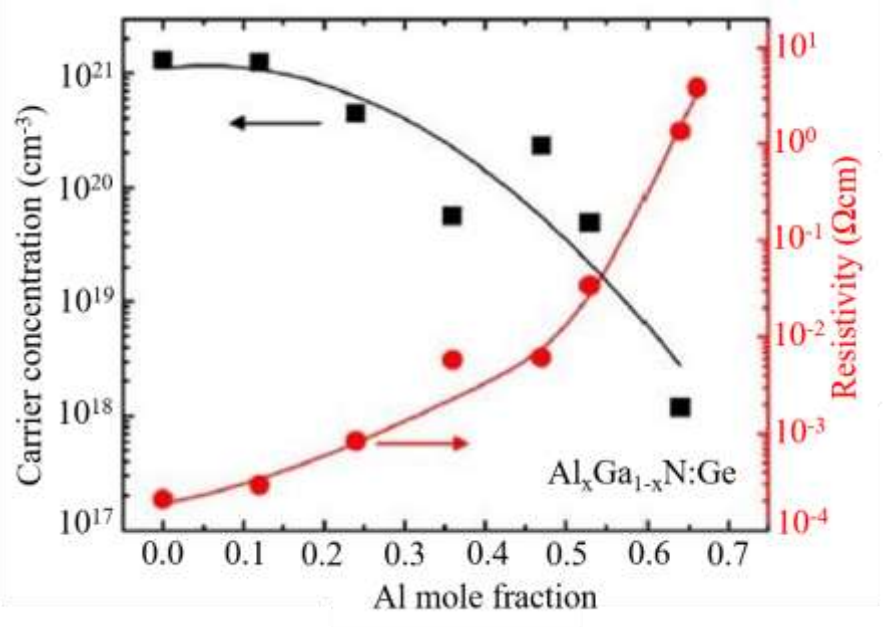

Figure 4: Carrier concentration and resistivity evolution as a function of Al mole fraction in Ge-doped $Al_xGa_{1-x}N$ alloys [59].

In this study, several practical considerations influenced the choice in using Si as the suitable choice for n-type doping in our (Al,Ga)N tunnel junction structures. The growth

conditions for Si doping by MBE are better understood and controlled, which leads to a more reliable and reproducible results. In addition, as opposed to Ge, Si has a smaller atomic radius and forms stronger bonds with N atoms in (Al,Ga)N, which reduces the tendency for segregation and clustering that can negatively affect material quality and device performance. Furthermore, Si-doped (Al,Ga)N is well-suited for integration with other III-nitride materials commonly used in LED and semiconductor device fabrication. This compatibility facilitates the design and fabrication of complex device structures. In addition, the process of incorporating Si as an n-dopant is more straightforward and predictable, leading to better control over the doping concentration and profile. This control is essential for achieving the desired electrical characteristics and device performance.

Overall, the decision to use Si is driven by the need to achieve reliable and high-performance tunnel junctions that are compatible with the requirements of (Al,Ga)N-based devices.

III.1.3. Tunnel junctions (Al,Ga)N-based UV LEDs

III.1.3.1. MBE full-growth of TJ (Al,Ga)N-based UV LEDs

In 2015, Zhang et al. from Professor Rajan's group at Ohio State University reported the first use of a tunnel junction on (Al,Ga)N-based UV LEDs. Their approach involved using an $Al_{0.3}Ga_{0.7}N$ tunnel junction with an $In_{0.25}Ga_{0.75}N$ interlayer on top of a UV LED consisting of three $Al_{0.2}Ga_{0.8}N$ quantum wells (QWs). The LED structures were grown using N_2 plasma-assisted MBE. The fabricated LEDs, with a size of 50 x 50 μm^2, exhibited uniform current spreading and emitted light at a wavelength of 327 nm (UV-A). The devices operated at a voltage of 6.5V with a current density of 1 kA/cm^2, producing an optical power of 0.6 mW at 20 mA and achieving a peak external quantum efficiency (EQE) of 1.5% [60].

Following this work, Prof. Rajan's group published a paper on the design of p-(Al,Ga)N cladding layers for UV-A TJ-LEDs. They proposed the concept of graded Al content profiles in the tunnel junction layers of a UV-B LED with a wavelength of 292 nm. The graded layers were designed to create a gradient in polarization, resulting in a three-dimensional negative polarization charge. This charge attracted a high density of free holes, thereby reducing the depletion barrier of the p+ (Al,Ga)N tunnel junction layer. The n+ and p+ layers were graded before and after the interlayer to enhance tunneling probability. It was observed that tunnel junctions with non-graded layers exhibited significantly higher tunneling resistances compared to the graded ones, highlighting the benefits of the three-dimensional polarization charges. However, the EQEs and WPEs (wall-plug efficiencies) of the devices were still not at the state-

of-the-art levels [61]. Two years later, the same research group published another report on a TJ-LED with a similar emission wavelength of 287 nm, but with optimized graded composition and contacts. These optimizations led to an improvement in the device performance, achieving a peak EQE of 2.8% and a WPE of 1.1% [62].

The same team also reported in 2017 the development of deep-ultraviolet (UV-C) tunnel junction UV LEDs using a full-MBE approach. They grew graded $Al_{0.75}Ga_{0.25}N$ tunnel junctions on (Al,Ga)N UV LEDs, which resulted in electroluminescence (EL) peaks at a wavelength of 257 nm. The graded contact layers played a crucial role in achieving low resistance Ohmic contacts with a resistance value of approximately 5×10^{-5} Ohms, eliminating the need for thermal annealing processes. The peak EQE achieved was 0.035% [63].

III.1.3.2. Hybrid growth of TJ (Al,Ga)N-based UV LEDs

MOCVD is the dominant growth method used in the conventional and UV LED industry. However, for the fabrication of LEDs with tunnel junctions, MOCVD is not considered the optimal technique. One of the main challenges is the re-passivation of Mg acceptors by hydrogen during the growth of the n-doped section of the tunnel junction, which limits the performance of the tunnel junction. This issue is of particular concern for UV LEDs due to the deeper activation energy of Mg acceptors in (Al,Ga)N and the resulting degradation of conductivity in p-(Al,Ga)N layers.

In 2014, Krishnamoorthy et al. proposed a hybrid growth method that combines MOCVD and MBE for tunnel junction-based LEDs. Initially, the regrowth surface after the active region was targeted because all-MOCVD-grown TJ LEDs were experiencing significant voltage drops across the tunnel junction, leading to considerable power losses in the LEDs. This issue primarily stemmed from challenges related to the activation of the buried p-type layers that were grown using MOCVD [64]. MBE-grown TJ LEDs, on the other hand, exhibited minimal bias or voltage drop when the LED operated in the forward direction. By utilizing MBE, they demonstrated a tunnel junction with exceptionally low on-resistance values found between 10^{-3} and 10^{-4} Ωcm^2 [65], [66]. Krishnamoorthy's work involved the integration of InGaN/GaN tunnel junctions into blue emitting LEDs (at 450 nm), resulting in a unique LED design that eliminated the need for a p-contact layer. Instead, they utilized a low spreading resistance n-GaN layer as the top contact layer. Their reported results indicated an operating voltage of 5.3 V at 100 mA, and this approach led to higher output power in TJ LEDs. This improvement was attributed to the reduced metal contact area on the top surface, made possible by the low spreading resistance of the upper n-type GaN contact layer [64]. However, in 2016,

Young et al. introduced a modification to this approach by placing the MBE regrowth after the p++GaN layer, resulting in the first hybrid tunnel junction (HTJ) structure [67]. The advantage that the hybrid growth method offered was that the growth parameters required for MBE growth of n++ (Al,Ga)N do not lead to the re-passivation of Mg acceptors. This distinction arose because the growth of GaN using NH_3 MBE occurred in an environment rich in hydrogen, although the hydrogen levels were much lower, by several orders of magnitude, compared to those observed during MOCVD growth. Consequently, NH_3 MBE resulted in the formation of high-quality, active p-GaN layers as part of the initial growth process [68], [69]. This characteristic facilitated the subsequent regrowth of n-type material on top of MOCVD grown p-type layers, a feature not typically achievable with MOCVD [67]. As a result, the p-(Al,Ga)N layers remain activated while the n-part of the tunnel junction is being grown. This allows for the activation of holes in the p-region and prevents the adverse effects on performance caused by the re-passivation of Mg acceptors.

By combining the benefits of MBE tunnel junction growth, which avoids Mg re-passivation, with the optimized quantum well structures achieved through MOCVD, the hybrid growth method offers a promising approach for fabricating tunnel junction-based LEDs with improved performance characteristics. This was demonstrated in CRHEA in the research work of Victor Fan Arcara et al. [70], where the HTJ growth mode was adopted. In this work, the growth of high Al content Ge-doped tunnel junction UV LEDs was also investigated. the enhancement of the hole injection efficiency and the improvement of the electrical behavior of the UV LEDs were achieved, leading to an optical power improvement factor of six for HTJ UV LEDs in comparison to standard UV LEDs, as shown in figure 5. However, it was also reported the challenges faced with low quality buffer layers having dislocation densities higher than 10^{10} cm^{-2}. The high dislocation densities of the buffer layers negatively affected the IQE of the HTJ UV LEDs, thus affecting the EQE [70].

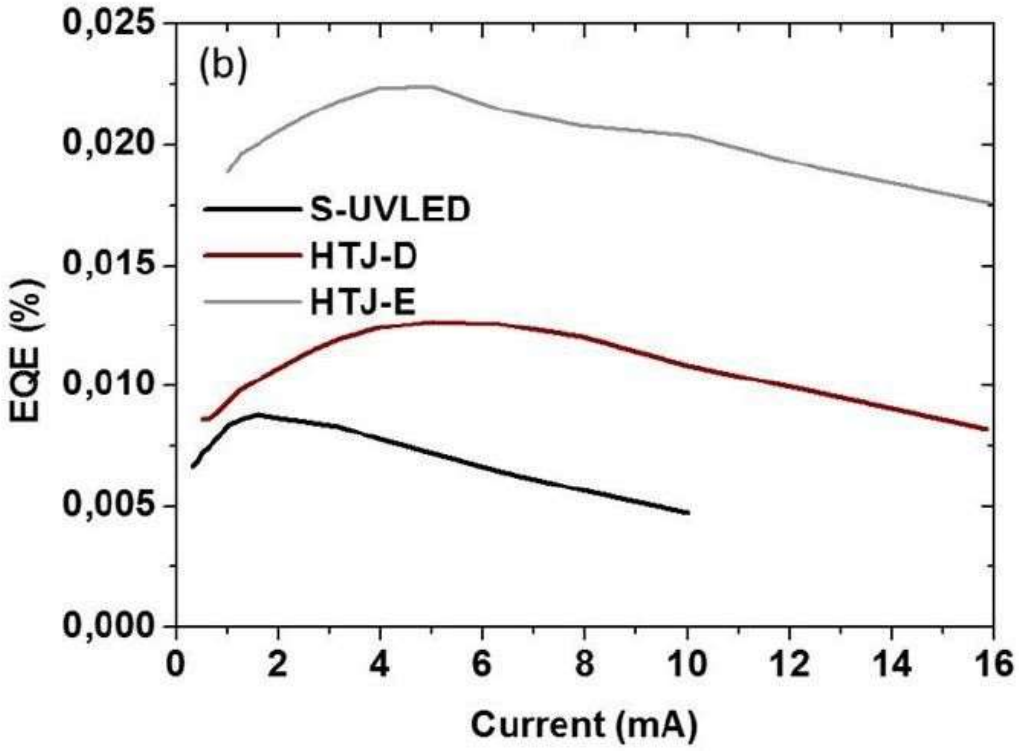

Figure 5: EQE (%) as a function of current (mA) for standard UV LED (S-UV LED) and hybrid tunnel junction (HTJ) UV LEDs [70].

In this thesis, and as discussed in chapter 2, one of our goals was the improvement of the AlN buffer layer by performing face-to-face high temperature annealing, which proved effective in significantly reducing the TDDs of the layer. This technique can be helpful in increasing the efficiency of TJ UV LEDs. Therefore, the next section of this chapter will concern the MOCVD growth of QWs-based standard (p-n) UV LEDs on annealed AlN PVD templates described in chapter 2. The electrical and optical characterizations will be discussed and the EQE will compared to the EQE of Dr. Fan Arcara's HTJ UV LEDs.

III.2. MOCVD growth of standard UV LEDs on annealed AlN PVD templates

The main goal of this section is to investigate the influence of the structural properties of the LED structures on the performances of UV LEDs. The structures were grown by MOCVD and compared to the initial studies in CRHEA reported in the PhD thesis of Victor Fan Arcara. To do so, we focused on the use of annealed AlN PVD templates grown on sapphire as substrates, and compared the results with the ones obtained with the direct growth on sapphire.

The LEDs structures were grown by Dr. Benjamin Damilano from CRHEA (Centre de Recherche sur l'Hétéro-Epitaxie et ses Applications) on annealed AlN PVD templates, as

discussed in Chapter 2, Part I. The growth process took place in a 7 x 2 in. Aixtron MOCVD reactor with a showerhead geometry (SHR). Trimethylgallium (TMGa) and triethylgallium (TEGa) were used as precursors for Ga, trimethylaluminium (TMAl) for Al, bis(cyclopentadienyl)magnesium (Cp_2Mg) for Mg, silane (SiH_4) for Si, and ammonia (NH_3) for N. Prior to growing the LED structures, the regrowth of an AlN layer on the high temperature annealed (HTA) AlN PVD templates was performed and investigated to optimize the growth conditions. A 1 µm thick layer of AlN was regrown under specific parameters: a growth temperature of 1325°C, a pressure of 25 mbar, and a growth speed of 13 nm/min. Following the regrowth, AFM measurements, performed by Aimeric Courville who is in charge of the AFM instruments, were conducted on areas of size (10 x 10) μm^2 and (1 x 1) μm^2. The results showed a smooth and uniform surface across the entire template, with a dislocation density in the 5 x 10^9 – 1 x 10^{10} cm^{-2} range. Figure 6 provides a visual representation of these findings.

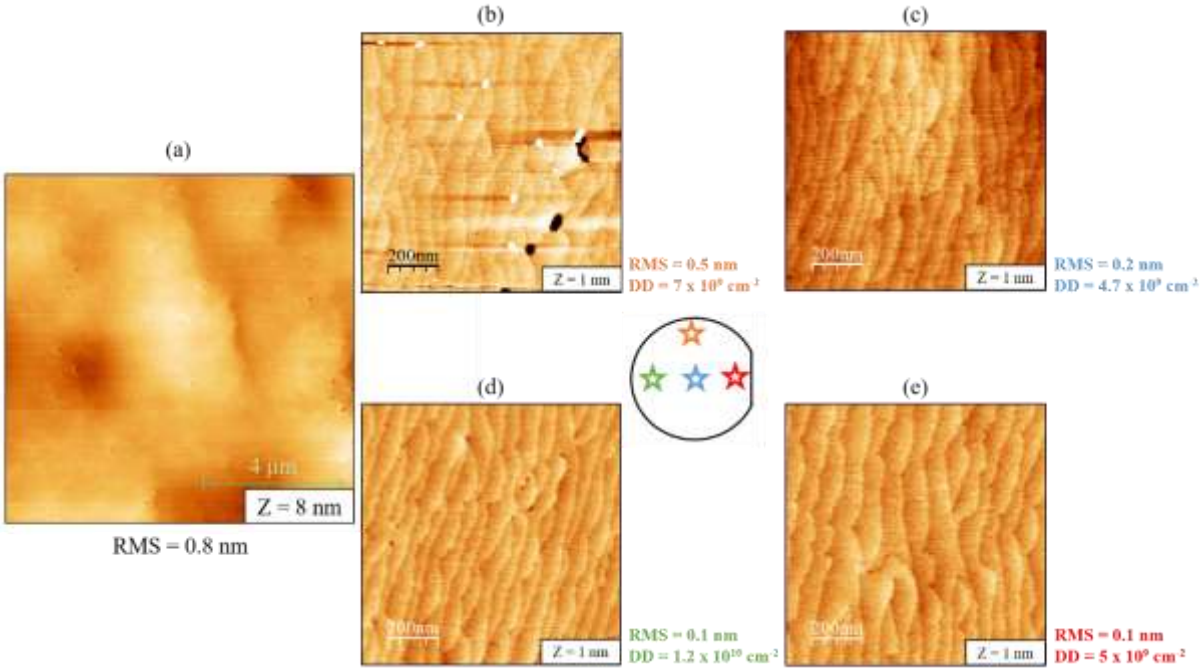

Figure 6: Atomic force microscopy images of annealed AlN PVD template after 1 µm AlN regrowth by MOCVD. (a) (10 x 10) μm^2 scan image, (b), (c), (d), and (e) are (1 x 1) μm^2 scan images of different zones on the wafer. The term Z represents the vertical scale and the variation in height in the AFM images, and its value is reported at the bottom right hand side of each image.

The growth of all LED structures began with the regrowth of a 200 nm thick layer of AlN. The crystalline quality of the AlN layer was studied by X-ray diffraction and showed FWHM values of 0.3° and 0.6° for the symmetric (0 0 0 2) and skew symmetric (1 0 −1 1) planes, respectively. The estimated threading dislocation densities (TDDs) from these XRD measurements coupled with the Dunn and Koch equation (see chapter 2 section II) were ~ 4 x

10^9 cm^{-2} and 3 x 10^{10} cm^{-2}, respectively. The growth conditions for this layer were a temperature of 1350°C, a pressure of 25 mbar, and a growth rate of 400 nm/h. The LED structures were divided into two series. The first series comprised three LED structures designed for UV-B emission, referred to as UVB-1, UVB-2, and UVB-3. The second series consisted of two LED structures intended for UV-C emission, known as UVC-1 and UVC-2.

III.2.1. UVB LEDs growth on annealed AlN PVD templates

In the first series of LED structures (UVB-1, UVB-2, and UVB-3), the main difference lies in the Cp_2Mg flow used for the doping of the (Al,Ga)N:Mg layer, which was varied to study its impact on LED power efficiency and electrical characteristics. It is expected that the p-type doping with Mg will result from a compromise: at low Mg concentrations (< 10^{19} cm^{-3}), the p-type doping level will be low and inefficient while at high Mg concentrations (> 10^{20} cm^{-3}), the p-type doping will be compensated by point defects and inverted pyramidal defects. Therefore, it is important to find the optimum Cp_2Mg flow that will give the highest (Al,Ga)N p-type doping and the maximum LED efficiency.

UVB-1 structure consisted of a 1 µm Si-doped $Al_{0.4}Ga_{0.6}N$ ([Si] = 1.3 x 10^{19} cm^{-3}) layer grown at a temperature of 1200°C, a pressure of 100 mbar, and a growth speed of 1.5 µm/h. Next, three [$Al_{0.31}Ga_{0.69}N$ (2 nm) / $Al_{0.48}Ga_{0.52}N$ (8 nm)] quantum wells were fabricated and followed by a 10 nm $Al_{0.7}Ga_{0.3}N$ electron-blocking-layer (EBL), a 25 nm p-$Al_{0.48}Ga_{0.52}N$ with a Cp_2Mg concentration of 80 cc, a 100 nm p-GaN and a 10 nm p++ cap of GaN. The UVB-2 and UVB-3 structures had identical structures as UVB-1 with the only difference being the Cp_2Mg concentration for the 25 nm p-$Al_{0.48}Ga_{0.52}N$ layer. The Cp_2Mg concentration was 160 cc, and 240 cc, for UVB-2 and UVB-3, respectively. The three UVB LED structures are illustrated in figure 7.

The cleanroom processing steps for fabricating the LED samples involved standard photolithography and reactive ion etching (ICP-RIE). The process, performed by Sébastien Chenot who is in charge of the clean room in CRHEA, started by creating rectangular mesas with a surface area of 0.0961 mm^2 (310 µm x 310 µm). After mesa formation, the contacts were deposited using e-beam evaporation. For the "n" bottom contacts, the contact stack consisted of Ti/Al/Ni/Au layers with thicknesses of 30 nm, 180 nm, 40 nm, and 200 nm, respectively. The Ti/Al/Ni/Au contacts were then annealed at a temperature of 750°C under N_2 for 30s.

For the "p" contact, a Ni/Au stack with thicknesses of 20 nm and 200 nm, respectively, was used. This stack ensures good electrical contact and low resistance to the p-type region of

the LED. Prior to depositing the p-contact, a semi-transparent Ni/Au electrode with thicknesses of 5 nm and 5 nm, respectively, was deposited on the entire emission surface and annealed using rapid thermal annealing under N_2 at 450°C for 5 min. This electrode was intended to induce homogeneous current spreading across the LED surface, ensuring uniform current distribution and improving device performance. After the deposition of contacts, the samples underwent annealing processes. These annealing steps help improve the electrical properties and adhesion of the contacts to the LED structure.

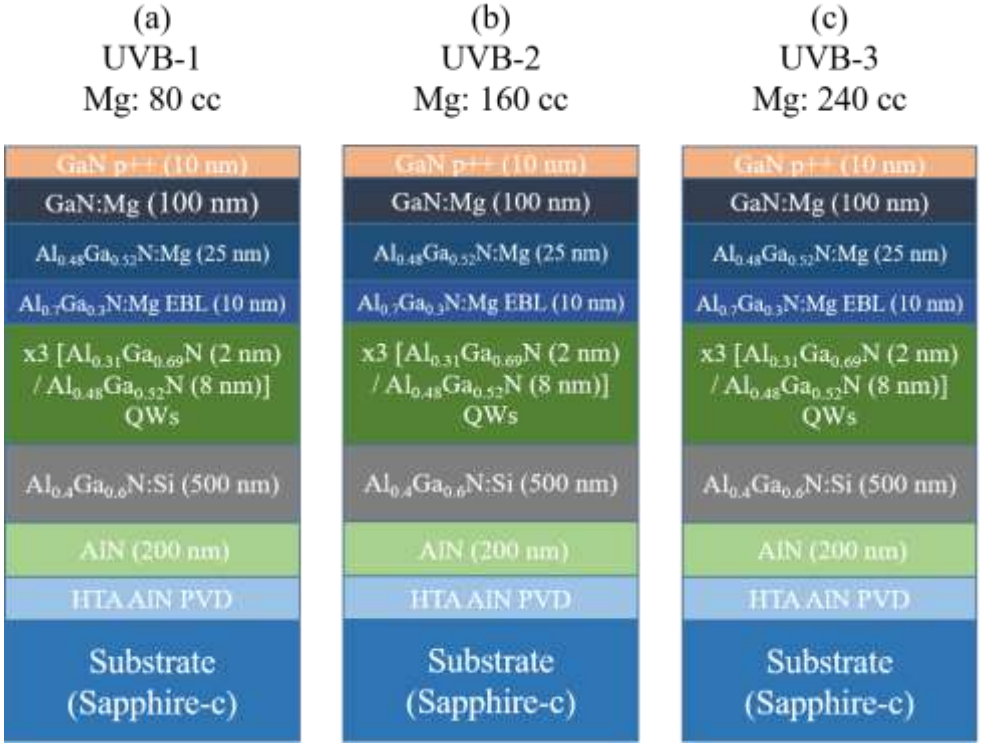

Figure 7: Schematic illustration of UVB LED structures. (a) UVB-1 with Mg: 80 cc, (b) UVB-2 with Mg: 160 cc, and (c) UVB-3 with Mg: 240 cc.

In figure 8(a), the electroluminescence (EL) intensity of the (310 x 310) μm^2 semi-transparent UVB LEDs is plotted as a function of the emission wavelength at a current of 20 mA. The UVB-1 LED exhibited an emission peak at 303 nm. The UVB-2 LED, on the other hand, had a slightly longer emission wavelength at 310 nm and its intensity was higher by a factor of 4 compared to UVB-1. The UVB-3 LED showed a dual-peak emission profile, with the first peak in the UVB region at 298 nm, which had the lowest intensity among the three UVB LEDs (lower by a factor of 12 compared to UVB-1). The second peak had a wider emission range, covering the UVA region from 315 nm to 400 nm. It is assumed that for UVB-3, the higher Mg doping in (Al,Ga)N leads to the creation of deep acceptor levels within the

bandgap, resulting in the broader emission peak with an emission at higher wavelengths, due to the increased concentration of holes occupying these deep acceptor states. These results suggest that the UVB-2 LED had the highest efficiency and intensity among the UVB LEDs, while UVB-1 LED exhibited a lower efficiency and UVB-3 LED showed a broader emission spectrum with relatively lower intensity in the UVB region. The current versus voltage (I-V) characteristics of the (310 x 310) μm^2 semi-transparent LEDs are shown in figure 8(b). At a current of 20 mA, the operating voltages were 10.8 V, 8.6 V, and 10 V, with a series resistances of 50 Ω, 32 Ω, and 31 Ω for the UVB-1, UVB-2, and UVB-3, respectively. Based on these results so far, it appears that the UVB-2 LED, with an Mg concentration of 160 cc, demonstrated the best performance in terms of electrical and optical properties. On the other hand, the UVB-1 LED, with an Mg concentration of 80 cc, exhibited the poorest performance, indicating that the Mg concentration has a strong impact on the overall performance of the LEDs. As anticipated, there is an optimum in the Mg flow to get the best electrical properties.

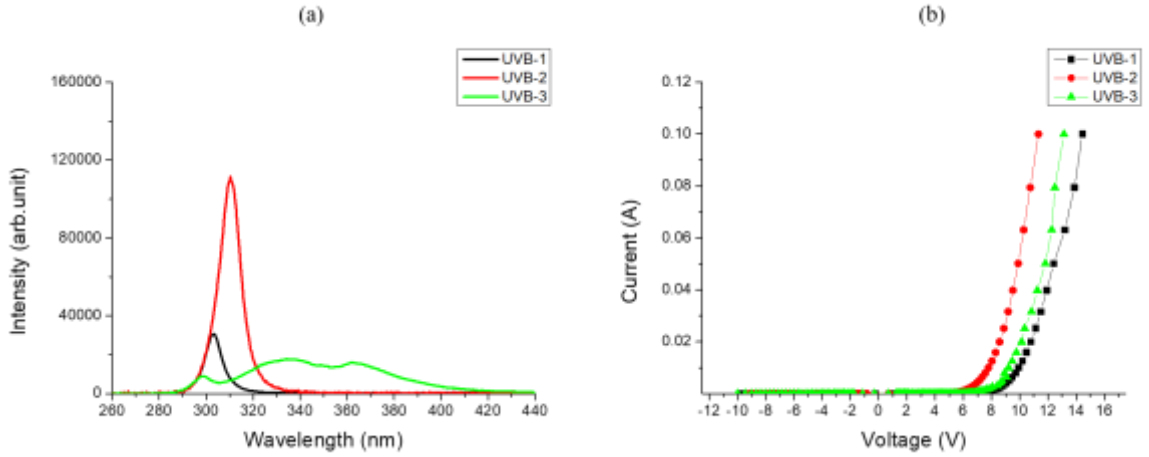

Figure 8: Electroluminescence (EL) intensity as a function of wavelength emission (a) and current vs voltage (I-V) curves (b) of UVB-1, UVB-2, and UVB-3.

The output power and external quantum efficiency (EQE) were also measured as a function of the current for the three LEDs (Figure 9 (a) and (b)). At a current of 20 mA, the light output power of the UVB-1 is 0.03 mW against 0.23 mW and 0.08 mW for UVB-2 and UVB-3, respectively. The peak external quantum efficiencies are 0.04%, 0.28% and 0.11% respectively for UVB-1, UVB-2, and UVB-3. The Cp_2Mg concentration variation in the p-$Al_{0.48}Ga_{0.52}N$ layer of the LEDs has shown its impact on the overall performance of the devices.

The results indicate that the choice of the Mg doping concentration plays a crucial role in determining the electrical and optical efficiency of the LED. The LED with a low Mg concentration (80 cc) exhibited degraded electrical and optical performance. This suggests that

the low concentration of Mg may not provide sufficient hole injection into the active region, leading to lower carrier recombination and reduced light emission. As a result, the LED's efficiency is compromised. On the other hand, the LED with a high Mg concentration (240 cc) showed better performance compared to the low concentration case. However, it did not reach optimal efficiency levels. This could be attributed to potential adverse effects associated with excessively high Mg concentrations, such as increased defect density, carrier trapping, or non-uniform doping profiles. The LED with an Mg concentration of 160 cc demonstrated optimal performance in terms of both electrical and optical efficiency. This indicates that the chosen doping concentration provided a suitable balance between efficient hole injection, reduced resistivity, and improved carrier recombination in the active region. As a result, this LED achieved the best overall performance among the tested variations. These results highlight the importance of carefully optimizing the Mg doping concentration in the p-AlGaN layer to achieve optimal device performance, balancing the trade-off between hole injection efficiency, material quality, and carrier recombination processes.

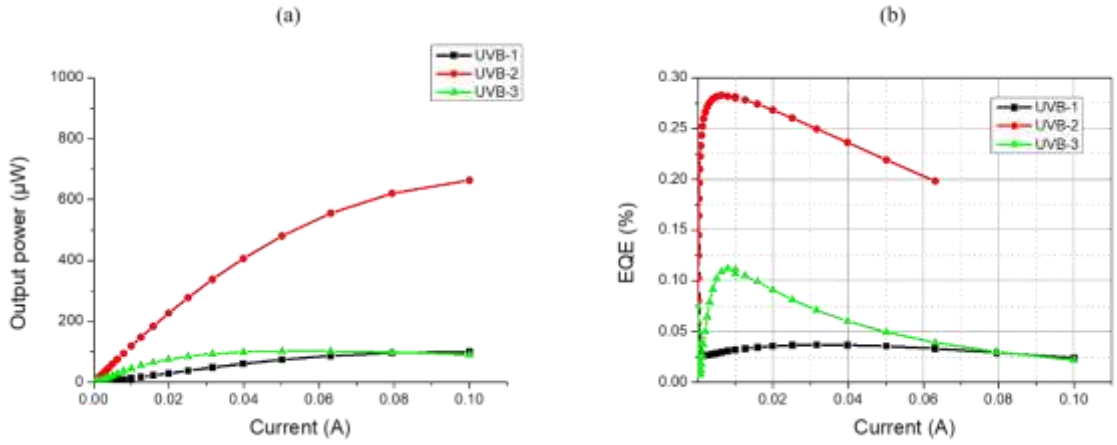

Figure 9: Optical power as a function of current (a) and External Quantum Efficiency as a function of current (b) for UVB-1, UVB-2, and UVB-3 LED devices.

In a next step, in order to study the impact of different contacts on the EQE, we conducted measurements of the backside emission through the sapphire substrate for the UVB-2 LED structure. Specifically, we measured the EQE using two different p-contacts. The first p-contact had a thin Ni/Au with thicknesses of 5 nm and 5 nm, respectively. The second p-contact had a thicker Ni/Au with thicknesses of 20 nm and 200 nm, respectively. By comparing the EQE values obtained for these two cases, we observed an increase in EQE. For the UVB-2 LED with the semi-transparent p-contact using thin Ni/Au, the maximum measured EQE was 0.29%. However, when using the semi-transparent p-contact with thick Ni/Au, the maximum

measured EQE improved to 0.32%. This represents an increase of approximately 10% in the EQE, as shown in figure 10.

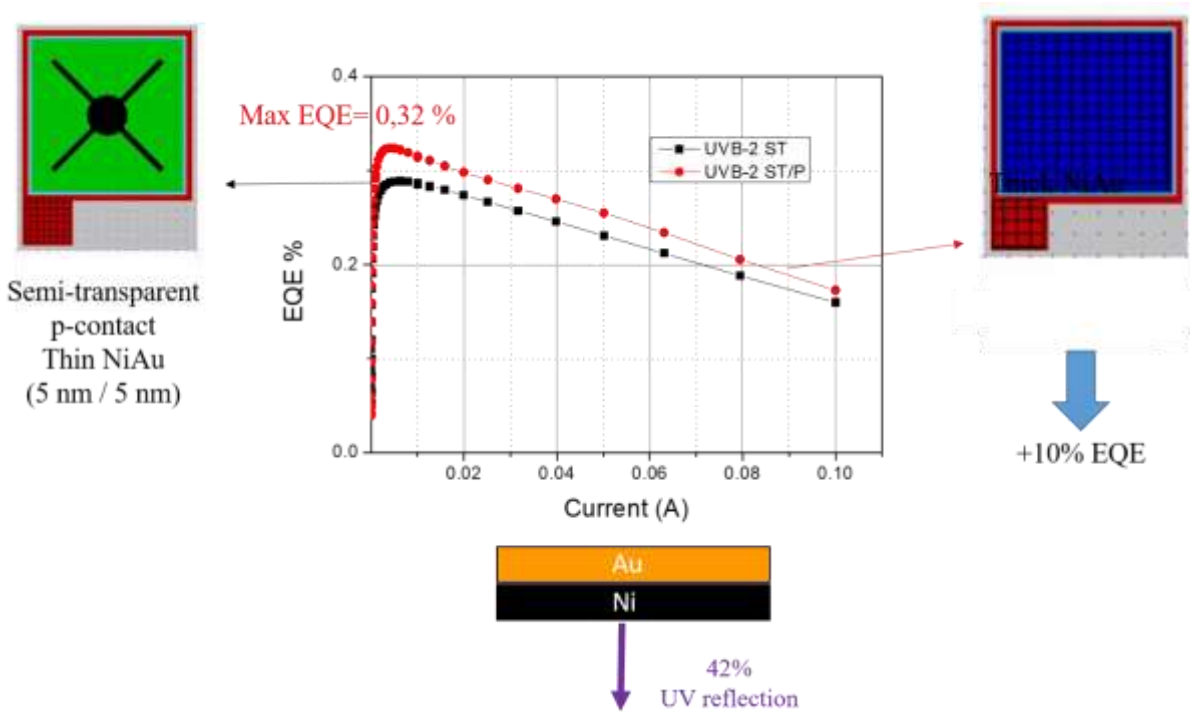

Figure 10: EQE as a function of current for semi-transparent thin Ni/Au and thick Ni/Au contacts.

The thin Ni/Au contact has a limited thickness, allowing some UV light to pass through and escape from the LED. However, when a thicker Ni/Au contact is used, it functions as a more effective reflector, redirecting a greater amount of generated photons out of the LED structure through the sapphire substrate. This helps to increase the overall efficiency of light extraction. Note that the reflectivity of Ni/Au is limited in the UV. It is only 42% at the emission wavelength of these LEDs (300-310 nm). The use of a metal with a higher reflectivity would improve the light extraction efficiency. The best choice for UV would be Al, which gives a reflectivity of more than 90% but its work function is not adapted for p-type contact on (Al,Ga)N. On the other hand, Al can constitute a good ohmic contact on n-AlGaN. Adding a TJ on the LED would give a top n-(Al,Ga)N layer and therefore would be compatible with a highly reflecting Al-based metallic contact layer.

It is worth noting that the p-GaN layer in the LED strongly absorbs UV light, which contributes to a decrease in the LED's EQE. Replacing the p-GaN layer with an n-(Al,Ga)N TJ, the LED can reduce the absorption losses, and improve both the carrier injection and light extraction thereby leading to a higher EQE compared to using a p-GaN layer.

III.2.2. UVC LEDs growth on annealed AlN PVD templates

The UVC-1 structure of the UVC LED series consisted of a 1060 nm Si-doped $Al_{0.9}Ga_{0.1}N$ layer (with [Si] = 1 x $10^{19}cm^{-3}$). The growth conditions for this layer included a growth temperature of 1200°C, a pressure of 100 mbar, and a growth speed of 1.5 µm/h. Following this layer, there were three quantum wells with a composition of [$Al_{0.45}Ga_{0.55}N$ (2 nm) / $Al_{0.65}Ga_{0.35}N$ (8 nm)]. These quantum wells were then followed by a 10 nm p-$Al_{0.8}Ga_{0.2}N$ EBL, a 25 nm p-$Al_{0.65}Ga_{0.35}N$ layer with a Cp_2Mg concentration of 130 cc, a 100 nm p-GaN layer, and a 10 nm p++ cap of GaN. The UVC-2 structure consisted of a 1060 nm Si-doped $Al_{0.54}Ga_{0.46}N$ layer (with [Si] = 1 x $10^{19}cm^{-3}$). Similarly to UVC-1, the growth conditions for this layer were a growth temperature of 1200°C, a pressure of 100 mbar, and a growth speed of 1.5 µm/h. Following the Si-doped layer, there were three quantum wells with a composition of [$Al_{0.4}Ga_{0.6}N$ (1.6 nm) / $Al_{0.57}Ga_{0.43}N$ (7.2 nm)]. These quantum wells were then followed by a 10 nm p-$Al_{0.69}Ga_{0.31}N$ EBL, a 25 nm p-$Al_{0.57}Ga_{0.43}N$ layer with a Cp_2Mg concentration of 230 cc, a 100 nm p-GaN layer, and a 10 nm p++ cap of GaN. Both UVC LED structures are depicted in figure 11. It is important to highlight that the Mg concentration remained unchanged, and both UVC-1 and UVC-2 structures featured an equal Mg concentration of approximately 10^{19} cm^{-3}. However, the modifications were made on the growth rate and the Mg flow to ensure the maintenance of this consistent Mg concentration for both structures that present different (Al,Ga)N compositions.

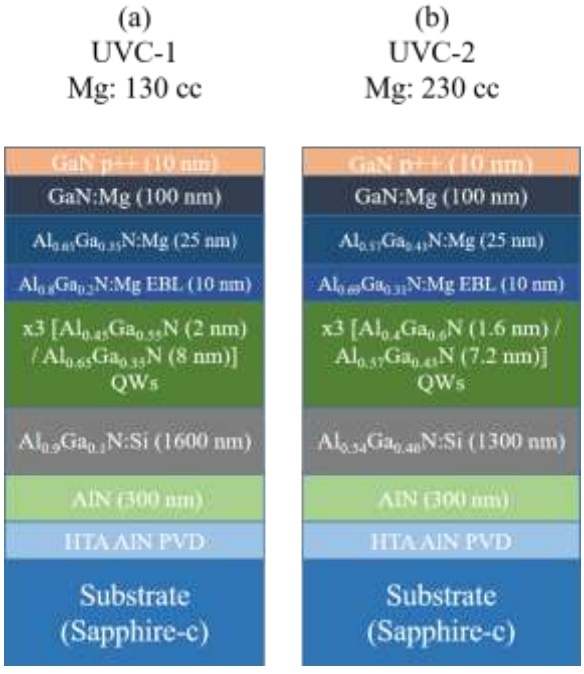

Figure 11: Schematic illustration of UVC LED structures. (a) UVC-1 with Mg: 130 cc, and (b) UVC-2 with Mg: 230 cc.

Figure 12(a) illustrates the EL emission of the (310 x 310) μm^2 semi-transparent LEDs at 20 mA for both UVC LEDs. The UVC-1 LED exhibits an emission peak at 263 nm. On the other hand, the UVC-2 LED has an emission wavelength of 279 nm and an emission in the UVB at 316 nm. We attribute the observed broad peak emission in the UVB to deep acceptor levels in the doped (Al,GaN) layers. Figure 12(b) displays I-V characteristics of the semi-transparent UVC LEDs with dimensions of (310 x 310) μm^2. At a current of 20 mA, the UVC-1 LED had an operating voltage of 18 V with a series resistance of 124 Ω, while the UVC-2 LED had an operating voltage of 10.5 V with a series resistance of 27 Ω.

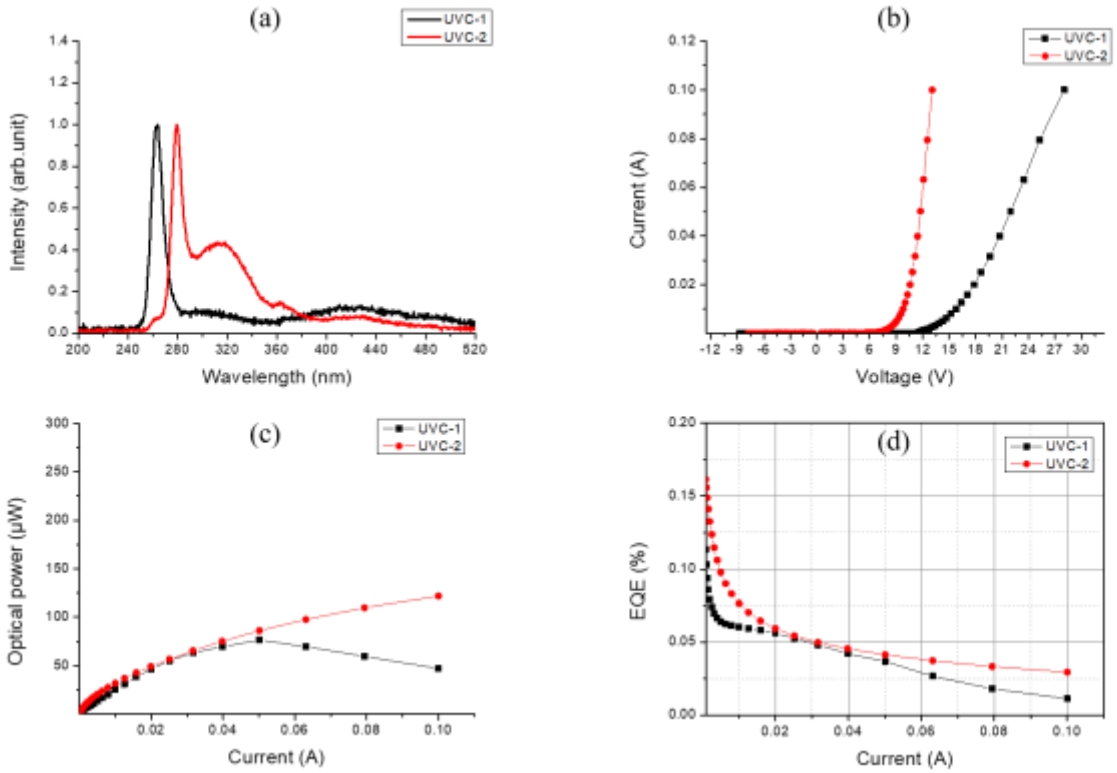

Figure 12: (a) Electroluminescence (EL) intensity as a function of wavelength emission at an injected current of 20 mA, (b) current vs voltage (IV), (c) optical power as a function of current, and (d) External Quantum Efficiency as a function of current curves for UVC-1 and UVC-2.

In terms of light output power, as shown in figure 12(c), the UVC-1 LED emitted a power of 46 µW at a current of 20 mA, whereas the UVC-2 LED had a slightly higher output power of 48.5 µW. Furthermore, figure 12(d) presents the peak EQE for both UVC LEDs. The UVC-1 LED exhibited a peak EQE of 0.11%, while the UVC-2 LED showed a higher peak EQE of 0.16%. These results demonstrate that the UVC-2 LED outperformed the UVC-1 LED in terms of operating voltage, light output power, and EQE. The increase in Al content in the UVC-1 LED to reach shorter wavelengths came with an increase in the activation energy (E_a) of (magnesium) Mg acceptors [36]. This rise in E_a had a cascading effect on the UVC-1 LED's

performance. Firstly, it led to a decrease in hole concentrations within the p-type layers, resulting in an overall reduction in the LED's electrical conductivity. Furthermore, the low carrier concentrations caused an increase in electrical resistance within the p-type layers of the LED structure. Consequently, this led to higher voltage drops across these layers, thereby decreasing the overall electrical efficiency of the LED. The decline in hole concentration also had implications for hole injection effectiveness, impacting the radiative recombination efficiency and reducing the LED's optical performance.

Figure 13 gives the EQE values for TJs UV LEDs achieved in the thesis of Dr. Victor Fan Arcara, where he demonstrated enhanced electrical and optical performances of TJ UV LEDs over standard UV LEDs thanks to the enhancement of the hole injection through the use of TJs. The thesis also highlighted that the low quantum efficiency values in UV LEDs were primarily attributed to the quality of the AlN buffer layers used, which had high threading dislocation densities (TDDs) larger than 10^{10} cm^{-2} [70]. In this work, we were able to achieve a significantly higher EQE value, specifically with the UVB-2 LED, which was ten times higher than the highest EQE value reported for TJ UV LEDs grown on AlN MOCVD, as depicted in figure 13. We attribute this result mainly to the improved crystalline quality; indeed, the dislocation density for the best AlN template used to fabricate the UVB-2 LED sample is 2 – 3 x $10^{9}cm^{-2}$. The findings suggest that utilizing TJs on annealed AlN templates holds promise for further enhancing the EQE values of future UV LEDs, surpassing the limitations encountered in previous works using AlN MOCVD growth and potentially achieving even higher levels of efficiency.

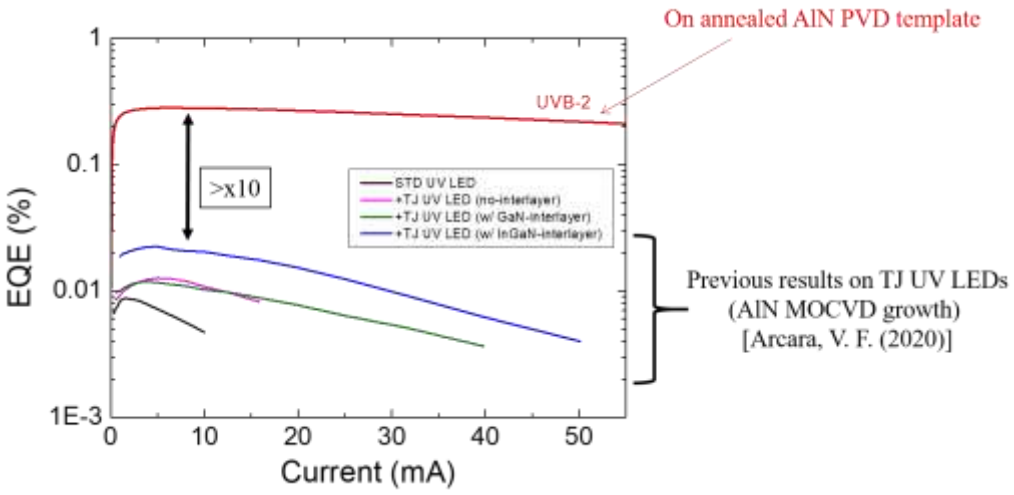

Figure 13: External quantum efficiency (EQE) values as a function of current obtained in previous work on TJ UV LEDs grown on AlN by MOCVD [70] versus EQE value obtained in this work on standard UV LED grown on annealed AlN PVD template.

III.3. MBE growth of standard and TJ QDs-based UV LEDs

In this section, we will focus on two main aspects. Firstly, we will examine the potential of $Al_yGa_{1-y}N$ QDs grown on $Al_{0.7}Ga_{0.3}N$ (0 0 0 1) templates as active regions for deep UV LEDs. By varying the Al concentration, we observe a broad range of photoluminescence spectra spanning from the ultraviolet A (UVA) to the ultraviolet C (UVC) regions. To fabricate LED structures, we utilize three to five planes of $Al_yGa_{1-y}N$ QDs grown by MBE. We conduct current-voltage measurements and thoroughly investigate the emission characteristics of these LEDs at varying current densities. Specifically, we fabricate LEDs emitting in the UVB and UVC regions and present their main electro-optical characteristics, such as optical power and external quantum efficiency.

In the second part, we shift our focus to the growth of TJ UV LEDs using MBE, aiming to enhance non-equilibrium hole injection and improve the overall injection efficiency. We discuss the improved electrical and optical performances resulting from this approach and compare them to the standard LEDs fabricated in the first part. We also highlight the significantly higher EQE achieved in the TJ UV LEDs and delve into a detailed analysis of their superior performance.

III.3.1. Standard QDs-based UV LEDs

The heterostructures were fabricated using MBE in a RIBER 32 reactor. The growth was performed on c-plane sapphire substrates, with AlN buffer layers (BL) acting as the foundation. NH_3 was used as the nitrogen source in combination with solid sources for Ga, Al, Si, and Mg. However, during the fabrication of $Al_yGa_{1-y}N$ QDs, a radio frequency (RF) plasma cell with N_2 gas was used instead of NH_3. The AlN BL was grown in a two-step process. First, a nucleation layer of 3 nm thickness was deposited at 500°C, followed by a 130 nm thick layer grown at 1000°C, following the conditions described in a previous study [71]. Subsequently, a 700 nm thick Si-doped $Al_{0.7}Ga_{0.3}N$ layer with a Si concentration of approximately 10^{19} cm^{-3} was deposited at 870°C. The LED active region consisted of five planes of $Al_yGa_{1-y}N$ QD separated by $Al_{0.7}Ga_{0.3}N$ cladding layers. The LED structures with different Al concentrations for the $Al_yGa_{1-y}N$ QD (y = 0.1, 0.2, 0.3, or 0.4) were investigated. After depositing a 2 nm thick $Al_yGa_{1-y}N$ layer, a post-growth annealing step was performed to enhance QD shape and size uniformity and prevent the formation of elongated QDs [72], [73]. The results discussed here have been presented at SPIE OPTO Conference, San Francisco (2021) [74].

Figure 14 displays AFM images of reference samples, including an AlN BL, an $Al_{0.7}Ga_{0.3}N$:Si layer, and $Al_yGa_{1-y}N$ QDs. The AFM images reveal smooth surfaces for both AlN and $Al_{0.7}Ga_{0.3}N$:Si, with root mean square (RMS) roughness values of 1.3 nm and 0.3 nm, respectively, for AlN, and 1.8 nm and 0.4 nm, respectively, for $Al_{0.7}Ga_{0.3}N$:Si, on surface areas of (10 x 10) μm^2 and (1 x 1) μm^2. The AlN BL surface does not exhibit any distinct features, while the surfaces of $Al_{0.7}Ga_{0.3}N$:Si show monoatomic steps oriented along the <1 1 −2 0> directions. The AFM image in figure 14(c) specifically focuses on $Al_yGa_{1-y}N$ QDs with y = 0.2. Based on the AFM measurements, QD densities ranging between (3 - 6) x 10^{11} cm^{-2} have been determined. These high QD densities are attributed to the low growth temperature of 720°C during the deposition of $Al_yGa_{1-y}N$, which leads to a low diffusion length of Ga and Al adatoms [75], [76]. Furthermore, the lateral dimensions of the QDs typically range between 5 and 15 nm, while their heights range between 1.5 and 2.5 nm.

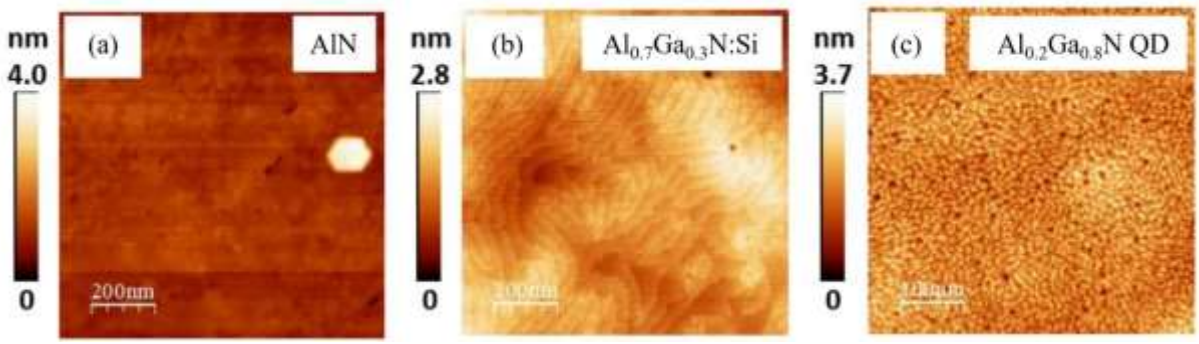

Figure 14: AFM images of: (a) AlN BL grown on sapphire c-plane substrate; (b) $Al_{0.7}Ga_{0.3}N$:Si grown on AlN / sapphire; (c) $Al_{0.2}Ga_{0.8}N$ QDs grown on $Al_{0.7}Ga_{0.3}N$ / AlN / sapphire [74].

Following the annealing step, a 10 nm thick Mg-doped $Al_{0.8}Ga_{0.2}N$ electron blocking layer and a 10 nm thick Mg-doped $Al_{0.7}Ga_{0.3}N$ layer were grown at 820°C. The structure was completed with a 30 nm thick Mg-doped GaN contact layer at 780°C, containing a Mg concentration of approximately 5 x 10^{19} – 1 x 10^{20} cm^{-3}. The LED structure is depicted in figure 15.

For the fabrication of LED structures with different $Al_yGa_{1-y}N$ QD active regions, clean room processes involving photolithography and electron cyclotron resonance reactive ion etching were employed. The LED mesas were square-shaped with dimensions of (310 x 310) μm^2. A thin semi-transparent Ni/Au (5/5 nm) layer served as the current spreading layer, followed by a Ni/Au (20/200 nm) contact as the top electrode connected to the p-GaN layer. The contact on the n-$Al_{0.7}Ga_{0.3}N$ layer consisted of a stacking of Ti/Al/Ni/Au (30/180/40/200 nm). The LED devices were characterized at room temperature by measuring their I-V

characteristics and EL properties. The EL measurements were performed from the sapphire side of the LED, with the emitted light collected through a UV-grade optical fiber connected to a linear CCD spectrometer featuring a spectral resolution of 2.5 nm. The optical power (P_{opt}) was measured from the backside of the devices using a calibrated UV-enhanced Si photodiode.

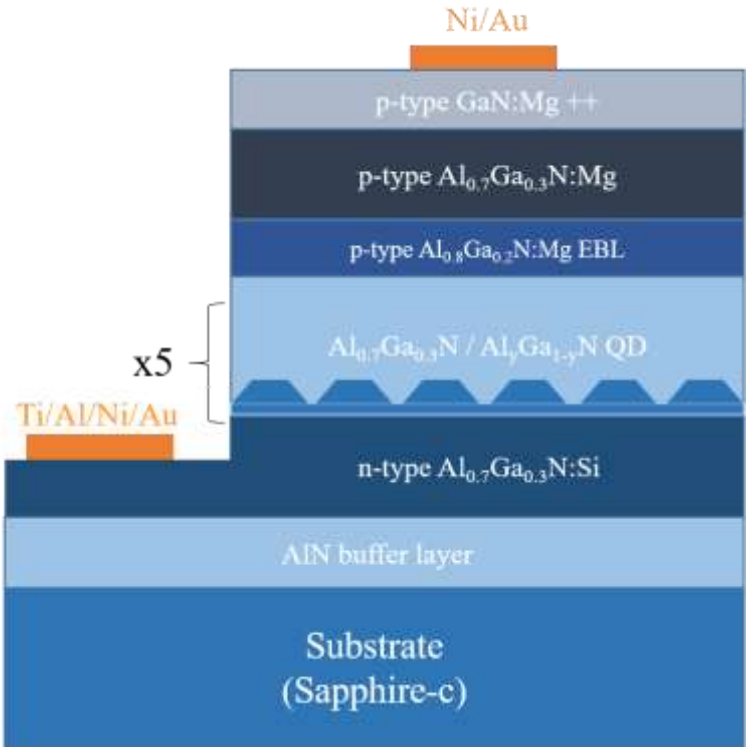

Figure 15: Schematic illustration of the $Al_yGa_{1-y}N$ QD-based UV LEDs structures grown on c-sapphire substrates.

Figure 16 presents PL measurements of reference $Al_yGa_{1-y}N$ QDs samples compared with GaN QDs. The PL measurements were conducted using a frequency-doubled Ar laser excitation source at 244 nm. The emission of $Al_yGa_{1-y}N$ QDs exhibits a significant shift towards shorter wavelengths as the Al concentration (y) increases. Specifically, $Al_{0.1}Ga_{0.9}N$ QDs emit in the range of 320-340 nm, $Al_{0.2}Ga_{0.8}N$ QDs emit between 310-330 nm, $Al_{0.3}Ga_{0.7}N$ QDs emit in the range of 290-320 nm, and $Al_{0.4}Ga_{0.6}N$ QDs emit between 260-290 nm. In contrast, GaN QDs demonstrate emission in the near UV range, spanning from 370-400 nm, and extending into the visible blue range from 400 to 480 nm [76], [77]. It is evident that the influence of the internal electric field (Fint) and the associated quantum confined Stark effect (QCSE) is more pronounced in GaN QDs. This effect is due to the larger lattice mismatch with the $Al_xGa_{1-x}N$ cladding layer, resulting in an increased Fint and a significant red-shift of the PL emission, surpassing the GaN band gap wavelength (approximately 360 nm at room temperature) [78]. Consequently, GaN QDs exhibit a much broader PL peak with full width at half maximum

(FWHM) values typically ranging from 300-400 meV, compared to $Al_yGa_{1-y}N$ QDs, which have FWHM values in the range of 150-200 meV. Despite the alloy disorder during $Al_yGa_{1-y}N$ growth [79], [80] and the inhomogeneity in QD sizes (heights), which lead to variations in the QD band structure and confinement energies, the internal quantum efficiencies of $Al_yGa_{1-y}N$ QDs were determined to be above 10%. This determination was based on time-resolved PL measurements at low temperature (8K) and temperature-dependent PL measurements ranging from 8K to 300K. Notably, these high quantum efficiencies were achieved despite the presence of a very high TDDs in the heterostructures, estimated to be around 5 x 10^{10} cm^{-2} [81].

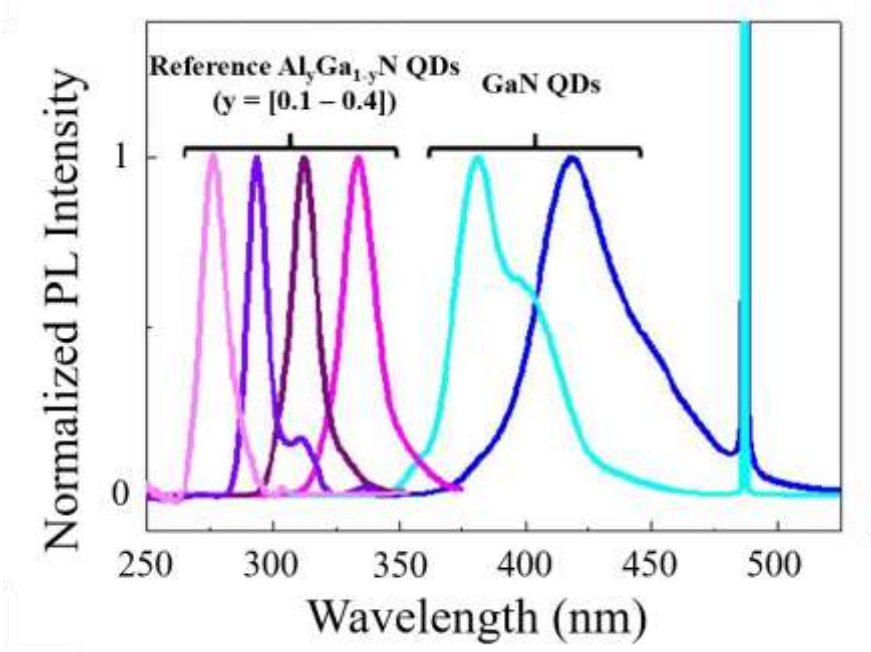

Figure 16: PL spectra of reference $Al_yGa_{1-y}N$ QDs and GaN QDs, with y varying from 0.1 to 0.4, grown on $Al_{0.7}Ga_{0.3}N$ (0 0 0 1) cladding layers. The sharp peak emission at 488 nm is the excitation laser (frequency-doubled Ar) second order line emission [74].

In Figure 17(a), an I-V characteristic is presented, demonstrating a diode behavior. The LED exhibits an operating voltage of 13 V at a current of 20 mA, and a series resistance value of 50 Ω. The average voltage range for most of the LEDs at 20 mA falls between 10 and 15 V, with series resistances ranging from 40 to 60 Ω. Figure 17(b) displays the EL spectra of three devices with different QD active regions. The EL spectra exhibit a single peak, which originates from the emission of the QDs. The maximum EL intensities are observed at wavelengths of 326 nm, 306 nm, and 269 nm for LEDs with QD nominal compositions of $Al_{0.1}Ga_{0.9}N$, $Al_{0.2}Ga_{0.8}N$, and $Al_{0.3}Ga_{0.7}N$, respectively. As expected, the LEDs with higher Al concentrations in the QD active regions emit at shorter wavelengths in the deeper UV range. However, it is worth noting that the emission from the $Al_{0.3}Ga_{0.7}N$ QD is found at a much shorter wavelength than

anticipated based on the PL measurements performed on reference structures. The main reason for the energy shift can be attributed to the fact that the PL measurements have been done on samples made of one (Al,Ga)N QD plane whereas the EL measurements have been performed on samples with multi-QD planes (five (Al,Ga)N QD planes). This multi-planes growth leads to an increase of the QDs size and composition dispersion, as also evidenced by the increase in the EL spectra FWHM values (up to 500 meV from EL measurements compared to 200 meV found for single QD planes PL measurements).

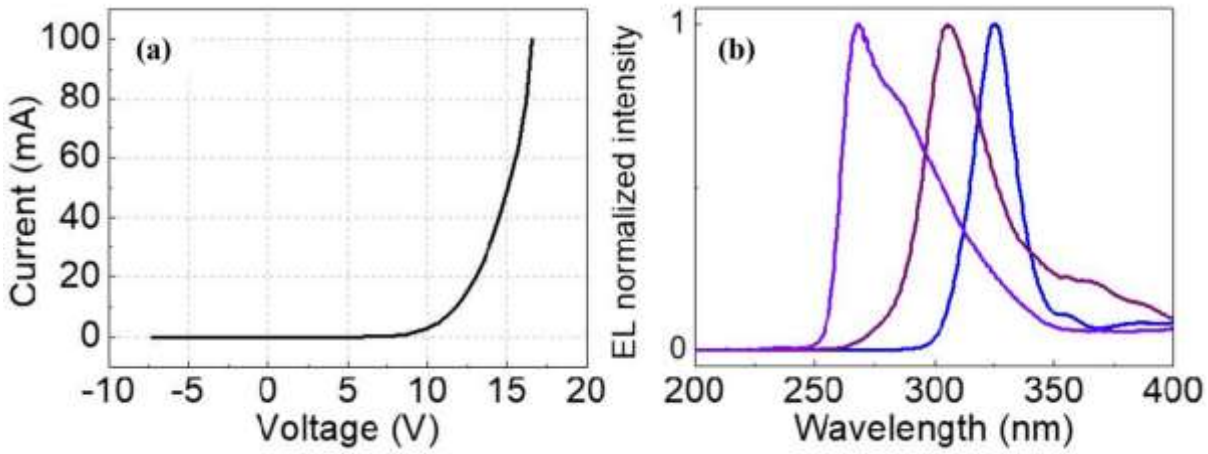

Figure 17: I-V characteristic of an $Al_{0.7}Ga_{0.3}N$ based QD-LED showing a rectifying behavior with a voltage at around 13 V at 20 mA. (c) EL spectra (normalized intensity) at an input current of 20 mA of 3 different LED emitting in the UVA, UVB and UVC regions between 340 nm and 265 nm [74].

In Figures 18 and 19, the main characteristics of the QD-based UV LED are summarized for the specific case of an active region consisting of $Al_{0.2}Ga_{0.8}N$ QDs. Similar trends are systematically observed for all the devices made of (Al,Ga)N QD active regions, as described elsewhere [76], [82]–[85]. Figure 18(a) shows that the LED emission strongly shifts into the UV region at shorter wavelengths as the input current density (J) increases. The emission wavelength decreases from 349 nm to 318 nm with increasing current density. Additionally, Figure 18(b) demonstrates that the full width at half maximum (FWHM) of the EL spectra is significantly reduced as the current density increases. The FWHM decreases from 63 nm to 31 nm, indicating a narrower spectral width of the emitted light. In these measurements, the wavelength is calculated as the arithmetic mean between the two wavelengths values measured at the full width at half maximum of each EL spectrum.

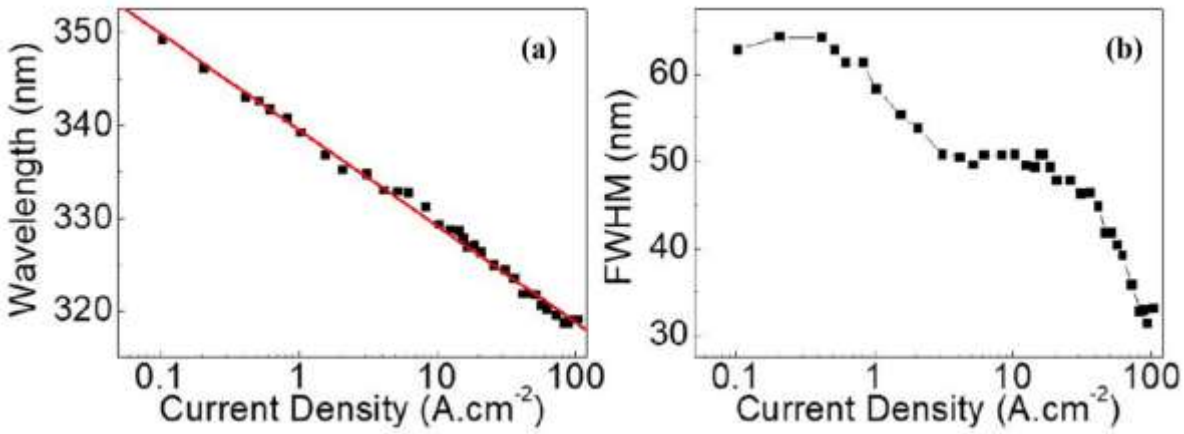

Figure 18: EL characteristics of the $Al_{0.2}Ga_{0.8}N$ QD-based LED. (a) Wavelength emission plotted as a function of the current density. The experimental measurements are represented by black squares, and the wavelength variation as a function of the current density is emphasized by the red line. (b) EL peak's FWHM variation as a function of the current density [74].

Figure 19 provides additional insights into the EQE and optical power characteristics of the LED as a function of J. The maximum EQE, reaching approximately 0.08%, is observed at around 10 $A.cm^{-2}$. Below and above this maximum, the EQE gradually decreases, reaching a minimum value of approximately 0.04% at the lowest and highest current densities of 0.1 and 100 $A.cm^{-2}$, respectively. This decrease at high current densities is commonly referred to as "efficiency droop", which is attributed to non-radiative processes such as Auger recombination and electron leakage contribution [86]. In terms of P_{opt}, the values are in the sub-μW range for current densities up to 0.5 $A.cm^{-2}$. The power then increases, reaching 55 μW at 20 $A.cm^{-2}$, and further increases to a maximum value of 155 μW at 100 $A.cm^{-2}$. However, the increase in optical power is not constant and varies with the current density following a power m. The value of m depends on the current density range: it is close to 1 between 0.1 and 20 $A.cm^{-2}$, which means that the optical power approximately linearly increases with increasing current density in this range suggesting that the LED is more efficient at converting current into light. Then, it decreases to 0.75 between 20 and 70 $A.cm^{-2}$, showing that the increase in optical power is still present but starts to exhibit a less-than-linear relationship with current density. It further decreases to 0.4 for current densities above 70 $A.cm^{-2}$, which indicates that for higher current densities, the optical power increases at a slower rate, indicating a strong sub-linear relationship; at highest current densities, the LED's efficiency decreases as current density increases.

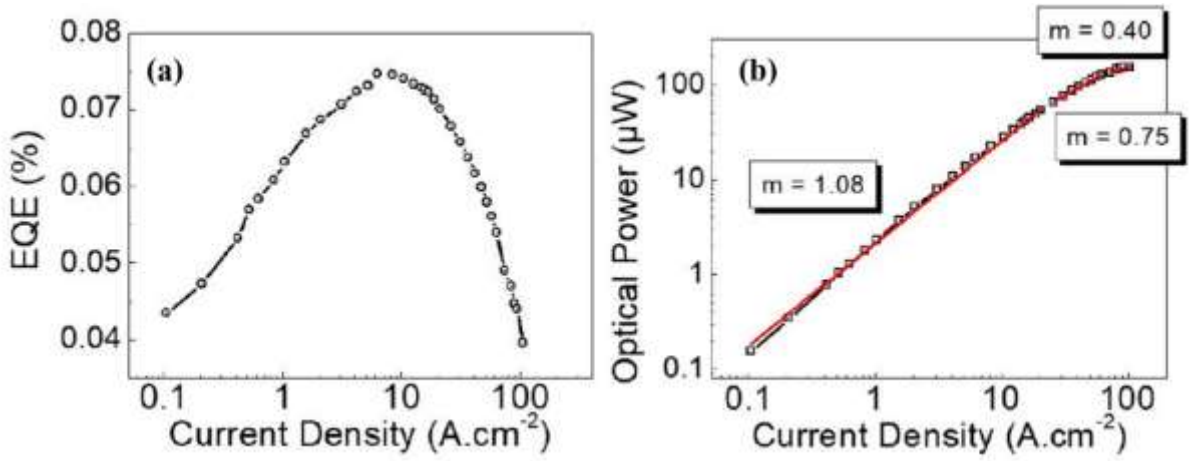

Figure 19: (a) EQE variation as a function of the current density (J); (b) P_{opt} variation as a function of J for $Al_{0.2}Ga_{0.8}N$ QD-based LED characteristics. The segments represent fits of the variation of Popt with a power law J^m, where m is a coefficient determined by the fit [74].

The PL measurements clearly point out a significant influence of the Fint and the QCSE on the QD emission. Due to the smaller Fint of $Al_yGa_{1-y}N$ QD (with $0.1 \leq y \leq 0.4$), a reduction in the FWHM is observed (see figure 16) and the red shift in the QD emission is limited compared to the extreme case of GaN QD. However, when comparing the PL emission with the EL of QD-based LED (figure 17(b)), an increase in the FWHM of the spectra is observed for the LED. In the case of $Al_{0.1}Ga_{0.9}N$ QD active region, the PL FWHM is ~ 16 nm (180 meV) while it is ~ 21 nm (250 meV) in the case of the EL. For $Al_{0.2}Ga_{0.8}N$ QD, a value of ~12 nm (150 meV) and ~ 30 nm (400 meV) for PL and EL FWHM, respectively. Finally, for $Al_{0.3}Ga_{0.7}N$ QD, a value of ~8 nm (115 meV) for the PL FWHM and ~ 34 nm (580 meV) for the EL FWHM are measured. Although the injection conditions (i.e. the carrier densities) in the QD differ between the LED and the reference PL structures for the measurements presented here, which has an impact on the EL FWHM as shown in figure 18(b), some tendencies can still be given:

1) First, a decrease of the FWHM of the PL spectra is observed as the Al concentration in the QD increases which is attributed to the reduction of Fint as the Al concentration between the cladding layer ($Al_{0.7}Ga_{0.3}N$) and the QD decreases.

2) Second, an increase of the FWHM is systematically observed for LED compared to the reference sample. This characteristic is attributed to the multi-QD planes in the LED structure compared to the single QD plane in the reference one, as this is the main difference in the active region design between the samples. It indicates that the QD composition and size (height) fluctuations increase when piling up the QD layers.

3) Third, an opposite behavior is observed regarding the FWHM dependence on the QD Al concentration between the LED and the reference sample: the FWHM decreases in the latter

case whereas it increases in the case of the LED. The FWHM reduction with the Al concentration increase for the reference samples can be seen as the direct consequence of the reduction of Fint whereas its increase in the LED structures is due to an enhancement of the QD composition and size fluctuations as already discussed. It is worth noting that the FWHM broadening becomes extreme as the nominal Al concentration of the QD increases to 30%, going from 250 meV up to 580 meV for $Al_{0.1}Ga_{0.9}N$ QD and $Al_{0.3}Ga_{0.7}N$ QD active regions, respectively. This result is attributed to an increase of the $Al_yGa_{1-y}N$ material intrinsic composition fluctuations as Al increases [79], [80], adding to the broadening which comes for Fint [84]. In addition, the emission from the $Al_{0.3}Ga_{0.7}N$ QD (nominal composition) based LED is found at a much shorter wavelength then expected from the PL measurements performed on reference structures (cf. figure 16 and figure 17(b)), which gives another hint about the $Al_yGa_{1-y}N$ composition fluctuations for larger Al concentrations.

Looking now at the EL evolution as a function of the input current density presented in figure 18(a), spectra for different current values have been extracted and are shown in figure 20. Although the EL spectra shape is influenced by Fabry-Perot interferences resulting from the refractive index contrasts at the (Al,Ga)N / sapphire and the air / (Al,Ga)N interfaces and the maximum intensity peak wavelength remains fairly constant (between 318 and 324 nm), a dependence of the EL as a function of the current is still observed. On the other hand, at lower currents, the broadening is mainly observed towards longer wavelengths (up to 380 nm), an opposite feature is seen at larger currents with an increase of the EL intensity at around 300-305 nm. This is a typical feature found in our LED: at lower J, carriers are preferentially injected in QD with lower Al concentrations (i.e. in deeper localization potentials) whereas a progressive injection into higher Al concentration $Al_yGa_{1-y}N$ QD occurs at larger J leading to an LED operation at shorter wavelengths [85].

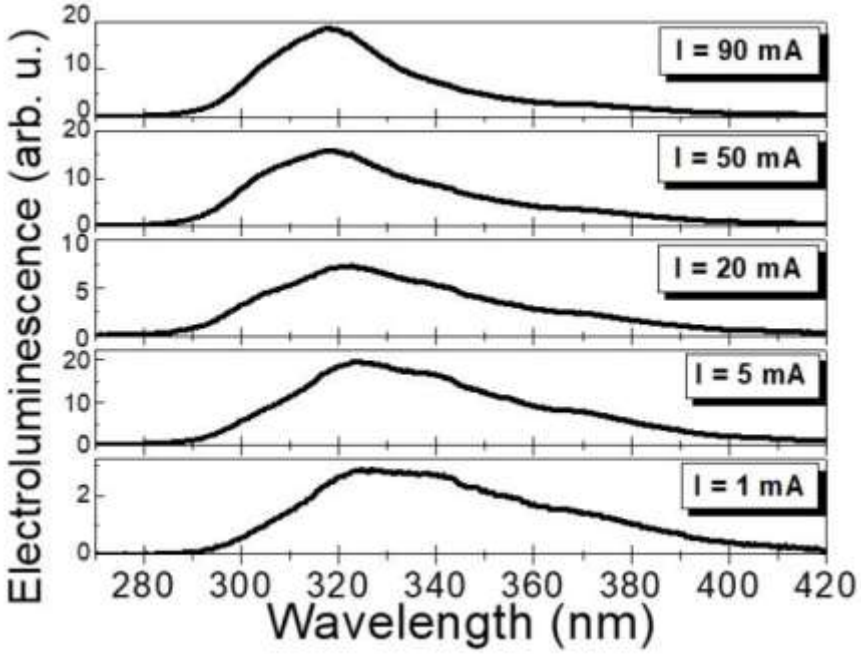

Figure 20: QD-based LED EL spectra measured at different input currents (between 1 and 90 mA) [74].

The LED EQE and P_{opt} are also dependent on the current density (Figure 19). The EQE is the product of the internal quantum efficiency (IQE), the injection efficiency (IE) and the extraction efficiency (EE). In our characterizations, the EE is constant and the variation of the EQE as a function of J points out a variation of the IQE and/or the IE. Combining the EQE measurements with the evolution of P_{opt}, it is then possible to draw some conclusions:

i) At lower J, the IQE is constant (between 0.1 and 20 $A.cm^{-2}$) as evidenced by a (quasi-) linear variation of P_{opt} (i.e. the coefficient m is close to 1), which means that the IE increases.

ii) At higher J, m is found below 1 ($m \sim 0.75$) and P_{out} increases sub-linearly as a function of J, leading to a decrease of the EQE.

iii) A more pronounced decrease of m down to 0.4 is determined at largest J, i.e. P_{out} starts to saturate, along with a strong drop in the EQE which is divided by 2 compared to its maximum value found at 8 $A.cm^{-2}$. The reduction in the optical power increase above 20 $A.cm^{-2}$ is related to thermal effects caused by a decrease of the (hole) injection efficiency into the QD active region (associated to Auger effects and/or electron overflow) [86].

Considering the typical operating voltages of the LED in the 10-15 V range, heating effect at the LED junction is seen as the main reason for the EQE decrease observed in our LED. Indeed, in the extreme case of highly resistive contacts and/or doped layers leading to even larger operating voltages as shown in the LED current – voltage measurements presented

in Figure 21(a), the impact of the injection efficiency on the LED performances is even more obvious: in this example, the LED turn-on voltage is 11 V and it increases to 27 V at 20 mA.cm^{-2}. The optical power variation reported in Figure 21(b) is found to be linear as a function of the input current below 2 A.cm^{-2} only and then increases sub-linearly. At 20 A.cm^{-2} only, P_{opt} saturates and even severely decreases at larger current densities leading to irreversible damages on the LED working operation.

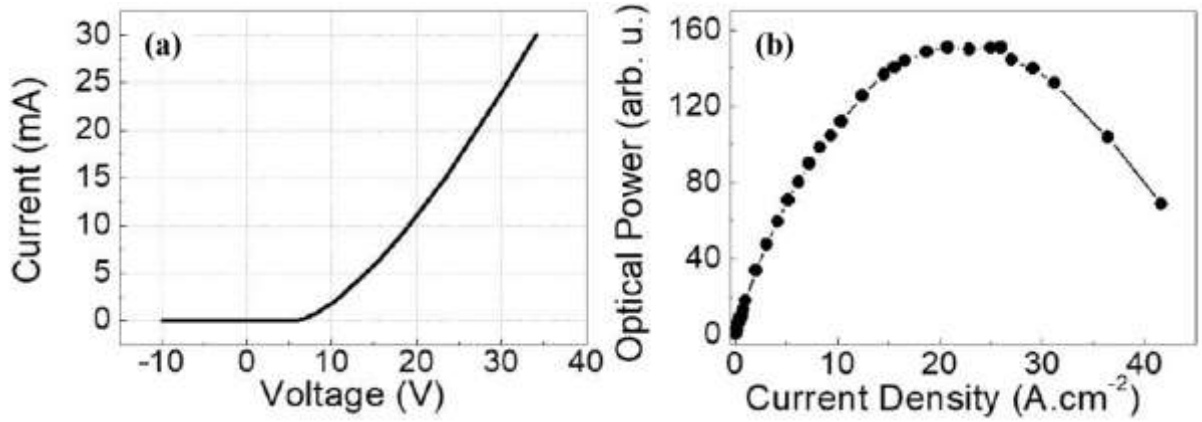

Figure 21: QD-based LED performances with degraded electric properties. (a) IV characteristics showing high voltages in operating conditions. (b) P_{opt} variation as a function of the current density. A strong decrease of the P_{opt} is observed for current densities above 20 A.cm^{-2} [74].

III.3.2. TJs QDs-based UV LEDs

The TJs LED structure was grown on (0 0 0 1) sapphire substrates by MBE in a RIBER 32 P reactor. Solid sources were used for the III-elements (Al,Ga) and the dopants (Si for n-type layers and Mg for p-type layers). Regarding the nitrogen source, ammonia (NH_3) was chosen as the precursor for the growth except for the fabrication of the QD active region for which a RIBER RF nitrogen (N_2) plasma source was used. The structure referred to as TJ UV LED was fabricated as described in figure 22. Similar to the UV LED structure growth discussed earlier, the TJs UV LED underwent the same growth conditions with modification only to the GaN p-type layer that was replaced by a tunnel junction and an n-type layer as the contact layer. First, a 3 nm thick AlN nucleation layer was initially grown at 500°C and followed by the growth of an 120 nm AlN layer at a temperature of 1000°C [71]. Next, the TJ LED structure was fabricated by first growing a 0.7 µm thick Si-doped n-$Al_{0.7}Ga_{0.3}N$ layer at 870°C, with a Si concentration estimated around 10^{19} atoms.cm^{-3}, and an active region consisting of five $Al_yGa_{1-y}N$ QD planes with different Al concentrations for the $Al_yGa_{1-y}N$ QD (i.e. with y = 0.2, 0.3, and 0.4) were investigated, separated by $Al_{0.7}Ga_{0.3}N$ barriers lattice matched to the $Al_{0.7}Ga_{0.3}N$ template. Next, a 5 nm thick cladding layer was grown in between the QD planes at 750°C. After the deposition of the last QD plane, a 20 nm thick $Al_{0.7}Ga_{0.3}N$

layer was grown at 830°C. This was followed by the p-type region composed of a 10 nm $Al_{0.8}Ga_{0.2}N$:Mg electron blocking layer and a 40 nm compositionally graded p-(Al,Ga)N layer from $Al_{0.8}Ga_{0.2}N$:Mg to $Al_{0.7}Ga_{0.3}N$:Mg layer grown at 820°C containing an Mg concentration of approximately 1 x 10^{20} – 2 x 10^{20} cm^{-3} atoms.cm^{-3}. Then, a 3 nm GaN interband tunneling layer was deposited at 800°C and followed by a 10 nm n++ graded-(Al,Ga)N with Al content increasing from 55% to 70%, and a final 200 nm n++ $Al_{0.7}Ga_{0.3}N$:Si layer with a Si concentration around 10^{20} atoms.cm^{-3}, which were grown at 820°C and 870°C, respectively. The compositional gradients have been used both for practical reason, i.e. to reduce as much as possible the number of growth interruptions and their duration, and also to potentially create bulk polarization charge that could potentially lead to an increase in the hole density [63].

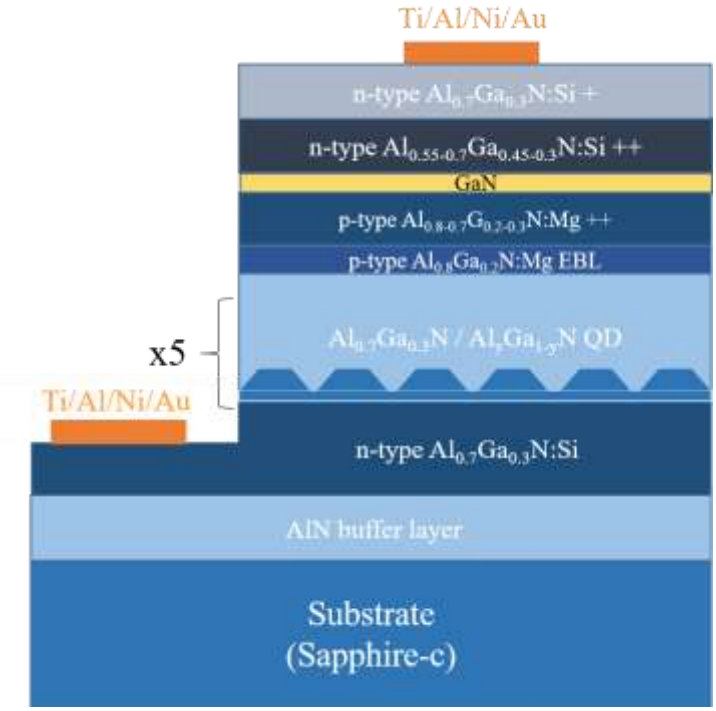

Figure 22: Schematic illustration of the $Al_yGa_{1-y}N$ QD-based TJs UV LEDs structures grown on c-sapphire substrate.

Similar to the standard UV LED structure fabrication process discussed in the previous part, photolithography and electron cyclotron resonance reactive ion etching were employed to fabricate the LED mesas in a square shape with dimensions of (310 x 310) μm^2. A stacking of Ti/Al/Ni/Au (30/180/40/200 nm) served as the top electrode connected to the n++ $Al_{0.7}Ga_{0.3}N$:Si top layer. The contact on the n-$Al_{0.7}Ga_{0.3}N$ layer also consisted of a stacking of Ti/Al/Ni/Au (30/180/40/200 nm). The LED devices were characterized at room temperature by measuring their I-V characteristics and EL properties. The EL measurements were performed from the sapphire side of the LED, with the emitted light collected through a UV-grade optical

fiber connected to a linear CCD spectrometer featuring a spectral resolution of 2.5 nm. The optical power (P_{opt}) was measured from the backside of the devices using a calibrated UV-enhanced Si photodiode. The results discussed here have been presented at the International Workshop on Nitride Semiconductors, Berlin (2022) [87].

In Figure 23 (a), we observe the EL spectra of three TJs LEDs, each having different quantum dot (QD) nominal compositions. The LED containing QDs with an $Al_{0.4}Ga_{0.6}N$ nominal composition exhibits its primary peak emission at 269 nm, accompanied by a secondary, less intense peak at 320 nm. Meanwhile, the LED incorporating QDs with an $Al_{0.3}Ga_{0.7}N$ nominal composition features a predominant, broad peak emission with its maximum EL intensity recorded at 296 nm. Lastly, the LED containing QDs characterized by an $Al_{0.2}Ga_{0.8}N$ nominal composition displays a primary broad emission peak at 307 nm, along with a secondary, less intense shoulder peak emitting at 321 nm. The emergence of this secondary peak emission might be due to: either inhomogeneity in the QDs with different Al compositions and size emitting within the QDs planes, or a variability in the emission of the QDs due to a variation of the QDs average size and/or composition between the five QDs planes that constitutes the LED active region. Furthermore, the EL peak FHWM values were found to be around 14, 23, and 43 nm for LEDs featuring QD nominal composition of $Al_{0.4}Ga_{0.6}N$, $Al_{0.3}Ga_{0.7}N$, and $Al_{0.2}Ga_{0.8}N$, respectively, which is attributed to fluctuations in both the QDs size and composition (Al concentration). In Figure 23 (b), we compare the current-voltage characteristics of a standard UV LED and the TJs UV LED. The TJs UV LED shows diode behavior but operates at a higher voltage, around 35 V at 20 mA, in contrast to the 15 V measured for the standard UV LED. Additionally, the TJs UV LED exhibits higher series resistance (Rs) at approximately 340 Ω, whereas the standard UV LED has a lower series resistance of 70 Ω.

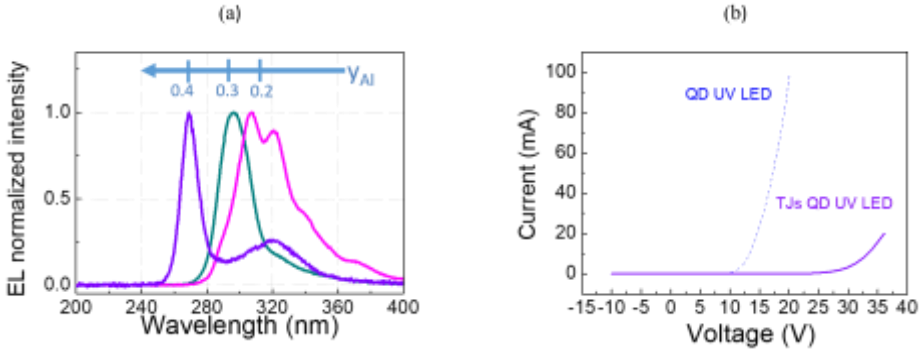

Figure 23: (a) Electroluminescence spectra (normalized intensity) at an input current of 20 mA of three TJs LEDs emitting in the UVB and UVC regions between 310 nm and 270 nm. (b) I-V characteristic of $Al_{0.7}Ga_{0.3}N$ based standard and TJs QD LEDs [87].

Figure 24 (a) and (b) present the wavelength evolution as a function of the current density for both types of LEDs. For the standard UV LED (figure 24 (a)), the LED emission is strongly shifting into the UV at shorter wavelengths (from 335 nm to 305 nm) as the input current density (J) increases. Conversely, the TJs UV LED (Figure 24 (b)) shows a less pronounced effect of increasing current density on the emission wavelength, with a slight shift from 304 nm to 296 nm. The advantage that TJs offer in terms of providing a direct pathway for carriers to be injected into the active region can help improve the current spreading and carrier distribution, which can lead to a more uniform emission across the active region. This, in turn, contributes to a more stable emission wavelength with increasing current density compared to standard UV LEDs where carriers experience uneven injection into QDs with different Al compositions at lower and higher current densities, which result in wavelength shifts and variations in emission intensity, leading to less stable emission characteristics.

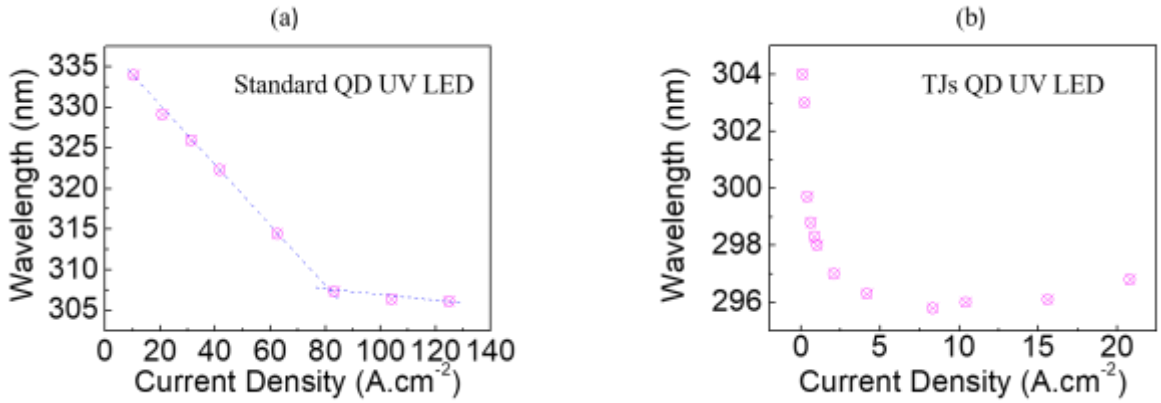

Figure 24: (a) and (b) represent the variation of the wavelength emission as a function of the current density for standard and TJs QD UV LEDs, respectively [87].

The optical power (P_{opt}) characteristics of the TJ UV LED as a function of the current density (J) have been studied and are illustrated in Figure 25 (a) and (b). In Figure 25 (a), as the current injection increases, P_{opt} also rises, reaching 240 µW at a current density of 10 A.cm^{-2}, and reaching a peak value of 400 µW at 20 A.cm^{-2}. This demonstrates a notable improvement in optical power compared to the 30-50 µW range typically observed for standard UV LEDs at 20 A.cm^{-2}, which can be attributed to both positive features: a better injection efficiency and the transparency in the TJ UV LED top contact layer since the p-GaN layer has been suppressed. However, the increase in optical power is not uniform as a function of the current density and exhibits variations with a constant power m as a function of J. The value of m is found to be close to 1 between 0.1 and 10 A.cm^{-2}, and below 1 for higher current densities. Specifically, a value of 0.7 is observed for J ranging from 10 to 20 A.cm^{-2}. Regarding the EQE shown in Figure

24 (b), a peak value close to 0.65% is observed at current densities between 2 and 5 A.cm^{-2}. Below and above this maximum, the EQE gradually decreases, reaching a minimum value of approximately 0.4% at the minimum and maximum current densities of 0.1 and 20 A.cm^{-2}, respectively. This reduction in EQE at higher current densities, known as efficiency droop, can be attributed to non-radiative processes influenced by Auger recombination and electron leakage contributions [86].

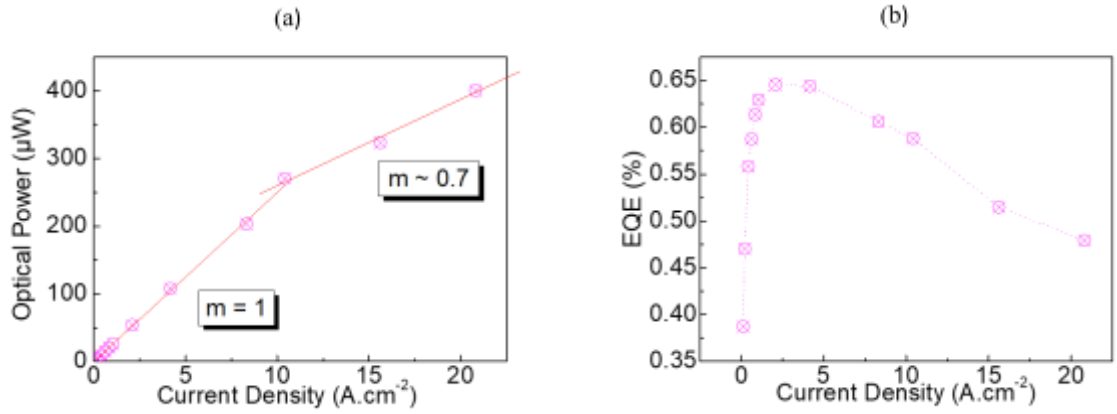

Figure 25: $Al_{0.2}Ga_{0.8}N$ QD-based TJs UV LED characteristics: (a) the variation of the optical power (P_{opt}) as a function of the current density (J); (b) the variation of the external quantum efficiency (EQE) as a function of J [87].

As previously discussed in section II.1, the efficiency of the TJs UV LED is represented by its EQE, which is the product of the internal quantum efficiency (IQE), the injection efficiency (IE), and the extraction efficiency (EE). During the characterization of the TJs UV LED, the EE remains constant, and the variation of the EQE with respect to the current density (J) (figure 25 (b)) indicates changes in the IQE and/or IE. By analyzing the EQE measurements along with the evolution of the optical power (P_{opt}) (figure 25 (a)), we can infer that at lower current densities (J < 10 A.cm^{-2}), the IQE remains constant (between 0.1 and 10 A.cm^{-2}), as indicated by the linear variation of P_{opt} (i.e., the coefficient m is 1). This suggests that the IE increases at these lower current densities. However, at higher current densities (J > 10 A.cm^{-2}), the coefficient m is found to be below 1 (approximately 0.7), and P_{out} increases sub-linearly with J, leading to a decrease in the EQE. This decrease in optical power can be attributed to thermal effects that affect the injection efficiency of carriers (holes) into the active region of the QDs, possibly influenced by Auger effects and/or electron overflow [86]. The observed decrease in EQE in the TJs UV LED is primarily attributed to the heating effect at the LED junction. Indeed, the TJs UV LED exhibits higher operating voltages compared to standard UV LEDs, as seen in the comparison of current-voltage measurements in figure 23 (b). These higher

operating voltages can be linked to the presence of p++ and n++ doped layers with the requirement to reach higher concentrations in the TJs UV LED compared to standard UV LED to limit the voltage drop at the tunnel junction [88].

Based on the previous results, we have conducted a comparative analysis of the optical power and EQE as functions of the current density for both standard and TJs UV LEDs, as depicted in figure 26 (a) and (b), respectively. The incorporation of TJs has resulted in a remarkable enhancement of the optical power. At a current density of 10 $A.cm^{-2}$, the P_{opt} for the standard LED reaches 30 µW, while for the TJs LED, it significantly rises to 240 µW, representing an eightfold increase, as illustrated in figure 26 (a). As discussed above, the improvement in the optical power between the standard and the TJs UV LEDs is related to an improvement in the EIE and in the LEE. Consequently, figure 26 (b) displays a significant increase in the EQE for TJs UV LED compared to the EQE of the standard UV LED. The EQE of the standard UV LED reaches a maximum value of approximately 0.08%, whereas for the TJs UV LED, it reaches around 0.65%, marking an eightfold increase in the EQE since the EQE is proportional to the optical power P_{opt}. Let us revisit the concept of external quantum efficiency (EQE), which is the product of internal quantum efficiency (IQE), electrical injection efficiency (EIE), and light extraction efficiency (LEE). The IQE is not expected to be influenced by the presence of the TJ. Therefore, our findings demonstrate a significant improvement in the electrical injection efficiency due to the presence of the TJ. The TJ introduces out-of-equilibrium holes into the LED, leading to an enhanced balance between electrons and holes within the active region, thus improving the injection efficiency. In standard UV LEDs, electrons tend to overflow above the active region due to the scarcity of holes, resulting in recombination in the p region. However, in TJ-based UV LEDs, electrons recombine within the active region as holes are injected from the TJ. This beneficial effect becomes evident as a remarkable advantage for TJ LEDs in the UV range. The incorporation of annealed AlN/sapphire templates, as discussed in chapter 2, featuring threading dislocation densities (TDDs) in the range of $10^9.cm^{-2}$ or even lower, holds the potential to minimize non-radiative recombinations within the LED structure. This reduction in non-radiative processes can lead to further enhancements in IQE and IE. Consequently, these improvements may result in even higher values of optical power and EQE for the TJs UV LEDs, surpassing the achievements observed in the current study.

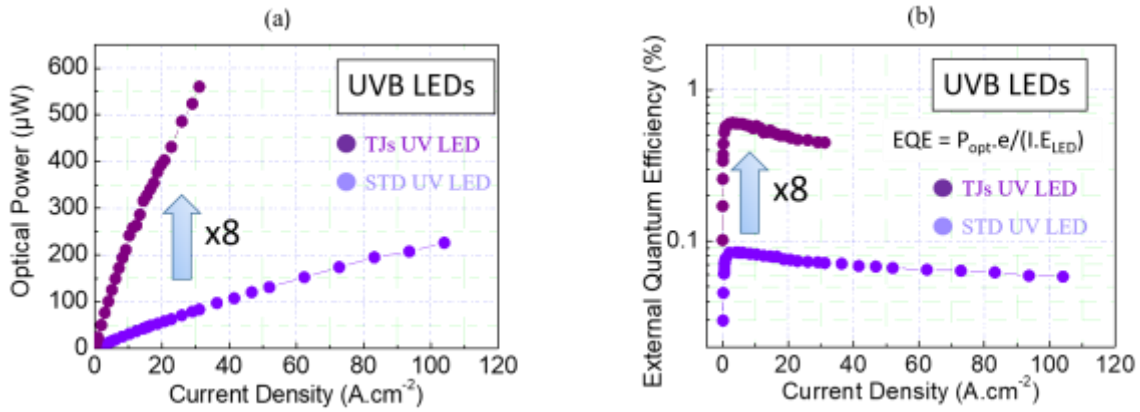

Figure 26. (a) and (b) represent a comparison between standard and TJs UV LEDs in term of the optical power and the external quantum efficiency as a function of current density, respectively [87].

III.4. Conclusion

In conclusion, this chapter provided a comprehensive exploration of tunnel junctions (TJs) and their applications in (Al,Ga)N-based UV LEDs. We began with an overview of the historical background of tunnel junctions, tracing their evolution from Mg to Si to Ge as doping materials. Understanding the development of tunnel junctions over time helped us appreciate their significance in modern semiconductor devices. We then delved into the growth techniques used for tunnel junction (Al,Ga)N-based UV LEDs. The full growth of TJ (Al,Ga)N-based UV LEDs by molecular beam epitaxy (MBE) displayed the precision and control offered by this method. Additionally, the hybrid growth approach, combining metalorganic chemical vapor deposition (MOCVD) and MBE, opened up new possibilities for realizing high-performance TJs UV LEDs. An essential aspect of our investigation focused on the MOCVD growth of standard UV LEDs on annealed AlN physical vapor deposition (PVD) templates. We were able to achieve a significantly higher EQE value with the UV LED grown on the annealed AlN template defined by better structural quality (low TDDs) and smooth surface morphology, which was ten times higher than the highest EQE value reported for TJ UV LEDs grown on AlN MOCVD by previous PhD student's work in the lab. These findings underscored the importance of template quality in shaping the performance characteristics of the resultant UV LEDs.

$Al_yGa_{1-y}N$ QDs UV LEDs emitting over a wide wavelength range, from 340 nm to 265 nm, were successfully fabricated by MBE and thoroughly investigated. The performance of these LEDs was closely correlated with the structural and optical properties of the QDs. Notably, significant differences were observed between the electroluminescence (EL) and photoluminescence (PL) properties, which were attributed to variations in QD composition and

size (height) inhomogeneities within the LED active regions, stemming from the use of multiple QD planes compared to a single plane used in the reference PL measurements. The investigation of LED characteristics involved an analysis of the external quantum efficiency (EQE) and optical power as a function of the current density (J). It was found that the reduction in EQE and optical power at higher J was mainly attributed to a decrease in the injection efficiency, associated with a heating effect. Furthermore, a notable dependence of the EL wavelength on J was observed, which was linked to the injection of carriers into different QD populations. At lower J, carriers exhibited preferential injection into QDs with deeper localization potentials, characterized by lower Al concentration and/or larger QD sizes (higher heights). To mitigate the dependence of EL wavelength on current density and to reduce EL peak broadening in QD LEDs, alternative approaches like non-polar or semi-polar orientations could be explored [76]. However, achieving comparable crystalline quality of heterostructures grown on high-index Miller planes as c-oriented heterostructures remains a challenge. Additionally, optimizing the surface morphology and cladding layer thickness between the $Al_yGa_{1-y}N$ QD planes could lead to improved vertical organization and size uniformity of the nanostructures, as demonstrated in the case of GaN QDs and other semiconductor systems [89]–[92]. For enhancing the injection efficiency, the use of tunnel junctions for non-equilibrium hole injection was developed.

Finally, we successfully fabricated $Al_yGa_{1-y}N$ QD-based TJs UV LEDs operating in the UVB and UVC ranges using MBE. We conducted a comprehensive investigation of the electrical and optical characteristics of these TJs LEDs and compared them to the standard MBE-grown QD-based UV LEDs. Notably, significant differences were observed between the two types of LEDs. Firstly, the TJs UV LED exhibited higher operating voltage, measuring around 35 V at 20 mA, in contrast to the standard UV LED, which required 15 V at the same current level. Additionally, the TJs UV LED displayed a higher series resistance (Rs) of approximately 340 Ω, while the standard UV LED had a lower series resistance of 70 Ω. Furthermore, the optical characterizations revealed distinct variations. The TJs UV LED achieved higher optical power, reaching a maximum value of 400 µW at 20 $A.cm^{-2}$, compared to the standard UV LEDs, which only reached around 30 µW at the same current density. Similarly, the external quantum efficiency (EQE) values were significantly enhanced in the TJs UV LED, with a maximum value of approximately 0.65%, in contrast to the standard UV LED, which peaked at around 0.08%. This resulted in an impressive eightfold increase in both the optical power efficiency and the EQE for the TJs LED. These promising outcomes demonstrate the advantages of adopting TJs in UV LEDs. To further improve performance, future research

directions may focus on enhancing the injection efficiency (IE) and reducing the threading dislocation densities (TDDs) by employing annealed AlN/sapphire templates with TDDs below 10^9.cm^{-2}. These advancements hold the potential to achieve even higher efficiency and superior performance in UV LED devices.

References:

[1] « A theory of the electrical breakdown of solid dielectrics », *Proc. R. Soc. Lond. A*, vol. 145, n° 855, p. 523-529, juill. 1934, doi: 10.1098/rspa.1934.0116.

[2] A. G. Chynoweth et K. G. McKay, « Internal Field Emission in Silicon p− n Junctions », *Physical Review*, vol. 106, n° 3, p. 418, 1957.

[3] L. Esaki, « New phenomenon in narrow germanium p− n junctions », *Physical review*, vol. 109, n° 2, p. 603, 1958.

[4] L. V. Keldysh, « Behavior of non-metallic crystals in strong electric fields », *Soviet Journal of Experimental and Theoretical Physics*, vol. 6, p. 763, 1958.

[5] E. O. Kane, « Zener tunneling in semiconductors », *Journal of Physics and Chemistry of Solids*, vol. 12, n° 2, p. 181-188, 1960.

[6] E. O. Kane, « Theory of tunneling », *Journal of applied Physics*, vol. 32, n° 1, p. 83-91, 1961.

[7] J. V. Morgan et E. O. Kane, « Observation of direct tunneling in germanium », *Physical Review Letters*, vol. 3, n° 10, p. 466, 1959.

[8] N. Holonyak Jr, I. A. Lesk, R. N. Hall, J. J. Tiemann, et H. Ehrenreich, « Direct observation of phonons during tunneling in narrow junction diodes », *Physical Review Letters*, vol. 3, n° 4, p. 167, 1959.

[9] H. S. Sommers, « Tunnel diodes as high-frequency devices », *Proceedings of the IRE*, vol. 47, n° 7, p. 1201-1206, 1959.

[10] S. L. Miller, M. I. Nathan, et A. C. Smith, « Pressure dependence of the current-voltage characteristics of Esaki diodes », *Physical Review Letters*, vol. 4, n° 2, p. 60, 1960.

[11] J. I. Pankove, « Influence of degeneracy on recombination radiation in germanium », *Physical Review Letters*, vol. 4, n° 1, p. 20, 1960.

[12] N. Holonyak et I. A. Lesk, « Gallium-arsenide tunnel diodes », *Proceedings of the IRE*, vol. 48, n° 8, p. 1405-1409, 1960.

[13] J. P. Van der Ziel et W. T. Tsang, « Integrated multilayer GaAs lasers separated by tunnel junctions », *Applied Physics Letters*, vol. 41, n° 6, p. 499-501, 1982.

[14] A. R. Sugg, E. I. Chen, T. A. Richard, S. A. Maranowski, et N. Holonyak Jr, « np (p. sup.+-n. sup.+)-n Al. sub. y Ga. sub. 1-y As-GaAs-In. sub. x Ga. sub. 1-x As Quantum-Well Laser With p. sup.+-n. sup.+ GaAs-InGaAs Tunnel Contact On n-GaAs », *Appl. Phys. Lett*, vol. 62, n° 20, p. 2510-2512, 1993.

[15] J. J. Wierer, P. W. Evans, N. Holonyak Jr, et D. A. Kellogg, « Lateral electron current operation of vertical cavity surface emitting lasers with buried tunnel contact hole sources », *Applied physics letters*, vol. 71, n° 24, p. 3468-3470, 1997.

[16] J. K. Kim, E. Hall, et O. Sj, « lund et al.. Epitaxially-stacked multiple-active-region 1.55 µm lasers for increased differential efficiency », *Appl. Phys. Lett*, vol. 74, n° 13, p. 3251-3253, 1999.

[17] J. J. Wierer, P. W. Evans, N. Holonyak Jr, et D. A. Kellogg, « Vertical cavity surface emitting lasers utilizing native oxide mirrors and buried tunnel contact junctions », *Applied physics letters*, vol. 72, n° 21, p. 2742-2744, 1998.

[18] J. T. Leonard *et al.*, « Demonstration of a III-nitride vertical-cavity surface-emitting laser with a III-nitride tunnel junction intracavity contact », *Applied Physics Letters*, vol. 107, n° 9, p. 091105, 2015.

[19] S. Lee *et al.*, « GaN-based vertical-cavity surface-emitting lasers with tunnel junction contacts grown by metal-organic chemical vapor deposition », *Appl. Phys. Express*, vol. 11, n° 6, p. 062703, juin 2018, doi: 10.7567/APEX.11.062703.

[20] C. A. Forman *et al.*, « Continuous-wave operation of *m* -plane GaN-based vertical-cavity surface-emitting lasers with a tunnel junction intracavity contact », *Applied Physics Letters*, vol. 112, n° 11, p. 111106, mars 2018, doi: 10.1063/1.5007746.

[21] J. M. Olson et S. R. Kurtz, « Tunnel junction multiple wavelength light-emitting diodes », US5166761A, 24 novembre 1992 Consulté le: 23 juin 2023. [En ligne]. Disponible sur: https://patents.google.com/patent/US5166761A/en

[22] I. Ozden, E. Makarona, A. V. Nurmikko, T. Takeuchi, et M. Krames, « A dual-wavelength indium gallium nitride quantum well light emitting diode », *Appl. Phys. Lett.*, vol. 79, n° 16, p. 2532-2534, oct. 2001, doi: 10.1063/1.1410345.
[23] M. J. Grundmann et U. K. Mishra, « Multi-color light emitting diode using polarization-induced tunnel junctions », *Phys. Status Solidi (c)*, vol. 4, n° 7, p. 2830-2833, juin 2007, doi: 10.1002/pssc.200675000.
[24] M. Saha, A. Biswas, et H. Karan, « Monolithic high performance InGaN/GaN white LEDs with a tunnel junction cascaded yellow and blue light-emitting structures », *Optical Materials*, vol. 77, p. 104-110, 2018.
[25] S. J. Kowsz *et al.*, « Using tunnel junctions to grow monolithically integrated optically pumped semipolar III-nitride yellow quantum wells on top of electrically injected blue quantum wells », *Optics Express*, vol. 25, n° 4, p. 3841-3849, 2017.
[26] X. Guo *et al.*, « High efficiency tunneling-regenerated multi-active region light-emitting diodes », in *Optoelectronic Materials and Devices II*, SPIE, 2000, p. 170-179.
[27] X. Guo *et al.*, « Tunnel-regenerated multiple-active-region light-emitting diodes with high efficiency », *Applied Physics Letters*, vol. 79, n° 18, p. 2985-2986, 2001.
[28] X. Guo *et al.*, « Thermal property of tunnel-regenerated multiactive-region light-emitting diodes », *Applied physics letters*, vol. 82, n° 25, p. 4417-4419, 2003.
[29] F. Akyol, S. Krishnamoorthy, et S. Rajan, « Tunneling-based carrier regeneration in cascaded GaN light emitting diodes to overcome efficiency droop », *Applied Physics Letters*, vol. 103, n° 8, p. 081107, 2013.
[30] F. Akyol, S. Krishnamoorthy, Y. Zhang, et S. Rajan, « GaN-based three-junction cascaded light-emitting diode with low-resistance InGaN tunnel junctions », *Applied Physics Express*, vol. 8, n° 8, p. 082103, 2015.
[31] S.-J. Chang, W.-H. Lin, et C.-T. Yu, « GaN-based multiquantum well light-emitting diodes with tunnel-junction-cascaded active regions », *IEEE Electron Device Letters*, vol. 36, n° 4, p. 366-368, 2015.
[32] S. R. Jeon, « Y,-H. Song, H.-J. Jang, GM Yang, SW Hwang, and SJ Son », *Appl. Phys. Lett*, vol. 78, p. 3265, 2001.
[33] J. Simon *et al.*, « Polarization-induced Zener tunnel junctions in wide-band-gap heterostructures », *Physical review letters*, vol. 103, n° 2, p. 026801, 2009.
[34] M. F. Schubert, « Interband tunnel junctions for wurtzite III-nitride semiconductors based on heterointerface polarization charges », *Physical Review B*, vol. 81, n° 3, p. 035303, 2010.
[35] M. F. Schubert, « Polarization-charge tunnel junctions for ultraviolet light-emitters without p-type contact », *Applied Physics Letters*, vol. 96, n° 3, p. 031102, 2010.
[36] C.-Z. Zhao, T. Wei, L.-Y. Chen, S.-S. Wang, et J. Wang, « The activation energy for Mg acceptor in AlxGa1-xN alloys in the whole composition range », *Superlattices and Microstructures*, vol. 109, p. 758-762, sept. 2017, doi: 10.1016/j.spmi.2017.06.006.
[37] S. Brochen, J. Brault, S. Chenot, A. Dussaigne, M. Leroux, et B. Damilano, « Dependence of the Mg-related acceptor ionization energy with the acceptor concentration in p-type GaN layers grown by molecular beam epitaxy », *Applied Physics Letters*, vol. 103, n° 3, p. 032102, 2013.
[38] B. Šantić, « Statistics of the Mg acceptor in GaN in the band model », *Semicond. Sci. Technol.*, vol. 21, n° 10, p. 1484, sept. 2006, doi: 10.1088/0268-1242/21/10/022.
[39] G. Namkoong, W. A. Doolittle, et A. S. Brown, « Incorporation of Mg in GaN grown by plasma-assisted molecular beam epitaxy », *Applied Physics Letters*, vol. 77, n° 26, p. 4386-4388, 2000.
[40] S. Pezzagna, P. Vennéguès, N. Grandjean, et J. Massies, « Polarity inversion of GaN (0 0 0 1) by a high Mg doping », *Journal of Crystal Growth*, vol. 269, n° 2-4, p. 249-256, 2004.
[41] P. Vennéguès *et al.*, « Pyramidal defects in metalorganic vapor phase epitaxial Mg doped GaN », *Applied Physics Letters*, vol. 77, n° 6, p. 880-882, 2000.
[42] N. H. Tran, B. H. Le, S. Zhao, et Z. Mi, « On the mechanism of highly efficient p-type conduction of Mg-doped ultra-wide-bandgap AlN nanostructures », *Applied Physics Letters*, vol. 110, n° 3, p. 032102, 2017.

[43] S. Neugebauer *et al.*, « All metalorganic chemical vapor phase epitaxy of p/n-GaN tunnel junction for blue light emitting diode applications », *Applied Physics Letters*, vol. 110, n° 10, p. 102104, 2017.
[44] A. Cremades, L. Görgens, O. Ambacher, M. Stutzmann, et F. Scholz, « Structural and optical properties of Si-doped GaN », *Physical Review B*, vol. 61, n° 4, p. 2812, 2000.
[45] P. Pampili et P. J. Parbrook, « Doping of III-nitride materials », *Materials Science in Semiconductor Processing*, vol. 62, p. 180-191, 2017.
[46] L. Lugani *et al.*, « n+-GaN grown by ammonia molecular beam epitaxy: Application to regrown contacts », *Applied Physics Letters*, vol. 105, n° 20, p. 202113, 2014.
[47] S. Pearton, *GaN and ZnO-based materials and devices*, vol. 156. Springer Science & Business Media, 2012.
[48] M. L. Nakarmi, K. H. Kim, K. Zhu, J. Y. Lin, et H. X. Jiang, « Transport properties of highly conductive n-type Al-rich Al x Ga 1− x N (x⩾ 0.7) », *Applied Physics Letters*, vol. 85, n° 17, p. 3769-3771, 2004.
[49] L. T. Romano, C. G. Van de Walle, J. W. Ager III, W. Götz, et R. S. Kern, « Effect of Si doping on strain, cracking, and microstructure in GaN thin films grown by metalorganic chemical vapor deposition », *Journal of Applied Physics*, vol. 87, n° 11, p. 7745-7752, 2000.
[50] A. Dadgar, J. Bläsing, A. Diez, et A. Krost, « Crack-free, highly conducting GaN layers on Si substrates by Ge doping », *Applied physics express*, vol. 4, n° 1, p. 011001, 2011.
[51] M. A. Moram, M. J. Kappers, F. Massabuau, R. A. Oliver, et C. J. Humphreys, « The effects of Si doping on dislocation movement and tensile stress in GaN films », *Journal of Applied Physics*, vol. 109, n° 7, p. 073509, 2011.
[52] A. Dadgar *et al.*, « MOVPE growth of GaN on Si–Substrates and strain », *Thin Solid Films*, vol. 515, n° 10, p. 4356-4361, 2007.
[53] S. Fritze *et al.*, « High Si and Ge n-type doping of GaN doping-Limits and impact on stress », *Applied Physics Letters*, vol. 100, n° 12, p. 122104, 2012.
[54] C. Nenstiel *et al.*, « Germanium–the superior dopant in n-type GaN », *physica status solidi (RRL)–Rapid Research Letters*, vol. 9, n° 12, p. 716-721, 2015.
[55] V. Fan Arcara *et al.*, « Ge doped GaN and Al0. 5Ga0. 5N-based tunnel junctions on top of visible and UV light emitting diodes », *Journal of Applied Physics*, vol. 126, n° 22, p. 224503, 2019.
[56] M. N. Fireman, G. L'Heureux, F. Wu, T. Mates, E. C. Young, et J. S. Speck, « High germanium doping of GaN films by ammonia molecular beam epitaxy », *Journal of Crystal Growth*, vol. 508, p. 19-23, 2019.
[57] P. Bogusławski et J. Bernholc, « Doping properties of C, Si, and Ge impurities in GaN and AlN », *Physical Review B*, vol. 56, n° 15, p. 9496, 1997.
[58] L. Gordon, J. L. Lyons, A. Janotti, et C. G. Van de Walle, « Hybrid functional calculations of D X centers in AlN and GaN », *Physical Review B*, vol. 89, n° 8, p. 085204, 2014.
[59] R. Blasco *et al.*, « Electrical and optical properties of heavily Ge-doped AlGaN », *Journal of Physics D: Applied Physics*, vol. 52, n° 12, p. 125101, 2019.
[60] Y. Zhang *et al.*, « Interband tunneling for hole injection in III-nitride ultraviolet emitters », *Applied Physics Letters*, vol. 106, n° 14, p. 141103, 2015.
[61] Y. Zhang *et al.*, « Design and demonstration of ultra-wide bandgap AlGaN tunnel junctions », *Applied Physics Letters*, vol. 109, n° 12, p. 121102, 2016.
[62] Y. Zhang *et al.*, « Tunnel-injected sub 290 nm ultra-violet light emitting diodes with 2.8% external quantum efficiency », *Applied Physics Letters*, vol. 112, n° 7, p. 071107, 2018.
[63] Y. Zhang *et al.*, « Tunnel-injected sub-260 nm ultraviolet light emitting diodes », *Applied Physics Letters*, vol. 110, n° 20, p. 201102, 2017.
[64] S. Krishnamoorthy, F. Akyol, et S. Rajan, « InGaN/GaN tunnel junctions for hole injection in GaN light emitting diodes », *Applied Physics Letters*, vol. 105, n° 14, p. 141104, 2014.
[65] S. Krishnamoorthy, F. Akyol, P. S. Park, et S. Rajan, « Low resistance GaN/InGaN/GaN tunnel junctions », *Applied Physics Letters*, vol. 102, n° 11, 2013.

[66] S. Krishnamoorthy, T. F. Kent, J. Yang, P. S. Park, R. C. Myers, et S. Rajan, « GdN Nanoisland-Based GaN Tunnel Junctions », *Nano Lett.*, vol. 13, n° 6, p. 2570-2575, juin 2013, doi: 10.1021/nl4006723.
[67] E. C. Young *et al.*, « Hybrid tunnel junction contacts to III–nitride light-emitting diodes », *Applied Physics Express*, vol. 9, n° 2, p. 022102, 2016.
[68] A. Dussaigne, B. Damilano, J. Brault, J. Massies, E. Feltin, et N. Grandjean, « High doping level in Mg-doped GaN layers grown at low temperature », *Journal of Applied Physics*, vol. 103, n° 1, 2008.
[69] C. A. Hurni, J. R. Lang, P. G. Burke, et J. S. Speck, « Effects of growth temperature on Mg-doped GaN grown by ammonia molecular beam epitaxy », *Applied Physics Letters*, vol. 101, n° 10, 2012.
[70] V. F. Arcara, « Tunnel junctions in nitride heterostructures for optoelectronic applications », Université Côte d'Azur, 2020.
[71] S. Matta *et al.*, « Properties of AlN layers grown on c-sapphire substrate using ammonia assisted MBE », *Journal of Crystal Growth*, vol. 499, p. 40-46, oct. 2018, doi: 10.1016/j.jcrysgro.2018.07.023.
[72] S. Matta *et al.*, « Influence of the heterostructure design on the optical properties of GaN and Al $_{0.1}$ Ga $_{0.9}$ N quantum dots for ultraviolet emission », *Journal of Applied Physics*, vol. 122, n° 8, p. 085706, août 2017, doi: 10.1063/1.5000238.
[73] S. Matta, « AlGaN quantum dots grown by molecular beam epitaxy for ultraviolet light emitting diodes », Université Montpellier, 2018.
[74] J. Brault *et al.*, « DUV LEDs based on AlGaN quantum dots », in *Gallium Nitride Materials and Devices XVI*, SPIE, 2021, p. 64-72.
[75] J. Brault *et al.*, « Investigation of AlyGa1− yN/Al0. 5Ga0. 5N quantum dot properties for the design of ultraviolet emitters », *Japanese Journal of Applied Physics*, vol. 55, n° 5S, p. 05FG06, 2016.
[76] J. Brault *et al.*, « Ultraviolet light emitting diodes using III-N quantum dots », *Materials Science in Semiconductor Processing*, vol. 55, p. 95-101, 2016.
[77] T. Huault *et al.*, « GaN/Al0. 5Ga0. 5N quantum dots and quantum dashes », *physica status solidi (b)*, vol. 246, n° 4, p. 842-845, 2009.
[78] M. Leroux *et al.*, « Stark effect in ensembles of polar (0001) Al0. 5Ga0. 5N/GaN quantum dots and comparison with semipolar (11− 22) ones », *Journal of Applied Physics*, vol. 116, n° 3, p. 034308, 2014.
[79] M. Gao *et al.*, « Compositional modulation and optical emission in AlGaN epitaxial films », *Journal of Applied physics*, vol. 100, n° 10, p. 103512, 2006.
[80] V. Fellmann *et al.*, « Ternary AlGaN alloys with high Al content and enhanced compositional homogeneity grown by plasma-assisted molecular beam epitaxy », *Japanese Journal of Applied Physics*, vol. 50, n° 3R, p. 031001, 2011.
[81] J. Brault *et al.*, « Internal quantum efficiencies of AlGaN quantum dots grown by molecular beam epitaxy and emitting in the UVA to UVC ranges », *Journal of Applied Physics*, vol. 126, n° 20, p. 205701, nov. 2019, doi: 10.1063/1.5115593.
[82] J. Brault *et al.*, « Polar and semipolar GaN/Al0. 5Ga0. 5N nanostructures for UV light emitters », *Semiconductor Science and Technology*, vol. 29, n° 8, p. 084001, 2014.
[83] J. Brault *et al.*, « Ultra-violet GaN/Al0. 5Ga0. 5N quantum dot based light emitting diodes », *Journal of crystal growth*, vol. 363, p. 282-286, 2013.
[84] J. Brault *et al.*, « UVA and UVB light emitting diodes with Al $_{y}$ Ga $_{1-y}$ N quantum dot active regions covering the 305–335 nm range », *Semiconductor Science and Technology*, vol. 33, n° 7, p. 075007, juill. 2018, doi: 10.1088/1361-6641/aac3bf.
[85] J. Brault *et al.*, « UVB LEDs grown by molecular beam epitaxy using AlGaN quantum dots », *Crystals*, vol. 10, n° 12, p. 1097, 2020.
[86] J. Piprek, « How to decide between competing efficiency droop models for GaN-based light-emitting diodes », *Applied Physics Letters*, vol. 107, n° 3, 2015.

[87] J. Brault *et al.*, « UVB and UVC LEDs with (Al, Ga)N Quantum Dots grown by MBE », in *International Workshop on Nitrides Semiconductor*, oct. 2022.
[88] J.-Y. Duboz et B. Vinter, « Theoretical estimation of tunnel currents in hetero-junctions: The special case of nitride tunnel junctions », *Journal of Applied Physics*, vol. 126, n° 17, 2019.
[89] J. Brault *et al.*, « Linear alignment of GaN quantum dots on AlN grown on vicinal SiC substrates », *Journal of Applied Physics*, vol. 93, n° 5, p. 3108-3110, mars 2003, doi: 10.1063/1.1538334.
[90] J. Brault *et al.*, « AlGaN-based light emitting diodes using self-assembled GaN quantum dots for ultraviolet emission », *Japanese Journal of Applied Physics*, vol. 52, n° 8S, p. 08JG01, 2013.
[91] J. Stangl, V. Holý, et G. Bauer, « Structural properties of self-organized semiconductor nanostructures », *Reviews of modern physics*, vol. 76, n° 3, p. 725, 2004.
[92] J. Brault *et al.*, « Staggered vertical self-organization of stacked InAs/InAlAs quantum wires on InP (001) », *Applied surface science*, vol. 162, p. 584-589, 2000.

Chapter 4

Prototype demonstration of $Al_yGa_{1-y}N$ quantum dots and (Al,Ga)N-based UV LEDs growth on hexagonal boron nitride

This chapter provides the interest in van der Waals epitaxy of two-dimensional (2D) materials and the MBE growth of $Al_yGa_{1-y}N$ QDs on a 2D material, specifically hexagonal boron nitride (h-BN). The focus is on exploring the potential of these structures for the fabrication of flexible UV LEDs. We delve into the investigation of UV-emitting $Al_yGa_{1-y}N$ QDs grown on h-BN and explore the exfoliation processes of the resulting structure. Additionally, we discuss the fabrication of QDs-based UV (Al,Ga)N LEDs on h-BN using MBE, serving as a proof of concept for their potential application. The aim is to establish a foundation for the future development of flexible UV LEDs based on these QD structures. This chapter covers:

- The motivation behind the growth of (Al,Ga)N on 2D materials.
- The MBE growth of UV emitting $Al_yGa_{1-y}N$ QDs on h-BN and its exfoliation processes.
- The fabrication of $Al_yGa_{1-y}N$ QDs based heterostructures and LEDs grown on h-BN by MBE for flexible UV emitters.

IV.1. Introduction

A material consisting of 2D layered structures arranged in a honeycomb hexagonal lattice pattern within each monolayer is referred to as a 2D material. Strong covalent bonds exist within each monolayer, while weak van der Waals forces operate between adjacent monolayers. Boron nitride (BN) stands as a versatile material composed of equal proportions of B and N atoms, configured in an alternating honeycomb arrangement. This configuration forms a hexagonal crystal structure for h-BN, characterized by crystallographic parameters a = 0.250 nm and c = 0.666 nm, with an interlayer spacing of 0.333 nm, as shown in figure 1. These attributes facilitate strong interactions with graphene due to the similar hexagonal lattice structure and the crystallographic parameters, such as the lattice constants a and c, as well as the interlayer spacing, which are very close between the two materials, thus offering substantial potential for diverse device applications. Much like in graphene, the primary interaction between distinct h-BN planes is the weak van der Waals force, while covalent bonds maintain intraplanar connectivity. This intraplanar covalence is marked by pronounced polarization due to the high sublattice asymmetry, giving rise to a substantial band gap of 6 eV [1]. The feeble interlayer interaction within h-BN results in van der Waals forces and electrostatic forces predominantly governing the interlayer distance, thereby determining optimal stacking configurations. Furthermore, h-BN exhibits low dielectric constant, piezoelectricity, and excellent stability at high temperatures [2].

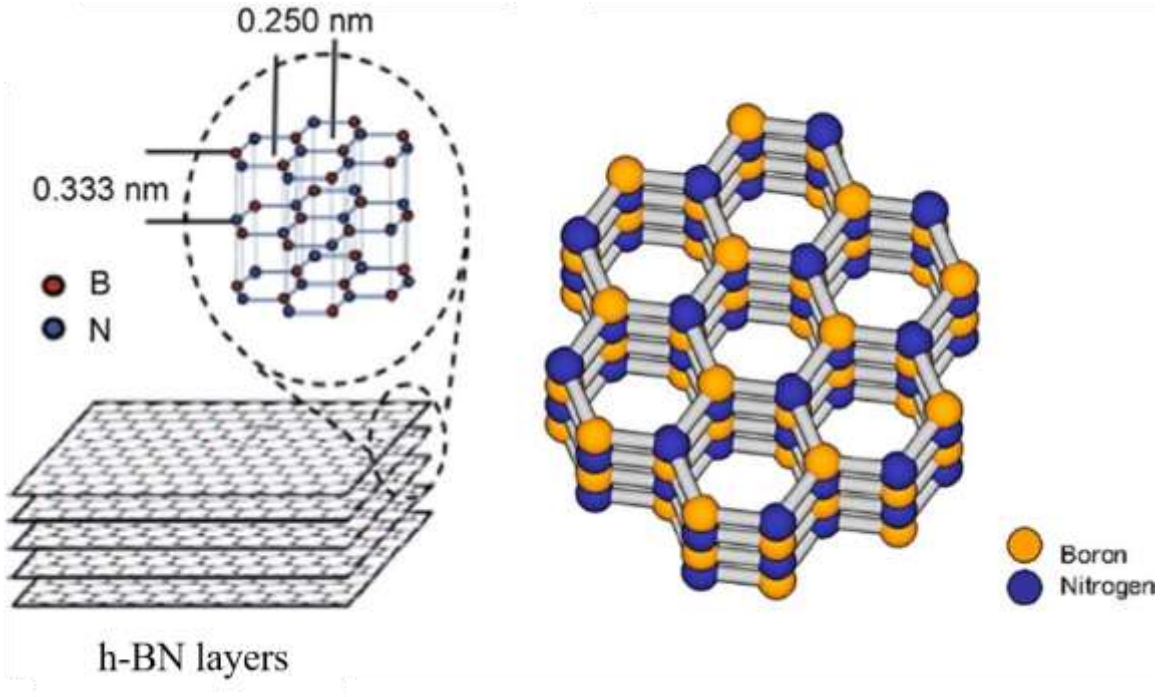

Figure 1. Schematic illustration of the atomic structure of h-BN [3].

Van der Waals Epitaxy (VdWE) is a process in which thin-film materials are grown on a substrate surface, resulting in a combination of the epilayer and substrate through weak van der Waals forces. This method was first introduced by Koma [4]. In vdWE, either the substrate, the epilayer, or both, exhibit no dangling bonds, and a lattice-mismatched heterointerface is formed. Among 2D crystals, including graphene, h-BN, and transition metal dichalcogenides (TMDs), many have proven successful as buffer layers for III-nitride vdWE. This success is primarily due to their exceptional chemical and thermal stability [5], [6], enabling them to withstand the high growth temperatures required for III-nitrides [7]. 2D materials function as buffer layers for III-nitride vdWE and serve as sacrificial layers for mechanical release in subsequent processes, as depicted in figure 2.

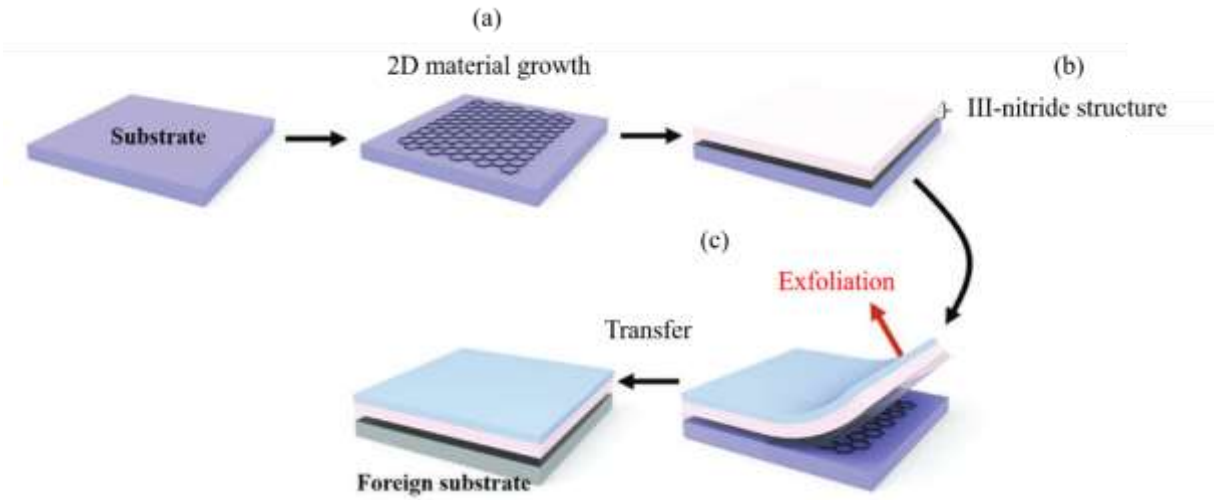

Figure 2. Schematic illustration of van der Waals Epitaxy (vdWE) and exfoliation of III-nitrides structure based on 2D buffer/release layers. The process includes three steps: (a) 2D material growth, (b) vdWE of III-nitride structure, and (c) exfoliation and transfer onto a foreign substrate. The light blue film represents the handling tape or adhesive sheet used for exfoliation [8].

Jiang et al. discovered a 5/4 coincidence ($5a_{h-BN} \approx 4a_{AlN}$) between h-BN and wurtzite AlN, resulting in a generalized lattice mismatch of approximately 0.58% [9]. Epitaxial alignments between h-BN and sapphire were identified by Paduano et al. and Kobayashi et al., with $[11{-}20]_{\text{h-BN}} \parallel [1{-}100]_{\text{sapphire}}$ and $[0001]_{\text{h-BN}} \parallel [0001]_{\text{sapphire}}$ orientations, along with a 30° in-plane rotation between them [10], [11]. This suggests a 2/1 coincidence between h-BN and sapphire [12], yielding a generalized lattice mismatch of no more than 5.5%. Additionally, Wang et al. investigated the mechanical exfoliation mechanism of III-nitride films using the h-BN release layer [13]. Their density functional theory (DFT) calculations indicated that h-BN/h-BN and GaN/h-BN interfaces have nearly free sliding paths, with a lower energy barrier for h-BN/h-BN separation (2.0 meV per atom) compared to the GaN/h-BN case (4.5 meV per

atom). This leads to a detached position between III-nitride epilayers and the vdWE substrate at the h-BN/h-BN interface, explaining the prevalence of multilayer h-BN as a release layer. Consequently, h-BN is an excellent buffer/release layer for manufacturing III-nitride flexible devices. Functioning as a III-nitride, h-BN can be epitaxially grown through MOCVD using triethylborane (TEB) and NH_3 as precursor gases [10]. This presents an opportunity to simplify the fabrication of III-nitride flexible devices by implementing in situ h-BN growth and III-nitride vdWE within the same MOCVD equipment.

Research on MBE growth of (Al,Ga)N heterostructures on h-BN is limited. Our group recently used face-to-face high-temperature annealing (FFA) to enhance the crystalline quality and surface morphology of AlN layers grown by MBE on h-BN / sapphire templates (as demonstrated in chapter 2 section II) [14]. Previous studies on nitride heterostructures grown on h-BN mainly used metal organic vapor phase epitaxy (MOVPE) growth modes. In their study, Qingqing Wu et al. conducted the growth of AlN and (Al,Ga)N-based deep ultraviolet (DUV) LEDs on monolayer h-BN that was grown via low-pressure chemical vapor deposition (LPCVD) on a copper (Cu) foil substrate and transferred onto a *c*-plane sapphire substrate by the aid of polymethylmethacrylate (PMMA). The quality of AlN films grown on h-BN/sapphire were smooth enough (surface root-mean-square (RMS) = 0.25 nm) to permit the fabrication of functioning DUV LEDs and the electroluminescence results have exhibited strong emissions with a peak wavelength of 290 nm [15], as depicted in figure 3(a) and (b).

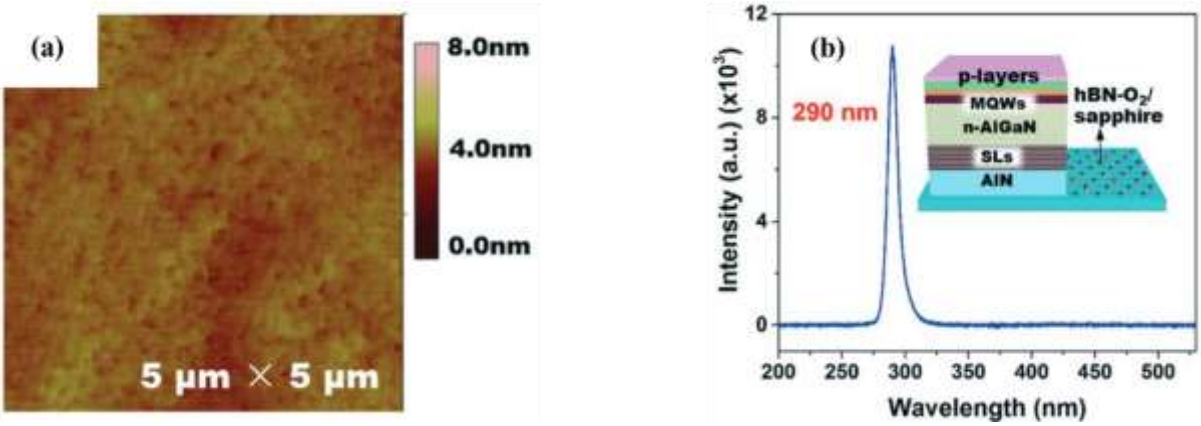

Figure 3. (a) Atomic force microscopy image of AlN on h-BN/sapphire. (b) Schematic diagram of an (Al,Ga)N-based DUV LED structure on the h-BN/sapphire and electroluminescence spectrum of the DUV LED structure [15].

The same research group also reported the successful development of crack-free crystalline AlN based heterostructures and DUV LEDs emitting at 281 nm on multilayer h-BN grown by MOVPE [16]. The AlN layer exhibited a flat and smooth surface, displaying minimal

voids and no crack. The RMS roughness measured only 0.19 nm over a scanning area of (1 × 1) μm² (as depicted in figure 4(a)). The step-flow growth mode of AlN on h-BN was indicated by the presence of atomic steps. X-ray diffraction rocking curves (XRCs) were employed to analyze the AlN film's crystalline quality. For the (0 0 0 2) and (1 0 –1 2) reflections, the full width at half maximum (FWHM) values were measured at 0.3° (1086 arcsec) and 0.9° (3240 arcsec), respectively, for an AlN film with a thickness of 1.65 μm (figure 4(b) and (c)). Subsequently, the DUV LED structure grown on AlN/h-BN/sapphire was evaluated, displaying forward voltages of 5.3 V at 20 mA, and a reverse leakage current of around 1 μA at −5 V (figure 4(e)). The electroluminescence (EL) spectra of the DUV LED chip, spanning an injected current range of 5 mA to 40 mA [16], were outlined in figure 4(f). Notably, the peak wavelength at 281 nm demonstrated minimal shift, attributed in part to the advantageous heat dissipation facilitated by the h-BN layers with high thermal conductivity [17]. The promising outcome of DUV LEDs emitting at 281 nm, showcasing robust electrical characteristics on multilayer h-BN, underscores the significant potential for mechanical device transfer.

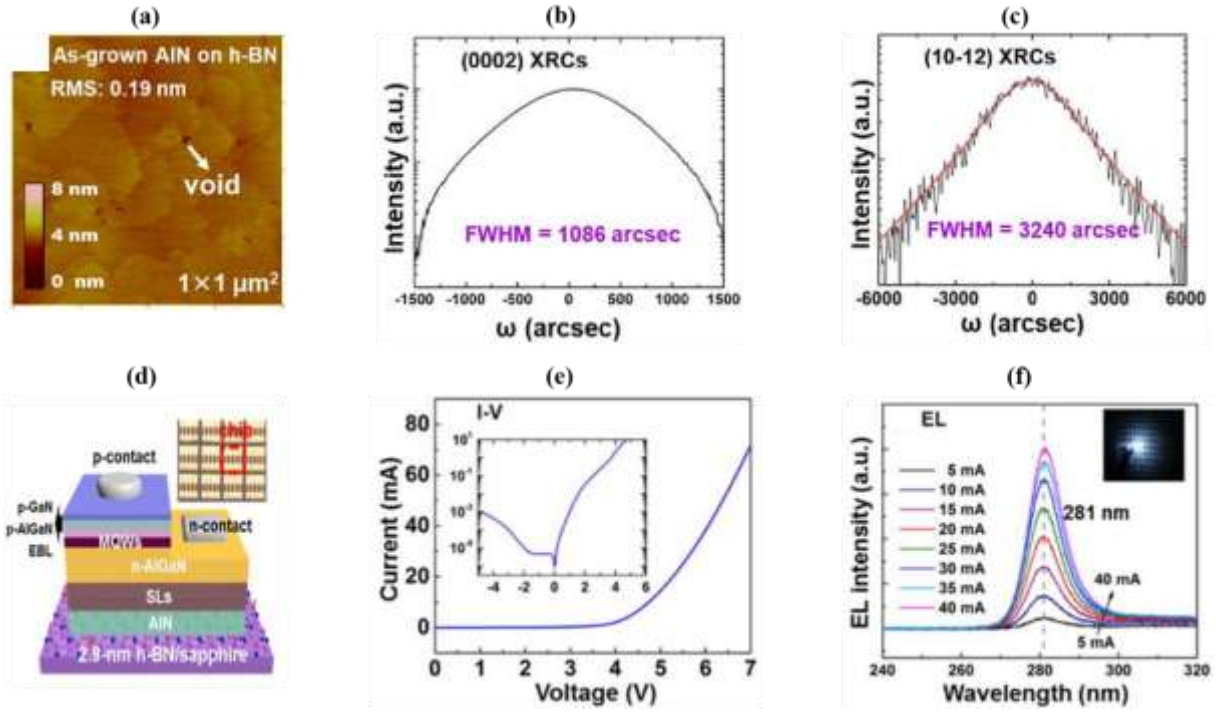

Figure 4. (a) Atomic force microscopy image of AlN on h-BN. X-ray rocking curves of (b) (0 0 0 2) and (c) (1 0 −1 2) AlN grown on h-BN. (d) Schematic diagram of DUV LED structure and optical microscope image of DUV LED chips on h-BN. (e) I-V curve of DUV LED chips on h-BN. (f) EL spectra of DUV LED chips on h-BN with an inset image of one DUV LED emission [16].

Professor Abdallah Ougazzaden's research group at the Georgia Tech Institute in Metz, France, demonstrated a wafer-scale approach to mechanically exfoliate a MOVPE-grown

(In,Ga)N/GaN multi-quantum well (MQW) structure from a 2 in. sapphire substrate using a 5-nm thick 2D h-BN layer and adhesive tape [18]. Subsequent GaN growth enables complete recovery to a 2D surface. XRD measurement of a phi scan was conducted for a (1 0 −1 2) GaN plane on (Al,Ga)N/h-BN (depicted in figure 5(b)). The diffraction peaks of GaN (1 0 −1 2) planes, exhibiting six-fold symmetry with 60-degree intervals, highlighted absence of azimuthal rotation. SEM images confirmed the comparable surface quality between the h-BN layer sample and the conventional GaN template. AFM measurements on the p-GaN surface yielded similar RMS roughness values of approximately 1.6 nm across a (5 x 5) μm² area, consistent with typical surfaces of this kind. The release of the MQW structure from the 2 in. sapphire substrate through adhesive tape was demonstrated. Figures 5(c) and (d) depict photographs of two MQW structures lifted off using an acrylic conductive adhesive layer on an aluminum foil and copper foil, respectively. Remarkably reproducible, the entire MQW structure was exfoliated from the substrate. Following the lift-off, multiple crack-free surfaces emerged, each encompassing several square millimeters. This size exceeded the dimensions of commercially available light-emitting diodes (LEDs) (300 x 300) μm². Electroluminescence from the MQW structure was acquired via probe tips, as shown in figure 5(f), revealing blue light emission from the exfoliated layers upon electrical injection, without the need for metal contact deposition [18].

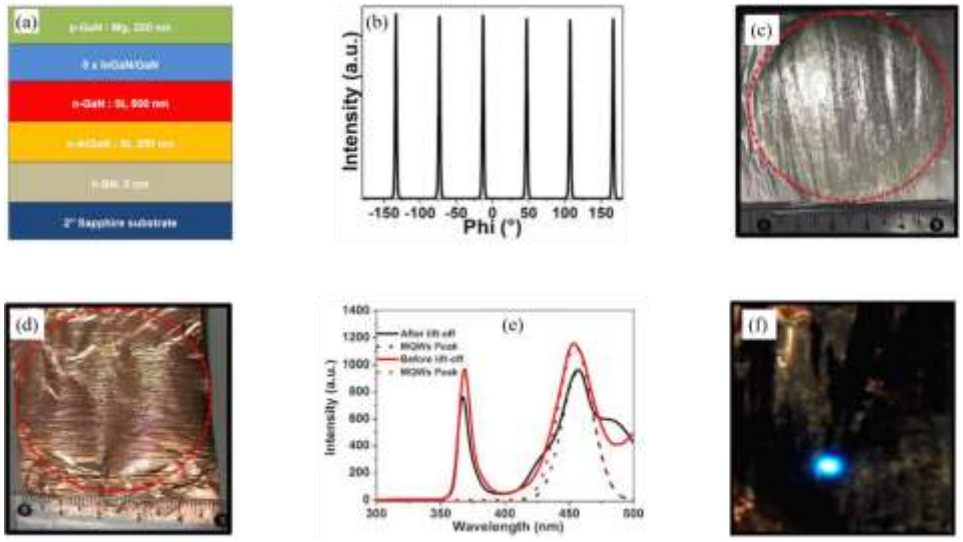

Figure 5. (a) Schematic illustration of the InGaN/GaN multi-quantum well (MQW) structure grown on 5 nm h-BN. (b) High Resolution X-Ray Diffraction (HRXRD) azimuthal off-axis phi scan of GaN (1 0 −1 2) on (Al,Ga)N/h-BN. (c) and (d) Photographs of the MQW structure after exfoliation using an aluminum foil and a copper foil, respectively. (e) Cathodoluminescence (CL) spectrum recorded at room temperature under an excitation of 17 kV before and after lift-off (excited from the p-doped layer) with fitted MQWs peaks in dotted lines. (f) Blue light emission by electrical injection from the exfoliated MQW structure [18].

However, the utilization of molecular beam epitaxial (MBE) techniques for growing QD-based (Al,Ga)N heterostructures on h-BN as a means to fabricate flexible deep ultraviolet (UV-C) LEDs has not yet been documented and constitutes a focal point of investigation in this thesis. Collaborating with the research group of Prof. Abdallah Ougazzaden at Georgia Tech-Europe in Metz, this study concentrates on the MBE growth of AlN, $Al_xGa_{1-x}N$ thick layers, and $Al_yGa_{1-y}N$ QDs layers on h-BN / sapphire templates. Furthermore, the influence of varying h-BN layer thicknesses on the surface morphology of the AlN epitaxial layers is explored. The h-BN layers, ranging from 1.5 nm to 6 nm in thickness, were directly deposited on 2-inch sapphire substrates using MOVPE. Additionally, the study delves into the implications of h-BN on the growth of AlN / $Al_xGa_{1-x}N$ layers, as well as the structural and optical characteristics of $Al_yGa_{1-y}N$ QDs. Subsequently, the exfoliation processes applied to the $Al_yGa_{1-y}N$ QDs structure grown on the 6 nm h-BN / sapphire are presented, along with an examination of the structural and optical properties of the QDs before and after the exfoliation procedures.

IV.2. Growth of (Al,Ga)N-based quantum dots heterostructures on h-BN

The growth of h-BN templates with thicknesses of 1.5 nm, 3 nm and 6 nm was performed using an Aixtron MOVPE close-coupled showerhead (CCS) reactor on (0 0 0 1) sapphire substrates. The process was carried out at a temperature of 1280 °C and a pressure of 90 mbar. Triethylboron (TEB) and ammonia (NH_3) were employed as precursor gases for boron (B) and nitrogen (N), respectively. More comprehensive information on the growth conditions for h-BN can be found in previously published reports [19]. The growth of (Al,Ga)N structures on the h-BN templates was performed using MBE in a RIBER 32P reactor. Solid sources for the III-elements (Al, Ga) and NH_3 as a nitrogen source were utilized for the growth of AlN and (Al,Ga)N, except for the QDs active region where NH_3 was replaced by a nitrogen (N_2) plasma source. This substitution was necessary to enable the formation of QDs and 3D islands, as NH_3 would result in a 2D growth mode that inhibits their formation [20]. Under N_2, a 2D-3D "Stranski-Krastonov" growth mode can be achieved [21], allowing for the growth of $Al_yGa_{1-y}N$ QDs on $Al_xGa_{1-x}N$ (with $x > y$) [22]. At first, the growth of AlN on h-BN templates was investigated, as a function of the h-BN thickness. Then, two structures, labelled as sample A and sample B, were fabricated on the 3 nm and 6 nm h-BN templates (see figure 6). The fabrication process for both samples was similar, except for the thickness of the $Al_xGa_{1-x}N$ layer. For both samples, a 200 nm thick AlN layer was initially grown with the following conditions: a 10 nm thick AlN buffer layer was grown at 1070°C with an ammonia flow rate of

50 sccm and a growth rate of 50 nm/h. Subsequently, the 200 nm AlN layer was grown at 1120°C with an ammonia flow rate of 50 sccm and a growth rate of 100 nm/h. Following this, a 500 nm thick $Al_{0.7}Ga_{0.3}N$ layer was grown at 870°C for sample A and a 330 nm thick layer for sample B, both at a growth rate of 290 nm/h. Next, an active region consisting of six $Al_{0.3}Ga_{0.7}N$ QD planes with an Al nominal composition (n.c.) of 0.3, separated by $Al_{0.7}Ga_{0.3}N$ barriers lattice matched to the $Al_{0.7}Ga_{0.3}N$ template, was deposited. The equivalent 2D thickness of the $Al_{0.3}Ga_{0.7}N$ (n.c.) QDs was 7 monolayers (MLs), approximately 1.8 nm, with 1 ML corresponding to half the c-lattice parameter, considering a variation of the lattice parameter following Vegard's law between AlN and GaN. In between the QD planes, 5 nm thick $Al_{0.7}Ga_{0.3}N$ cladding layers were grown for both samples. After the deposition of the fifth QD plane, a 30 nm thick $Al_{0.7}Ga_{0.3}N$ layer was grown at 820°C. Finally, the sixth and last QD plane was deposited on the surface of the top cladding layer for both samples.

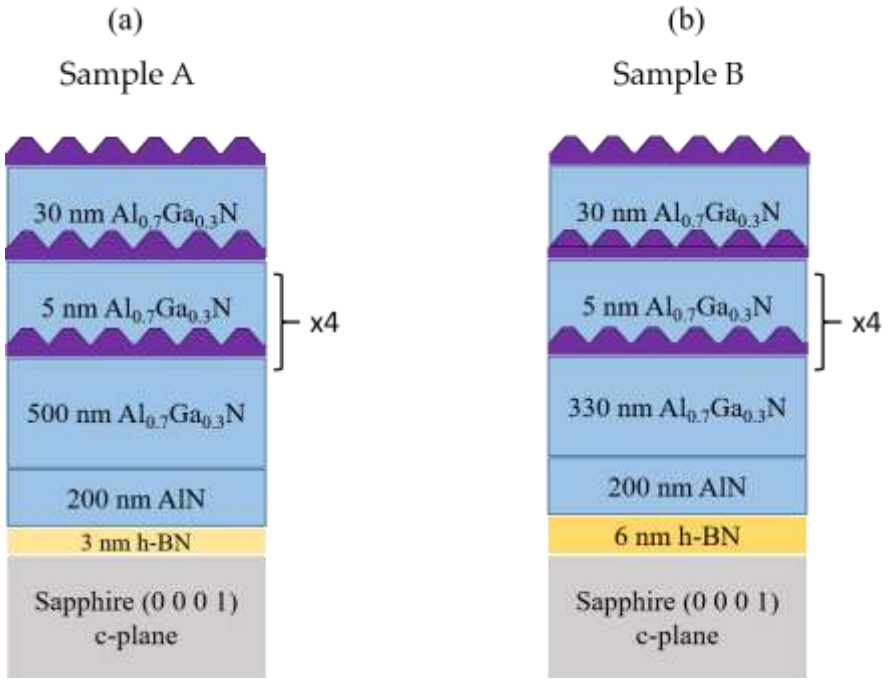

Figure 6. Schematics of the two $Al_yGa_{1-y}N$ quantum dots (QDs) structures grown on h-BN / sapphire templates. (a) $Al_yGa_{1-y}N$ QDs structure grown on 3 nm h-BN on sapphire (sample A). (b) $Al_yGa_{1-y}N$ QDs structure grown on 6 nm h-BN on sapphire (sample B).

Atomic force microscopy (AFM) EDGE-DIMENSION (BRUKER, Billerica, MA, USA), operating in tapping mode with a silicon tip having a radius between 5 – 10 nm was used to study the surface morphologies of h-BN and AlN. In addition, a diamond coated tip with a typical radius between 5 – 10 nm was also used to investigate the morphology of the surface QDs plane and all data were processed using WSxM software [23]. Furthermore, X-ray diffraction (XRD) measurements were conducted using a PANalytical X'Pert PRO MRD four-

circle diffractometer (Malvern Panalytical, Malvern, United Kingdom) to assess the crystalline quality of the $Al_xGa_{1-x}N$ / AlN layers and examine the impact of h-BN on the subsequent layers. Regarding the optical characteristics, continuous wave PL measurements were carried out at room temperature (RT) and low temperature (LT), i.e. at 300 K and 12 K, in a closed cycle Helium (He) cryostat using a frequency-doubled Argon (Ar) laser at 244 nm (5.08 eV) with an excitation power of 20 mW.

In the first part of this section, the growth of AlN on h-BN templates and the study of its surface roughness evolution as a function of the AlN thickness are presented. The second part is devoted to an in-depth XRD characterization of $Al_{0.7}Ga_{0.3}N$, as well as $Al_{0.3}Ga_{0.7}N$ (n.c.) QDs main structural and optical properties including surface morphology study by AFM and PL measurements.

IV.2.1. AlN growth by MBE

IV.2.1.1. Characterization of h-BN templates before growth

To analyze the surface morphology, the 1.5 nm, 3 nm and 6 nm thick h-BN layers on sapphire samples were initially examined. AFM topographic images of (10 x 10) μm^2 and (2 x 2) μm^2, along with their corresponding root-mean-square (RMS) values, are depicted in figures 7(a), (b), and (c).

Figure 7 (a) shows a (10 x 10) μm^2 AFM scan image of the 1.5 nm h-BN layer exhibiting a smooth surface morphology with a measured surface RMS roughness of 0.6 nm. The inset is a (2 x 2) μm^2 AFM scan image with a surface RMS roughness measured of 0.6 nm Figure 7(b) is a (10 x 10) μm^2 AFM scan that shows the 3 nm h-BN layer covering the entire wafer surface with a measured surface RMS roughness of 1.1 nm. The inset of (2 x 2) μm^2 AFM scan has a surface RMS roughness measured of 1.1 nm. Figure 7(c) shows instead the 6 nm h-BN layer with a surface RMS roughness of 1.3 nm. The inset of (2 x 2) μm^2 scan is closely similar to the one in figure 7(b) with a surface RMS roughness of 1.2 nm. The occurrence of wrinkles, represented by the white segments observed in the AFM images in figures 7(b) and (c), is a common characteristic of 2D materials. Regarding h-BN, these wrinkles are primarily caused by the variation in the thermal expansion coefficient (TEC) between h-BN and sapphire substrates. During the cooling process, this TEC mismatch leads to the generation of compressive strain within the h-BN layer, resulting in the formation of wrinkles. The wrinkling instability facilitates the release of energy, resulting in the creation of surface roughness in the sample [19], [24], [25]. The surface morphology of the 1.5 nm h-BN template displayed in

figure 7(a) shows the absence of wrinkles, which could suggest that the actual thickness might be less than the specified 1.5 nm and possibly thinner. This observation aligns with the findings reported by Dipankar Chugh et al. in their study involving thin h-BN (≤1.5 nm) on sapphire templates, who reported the absence of wrinkles for an h-BN deposited thickness below 1.5 nm [26].

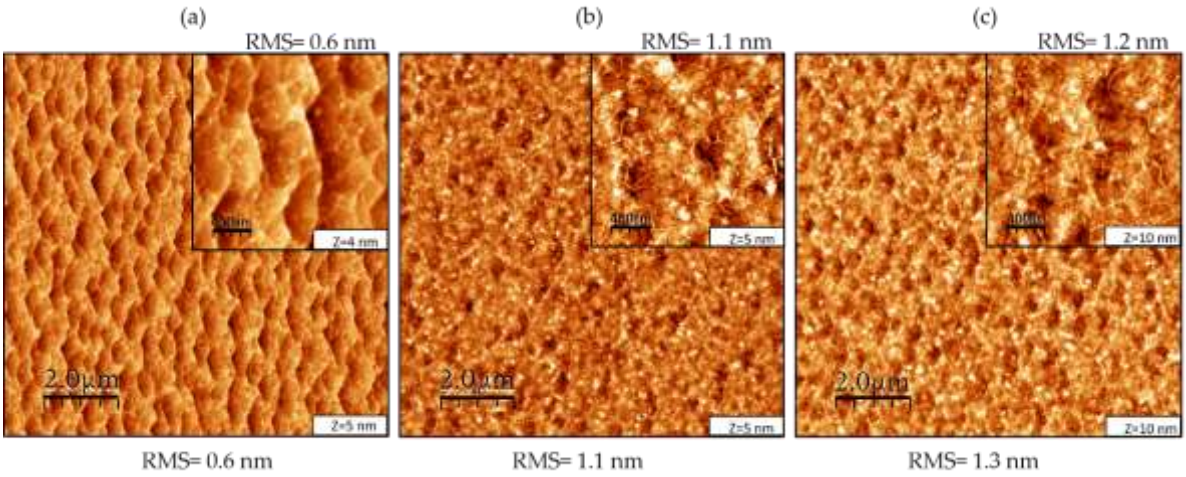

Figure 7. Atomic force microscopy (10 × 10) μm^2 scan images of: (a) 1.5 nm thick h-BN layer grown on sapphire c-plane substrate. (b) 3 nm thick h-BN layer grown on sapphire c-plane substrate, (c) 6 nm thick h-BN layer grown on sapphire c-plane substrate. The inset shows (2 × 2) μm^2 scan images. The term Z represents the vertical scale and the variation in height in the AFM images, and its value is reported at the bottom right hand side of each image.

IV.2.1.2. AlN growth on h-BN / sapphire templates by MBE

We proceeded to grow AlN (total thickness of 200 nm) on the 1.5 nm, 3 nm and 6 nm thick h-BN / sapphire templates by using ammonia-assisted MBE. The 200 nm layers were grown in three steps: First, a 50 nm layer was grown followed by another 50 nm thick layer and a 100 nm final layer. This systematic growth was done as a way to study the evolution of the AlN layer growth on h-BN in term of surface morphology with increasing thickness. It resulted in the growth of Al-polar layers with predominantly 2D surfaces, which were accompanied by the presence of 3D islands, as illustrated in figure 8(a). As the subsequent AlN layers were grown and their thicknesses increased from 50 nm to 200 nm, a transition in the reflection high-energy electron diffraction (RHEED) pattern was observed, shifting from an initial 3D growth mode to a 2D growth mode, as depicted in figure 8(b). This transition was characterized by a decrease in the density of 3D islands and a reduction in the RMS roughness at smaller length scales. Consequently, when performing (2 × 2) μm^2 scans in the areas between the 3D islands, low RMS values below 1 nm were obtained.

Figures 9 and 10 illustrate the surface morphology evolution when the AlN thickness increased from 50 nm to 200 nm for the three samples.

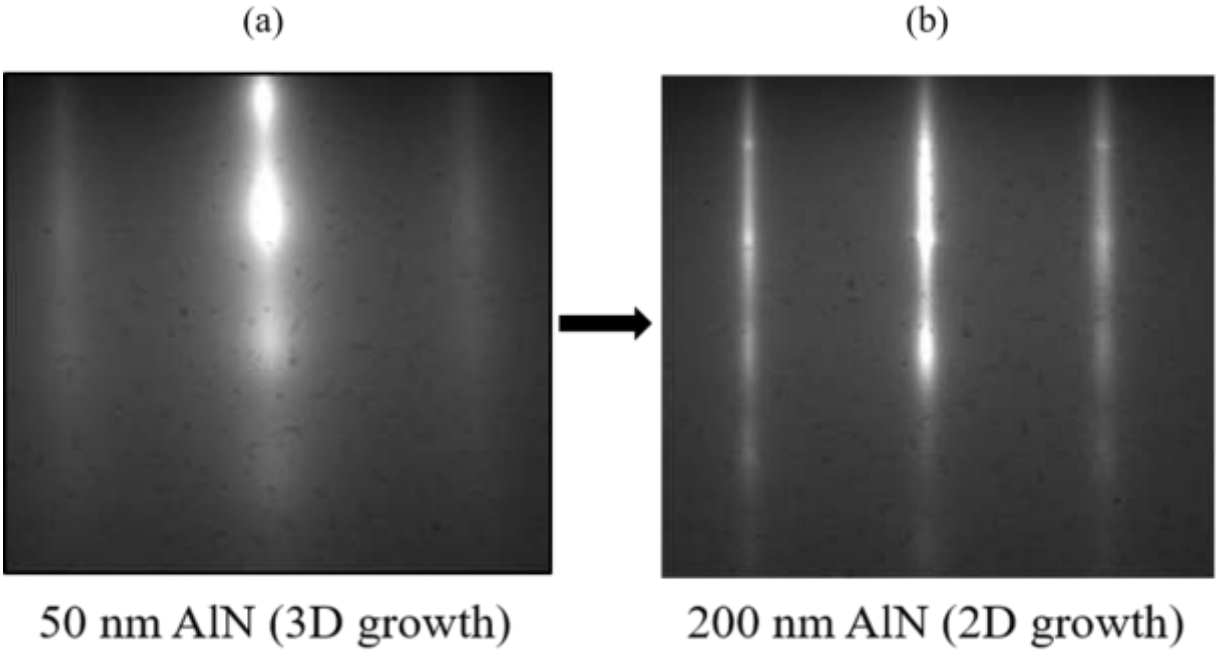

Figure 8. Reflection high-energy electron diffraction (RHEED) images, along the <1−100> direction, of the AlN growth on h-BN / sapphire templates. (a) For a 50 nm thick AlN layer, which surface morphology is defined by Bragg spots indicating the presence of 3D islands on the surface. (b) For a 200 nm thick AlN layer that is mainly characterized by diffraction lines, indicating a smoother 2D surface morphology. This modification of the RHEED pattern comes from the smoothening of the surface morphology and the reduction 3D islands density as the AlN layer thickness increases.

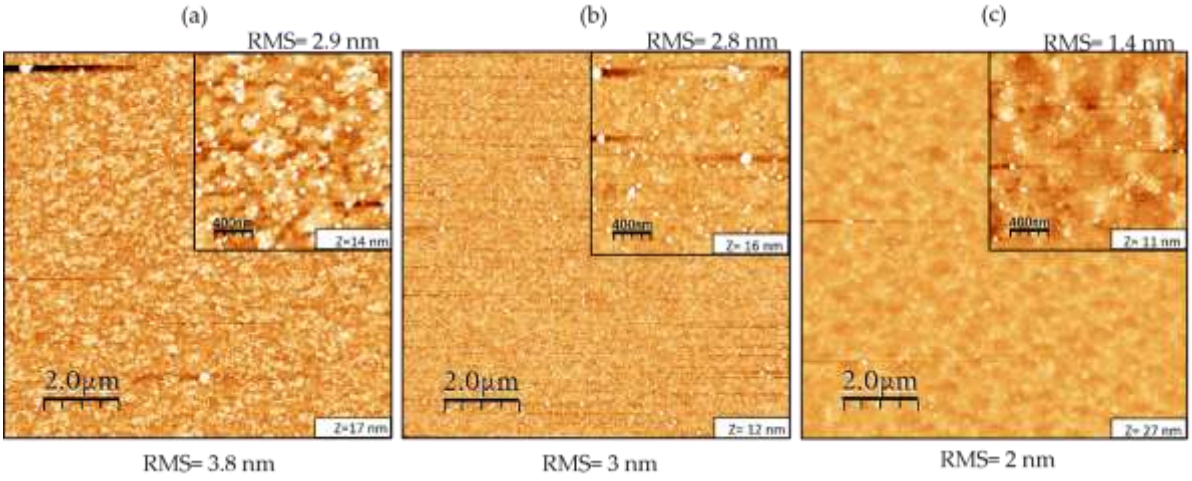

Figure 9. Atomic force microscopy (10 × 10) μm^2 scan images of: (a) 50 nm AlN grown on 1.5 nm h-BN, (b) 50 nm AlN grown on 3 nm h-BN, and (c) 50 nm AlN grown on 6 nm h-BN. The inset shows (2 × 2) μm^2 scan images. The term Z represents the vertical scale and the variation in height in the AFM images, and its value is reported at the bottom right hand side of each image.

For the h-BN templates of different thicknesses, the initial surface characteristics of the 50 nm thick AlN layer varied. In the case of the 1.5 nm h-BN template, the initial surface exhibited a roughness with a root mean square (RMS) value of 3.8 nm when scanned over a (10 x 10) μm^2 area. This roughness was primarily due to a high density of 3D island-like structures, numbering around 2 x 10^{10} cm^{-2}. These island structures had heights of approximately 30 nm with a variance of ± 5 nm and lateral dimensions around 100 nm with a variance of ± 20 nm. As the thickness of the AlN layer increased to 200 nm, there was a significant improvement in the surface morphology. The RMS roughness decreased to 0.8 nm for the same scan area, and the density of 3D island-like structures reduced to approximately 2 x 10^9 cm^{-2}. The height of these structures decreased to around 9 nm with a variance of ± 2 nm, while their lateral size increased to about 145 nm with a variance of ± 25 nm. For the 3 nm h-BN template, the initial surface morphology of the 50 nm thick AlN layer was also rough, with an RMS value of 3 nm when scanned over a (10 x 10) μm^2 area. Similar to the previous case, a high density of 3D island-like structures was dominant, with a density of approximately 3 x 10^{10} cm^{-2}. These island structures had heights of around 32 nm ± 10 nm and lateral dimensions of approximately 120 nm ± 30 nm. Increasing the AlN thickness to 200 nm led to a rougher surface morphology, with an RMS increase to 3.5 nm. However, the density of 3D island-like structures decreased to approximately 8 x 10^9 cm^{-2}, and their height reduced to about 25 nm ± 5 nm, while their lateral size increased to roughly 150 nm ± 30 nm. Additionally, the surface between the islands, as observed in the inset image when scanned over a (2 x 2) μm^2 area, appeared smoother with an RMS value of 1.9 nm compared to the (10 x 10) μm^2 scan range. Finally, for the 6 nm h-BN template, the initial surface morphology of the 50 nm thick AlN layer was rough as well, with an RMS value of 2 nm when scanned over a (10 x 10) μm^2 area. This roughness was attributed to the presence of 3D island-like structures, with a density of around 4.5 x 10^9 cm^{-2}, heights averaging 22 nm ± 5 nm, and lateral dimensions averaging 85 nm ± 15 nm. Upon increasing the AlN thickness to 200 nm, the surface roughness also increased, resulting in an RMS value of 2.7 nm. This evolution was similar to the surface changes observed for the 3 nm h-BN template. The density of the islands decreased to approximately 1 x 10^9 cm^{-2}, while their height and lateral size increased to approximately 40 nm ± 15 nm and 125 nm ± 20 nm, respectively. Notably, the surface morphology in-between the islands, as observed in the inset image when scanned over a (2 x 2) μm^2 area, displayed a very smooth surface with an RMS value of 0.5 nm, contrasting with the rougher (10 x 10) μm^2 scan range.

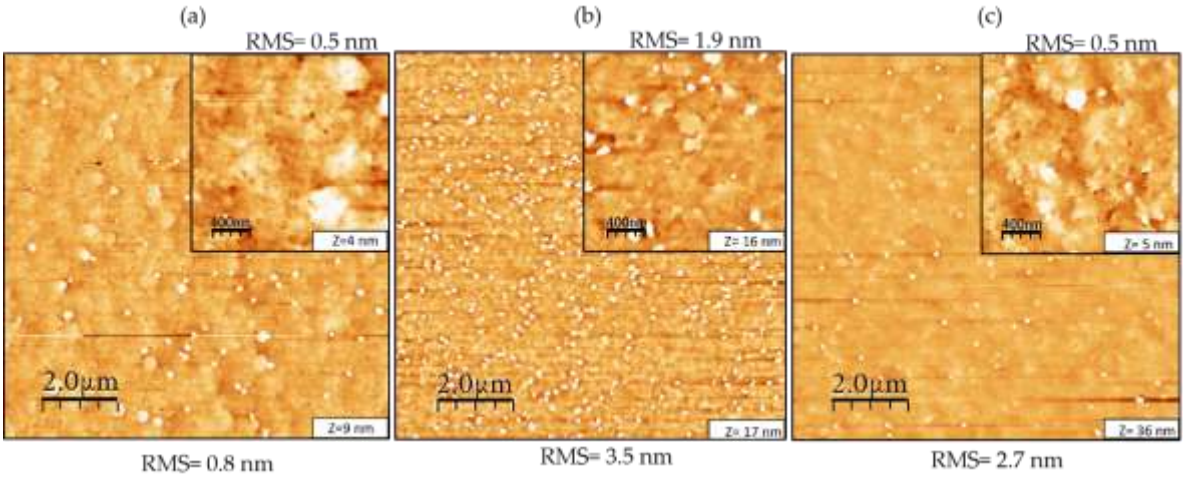

Figure 10. Atomic force microscopy (10 × 10) µm^2 scan images of: (a) 200 nm AlN grown on 1.5 nm h-BN, (b) 200 nm AlN grown on 3 nm h-BN, and (c) 200 nm AlN grown on 6 nm h-BN. The inset shows (2 × 2) µm^2 scan images. The term Z represents the vertical scale and the variation in height in the AFM images, and its value is reported at the bottom right hand side of each image.

With the increase in AlN thickness, the RMS roughness of the surface improved positively for the three samples. Initially, the increase in AlN thickness resulted in a reduction in the 3D island density, although the individual islands grew larger in size. As a result, the surface between the islands became smoother, contributing to the improved RMS roughness. The growth of AlN on the 1.5 nm thick h-BN template led to a more significant improvement in surface morphology compared to the growth on the 3 nm and 6 nm h-BN templates. This improvement is evident in terms of reduced surface RMS roughness and the islands' height. It can be attributed to the initially smooth and wrinkle-free surface morphology of the 1.5 nm h-BN template, which had an RMS value of 0.6 nm even before the growth process started. A difference can still be seen between the AlN growth on the 3 nm and 6 nm thick h-BN templates where smoother AlN layers with lower islands density have been obtained on the 6 nm h-BN compared to the 3 nm h-BN template despite both h-BN templates having the same initial surface RMS roughness values of 1.2 nm. The RMS roughness evolution as a function of the AlN thickness for the three samples for scan ranges of (10 x 10) µm^2 and (2 x 2) µm^2 is summarized in figure 11.

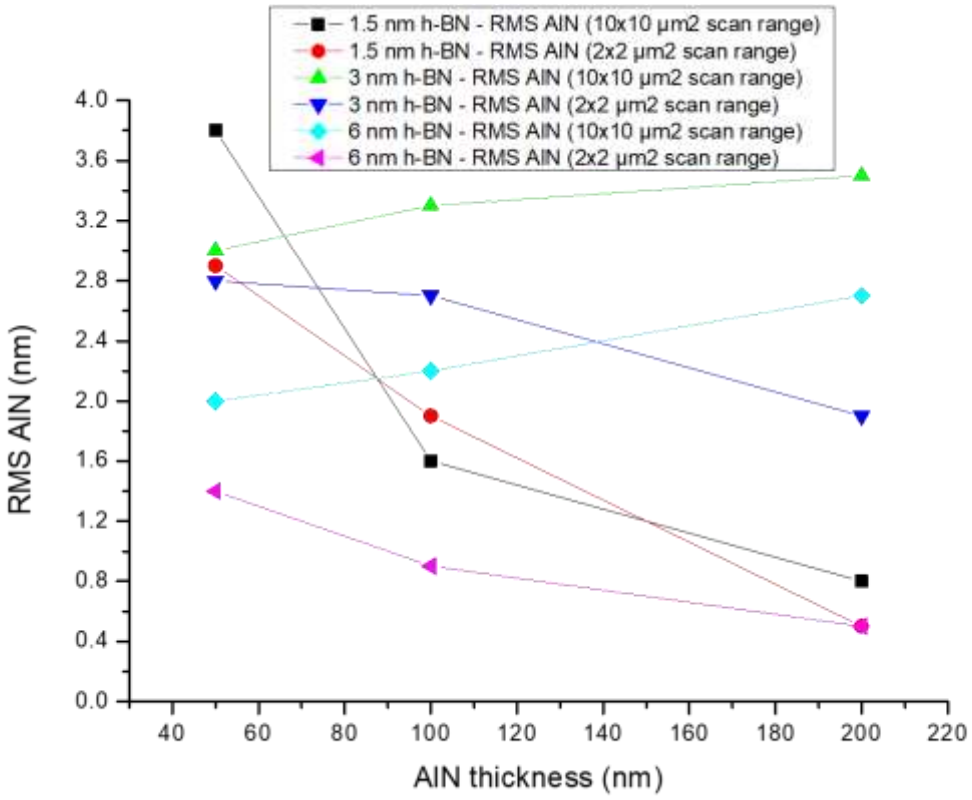

Figure 11. RMS roughness evolution as a function of the AlN thickness for 1.5 nm, 3 nm, and 6 nm h-BN templates. The RMS values were measured on atomic force microscopy topographic images of size (10 x 10) µm^2 and (2 x 2) µm^2.

IV.2.2. $Al_{0.3}Ga_{0.7}N/Al_{0.7}Ga_{0.3}N$ QDs structural and optical properties

IV.2.2.1. Morphological properties

We chose to grow $Al_{0.7}Ga_{0.3}N$ layers and an $Al_{0.3}Ga_{0.7}N$ QDs active region exclusively on the 3 nm and 6 nm h-BN templates, despite the 1.5 nm h-BN template displaying the smoothest surface morphology after the AlN growth among the three options. This decision was made to investigate the influence of h-BN thickness on the quantum dots (QDs) growth and properties, while also considering the functionality of h-BN as a release or transfer layer in our experiments. The choice of these specific thicknesses ensured complete coverage of h-BN on the sapphire substrate, enabling more efficient subsequent exfoliation of the layer. By utilizing scotch-tape, the exfoliation process became simpler, allowing for the lifting of the entire wafer due to the presence of h-BN layers [18], [25], [27].

After the growth of the $Al_{0.7}Ga_{0.3}N$ layers and $Al_{0.3}Ga_{0.7}N$ QDs active region, AFM has been performed in order to investigate the QDs structural properties. Figures 12(a) and (b) show AFM images of samples A and B for (500 x 500) nm^2 and (200 x 200) nm^2 scan ranges.

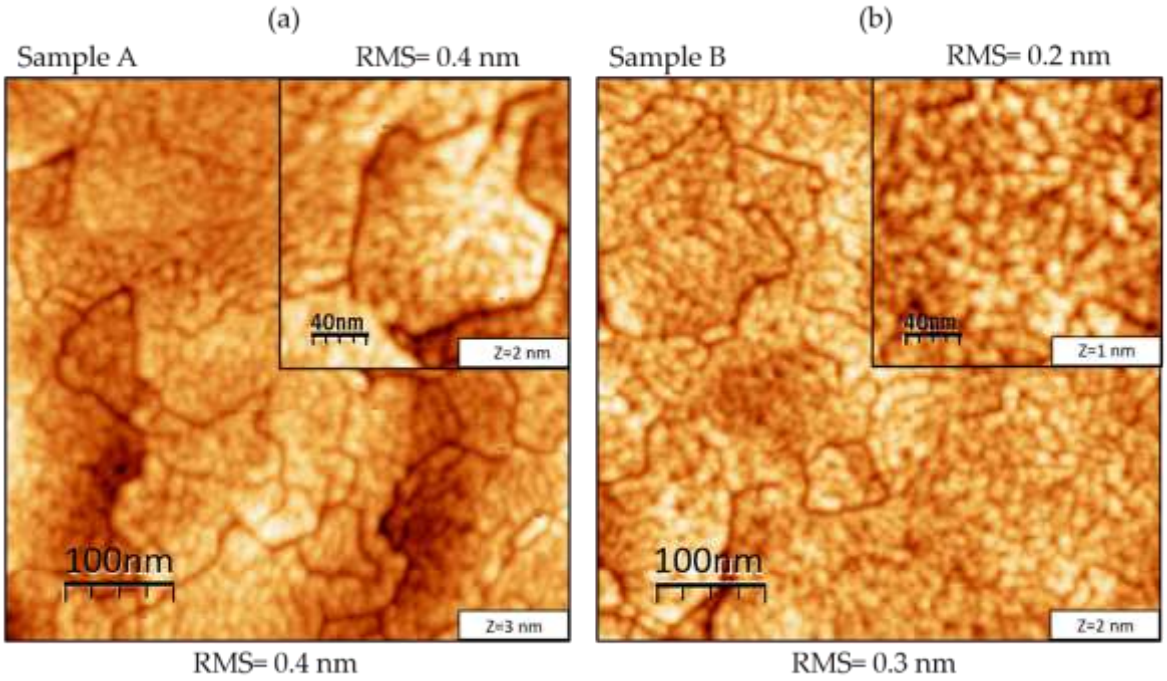

Figure 12. Atomic force microscopy scan images of (500 × 500) nm^2 with an inset of (200 × 200) nm^2 showing the morphology of the QDs on the surface for (a) sample A and (b) sample B.

The QDs densities, height and diameter were determined from AFM measurements for both samples. For sample A, the QDs average height was found to be ranging between 6 MLs to 8 MLs with the highest QDs population having a height of 7 MLs based on the histogram (red sticks) in figure 13(a). The QDs average diameter was found around 13 nm ± 3 nm. Furthermore, for sample B, the QDs height was also found to be ranging between 6 MLs and 8 MLs based on the histogram (blue sticks) in figure 13(b), with the highest QDs number for 7 MLs and the QDs average diameter around 15 nm ± 2 nm. The QDs height results for both samples are similar to previous results obtained by our group on $Al_yGa_{1-y}N$ QDs grown by MBE [28]. Regarding the QDs density, it was estimated at 4 x 10^{11} cm^{-2} for both samples. This trend of high QDs density (>10^{11} cm^{-2}) is usually observed in the case of $Al_yGa_{1-y}N$ QDs compared to GaN QDs [28], [29], which is attributed to the lower surface mobility characteristic of Al adatoms compared to Ga ones. Meanwhile, both samples present domains on their surface, which are separated by surface depressions (depression depth for both samples ~ 8 Å) with a density ranging around 3 x 10^7 to 4 x 10^7 cm^{-1}. The significant thermal expansion difference between h-BN with α_c= 37.7x10^{-6} K^{-1} and α_a= -2.72x10^{-6} K^{-1} [30], AlN and GaN (see Chapter I Table I.1 for the thermal expansion coefficients of AlN and GaN) can lead to thermal stress, which can be at the origin of material deformation and cracks.

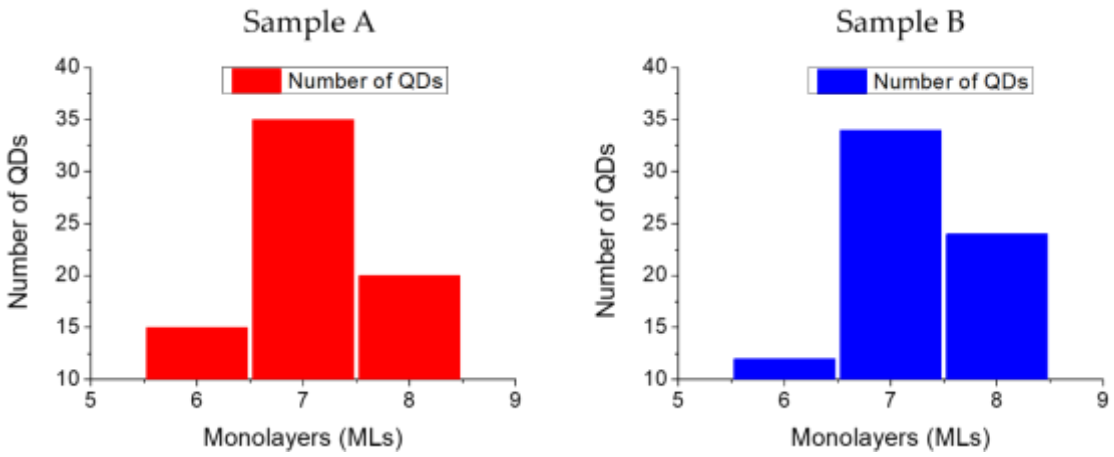

Figure 13. Histograms showing the QDs height distribution as a function of monolayer (ML) units (1 ML = 0.257 nm) for (a) sample A and (b) sample B.

IV.2.2.2. Crystal properties by X-ray diffraction and transmission electron microscopy

Figure 14 illustrates the 2θ-ω X-ray diffraction diagram performed on samples A and B ranging from 10° to 170° in order to study all the layers orientations along the growth direction. For both samples, only the (0 0 0 1) orientation is observed for nitride layers: at an angle of 36°, the $Al_xGa_{1-x}N$ and AlN (0 0 0 2) peaks are mingled. The $Al_xGa_{1-x}N$ and AlN (0 0 0 4) peaks can be respectively seen at 75.3° and 76.5°. The $Al_xGa_{1-x}N$ and AlN (0 0 0 6) peaks are well separated at 132.9° and 136.38°. The thinner peaks correspond to the sapphire substrate: the (0 0 0 6) and (0 0 0 12) reflections are observed with high intensities and three forbidden reflections of sapphire are detected. It should be mentioned that two peaks, observed at 17.8° and 44.4°, are coming from the sample holder itself since the studied samples are smaller than the X-ray beam footprint.

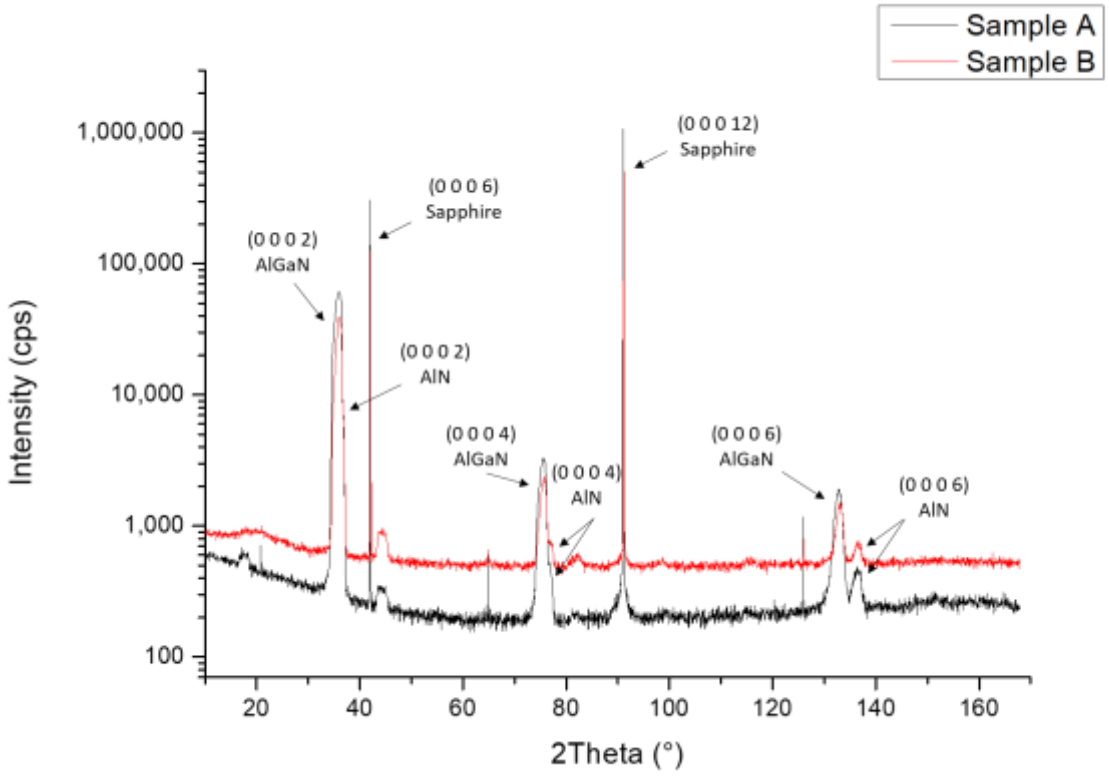

Figure 14. XRD 2θ-ω scan for sample A and B.

Figure 15 illustrates the XRD Phi (in-plane rotation of the sample) scans of the (1 0 −1 1) $Al_{0.7}Ga_{0.3}N$ layer and (1 0 −1 4) sapphire substrate performed on sample A. Twelve peaks have been observed for the $Al_{0.7}Ga_{0.3}N$ layer instead of the six peaks expected for a hexagonal structure. This result can be explained by the presence of two domains twisted by 30° in the growth plane.

When (Al,Ga)N hexagonal layers are grown directly on sapphire, the (Al,Ga)N unit cell is turned by an angle of 30° compared to that of sapphire. Thereby, the sharp peaks have the classic orientation of (Al,Ga)N on sapphire. The wide peaks represent a new in-plane orientation turned by 30°, thus creating two different orientations in the growth plane. The h-BN layer permitted this structural arrangement since it is forbidden for such orientations to happen on sapphire.

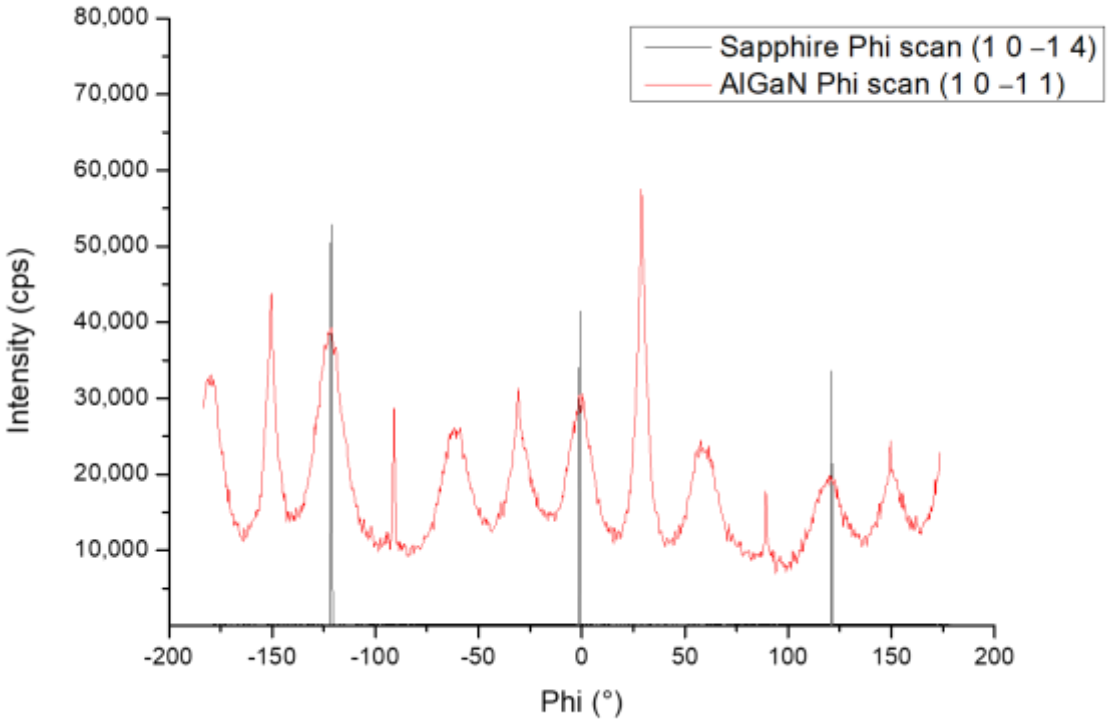

Figure 15. XRD Phi scan performed on sample A along the (1 0 −1 1) and the (1 0 −1 4) skew planes for $Al_{0.7}Ga_{0.3}N$ and sapphire, respectively.

The study continued on the $Al_{0.7}Ga_{0.3}N$ (1 0 −1 1) plane by performing two omega scans at Phi = 0° and Phi = 30°, respectively. The two omega scans show different intensities and FWHM values, as illustrated in figure 16. The ω scan peak in red color (Phi = 0°), corresponds to the $Al_{0.7}Ga_{0.3}N$ orientation due to the presence of h-BN on the sapphire surface. The FWHM of this peak is equal to 20°, indicating crystalline domains with a high defects density. On the other hand, the ω scan peak in black color (Phi = 30°), corresponds to the $Al_{0.7}Ga_{0.3}N$ orientation typically observed on sapphire. However, it presents an unusual peak shape: a careful analysis shows that this peak is composed of a base similar to the large peak presented in red color (Phi = 0°). This feature suggests that in this classical orientation of $Al_{0.7}Ga_{0.3}N$, two domains are present. One of which, that corresponds to the thinner part of the peak (FWHM = 7°), is of better crystalline quality than the domain corresponding to the wider part of the peak (FWHM = 20°).

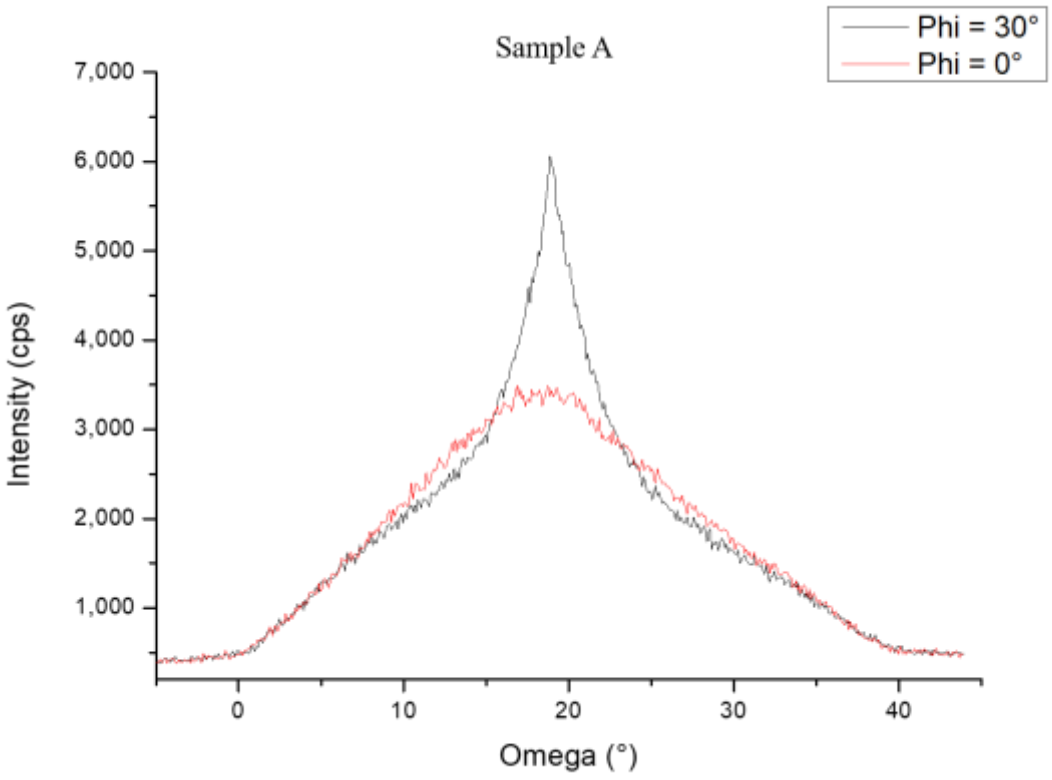

Figure 16. XRD omega scan along the AlGaN (1 0 −1 1) skew plane for sample A chosen from two different Phi peaks (0° and 30°).

Our investigation continued by performing XRD Phi scan of the (1 0 −1 1) $Al_{0.7}Ga_{0.3}N$ layer and (1 0 −1 4) sapphire substrate in sample B, as depicted on figure 17. In contrast to the results obtained from sample A, where twelve peaks could also be expected, only six peaks were observed for the $Al_{0.7}Ga_{0.3}N$ layer in sample B. This discrepancy suggests the presence of a single domain twisted by an angle of 30° relative to the sapphire substrate, confirming the conventional orientation of (Al,Ga)N on sapphire. This outcome implies potential differences in the crystalline quality between the 3 nm and 6 nm thick h-BN templates.

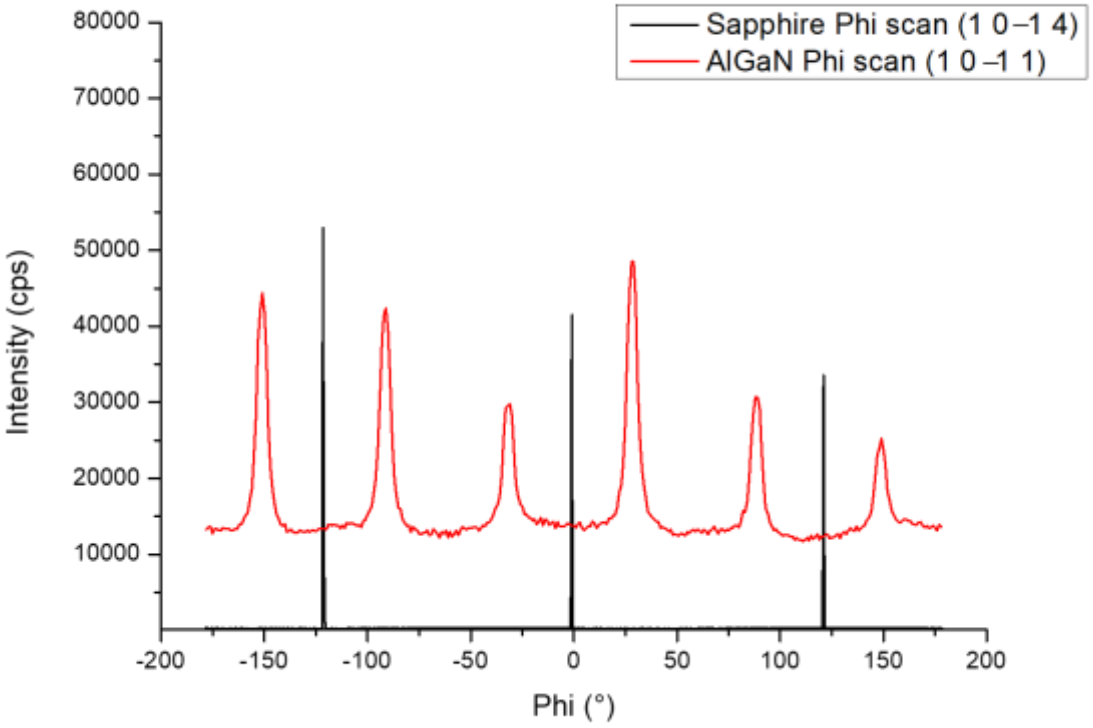

Figure 17. XRD Phi scan performed on sample B along the (1 0 −1 1) and the (1 0 −1 4) skew planes for $Al_{0.7}Ga_{0.3}N$ and sapphire, respectively.

To delve deeper into this matter, we conducted an omega scan at Phi = 30° on the $Al_{0.7}Ga_{0.3}N$ (1 0 −1 1) plane of sample B, as illustrated in figure 18. Similar to sample A, the peak exhibited an unusual shape, with a base resembling the prominent red peak (Phi = 0°) shown in figure 16. This suggests the presence of two domains in this classical orientation of $Al_{0.7}Ga_{0.3}N$. Specifically, one domain, corresponding to the narrower part of the peak (FWHM = 6.3°), exhibits superior crystalline quality compared to the domain associated with the broader section of the peak (FWHM = 22°).

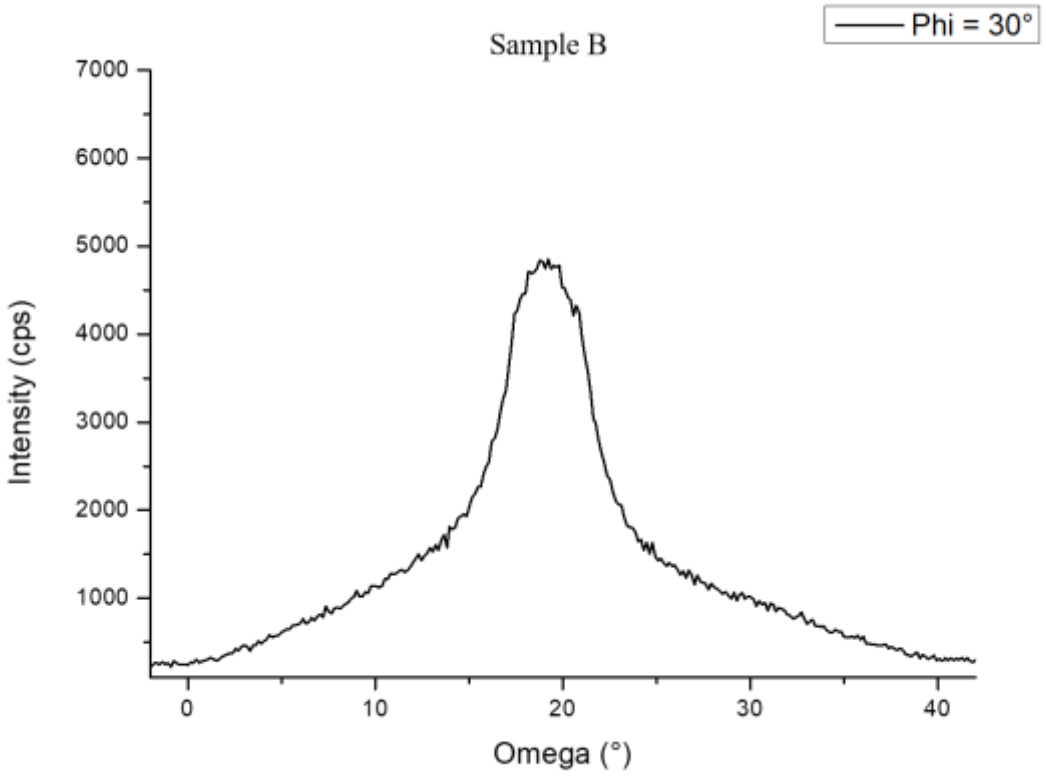

Figure 18. XRD omega scan along the AlGaN (1 0 −1 1) skew plane for sample B chosen from Phi = 30°.

The comprehensive investigation of sample B's crystal properties continued through a transmission electron microscopy (TEM) study. Philippe Vennéguès from CRHEA (CNRS) conducted the study, including sample preparation and most of the observations. The high-angle annular dark-field scanning transmission electron microscopy (HAADF-STEM) image in figure 19(b) portrays the complete structure of sample B, thereby confirming the thicknesses of AlN and (Al,Ga)N within the heterostructure original design. These thickness values were previously determined during the growth process, as illustrated in figure 19(a). The TEM image reveals that the AlN layer possesses a thickness of 200 nm, while the (Al,Ga)N layer's thickness ranges from 320 nm to 330 nm prior to the addition of the QDs planes.

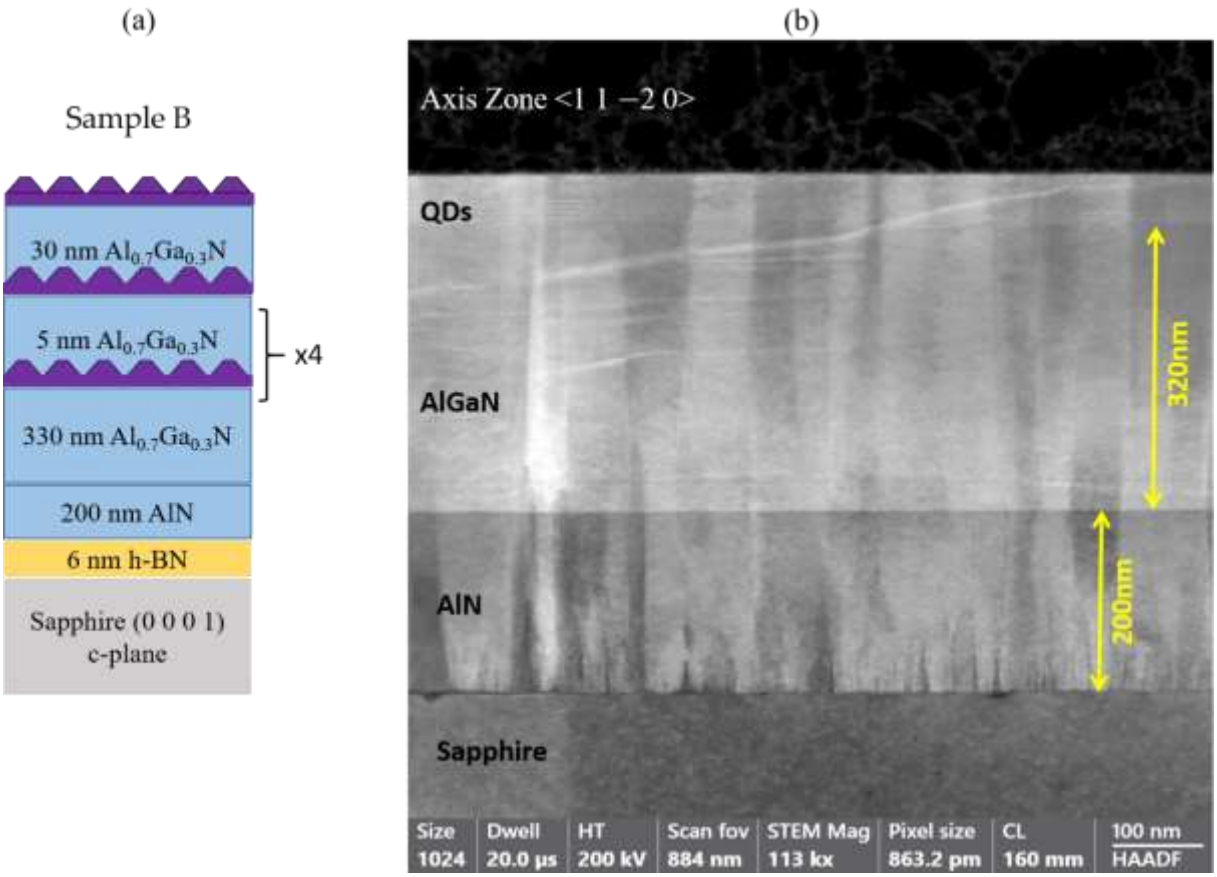

Figure 19. (a) Schematic of the $Al_yGa_{1-y}N$ quantum dots (QDs) structure grown on 6 nm h-BN / sapphire template (sample B). (b) HAADF-STEM image of sample B along the <1 1 −2 0> zone axis.

Figure 20 shows an energy dispersive X-ray chemical map (a) together with a chemical profile (b) for sample B. By plotting the atomic fraction (%) against the position, the composition pattern emerged. Beginning with the AlN layer, the composition was determined to be around 100% Al (i.e. not completely 100% because of the measurement error). However, this composition sharply diminishes as it goes from the AlN layer through the (Al,Ga)N layers. In these layers, the composition ratio was revealed to be approximately 60% Al and 40% Ga. It is noteworthy that this estimation contrasts with the Al composition of 70% targeted by setting the growth conditions of the (Al,Ga)N cladding layer. Additionally, selected area electron diffraction (SAED) measurement conducted along the <1 −1 0 0> axis zone has revealed additional spots aligning with the <1 1 −2 0> azimuth, as illustrated in figure 21(a). These extra spots are indicative of domains that exhibit a 30° twist, a characteristic further evident in the dark-field cross-sectional TEM image captured along the <1 −1 0 0> axis zone (depicted in figure 21(c)). The presence of high dislocation density is also evident from the image in figure 21(b). The significant insights gained from TEM analysis contribute to a more comprehensive interpretation of the XRD results obtained for sample B. Although sample A displayed twelve

peaks while sample B exhibited only six, the TEM results, indicating a 30° domain rotation, suggest that sample B likely experiences two distinct orientations in its growth plane due to h-BN, albeit to a lesser extent compared to sample A.

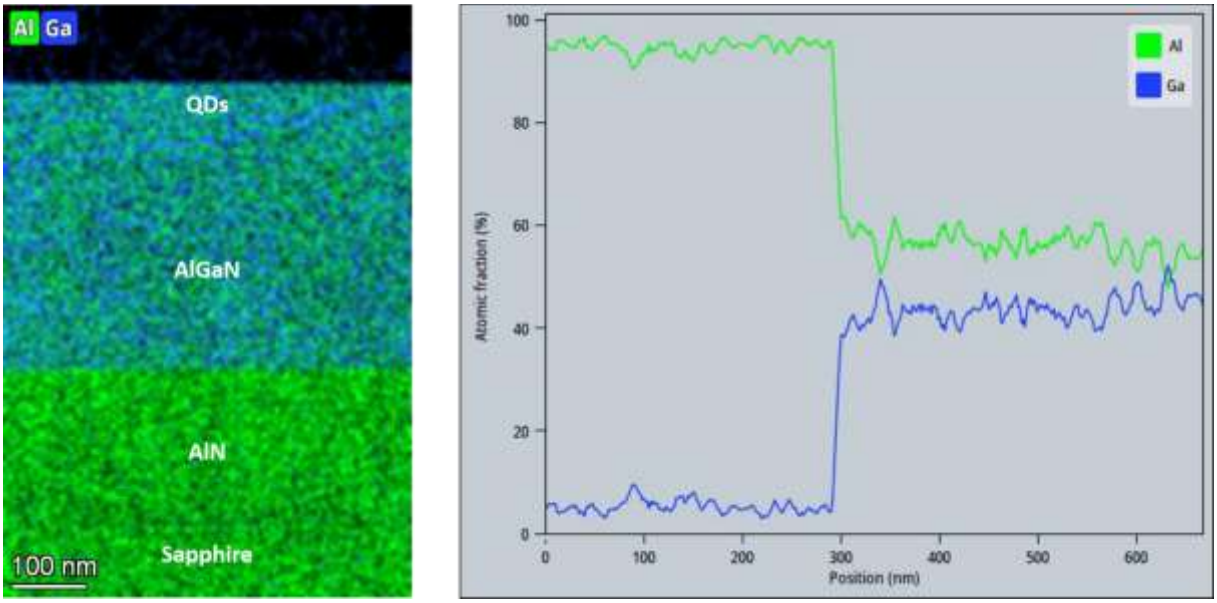

Figure 20. On the left, atomic composition calculation of Al and Ga in the heterostructures of sample B based on the HAADF-STEM image. The right graph is a plot of the atomic fraction (%) as a function of the position (nm).

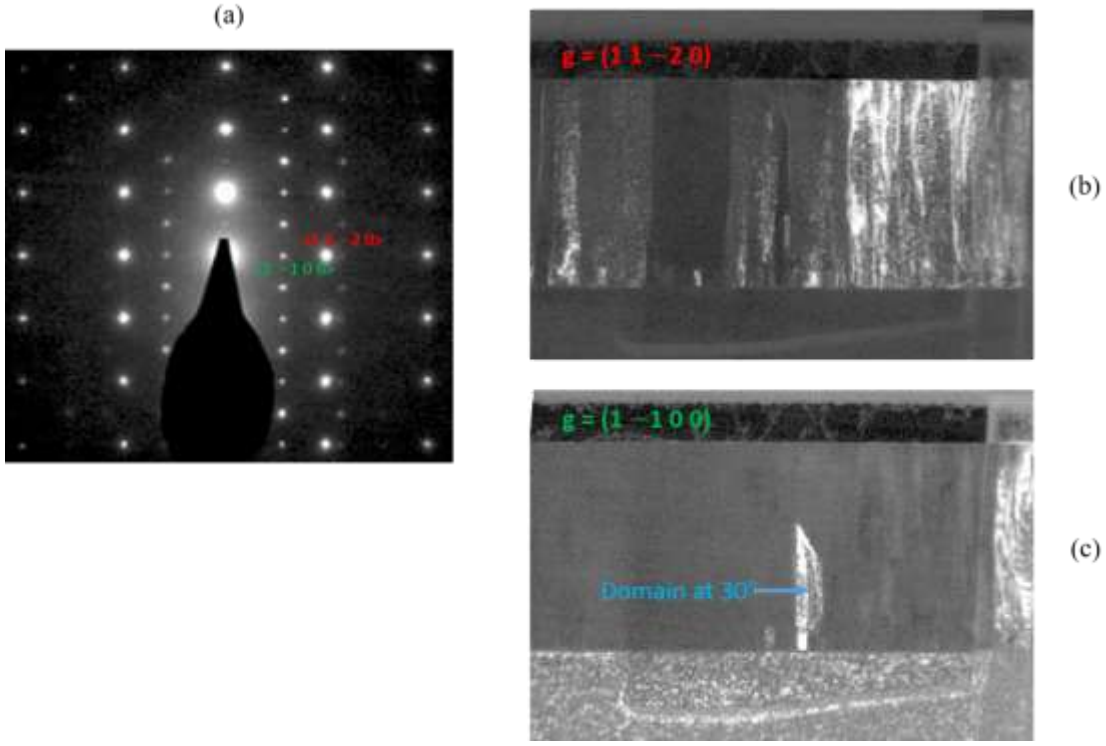

Figure 21. (a) Selected area electron diffraction (SAED) image along the <1 −1 0 0> axis zone revealing additional spots aligning with the <1 1 −2 0> azimuth. (b) and (c) (1 1 −2 0) and (1 −1 0 0) dark-field cross-sectional images, respectively.

Concerning the QDs, the successful growth of six $Al_{0.3}Ga_{0.7}N$ QD planes is confirmed by the HAADF-STEM image shown in figure 22(a). These six planes consist of five QDs planes that are separated by $Al_{0.7}Ga_{0.3}N$ cladding layers with a spacing of 5 nm, and a final sixth plane positioned at the surface, separated by a 30 nm $Al_{0.7}Ga_{0.3}N$ cladding layer. For a closer examination of the QDs planes, HAADF images along the <1 1 −2 0> and <1 −1 0 0> zone axes are presented in figures 22(b) and (c), respectively. The calculated thickness of each QD plane was approximately 1.8 nm, which corresponds to the deposited 7 monolayers (MLs) of $Al_{0.3}Ga_{0.7}N$. It's noteworthy that 1 ML is equivalent to half the c-lattice parameter, taking into account the lattice parameter variation following Vegard's law between AlN and GaN.

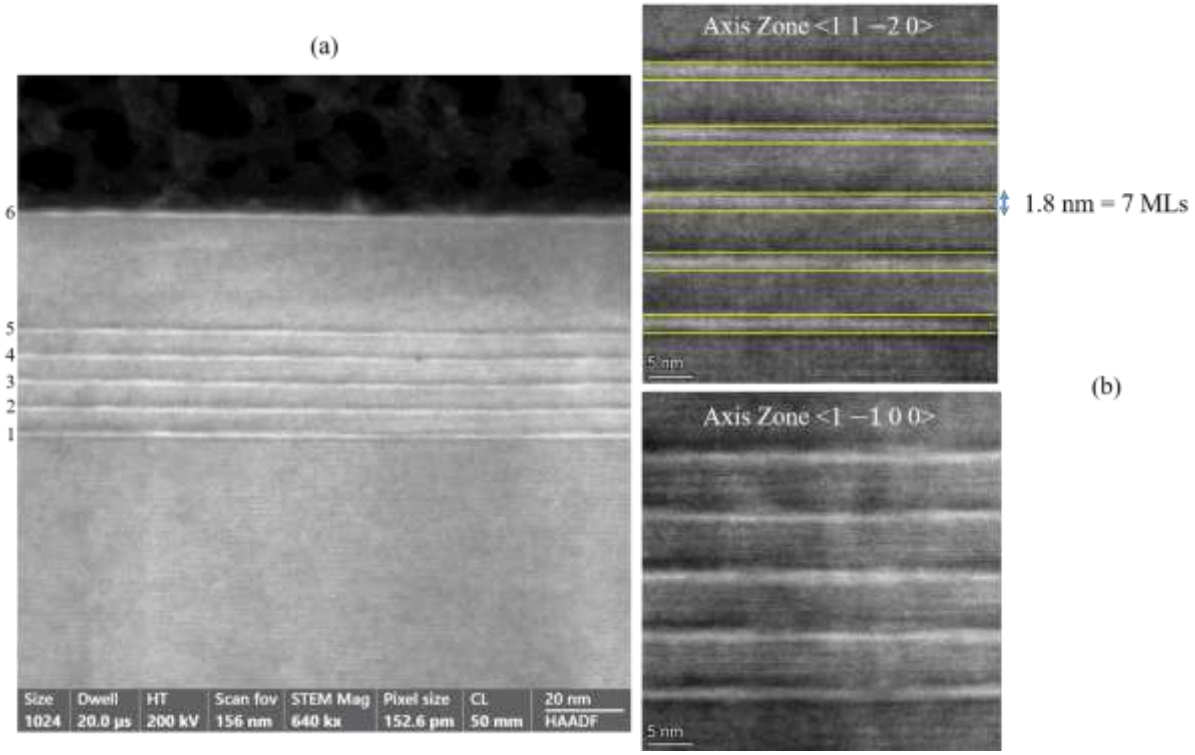

Figure 22. (a) HAADF-STEM image showing the six QDs planes. (b) HAADF images along the <1 1 −2 0> (top) and <1 −1 0 0> (bottom) axis zones of the five $Al_{0.3}Ga_{0.7}N$ (n.c.) QDs planes with an average height (i.e. thickness) of 1.8 nm (corresponding to 7 MLs of $Al_{0.3}Ga_{0.7}N$) and separated by a 5 nm-thick $Al_{0.7}Ga_{0.3}N$ capping layer.

IV.2.2.3. Optical properties

IV.2.2.3.1. Continuous wave photoluminescence

In order to study the optical characteristics of the $Al_{0.3}Ga_{0.7}N$ QDs, continuous PL measurements at LT (12K) and at RT (300K) were performed and compared for both samples using the same excitation conditions. This study was performed by Nikita Nikitskiy, PhD student in CRHEA. Figure 23 shows the PL spectrum at 12K and 300K for both samples. For sample A with $Al_yGa_{1-y}N$ QD nominal composition (n.c.) y of 0.3, two PL peak emissions were observed at LT. A main PL peak with the highest intensity has an emission in the UV-C region at 275 nm (4.5 eV). It originates from the exciton radiative recombination in the $Al_{0.3}Ga_{0.7}N$ (n.c.) QDs. In addition to this main PL peak, a low energy shoulder peak at 283 nm (between 4.3 eV and 4.4 eV) with a lower intensity has also been observed. The modulation of PL intensity is affected by Fabry-Perot interference fringes caused by the significant differences in refractive indices at the interfaces of (Al,Ga)N / sapphire and air / (Al,Ga)N. As shown in figure 23(a), a weak decrease of both the QDs PL peaks is observed from LT to RT that confirms the strong 3D carrier confinement in the $Al_{0.3}Ga_{0.7}N$ (n.c.) QDs. The FWHM of the PL peak at RT was 18 nm. On the other hand, sample B with the same QD n.c. y of 0.3 as sample A, had one clear PL peak emission observed at both LT and RT in the UV-C region at a very close wavelength of 280 nm (4.43 eV). As shown in figure 23(b), a decrease of the QDs PL peak intensity is observed from LT to RT. The FWHM of the PL peak at RT was 16 nm, a value roughly similar to sample A.

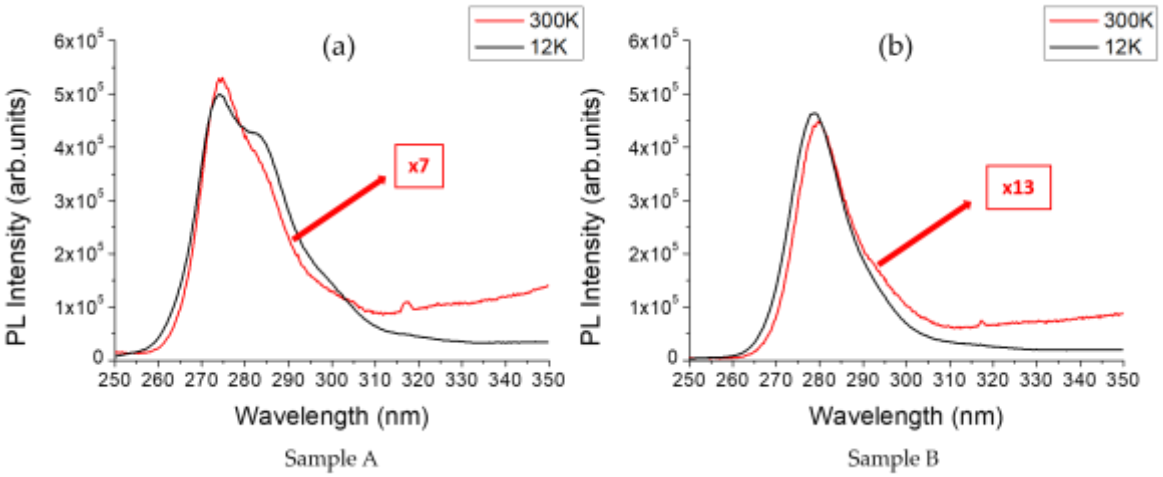

Figure 23. Photoluminescence (PL) spectrum, at 12K and 300K , of $Al_{0.3}Ga_{0.7}N$ (n.c.) QDs with an $Al_{0.3}Ga_{0.7}N$ deposited amount of 7MLs for samples A (a) and B (b). In figure (a), the PL intensity has been multiplied by 7 for the spectrum obtained at 300K while in figure (b) the PL intensity has been multiplied by 13 for the spectrum obtained at 300K.

From these measurements, it is found that the spectrally integrated PL intensity ratio (I (300K) / I (12K)) of the QD emission peak between RT and LT is roughly around 10%. It is rather high compared to the case of QWs on high dislocations density (Al,Ga)N materials, which is below 10^{-2} [31]. In addition, the PL integrated intensity of samples A and B was compared to a reference structure based on a QD plane grown on sapphire, as depicted in figure 24. In this case, the QDs are made of $Al_{0.1}Ga_{0.9}N$ (n.c.) QDs in $Al_{0.5}Ga_{0.5}N$ cladding layers and therefore emit at a higher wavelength, but the comparison has been done to investigate more deeply the radiative efficiency of QDs grown on h-BN templates. Besides, the PL intensity has been corrected based on the detection and optical fiber sensitivities as a function of the emitted wavelength. It has been found that the PL integrated intensity of the QDs grown on h-BN templates (samples A and B) is lower by 15 to 45 times compared to a reference structure based on QDs grown on sapphire. This result indicates that there is still room for improvement in the structure design and growth conditions optimizations of both h-BN and (Al,Ga)N materials for UVC LEDs.

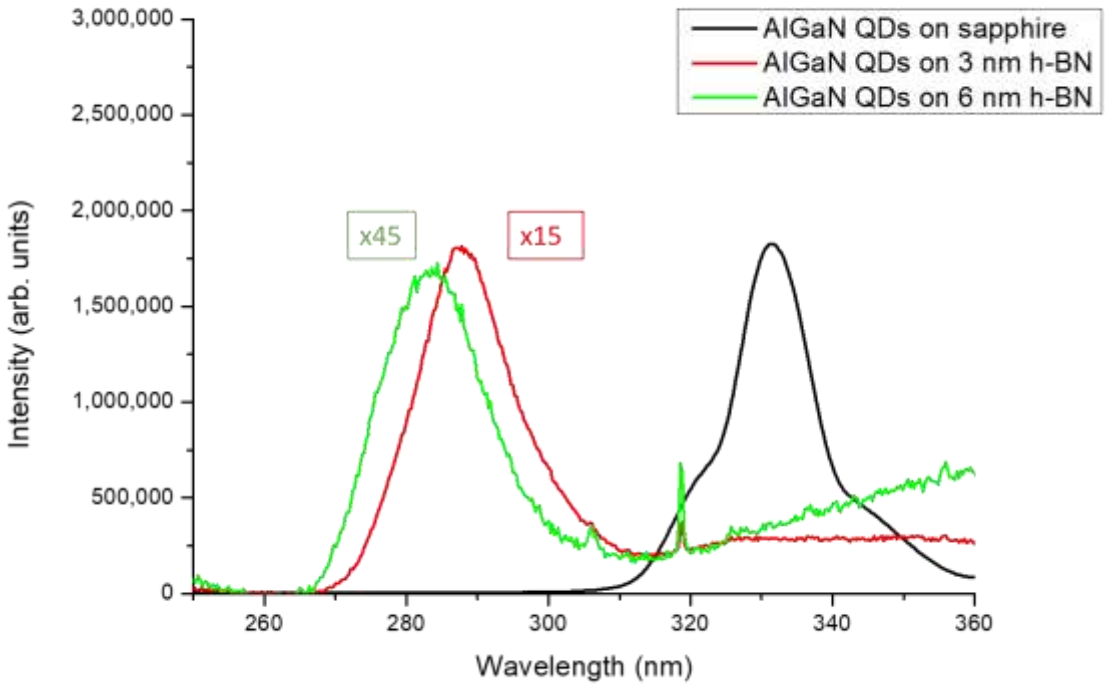

Figure 24. Photoluminescence measurements of an $Al_yGa_{1-y}N$ QD plane at room temperature (300K) for: a reference sample with $Al_{0.1}Ga_{0.9}N$ (n.c.) QDs / $Al_{0.5}Ga_{0.5}N$ grown on sapphire (black color), a sample with $Al_{0.3}Ga_{0.7}N$ (n.c.) QDs / $Al_{0.7}Ga_{0.3}N$ grown on 3 nm h-BN template on sapphire (red color), and a sample with $Al_{0.3}Ga_{0.7}N$ (n.c.) / $Al_{0.7}Ga_{0.3}N$ QDs grown on 6 nm h-BN template on sapphire (green color). The spectra show that the PL integrated intensity is around 15 times (red spectrum) to 45 times (green spectrum) lower compared to the reference sample.

IV.2.3. Discussion

The proposed study, which focuses on both 3 nm and 6 nm h-BN thicknesses, aimed to explore the impact of such h-BN templates on the nucleation and growth of (Al,Ga)N based heterostructures and quantum dots (QDs) active regions, targeting UVC emitters. Therefore, the choice of these specific thicknesses ensured complete coverage of h-BN on the sapphire substrate, enabling both an efficient nucleation of the AlN layer and opening the perspective of a possible subsequent exfoliation of the layer, as it was already reported in previous studies by Prof. Ougazzaden's group [18], [27]. By employing ammonia-based MBE, the growth of AlN on h-BN / sapphire templates resulted in the formation of Al-polar layers characterized by predominantly 2D surfaces. However, the presence of 3D islands disrupted the otherwise flat morphology of the layers. Following the subsequent AlN layers growth and thickness increase from 50 nm to 200 nm in total, the surface RMS roughness estimated by AFM measurements for a large (10 x 10) μm^2 scan range increased for both samples, while it decreased for a small (2 x 2) μm^2 scan range. This feature originates from the presence of large 3D AlN islands [14] originating from an initial 3D growth mode (figure 8(a)), which have also been observed for AlN growth on sapphire [32], and lead to an important increase of the surface RMS roughness. As the AlN layer thickness is increased and the 3D islands density is decreased, the surface RMS roughness at smaller scale can be reduced, consequently leading to low RMS values for (2 × 2) μm^2 scans in-between the 3D islands. After the growth of the $Al_{0.7}Ga_{0.3}N$ layers and $Al_{0.3}Ga_{0.7}N$ (n.c.) QDs active region, AFM measurements showed a homogenous distribution of QDs with the majority of QDs having a height of 7 MLs, which was confirmed by TEM (figure 22(b)) and a density around 4 x 10^{11} cm^{-2} for both samples. In addition, the XRD symmetric 2θ-ω scan of samples A and B showed that all the layers observed in both samples are grown along the growth axis (c-axis). On the other hand, the XRD 360° Phi scan for sample A showed twelve peaks instead of the usual six peaks observed on $Al_xGa_{1-x}N$ structures grown on sapphire. After performing a Phi scan on the sapphire template, it was found that the six other peaks are actually coming from another domain that is rotated in the growth plane by an angle of 30°, compared to the domain that originate from the wurtzite crystal structure of the (Al,Ga)N layers grown on sapphire. This is due to the h-BN template that created two different orientations in the growth plane. The TEM study confirmed the existence of the 30° rotated domain, as shown in figure 21(c). These results confirm the orientation guidance from h-BN observed in a previous study done by S. Sundaram et al. where III-nitrides were grown on h-BN on c-plane sapphire [27]. They observed that the varying degrees of misorientation that can

be observed in III-nitrides are depending on the crystalline quality of h-BN. The III-nitrides could be even amorphous beyond a certain crystallinity limit of h-BN. This observation shows the importance of growing good crystalline quality h-BN layers. Furthermore, the QDs PL emission showed a maximum intensity in the UV-C range between 275 and 280 nm at room temperature and with a FWHM around 16 – 18 nm, which is attributed to fluctuations in both the QDs size and composition (Al content) [33]–[35].

In our study, the structural properties of (Al,Ga)N layers grown on h-BN were compared to those obtained in a previous study conducted by our research group, where we investigated the growth of $Al_yGa_{1-y}N$ / $Al_xGa_{1-x}N$ QDs on sapphire using MBE and are shown in table I. Based on X-ray measurements, it was found that the FWHM of the $Al_xGa_{1-x}N$ layers grown on sapphire [28] is significantly narrower compared to the FWHM of the $Al_xGa_{1-x}N$ layers grown on h-BN.

	FWHM	
	(0 0 0 2) (°)	(1 0 −1 3) (°)
$Al_{0.7}Ga_{0.3}N$/AlN/Sapphire structure (1)	0.3	0.4
$Al_{0.7}Ga_{0.3}N$/AlN/Sapphire structure (2)	0.3	0.5
$Al_{0.7}Ga_{0.3}N$/AlN/Sapphire structure (3)	0.5	0.6
$Al_{0.7}Ga_{0.3}N$/AlN/3 nm h-BN/Sapphire (Sample A)	1.1	6.6
$Al_{0.7}Ga_{0.3}N$/AlN/6 nm h-BN/Sapphire (Sample B)	0.8	3.3

Table I. X-ray rocking curve diffraction measurements of (0 0 0 2) and (1 0 −1 3) symmetric and asymmetric reflections for $Al_{0.7}Ga_{0.3}N$ structures grown on sapphire and $Al_{0.7}Ga_{0.3}N$ structures grown on h- BN / sapphire.

However, and importantly, the temperature dependence of the PL integrated intensity of $Al_{0.3}Ga_{0.7}N$ QDs / $Al_{0.7}Ga_{0.3}N$ on sapphire was observed to be similar to that of $Al_{0.3}Ga_{0.7}N$ QDs / $Al_{0.7}Ga_{0.3}N$ on h-BN, showing a PL integrated intensity ratio between 10K and 300K of the same order of magnitude [28], as shown in table II. It can be found that: 1) the best $Al_{0.3}Ga_{0.7}N$ QDs sample grown on sapphire (sample 2), which has a PL ratio of 1.4, compared to the PL ratio of the less efficient sample grown on h-BN (sample B), which has a PL ratio of 13, shows that the PL intensity between LT and RT drops approximately 10 times more in the case of AlGaN QDs grown on h-BN. 2) Secondly, when comparing the PL ratio of the least efficient sample grown on sapphire (sample 3) with a PL ratio of 6.9 to the PL ratio of the most efficient

sample grown on h-BN (sample A) with a value of 7, it points out at a very similar drop of the PL intensity between LT and RT for both samples. Lastly, comparing the PL ratio of the best sample grown on sapphire (sample 2) with a PL ratio of 1.4 to the PL ratio of the best sample grown on h-BN (sample A) with a PL ratio of 7, it shows that the PL intensity for the QDs structure grown on h-BN decreases 5 times faster only than for the best QDs sample directly grown on sapphire.

	Sample 1 (grown on sapphire)	Sample 2 (grown on sapphire)	Sample 3 (grown on sapphire)	Sample A (grown on h-BN/ sapphire)	Sample B (grown on h-BN/ sapphire)
	$Al_{0.7}Ga_{0.3}N$ /$Al_{0.3}Ga_{0.7}N$ QDs	$Al_{0.7}Ga_{0.3}N$ /$Al_{0.3}Ga_{0.7}N$ QDs	$Al_{0.7}Ga_{0.3}N$ /$Al_{0.3}Ga_{0.7}N$ QDs	$Al_{0.7}Ga_{0.3}N$ /$Al_{0.3}Ga_{0.7}N$ QDs / 3nm h-BN	$Al_{0.7}Ga_{0.3}N$ /$Al_{0.3}Ga_{0.7}N$ QDs / 6 nm h-BN
Wavelength (nm) at 12K	292	294	298	275	279
Wavelength (nm) at 300K	300	301	306	275	280
PL Integrated intensity ratio (LT/RT)	2.0	1.4	6.9	7	13

Table II. Wavelength emission and PL integrated intensity ratio between LT and RT for different $Al_yGa_{1-y}N$ QDs / $Al_xGa_{1-x}N$ structures grown on sapphire and on h-BN.

Put together, these results suggest that while there may be significant differences in the structural properties of heterostructures grown on sapphire or on h-BN templates, the temperature-dependent behavior and overall PL characteristics of UVC emitting $Al_{0.3}Ga_{0.7}N$ QDs / $Al_{0.7}Ga_{0.3}N$ active regions remain comparable. We propose that the temperature dependence of the PL integrated intensity of $Al_yGa_{1-y}N$ QDs is not strongly influenced by the crystalline quality of the material, and this can be attributed to the robustness of the QDs resulting from their 3D confinement of excitons at the nanoscale. It is worth noting that variations in PL characteristics can still be observed among different samples, including those grown directly on sapphire, but with a maximum magnitude limited to 10 only when comparing the most and less radiatively efficient samples.

IV.2.4. Conclusion

$Al_{0.3}Ga_{0.7}N$ QDs-based structures emitting in the UV-C range have been grown on h-BN / sapphire templates by MBE using two different h-BN thicknesses: 3 nm and 6 nm. The structural properties of $Al_{0.7}Ga_{0.3}N$ layers have been studied showing an impact of the h-BN layers on the subsequent structures in the form of an orientation guidance and creating two different orientations in the growth plane affirming the crucial importance of growing high crystalline quality h-BN layers. Optical characterizations have shown that the QDs emission for sample A and sample B had emissions in the UV-C with a maximum intensity emission ranging between 275 nm (4.5 eV) and 280 nm (4.43 eV). In addition, the spectrally integrated PL intensity ratio (I (300K) / I (12K)) of the QD emission peak between RT and LT for samples A and B has been determined to be around 10%. This study has demonstrated the successful growth of UV-C emitting $Al_{0.3}Ga_{0.7}N$ QDs structures by MBE on h-BN / sapphire templates. This result will enable us to move to the next step that is the exfoliation of (Al,Ga)N heterostructures grown on h-BN / sapphire and the fabrication of QDs-based UV-C LEDs, hence, demonstrating the possible fabrication of flexible UV-C LEDs.

IV.3. Mechanical release transfer of the (Al,Ga)N-based quantum dots heterostructure grown on h-BN

IV.3.1. Exfoliation of the structure by scotch-tape

Exfoliation involves applying an external force to overcome the cohesive van der Waals interactions between layers of 2D materials. In the scotch-tape method, the exerted force disrupts the weak van der Waals interfaces among h-BN layers, ultimately detaching the (Al,Ga)N heterostructure from the substrate. We proceeded to study the mechanical exfoliation process by scotch-tape on sample B, i.e. (Al,Ga)N QDs structure grown on 6 nm h-BN / sapphire and investigated the structural and optical properties of the QDs after exfoliation. Figure 25 is a schematic description of the mechanical exfoliation process by scotch-tape on sample B that was performed by Dr. Antoine Reserbat-Plantey at CRHEA (Centre de Recherche sur l'Hétéro-Epitaxie et ses Applications) in Valbonne, France.

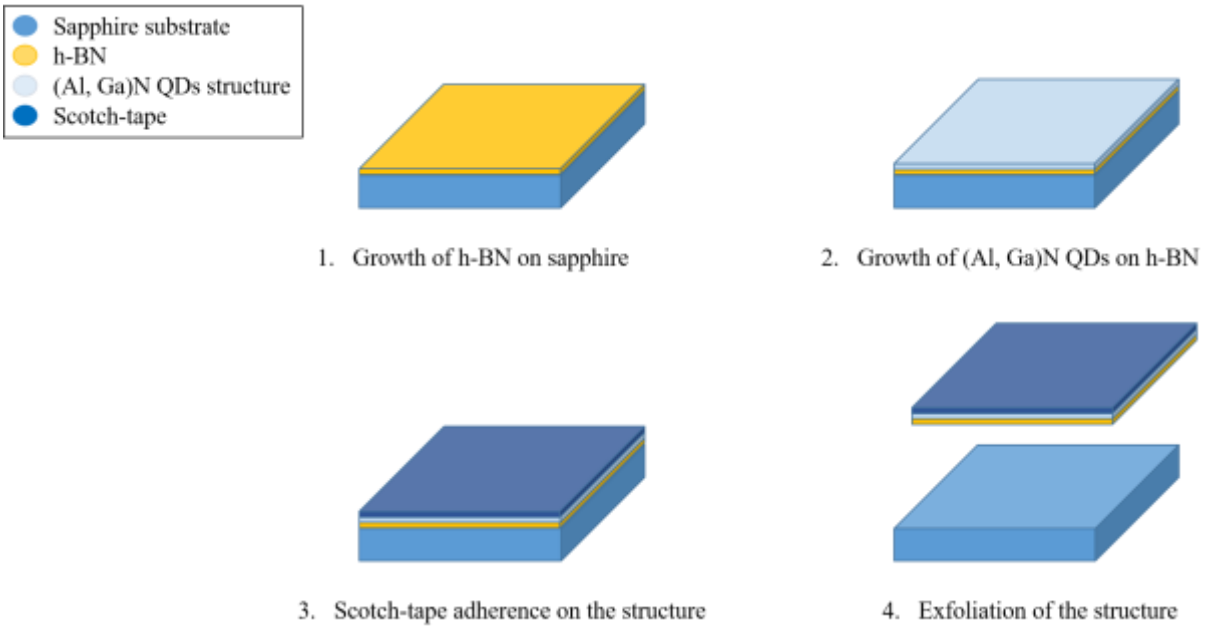

Figure 25. Schematic description of the mechanical exfoliation process by scotch-tape performed on the (Al,Ga)N-based quantum dots structure grown on 6 nm h-BN / sapphire (sample B).

Figure 26 illustrates images of the exfoliated structure. As demonstrated in figure 26(a), the exfoliation process using scotch-tape was effective, resulting in a clearly visible exfoliated structure. In figure 26(b), sections of the exfoliated structure, with lateral dimensions of about 100 µm or more, have been successfully detached from the original substrate and positioned on the tape. However, figure 26(c) reveals that the exfoliation process was not completely successful in detaching the entire structure from the sapphire substrate, leaving some parts of

the structure on the sapphire substrate. The different colors observed in figures 26(b) and (c) are due to interference patterns formed by the thickness variation of the exfoliated structure.

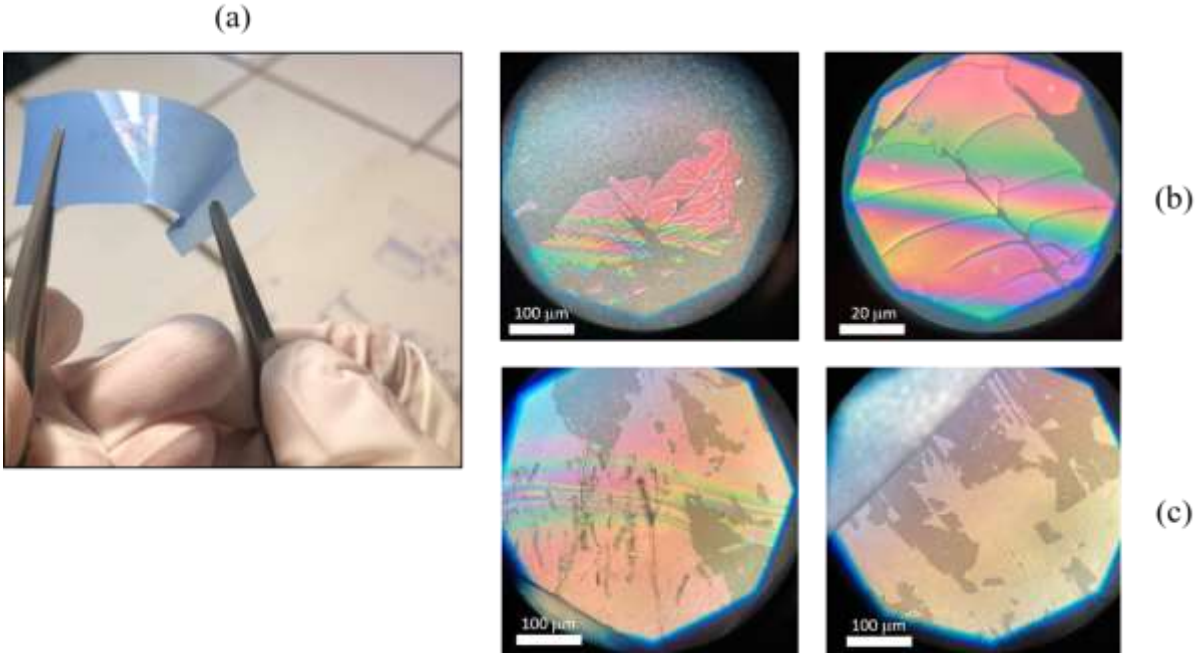

Figure 26. (a) Image of the (Al,Ga)N-based QDs / h-BN structure exfoliated on the scotch-tape. (b) and (c) are optical microscope images of the exfoliated structure on tape and the remaining structure on the sapphire substrate, respectively.

IV.3.1.1. Morphological properties

To verify the exfoliation originating from the separation of the MBE grown (Al,Ga)N structure from the h-BN layers, we conducted a comprehensive surface morphology analysis on the exfoliated structure. This involved utilizing AFM characterization and performing angle distribution calculations by using ImageJ (image processing software) [36] to assess the step patterns on the exfoliated structure's surface. A comparison between the surface morphology and step angle distribution of a 3 nm h-BN layer grown on sapphire and the exfoliated structure on the scotch-tape is presented in figures 27(a) and (b). Notably, the surface morphology of the exfoliated structure (figure 27(b)) closely resembles the typical h-BN morphology observed on sapphire (figure 27(a)), signifying the presence of h-BN in the structure following exfoliation. Moreover, calculations of the step angle distribution revealed an identical angle of 123° for both layers, providing further evidence of the existence of h-BN on the top of the exfoliated structure.

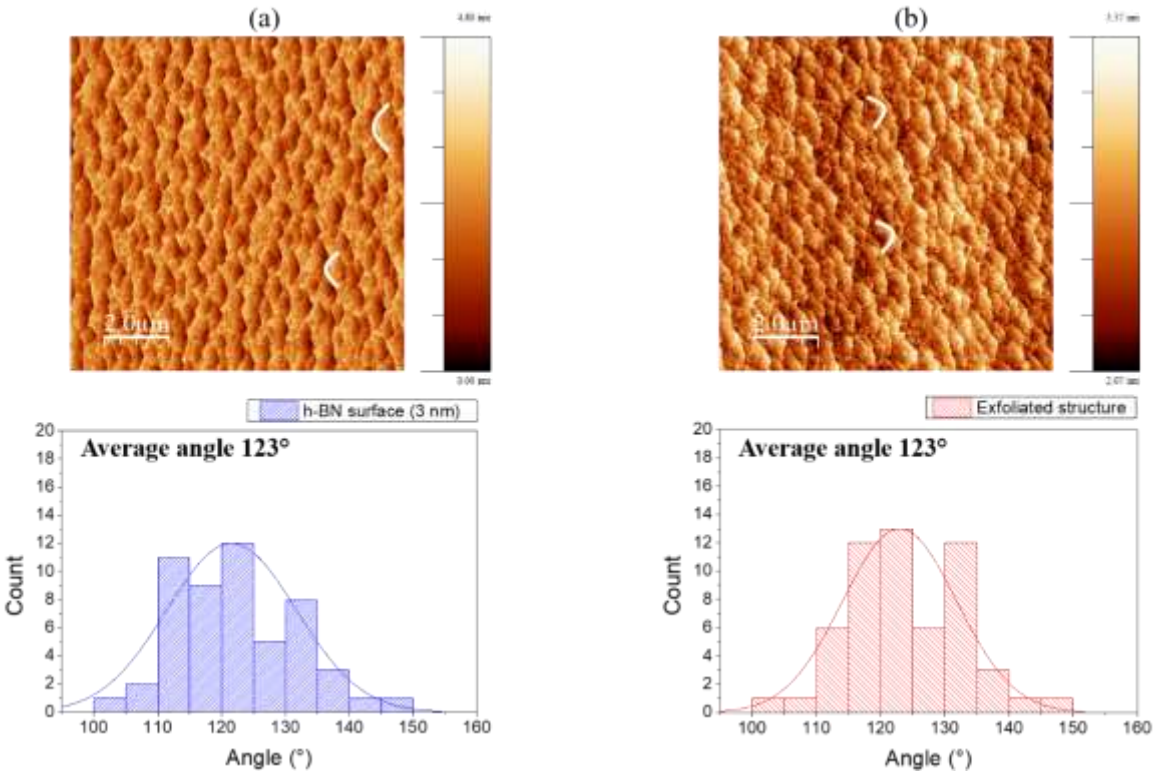

Figure 27. Atomic microscope image and histogram of angle distribution of: (a) 3 nm h-BN grown on sapphire, (b) exfoliated structure on scotch-tape. The white marks on both AFM images represent the way the angles were measured.

Subsequently, we conducted AFM characterization on the residual structure parts remaining on the sapphire substrate after exfoliation. This analysis aimed to provide insight into the extent of structure removal achieved through exfoliation. Ideally, the entire (Al,Ga)N / AlN structure should have been exfoliated, as detachment occurs among the h-BN layers. Figure 28(a) validates the complete exfoliation of the (Al,Ga)N / AlN structure from the substrate, as the AFM image showcases a height difference between the exposed sapphire surface and the residual structure that remains attached to it. Given that our (Al,Ga)N / AlN structure possesses a thickness of approximately 600 nm, the profile image in figure 28(a) unequivocally confirms this height difference with the sapphire substrate.

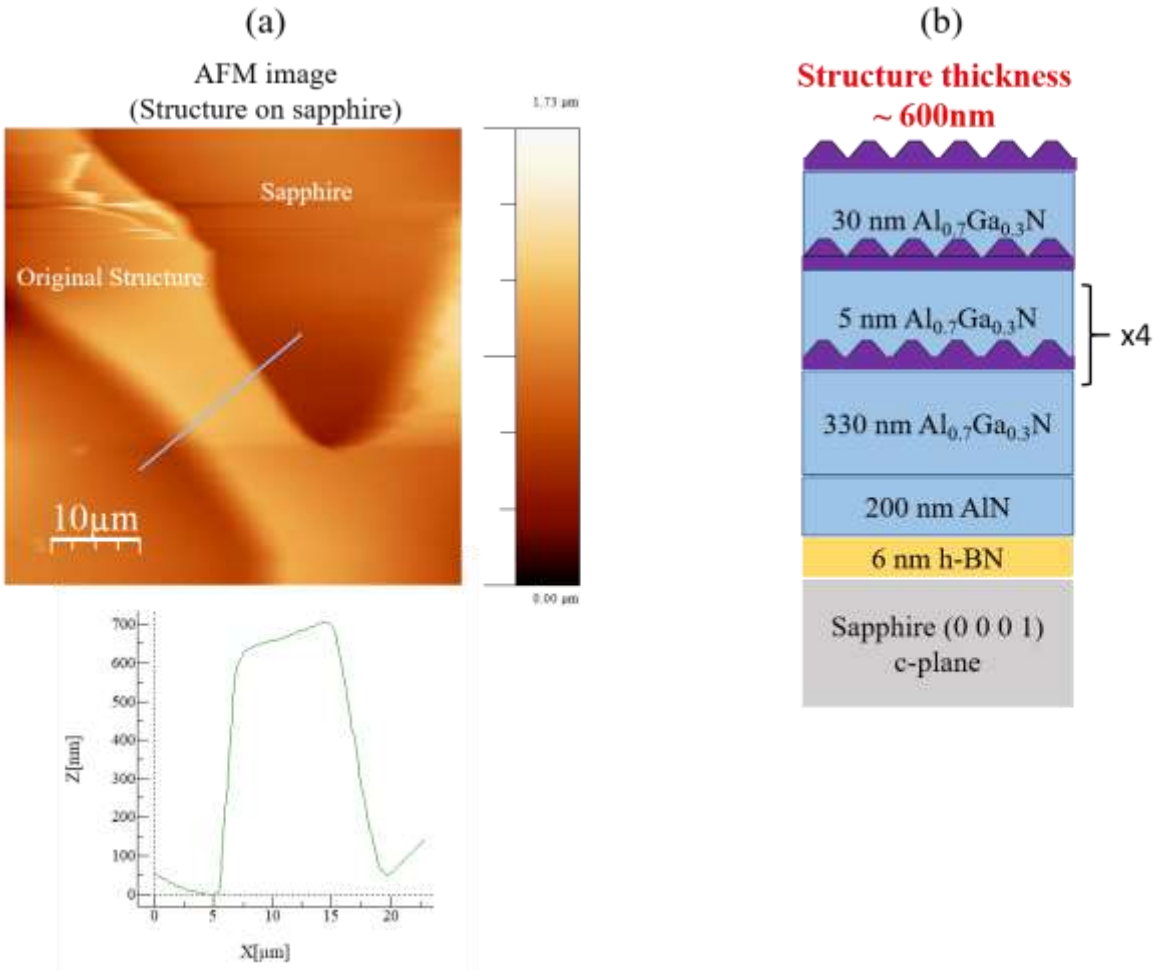

Figure 28. (a) Atomic force microscopy image of the remaining structure on sapphire after the exfoliation. (b) Schematic of sample B's structure before exfoliation with a thickness ~ 600 nm excluding the sapphire substrate.

IV.3.1.2. Optical properties

IV.3.1.2.1. Continuous wave photoluminescence

To investigate the optical properties of the exfoliated $Al_{0.3}Ga_{0.7}N$ QDs, continuous photoluminescence (PL) measurements at room temperature (RT, 300K) were conducted using a closed-cycle Helium (He) cryostat. The measurements utilized a frequency-doubled Argon (Ar) laser emitting at 244 nm (5.08 eV) with an excitation power of 20 mW. Figure 29(a) displays the QDs post-exfoliation, revealing a broad emission peak spanning from the UVB to UVC spectral ranges (278 nm to 300 nm). This is in contrast to the pre-exfoliation state (figure 23(b)), where a single peak emission was observed at 280 nm. Additionally, a broad peak emission emerged between 300 nm and 360 nm following exfoliation, an emission that was not present prior to the process (as seen in figure 23(b)). The investigation extended to probing the source of this newfound emission peak, involving PL measurements on a reference bare scotch-

tape, i.e. without any exfoliated structure. Figure 29(b) portrays the tape exhibiting a broad peak emission ranging from 300 nm to 360 nm, thus identifying it as a source of the observed emission peak in the QDs.

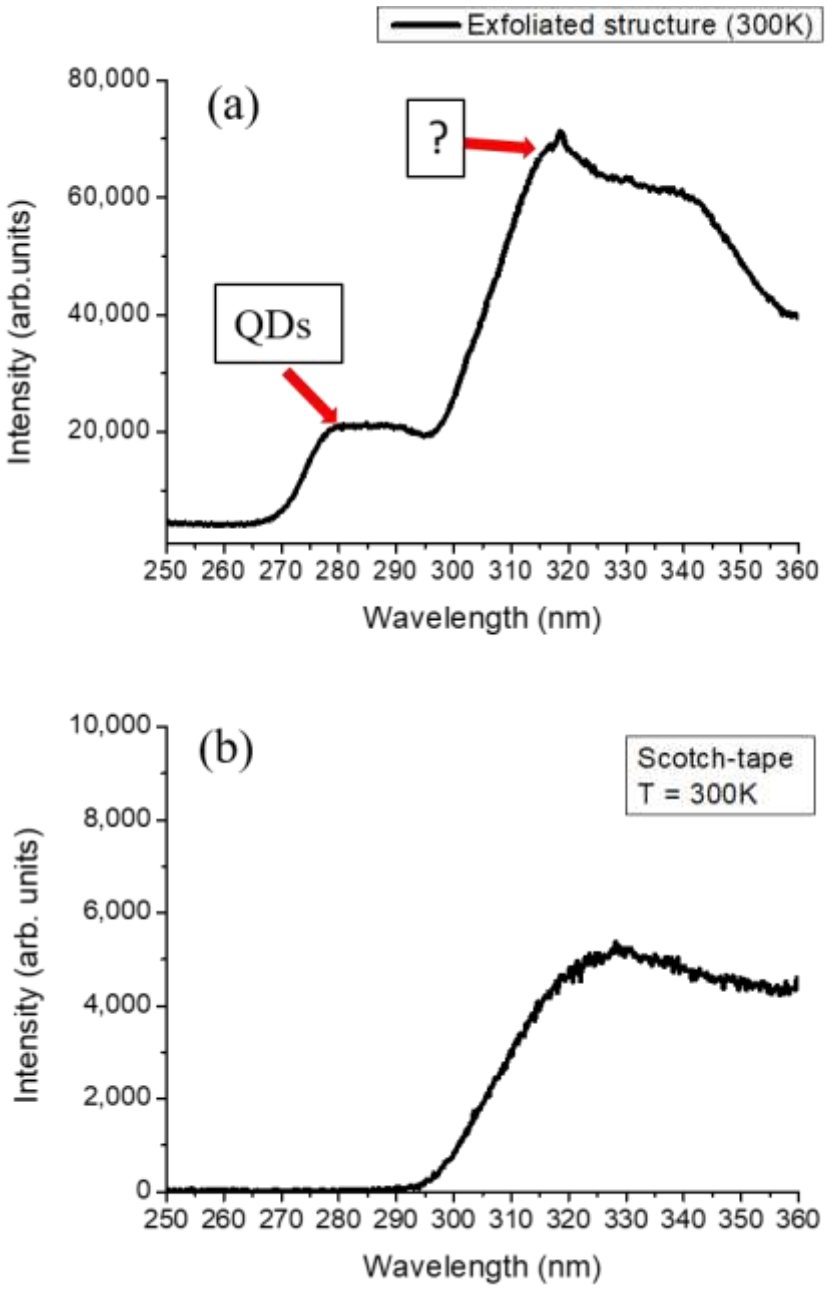

Figure 29. Photoluminescence measurements at 300 K for: (a) exfoliated (Al,Ga)N QDs structure on scotch-tape, (b) bare scotch-tape (without exfoliated structure).

To exclude the contribution of deep-level emission from the (Al,Ga)N cladding layers, a different type of scotch-tape, i.e. with an optical response outside the UV range, was utilized. The PL characterization of this tape, depicted in figure 30(b), revealed a broad emission peak spanning from 400 nm to 600 nm. Therefore, no emission is coming from the tape below 400

nm. Subsequently, another piece of the (Al,Ga)N QDs structure was exfoliated again using this alternative scotch-tape, and its PL properties were investigated. The PL spectrum, presented in figure 30(c), showed a UVC emission centered at around 280 nm, along with a broad UVB emission ranging from 300 nm to 360 nm. Importantly, the emission intensity at longer wavelengths was strongly reduced compared to the first exfoliated structure (figure 29 (a)).

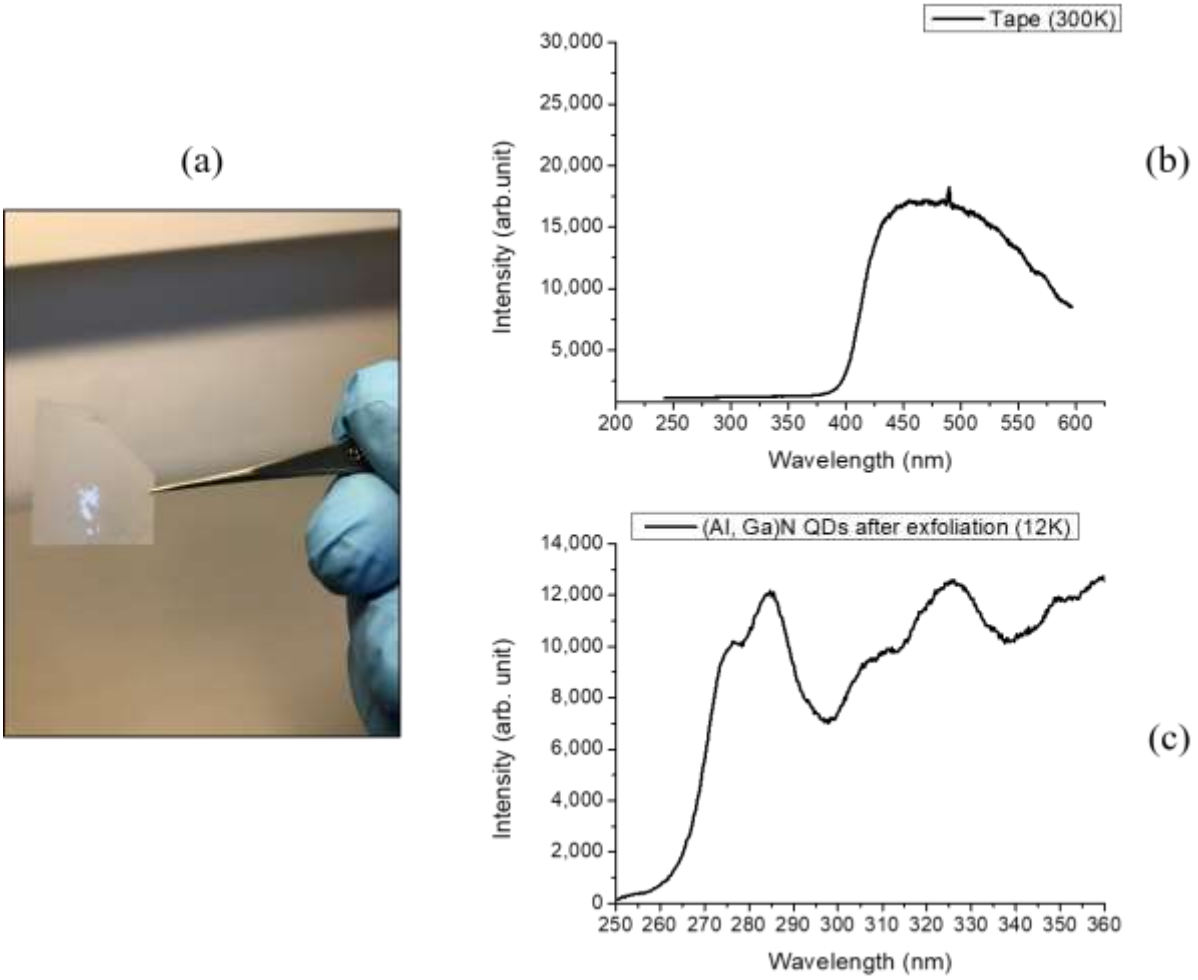

Figure 30. (a) Image of the (Al,Ga)N / h-BN structure exfoliated on a scotch-tape presenting no emission in the UV range. (b) and (c) are photoluminescence measurements of: (b) the scotch-tape emitting above the UV range, and (c) the (Al, Ga)N QDs structure after exfoliation.

However, the remaining presence of an emission at wavelengths above 300 nm underscores an origin that is not limited to the emission from the initial scotch-tape only. In fact, the deep-level emission from the (Al,Ga)N cladding layers also plays a role in the observed emission that was confirmed by spectral and monochromatic imaging Cathodoluminescence (CL) measurements, as depicted in figure 31.

IV.3.1.2.2. Cathodoluminescence

The CL measurements have been done in a Scanning Electron Microscope at 5 kV at room temperature. In spectral mode, the sample emission recorded on a (2.5 x 2.5) μm^2 sample area (whose typical SEM morphology is shown in figure 31(d)) is featured by two primary peaks: one centered around 278 nm and a second, more intense peak at approximately 335 nm, as illustrated in figure 31(a). Performing monochromatic CL imaging on this sample area at 278 nm and subsequently at 335 nm allows to evidence two opposite trends. At first, we observe a non-uniform surface emission characterized by localized zones emitting light at 278 nm, which can be attributed to clusters of QDs (figure 31(b)). On the other hand, we observe a uniform emission over the whole sample area at 330 nm (figure 31(c)). This should originate from the sample's volume itself, likely associated with the $Al_{0.7}Ga_{0.3}N$ layers. By comparing figures 31(b), (c), and (d), it becomes evident that the surface pits observed have no impact on the emitted light.

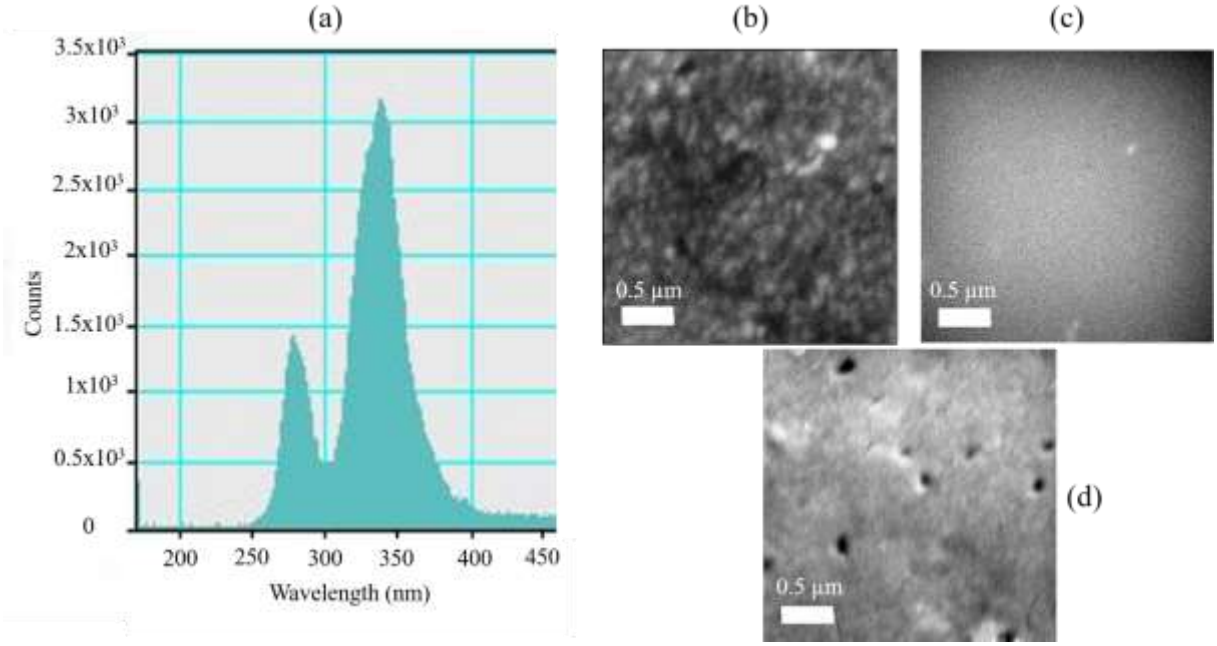

Figure 31. Scanning electron microscope cathodoluminescene (SEM-CL) of the (Al,Ga)N QDs structure: (a) total spectrum measured on a (2.5 x 2.5) μm^2 area, (b) monochromatic CL recorded at 278 nm; (c) monochromatic CL recorded at 330 nm, and (d) SEM image of the surface morphology of the measured zone.

IV.3.1.2.3. Temperature-dependent photoluminescence

Continuous PL measurements were conducted at both low temperature (LT, 12K) and room temperature (RT, 300K) on the QDs structure, both before and after exfoliation, utilizing identical excitation conditions for comparison. Illustrated in figure 32, the PL spectra at 12K

and 300K reveal the characteristics of the QDs before and after exfoliation. Prior to exfoliation, a distinct single PL peak emission was evident in the UV-C region at approximately 280 nm (4.43 eV), observed consistently at both LT and RT. The PL peak intensity exhibited a decline from LT to RT, as depicted in figure 32(a). Subsequent to exfoliation, a main PL peak emission emerged at LT. The peak was observed in the UV-C region with a maximum intensity at 278 nm (4.5 eV). Additionally, a broadening at lower energy (i.e. at 290 nm, 4.3 eV) was also seen. As illustrated in figure 32(b), after the exfoliation process, a limited reduction in the PL peaks' intensities from LT to RT was found between 270 and 290 nm, confirming the benefit of the 3D carrier confinement in the $Al_{0.3}Ga_{0.7}N$ QDs. The integrated PL intensity ratio (I (300K) / I (12K)) for the QD emission peak between RT and LT following exfoliation was found to be as high as 0.5. However, the emission above 300 nm was found to be surprisingly enhanced at room temperature, showing that recombination mechanisms were strongly modified on the (Al,Ga)N QDs structure exfoliated on tape (i.e. in this case the laser excitation is mainly absorbed in the thick $Al_{0.7}Ga_{0.3}N$ cladding layers as the structure layout has been inverted by the exfoliation process).

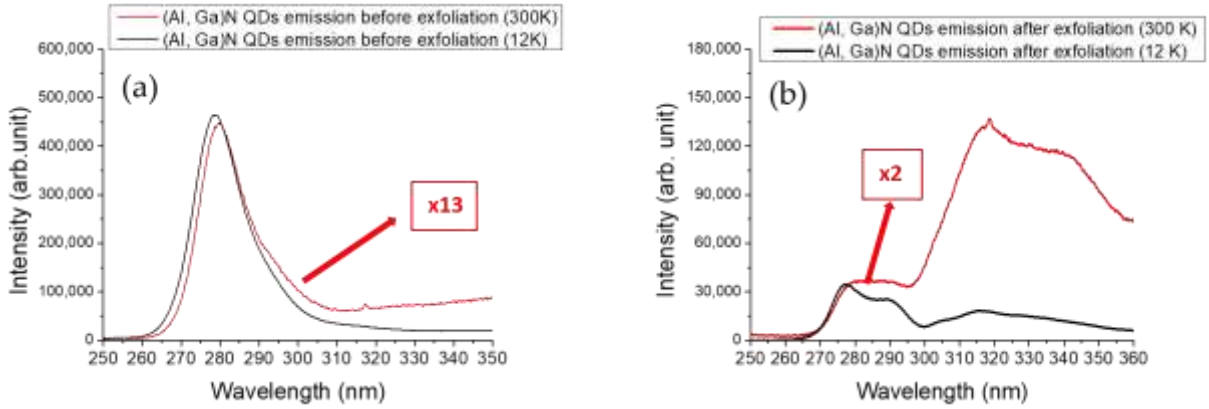

Figure 32. Photoluminescence (PL) spectrum of $Al_{0.3}Ga_{0.7}N$ QDs with an $Al_{0.3}Ga_{0.7}N$ deposited amount of 7MLs at 12K and 300K before and after exfoliation. (a) The PL intensity has been multiplied by 13 for the spectrum obtained at 300K. (b) The PL intensity has been multiplied by 2 for the spectrum obtained at 300K.

IV.3.2. Dry transfer of the structure on silicon dioxide / silicon substrate

We proceeded to investigate the feasibility of transferring the (Al,Ga)N-QDs based structure from the exfoliating tape onto a silicon dioxide (SiO_2) / silicon (Si) substrate. The aim was to assess the potential for successfully relocating the structure from its original substrate to an alternative host substrate while maintaining continuous QDs emission. The choice of a 285

nm SiO_2 / Si substrate as the host substrate was made since it is widely used in the 2D materials field. It enables to get specific optical response by generating strong interference effects, which let the 2D material's monolayers give sufficient contrast for their optical detection [37]. Illustrated in figure 33, a schematic representation elucidates the process of transferring from the exfoliated state to the host substrate. In accordance with the schematic depiction, the (Al,Ga)N-based QDs structure on tape is placed onto the surface of the SiO_2 / Si substrate. The process involves the application of a force to enhance adhesion and eliminate air pockets, while simultaneously applying heat to the backside of the tape. This combined approach aims to facilitate improved adhesion, structure delamination, and successful transfer onto the substrate.

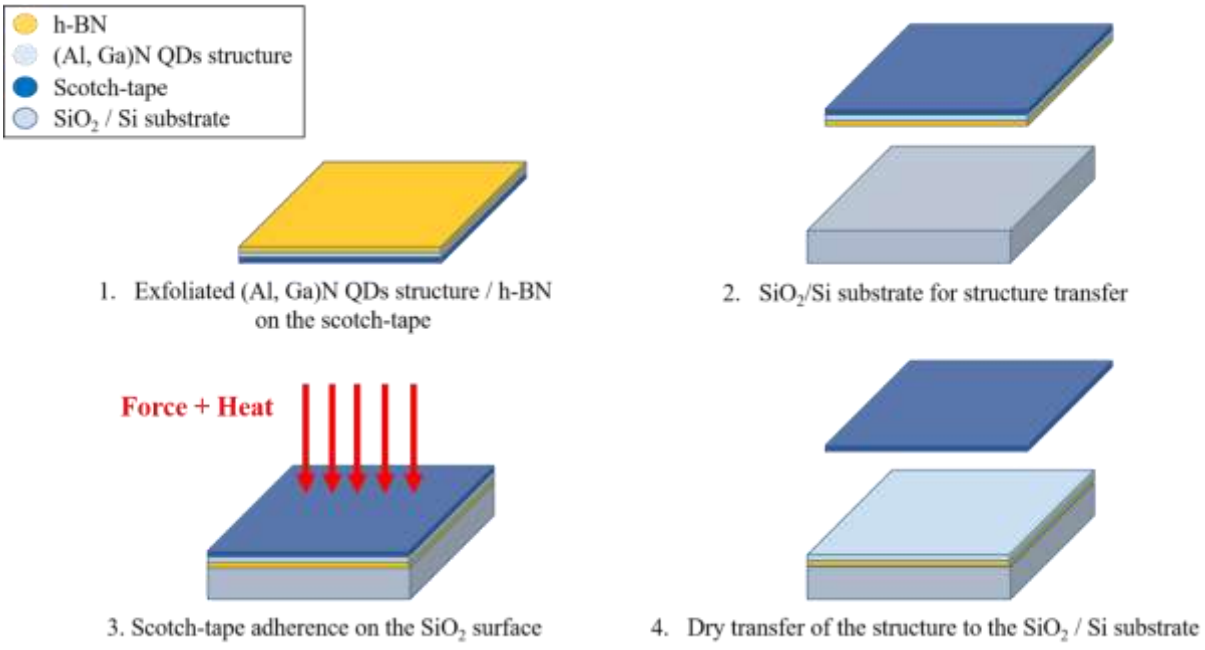

Figure 33. Schematic description of the dry transfer process from the scotch-tape to the SiO_2 / Si substrate of the (Al,Ga)N-based quantum dots structure grown on 6 nm h-BN / sapphire (sample B).

Figure 34 provides visual representations of the structure subsequent to its transfer onto the substrate. As depicted in figure 34(a), the dry transfer process from the scotch-tape to the substrate was successful. Additionally, figure 34(b) illustrates that portions of the exfoliated structure, exceeding dimensions of ≥ 100 µm, have been effectively separated from the tape and are now positioned on the SiO_2 / Si substrate.

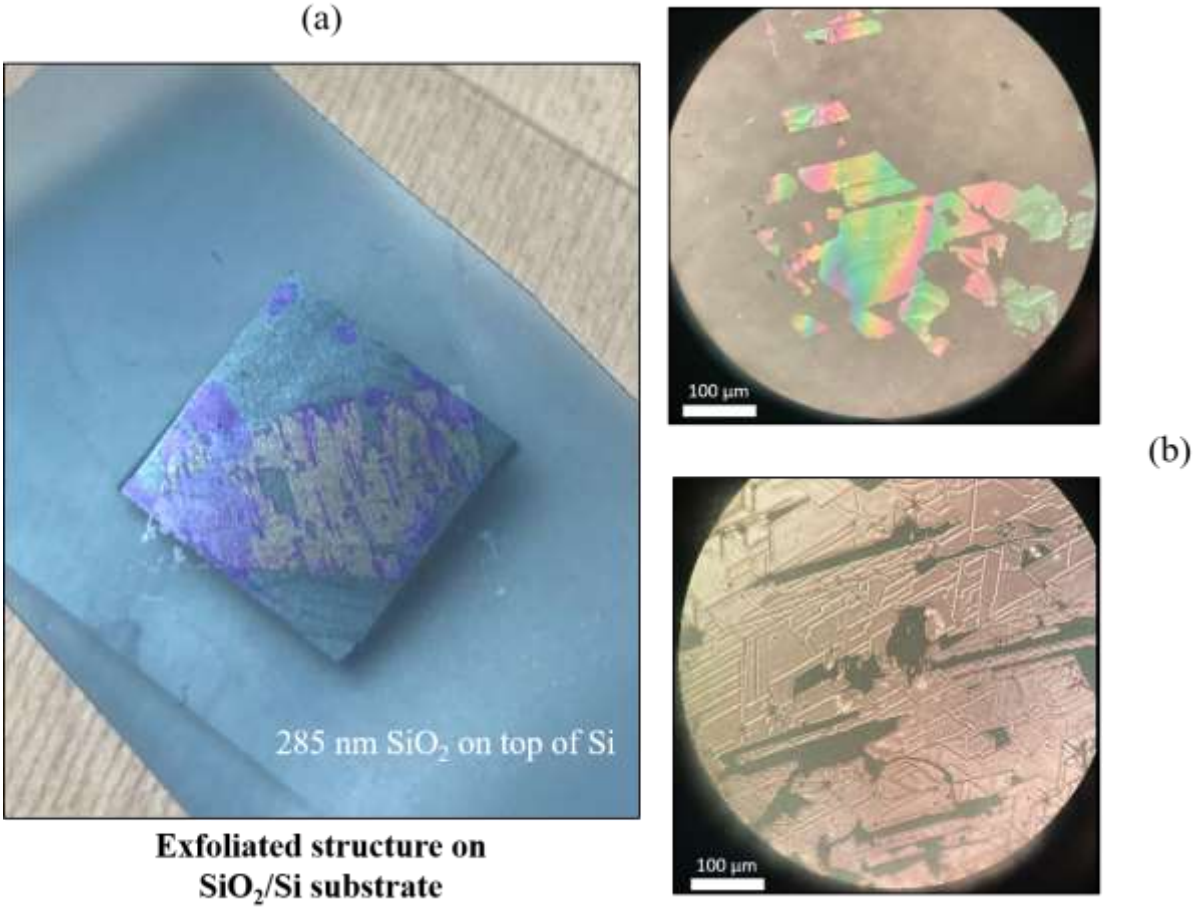

Figure 34. (a) Image of the (Al,Ga)N-based QDs / h-BN / tape structure transferred to a SiO_2/Si substrate. (b) Optical microscope images of the transferred structure on the substrate.

IV.3.2.1. Morphological properties

Subsequent to the transfer process, we proceeded with AFM characterizations of parts of the structure that remained on the tape. This analysis was conducted to assess the effectiveness of the dry transfer procedure for the exfoliation of the (Al,Ga)N-based QDs structure. As depicted in figure 35(a), the AFM image substantiates the complete exfoliation of the (Al,Ga)N / AlN structure from the tape, as evidenced by the noticeable difference in height between the exposed tape surface and the residual structure that remained on it. Considering that the (Al,Ga)N / AlN structure possesses a thickness of approximately 600 nm, the profile image in figure 35(a) corroborates the observed height variation relative to the scotch-tape.

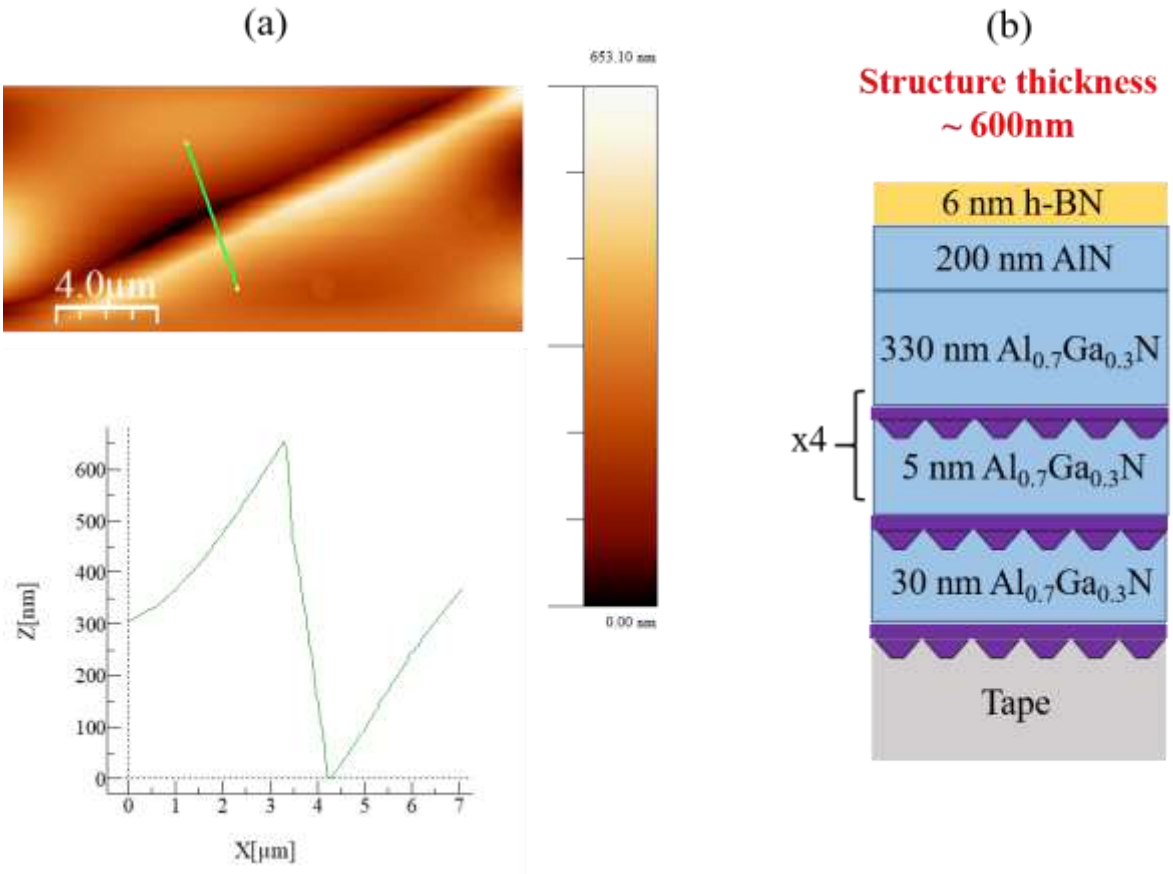

Figure 35. (a) Atomic force microscopy image of the remaining structure on the scotch-tape after the dry transfer. (b) Schematic of sample B's structure after exfoliation on the scotch-tape, with a thickness of ~ 600 nm (excluding the tape).

IV.3.2.2. Calculation of surface area coverage for scotch-tape exfoliation and dry transfer

We then proceeded to assess the exfoliation and dry transfer efficiencies involved in removing the (Al,Ga)N QDs-based structure from the substrate, utilizing the ImageJ software [36] to calculate the percentage of surface area covered by the structure. Figure 36 provides an explanation of the calculations performed by the software, with optical microscope images showcasing the exfoliated (Al,Ga)N structure on a surface. The regions devoid of structure are highlighted in red, while the white regions represent the structure itself. The software's estimation of the red area is displayed in small windows adjacent to the images. In the upper image, calculations indicate that approximately 72.5% of the area is colored in red, implying that the structure occupies around 27.5% of the surface. Similarly, the lower image reveals calculations where red areas cover approximately 54%, indicating that the (Al,Ga)N structure occupies approximately 46% of the surface. These calculations provide insights into the extent of structure detachment from the original sapphire substrate as well as the proportion of the

structure that was successfully transferred to the SiO_2 / Si substrate following both the exfoliation and dry transfer processes.

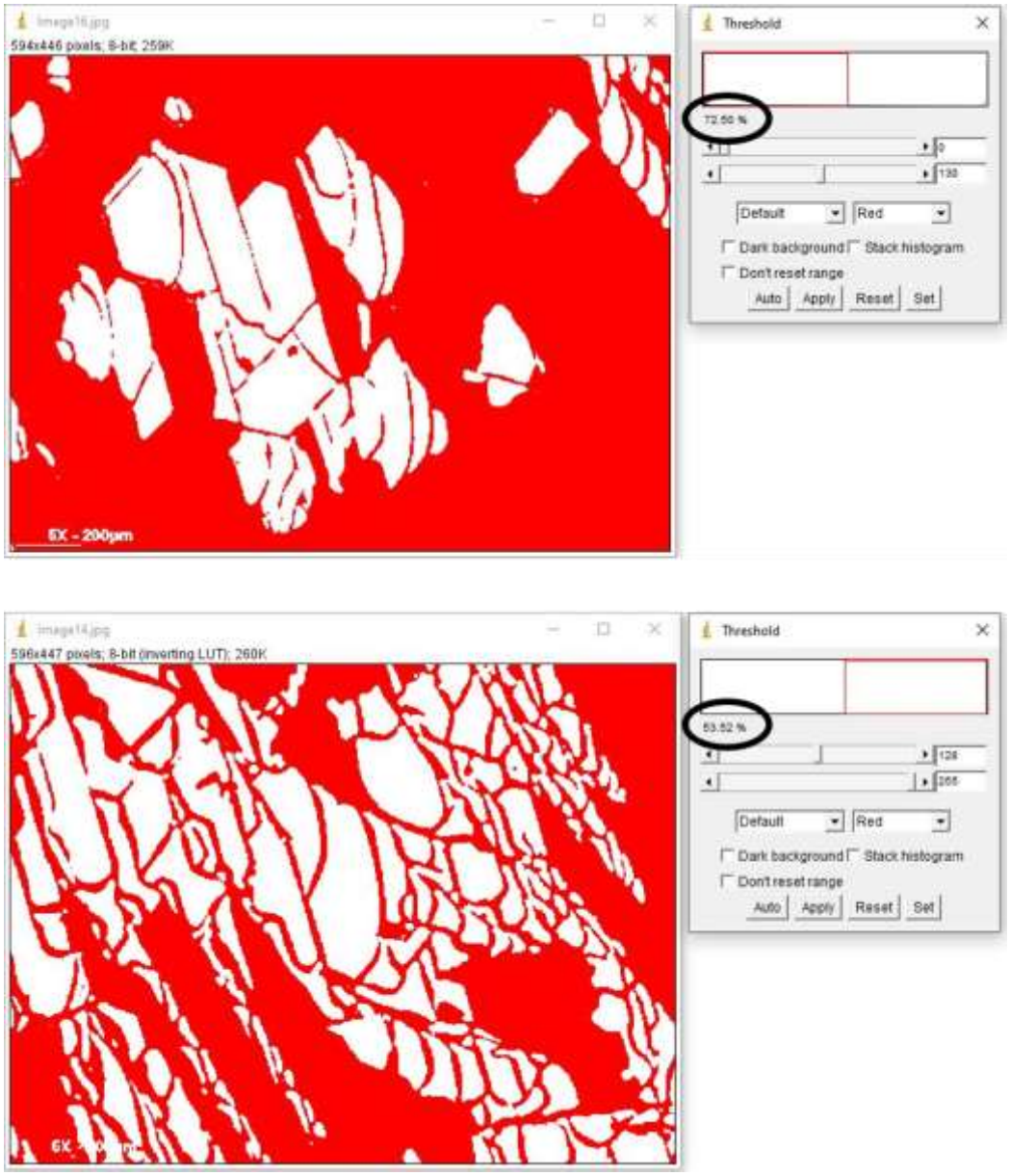

Figure 36. (Al,Ga)N QDs based structure surface area coverage calculations generated by the image processing software ImageJ [36]. The red color represents areas uncovered by the (Al,Ga)N structure while the white color represents the areas covered by it.

The ultimate assessment of the effectiveness of the exfoliation and dry transfer procedures in successfully detaching the (Al,Ga)N structure from its original sapphire substrate is presented in figure 37. The results reveal that the scotch-tape exfoliation method has effectively removed approximately 66% of the structure from the central region of the sapphire substrate. However, the efficiency is lower towards the edges of the tape, with only half or less of the structure being transferred onto the scotch-tape. Upon completion of the transfer process

from the tape to the SiO_2 / Si substrate, approximately 50%—representing half of the initially grown structure on the sapphire substrate—has successfully reached its ultimate substrate destination.

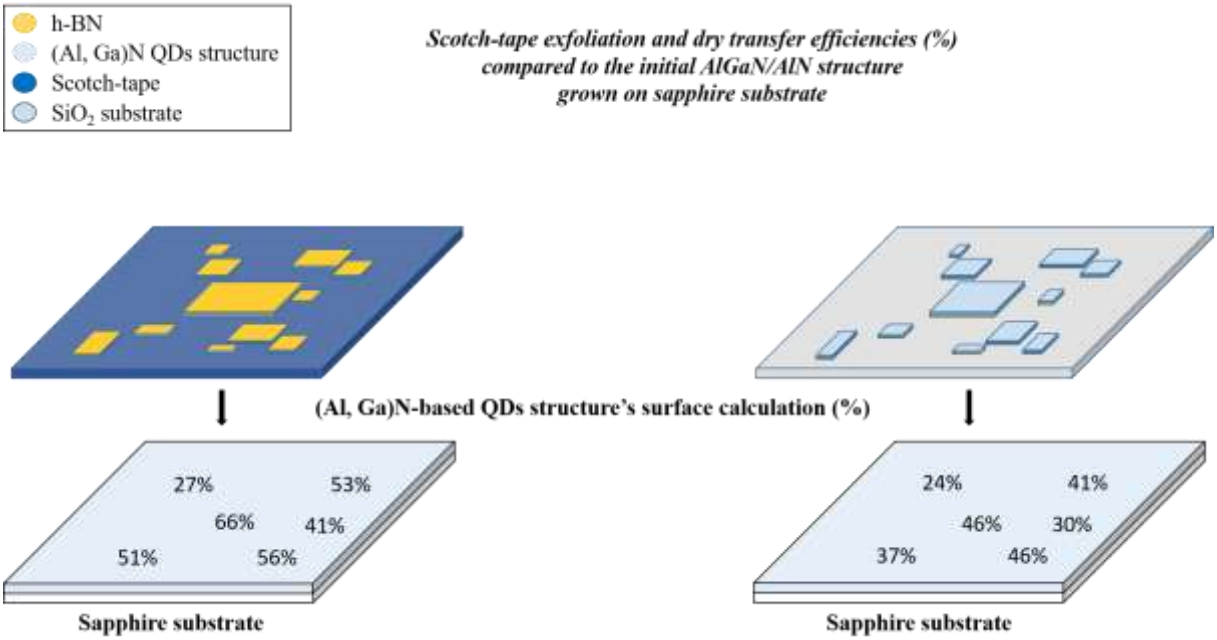

Figure 37. Exfoliation and dry transfer procedures efficiency calculation in successfully detaching the (Al,Ga)N structure from its original sapphire substrate. The calculations were performed by the image processing software ImageJ [36].

IV.3.2.3. Temperature-dependent photoluminescence

PL measurements were performed at both low temperature (LT, 12K) and room temperature (RT, 300K) on the QDs structure following its transfer onto the SiO_2 / Si substrate, utilizing consistent excitation parameters for direct comparison. As depicted in figure 38, the PL spectra at 12K and 300K exhibit the distinctive characteristics of the QDs, demonstrating their continued emission capabilities post-transfer from the scotch-tape onto the SiO_2 / Si substrate. An evident and intense PL peak emission is observed in the UV-C range, approximately at 280 nm (4.43 eV) during LT measurements. Additionally, several low-intensity peak emissions are observed within the UV-B and UV-C regions. The PL peak intensity displays a reduction from LT to RT, while the peak centered at 290 nm (4.3 eV) experiences a substantial increase in intensity. The ratio of integrated PL intensities (I (300K) / I (12K)) between RT and LT after the transfer is measured to be 7%, indicating commendable thermal stability due to the robust 3D carrier confinement within the QDs. The presence of multiple emission peaks not initially observed on the sapphire substrate or after exfoliation on

the scotch-tape could be attributed to an interference emission behavior originating from the SiO_2 / Si substrate.

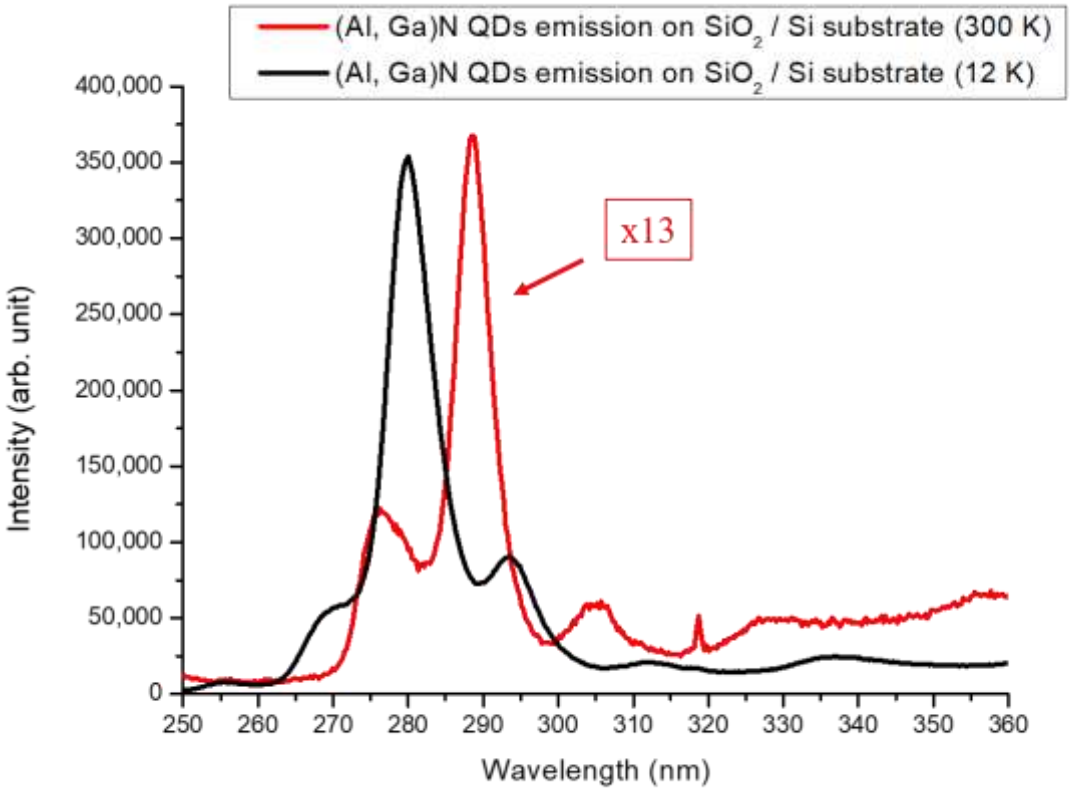

Figure 38. Photoluminescence (PL) spectrum of $Al_{0.3}Ga_{0.7}N$ QDs (with an equivalent $Al_{0.3}Ga_{0.7}N$ deposited amount of 7MLs) at 12K and 300K after the transfer of the structure on an SiO_2 / Si substrate. The PL intensity has been multiplied by 13 for the spectrum obtained at 300K.

IV.3.2.4. Calculation of the optical absorption in the multilayer (Al,Ga)N QDs heterostructures

Pr. Guillaume Cassabois from Charles Coulomb laboratory (L2C) performed the calculations of the optical absorption in the multilayer (Al,Ga)N QDs heterostructures, either on sapphire or on SiO_2/Si substrates, by computing the time-averaged Poynting vector within a transfer matrix approach [38] in the two following configurations:

-case (i): nominal as-grown epilayers, i.e. semi-infinite Sapphire / 6 nm h-BN / 200 nm AlN ~ 400 nm $Al_{0.7}Ga_{0.3}N$ and $Al_{0.3}Ga_{0.7}N$ QDs structure.

-case (ii): exfoliated sample, i.e. semi-infinite Si / 285 nm SiO_2 / 6 nm h-BN / 200 nm AlN ~ 400 nm $Al_{0.7}Ga_{0.3}N$ and $Al_{0.3}Ga_{0.7}N$ QDs structure.

For the calculations, the complex refractive index of h-BN, SiO_2, and Si were taken from references [39]–[41], respectively, and the refractive index of (Al,Ga)N alloys from reference

[42]. The QD optical response is modelled by a complex susceptibility centered at 4.35 eV (i.e. at a wavelength of 285 nm), and with a FWHM of 160 meV. The results are presented in figure 39.

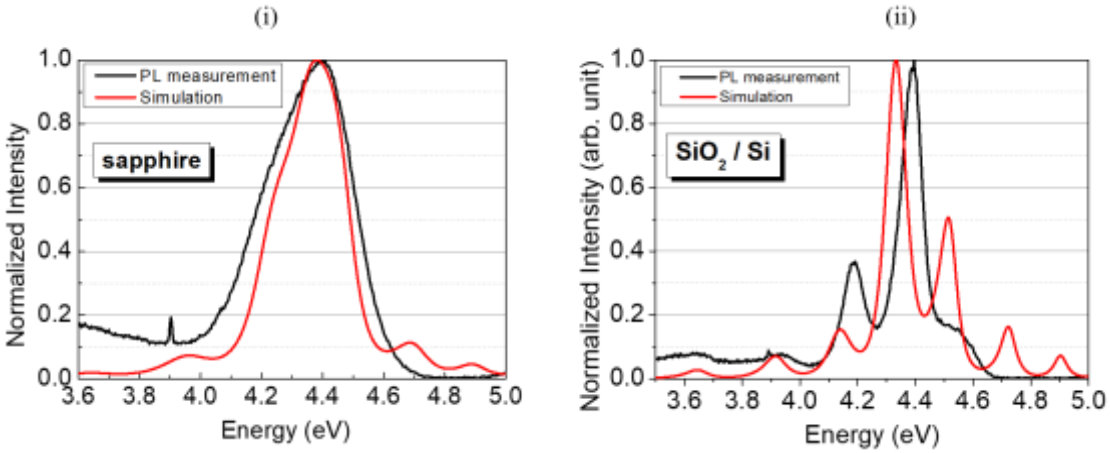

Figure 39. Computation of the optical absorption by calculating the time-averaged Poynting vector within a transfer matrix approach [38] for: (i) nominal as-grown (Al,Ga)N epilayers on h-BN / sapphire, and (ii) exfoliated (Al,Ga)N epilayers on h-BN on 285 nm SiO_2 / Si substrate (red curves). In comparison, the PL emission for the structures are also presented in the figures in black curves.

In figure 39(i), the simulation was performed based on the as-grown structure of the sample grown on a sapphire substrate. The results confirm the PL spectrum observed experimentally, with a weak perturbation from optical interferences in the air/nitride/sapphire substrate structure, where the QDs emission mostly reflects the statistical distribution of the QDs emission energies arising from size variations. In figure 39(ii), the simulation of the 285 nm SiO_2/Si substrate with the exfoliated QD-based (Al,Ga)N structure shows a very different result: in this case, well-resolved interferences originating from the air/nitride/SiO_2/Si substrate structure are found, confirming the experimental PL measurements and the strong influence of the substrate. However, as it was found that the peaks in the calculations do not precisely align with the measured PL peaks, additional simulations were performed. More precisely, simulations were performed by varying the SiO_2 thickness from 255 nm to 285 nm (by 5 nm steps), and the results are illustrated in figure 40.

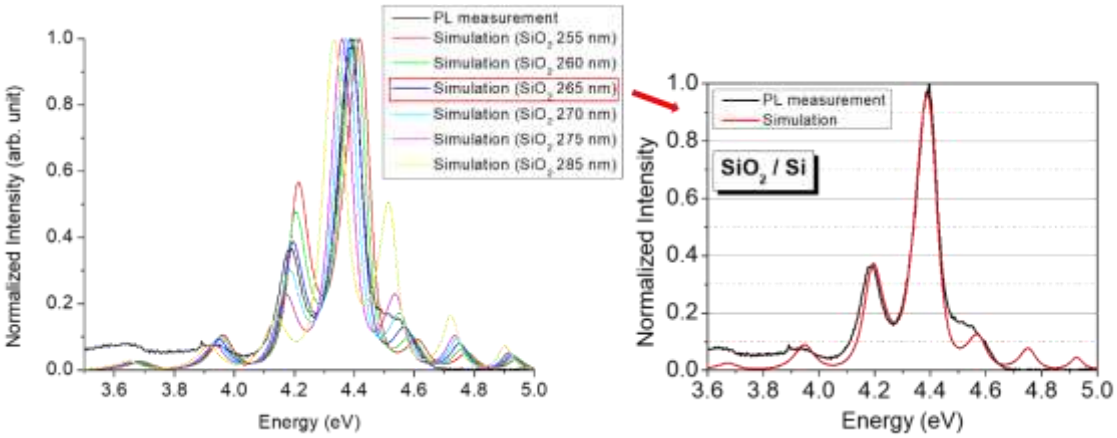

Figure 40. Computation of the time-averaged Poynting vector within a transfer matrix approach [38] for the exfoliated sample on SiO_2/Si with varying the SiO_2 thickness from 255 nm to 285 nm.

The initial observations regarding the influence of the SiO_2 thickness variations reveal that an increase in the SiO_2 thickness corresponds to a reduction in the interference amplitude from the SiO_2/Si substrate due to absorption losses. Notably, the simulation with a SiO_2 thickness of 265 nm aligns well with the measured PL. It's important to emphasize that adjusting the SiO_2 thickness served as a straightforward method to investigate and confirm that the spectral discrepancy was likely attributed to minor factors, such as inaccuracies in the precise thickness of certain layers or errors in the refractive index of these layers. Hence, the observed differences between the data and simulations are likely the result of slight variations between the nominal and actual values of layer thickness or refractive index.

IV.4. Growth of (Al,Ga)N QDs-based LED on h-BN

Following the successful fabrication of: 1) (Al,Ga)N QDs-based heterostructures on h-BN templates; along with 2) the observation of a UV-C emission coming from the QDs both before and after the exfoliation process; as well as following 3) their transfer onto an SiO_2 / Si substrate, our study aimed to expand its scope. Along this view, we designed and fabricated (Al,Ga)N QD-based LEDs on 1.5 nm h-BN by MBE, targeting an emission in the UV-C range. The reason behind opting for a thinner h-BN layer (1.5 nm) compared to the previously mentioned 3 nm and 6 nm thicknesses was to enhance the quality of (Al,Ga)N heterostructures produced through MBE (see section 1.1). Previous research on MOCVD growth of III Nitrides on h-BN has indicated that thinner h-BN layers result in improved crystalline quality of III Nitrides: For instance, the Air Force Lab research group demonstrated this effect by analyzing various BN template thicknesses with smooth surface morphologies for BN thicknesses below 3 nm. Their study delved into the impact on structural, optical, and transport properties of

GaN/AlGaN heterostructures grown on these templates [43]. Additionally, the research group led by Pr. Abdallah Ougazzaden at Georgia Tech Europe has also demonstrated the use of 3 nm h-BN for the lift-off of GaN-based devices grown on h-BN [27]. Their investigation covered h-BN templates of different thicknesses, revealing that reducing h-BN thickness resulted in decreased roughness and a lower FWHM of the E2g h-BN peak, as observed through AFM and Raman spectroscopy, respectively [27]. They also noted an enhancement in GaN quality with reduced h-BN thickness [27]. For h-BN thicknesses below 2 nm, they are presently exploring alternative methods for lifting off GaN devices from h-BN to prevent cracks and degradation, alongside utilizing scotch-tape for exfoliation. Their goal is to validate this approach before adopting thinner h-BN templates. Drawing from these studies, our research centered on the growth of $Al_yGa_{1-y}N$ QDs / $Al_xGa_{1-x}N$ using thinner h-BN templates (< 2 nm) to achieve improved structural and optical properties compared to the study involving 3 nm and 6 nm h-BN templates. Furthermore, we collaborated with Prof. Ougazzaden's group at Georgia Tech Europe, leveraging their expertise in exfoliating III-nitrides heterostructures grown on h-BN and their interest in exploring the lift-off of III-nitrides heterostructures grown on thinner h-BN layers (< 2 nm).

IV.4.1. Epitaxial growth and LED fabrication procedure

The growth of the h-BN template with a thickness of 1.5 nm was performed using an Aixtron MOVPE close-coupled showerhead (CCS) reactor on (0 0 0 1) sapphire substrate by Pr. Abdallah Ougazzaden's group in Georgia Tech, Metz, France. The process was carried out at a temperature of 1280 °C and a pressure of 90 mbar. Triethylboron (TEB) and ammonia (NH_3) were employed as precursor gases for boron (B) and nitrogen (N), respectively. More comprehensive information on the growth conditions for h-BN can be found in previously published reports [19]. The LED structure was grown using MBE in a RIBER 32 reactor at CRHEA-CNRS in Valbonne, France. The growth was performed on the 1.5 nm h-BN / c-plane sapphire template. NH_3 was used as the nitrogen source in combination with solid sources for Ga, Al, Si, and Mg. However, during the fabrication of $Al_yGa_{1-y}N$ QDs, a radio frequency (RF) plasma cell with N_2 gas was used instead of NH_3. A 260 nm thick AlN layer was initially grown with the following conditions: a 10 nm thick AlN buffer layer was grown at 1110°C with an ammonia flow rate of 50 sccm and a growth rate of 130 nm/h. Subsequently, the 200 nm AlN layer was grown at 1110°C maintaining an ammonia flow rate of 50 sccm and a growth rate of 130 nm/h. Following this, a 500 nm thick Si-doped $Al_{0.7}Ga_{0.3}N$ layer with a Si concentration of approximately 10^{19} cm^{-3} was deposited at 880°C at a growth rate of 300 nm/h. Next, an active

region consisting of five $Al_{0.3}Ga_{0.7}N$ QD planes with an Al nominal composition (n.c.) of 0.3, separated by $Al_{0.7}Ga_{0.3}N$ barriers lattice matched to the $Al_{0.7}Ga_{0.3}N$ template, was deposited. The equivalent 2D thickness of the $Al_{0.3}Ga_{0.7}N$ (n.c.) QDs was 7 monolayers (MLs), approximately 1.8 nm, with 1 ML corresponding to half the c-lattice parameter, considering a variation of the lattice parameter following Vegard's law between AlN and GaN. In between the QD planes, 5 nm thick $Al_{0.7}Ga_{0.3}N$ cladding layers were grown for both samples. After the deposition of the fifth QD plane, a 20 nm thick $Al_{0.7}Ga_{0.3}N$ layer was grown at 830°C. This was followed by the p-type region composed of a 10 nm $Al_{0.85}Ga_{0.15}N$:Mg electron blocking layer (EBL) and a 10 nm $Al_{0.7}Ga_{0.3}N$:Mg layer grown at 820°C containing an Mg concentration of approximately $5 \times 10^{19} – 1 \times 10^{20}$ cm^{-3} atoms.cm^{-3}. The structure was completed with a 30 nm thick Mg-doped GaN contact layer at 780°C, containing an Mg concentration of approximately $5 \times 10^{19} – 1 \times 10^{20}$ cm^{-3}. The LED structure is depicted in figure 41.

Photolithography and inductively coupled plasma reactive ion etching (ICP-RIE) were employed. The LED mesas were square-shaped with dimensions of (310 x 310) μm^2. A thin semi-transparent Ni/Au (5/5 nm) layer served as the current spreading layer, followed by a Ni/Au (20/200 nm) contact as the top electrode connected to the p-GaN layer. The contact on the n-$Al_{0.7}Ga_{0.3}N$ layer consisted of a stacking of Ti/Al/Ni/Au (30/180/40/200 nm). The LED devices were characterized at room temperature by measuring their I-V characteristics and EL properties. The EL measurements were performed from the sapphire side of the LED, with the emitted light collected through a UV-grade optical fiber connected to a linear CCD spectrometer featuring a spectral resolution of 2.5 nm. The optical power (P_{opt}) was measured from the backside of the devices using a calibrated UV-enhanced Si photodiode.

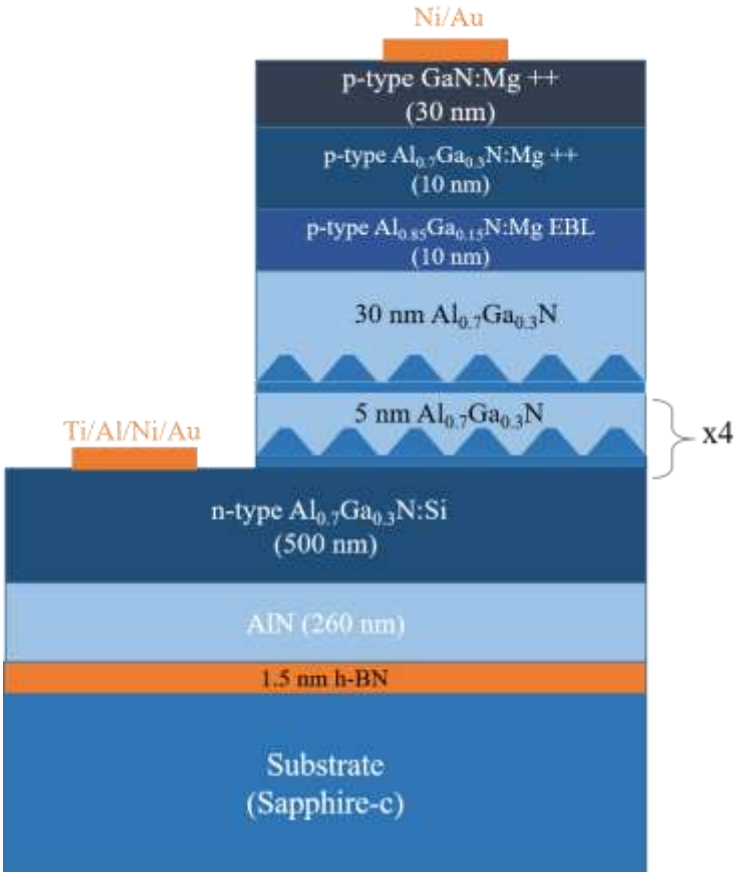

Figure 41. Schematic illustration of the $Al_{0.3}Ga_{0.7}N$ QD-based UV LEDs structures grown on 1.5 nm h-BN / c-sapphire template.

IV.4.2. Crystal properties

XRD Phi scans were conducted on the (1 0 −1 1) $Al_{0.7}Ga_{0.3}N$ layer and (1 0 −1 4) sapphire substrate, and the results are illustrated in figure 42. Six peaks were identified for the $Al_{0.7}Ga_{0.3}N$ layer, indicating the presence of a single domain twisted by an angle of 30° relative to the sapphire substrate. This confirms the conventional orientation of (Al,Ga)N on sapphire. In contrast, the Phi scans for the (Al,Ga)N layers on 3 nm and 6 nm h-BN templates revealed a second in-plane orientation turned by 30°, resulting in two different orientations in the growth plane due to the influence of h-BN. This suggests that thinner h-BN (< 3 nm) may not have a significant effect capable of creating two different orientations in the growth plane probably due to the stronger epitaxial relationship between (Al,Ga)N and sapphire.

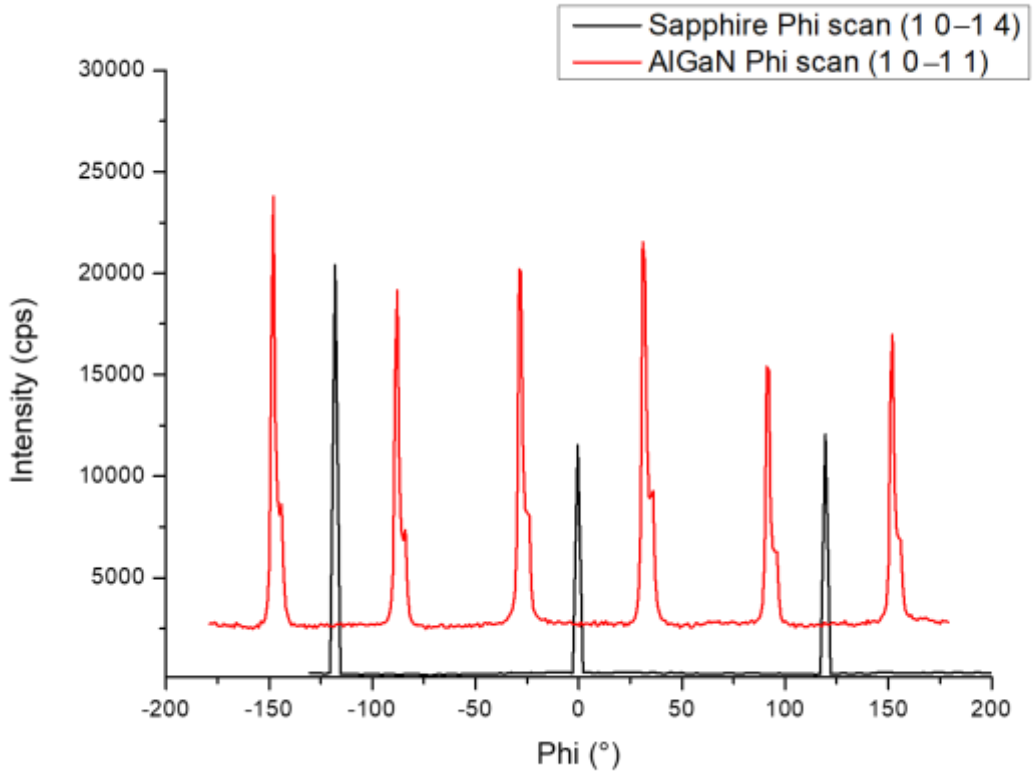

Figure 42. XRD Phi scan performed on the (Al,Ga)N LED structure grown on the 1.5 nm h-BN template along the (1 0 −1 1) and (1 0 −1 4) skew planes for $Al_{0.7}Ga_{0.3}N$ and sapphire, respectively.

X-Ray Diffraction (XRD) rocking curve (RC) full-width-at-half-maximum (FWHM) of the symmetric (0 0 0 2) and skew symmetric (1 0 −1 1) diffractions for the $Al_{0.7}Ga_{0.3}N$ layer in the LED was studied and presented in figure 43.

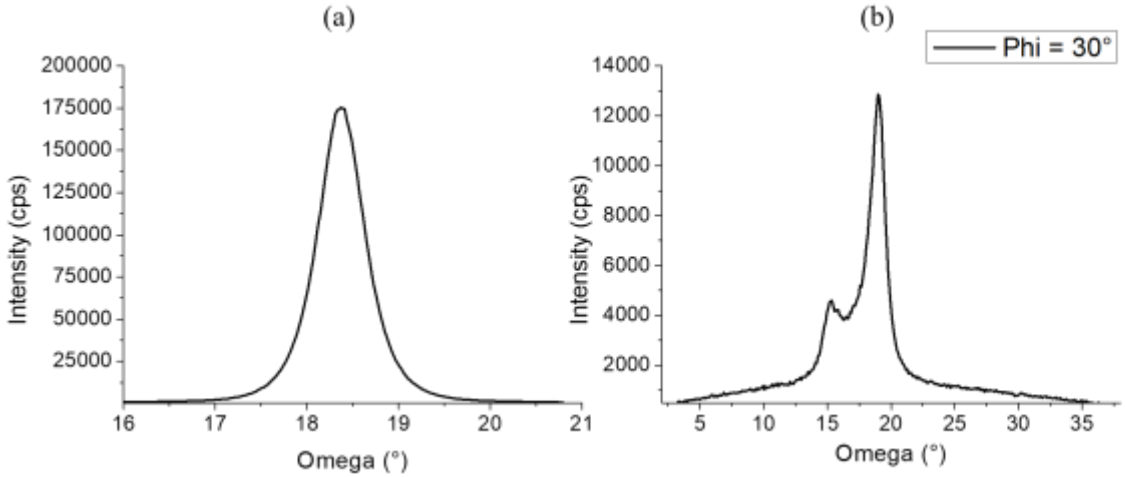

Figure 43. (a) and (b) are XRD omega scans along the AlGaN (0 0 0 2) symmetric plane and AlGaN (1 0 −1 1) skew plane, respectively.

By coupling the XRD measurements with the Dunn and Koch equation [44], it was then possible to correlate mixed and edge threading dislocation densities (TDDs) with the FWHM of the symmetric and skew symmetric reflections [44], [45]. It is critical to mention that the screw TDDs were neglected as they are present in very low proportion (~1%) in nitrides [46]. The values of the FWHM for both symmetric and skew symmetric planes along with the estimated mixed and edge TDDs are summarized in table III.

	(0 0 0 2) (°)	(1 0 −1 1) (°)	Estimated Mixed TDD (cm^{-2})	Estimated Edge TDD (cm^{-2})
(Al,Ga)N QD-based LED on 1.5 nm h-BN	0.6	1.4	1.6×10^{10}	1.6×10^{11}

Table III. Table summarizing the main crystalline properties of the LED measured by X-ray diffraction of the $Al_{0.7}Ga_{0.3}N$ layer.

The XRD measurements of the $Al_{0.7}Ga_{0.3}N$ crystalline structure in the LED revealed FWHM values of 0.6° for the (0 0 0 2) plane and 1.4° for the (1 0 −1 1) plane (for the main and most intense peak). These values indicate a high level of crystalline defects within the structure. The calculated mixed and edge TDDs further supported this observation, with defect densities exceeding 10^{11} cm^{-2}. This underscores the complexity and challenges associated with growing nitride materials on 2D substrates like h-BN, as exemplified in Section II. Despite the elevated FWHM and TDDs values, growth on thinner h-BN layers (such as 1.5 nm in our case) has shown improved crystalline structure compared to our previous attempts of MBE growth of (Al,Ga)N on h-BN templates with thicknesses of 3 nm and 6 nm.

We further continued to study the strain property in the $Al_{0.7}Ga_{0.3}N$ layer by performing asymmetrical reciprocal space mapping (RSM) along the (−1 −1 2 4) reflection and the results presented in figure 44 showed a total relaxation of the $Al_{0.7}Ga_{0.3}N$ layer in the structure. The complete relaxation of the (Al,Ga)N layer is typically due to its important thickness (~ 600 nm).

In addition, calculation of Al composition in AlGaN showed 77% Al composition.

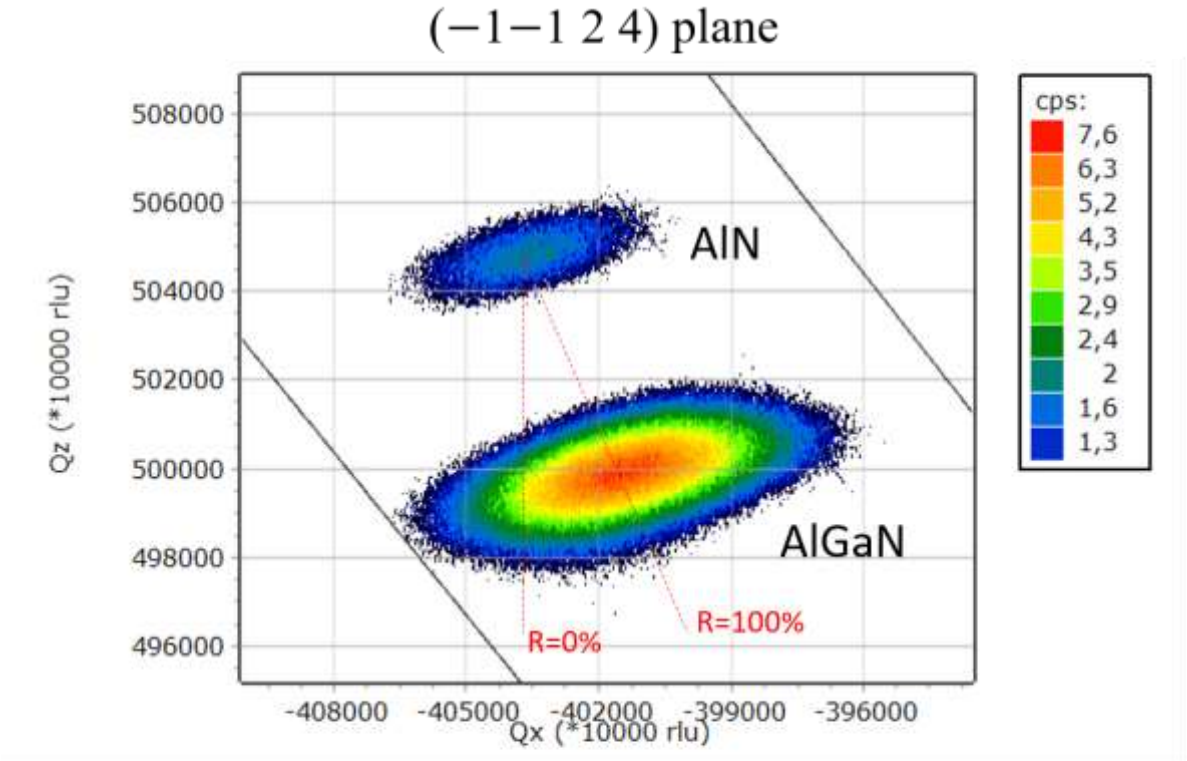

(−1−1 2 4)	w	2th	a (A)	c (A)	%Al	R (%)
AlGaN	90.578	103.626	3.130	5.028	77	103
AlN	91.048	104.812	3.114	4.979	100	100

Figure 44. Asymmetrical reciprocal space mapping (RSM) along the (−1 −1 2 4) reflection for the $Al_{0.7}Ga_{0.3}N$ layer.

IV.4.3. Electroluminescence and electrical properties

Electroluminescence (EL) measurements of the LED were conducted while varying the input current and a comparison of the spectra at six distinct current levels is depicted in figure 45(a). Across all EL spectra obtained at various injection currents, a solitary peak emission within the UV-C range (270 nm) has been consistently identified, originating from the emission of the QDs. Furthermore, only a marginal shift of 1 nm towards shorter wavelengths was observed as the current increased, indicating a robust emission stability with rising current injection. As depicted in Figure 45(b), the EL emission of the LED originates exclusively from the mesa's side. The presence of deep-level emission coming from the p-doped AlGaN and GaN layers observed at the mesa edges of the LED suggests that carriers are mainly recombining at that location, which is also assumed to be the principal region for the carriers' recombination in the QDs active region that leads to the UV emission (although not observable with the naked

eye). This behavior is likely linked to the highly resistive n-$Al_{0.7}Ga_{0.3}N$ contact, which will be examined in more detail in the subsequent sections.

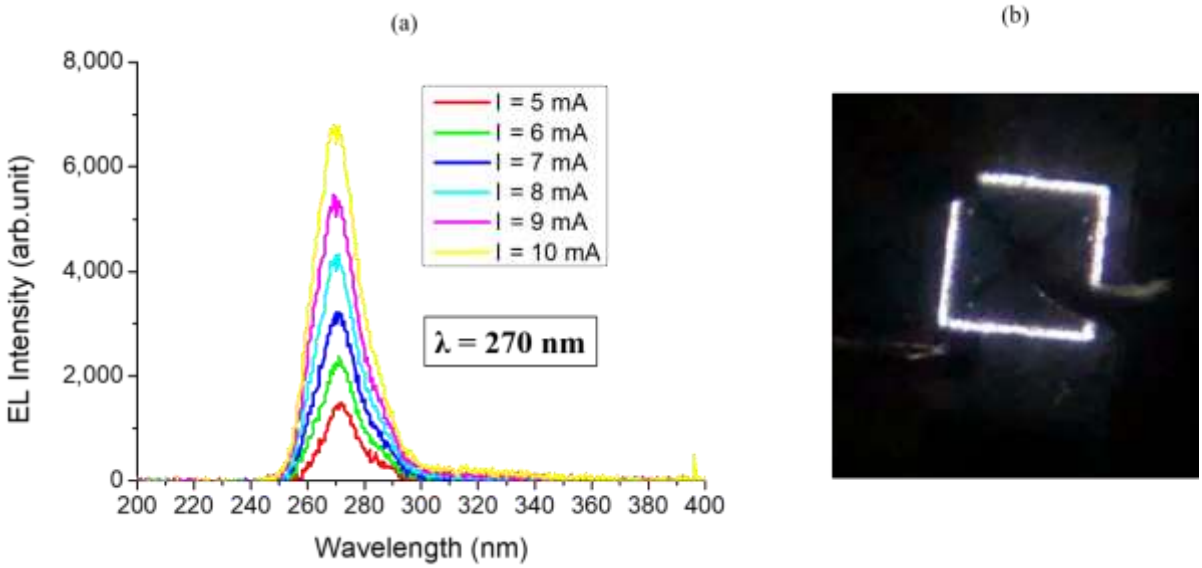

Figure 45. (a) Evolution of the electroluminescence (EL) emission as a function of the input current (I) for the LED. (b) Photograph capturing the operational LED emitting light in real-time.

The I-V curves of the LED are illustrated in figure 46. Focusing first on the behavior under forward bias conditions, the operational voltage is determined to be approximately 69 V at an 8 mA current, accompanied by a series resistance of the order of 6 KΩ. To safeguard against potential contact or device damage, due to the extremely high voltage values, we opted to work with lower injection currents (below 10 mA), allowing us to comprehensively analyze the I-V characteristics of our LEDs and extract crucial parameters. The elevated operating voltages can be attributed to the limited conductivities within the doped $Al_{0.7}Ga_{0.3}N$ and $Al_{0.85}Ga_{0.15}N$ layers, especially the p-type layers characterized by notably high activation energies (≥ 400 meV) of the Mg dopants [47]. The significant series resistance (R_s) value can be attributed to potential excessive contact resistances. When examining the behavior under reverse bias conditions, a leakage current of 1 µA is observed at -1 V. The significant leakage current points out important leakage paths in the device. This strong leakage can be mainly due to the high defects density in the epitaxial layers (TD > 10^{10} cm^{-2}) [48] that was also measured in our LED structure (table III).

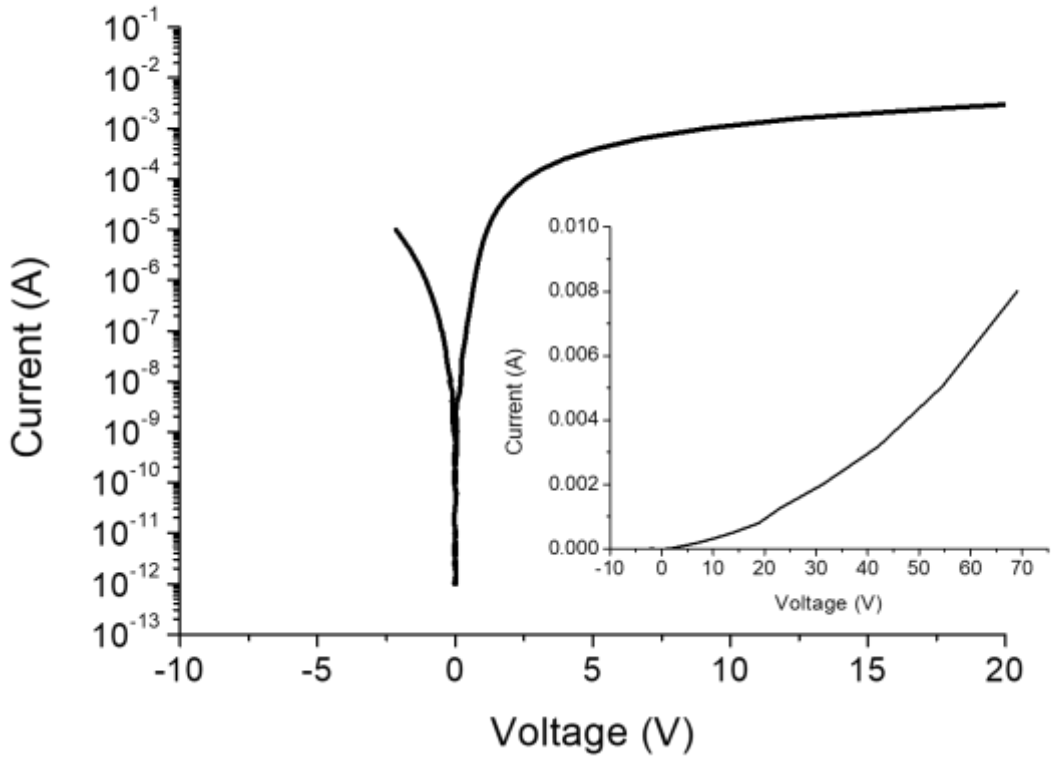

Figure 46. Current-Voltage measurements of the (Al,Ga)N based QD-LED on h-BN.

The Transmission Line Method (TLM) provides a simple and rapid tool for determining the resistivity of semiconductor layers and specific contact resistances. TLM patterns are also fabricated during the fabrication of LEDs (i.e. using different patterns on the etching mask) in the clean room technology center. They consist of three rows of 8 rectangular contacts (figure 47), each measuring 60 µm x 130 µm (L x w). The separations between two adjacent contacts (l) are 5, 10, 20, 40, 80, 120, and 160 µm, respectively.

The n row consists of a sequence of 8 contacts n-Ti/Al/Ni/Au (30 nm / 180 nm / 40 nm / 200 nm) that have been directly deposited on the n-type $Al_{0.7}Ga_{0.3}N$: Si layer. The p row is composed of a GaN: Mg mesa upon which the *p*-contacts Ni/Au (20 nm / 200 nm) are placed. The p ST row is nearly identical to the p row, except that the deposition of a semi-transparent p-contact precedes the deposition of the p-contact. In other words, the structure of the contact is indeed Ni/Au but thinner (5 nm / 5 nm).

Current-voltage (I-V) characteristics are measured in pairs between two adjacent contacts. A voltage ranging from -2 to 2 V is applied. This way, a set of seven I-V curves is obtained for each series of contacts. Their characteristics are ohmic in the ideal case.

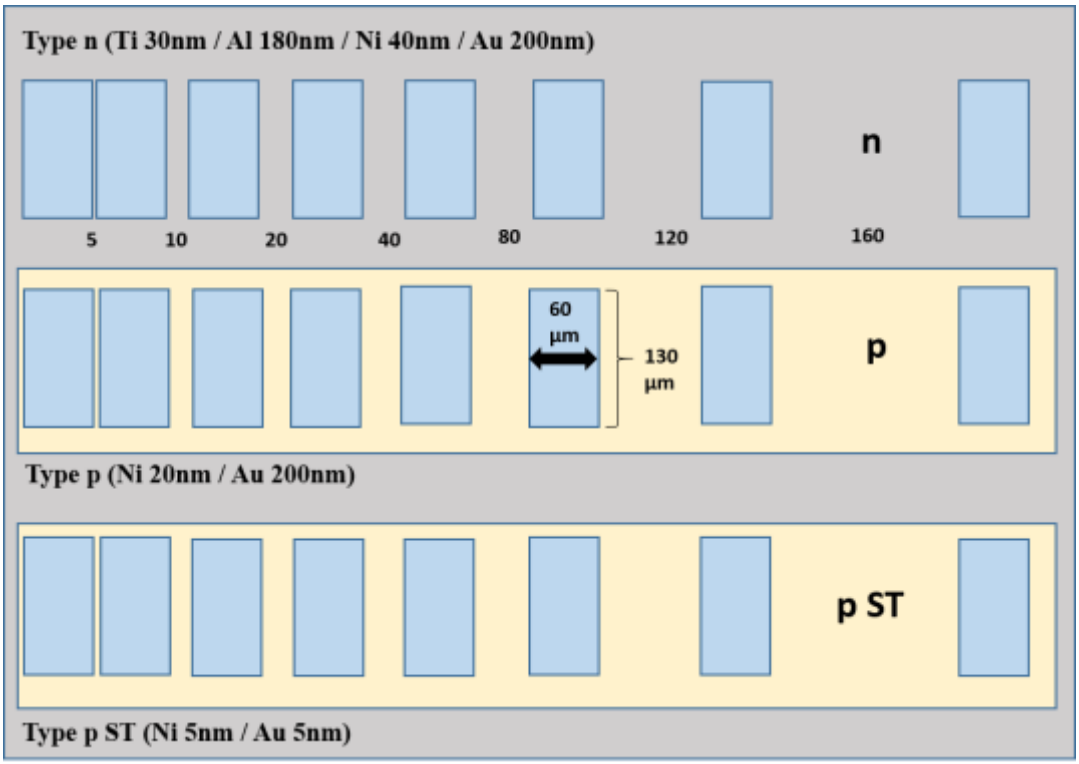

Figure 47. The TLM pattern consisting of one row of n contacts *n*-Ti /Al /Ni / Au and two rows of contacts: *p*-Ni 20 nm /Au 200 nm (p) and *p*-Ni 5 nm / Au 5 nm (p ST).

Figures 48(a), (b), and (c) present the resistance dU/dI associated with each I-V curve in relation to the distance between two contacts for the three rows of n, p, and p ST contacts, respectively. The insets in the figures also illustrate the rectifying and ohmic behaviors of the contacts through their I-V curves. For the n contacts, the specific contact resistance (ρ_c) was determined to be 1.7 Ω.cm^{-2}, indicative of the contacts' high resistivity. The contact resistance (Rc) was also notably high at 35 KΩ. As for the p contacts, ρ_c measured 0.01 Ω.cm^{-2} and Rc was approximately 7 KΩ. Furthermore, the p ST contacts exhibited ρ_c of 0.02 Ω.cm^{-2} and Rc of around 11 KΩ. The p contacts showed lower resistance than the n contacts. The cause of the highly resistive behavior in the n contact is uncertain and should be further investigated. It could stem from a Si doping concentration lower than expected (fluctuation in the Si flux) or related to potential issues in the LED fabrication process, particularly in the etching stage. This might have led to the observed high-resistive behavior seen in the I-V characteristic measurements depicted in figure 46.

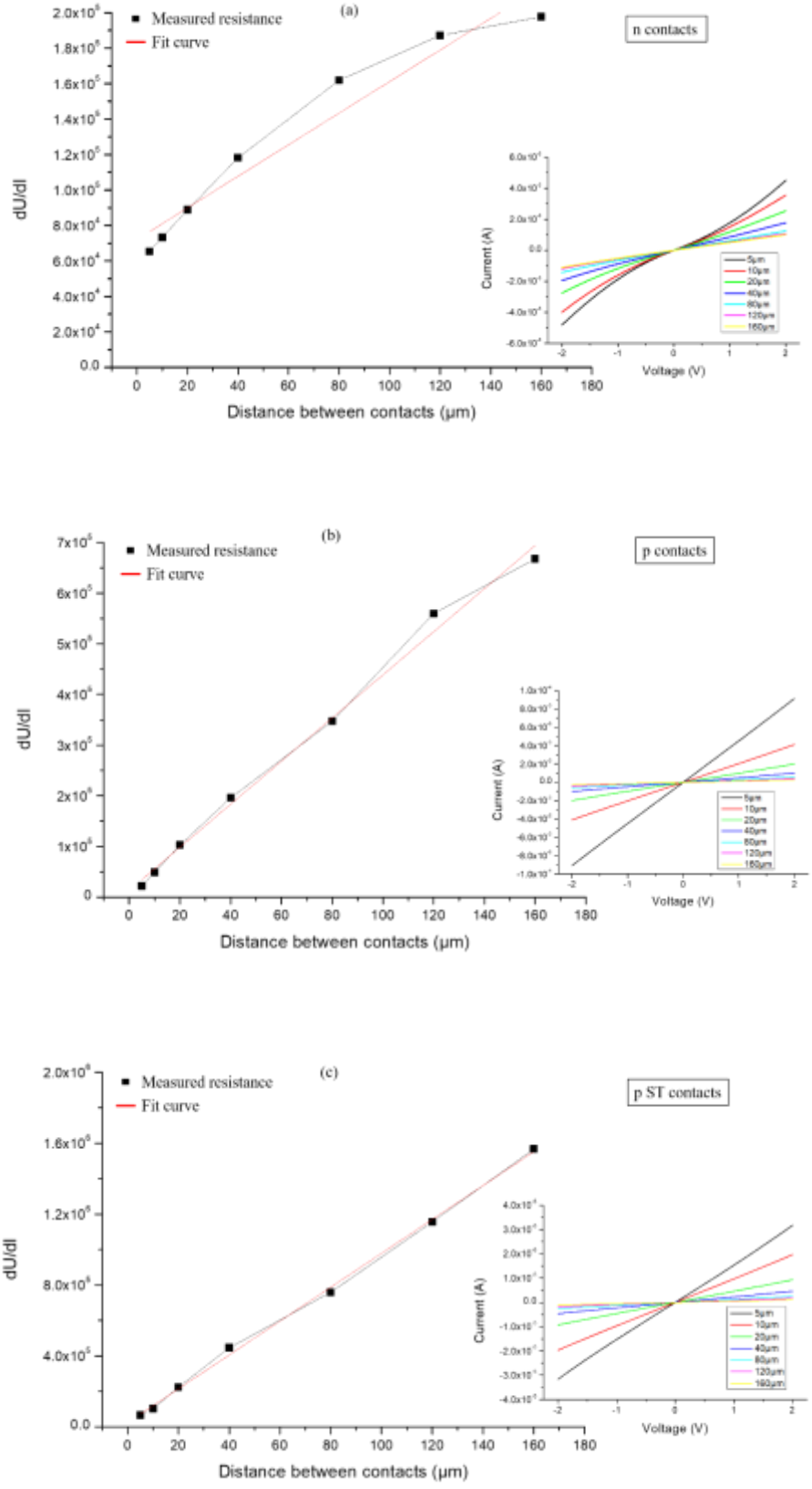

Figure 48. Measured resistances between two adjacent contacts, reported as a function of the distance for n, p, and p ST contacts, respectively. The insets in the figures show the I-V curves measured between two adjacent contacts for the n, p, and p ST contacts, respectively.

Figure 49 provides additional insights into the external quantum efficiency (EQE) and optical power (P_{opt}) characteristics of the LED as a function of the current (I). The maximum EQE, reaching approximately 0.007%, is observed at around 4 mA. Above this maximum, the EQE gradually decreases, reaching a minimum value of approximately 0.005% at 8 mA. This immediate decrease at slightly higher currents is attributed to non-radiative processes such as electron leakage contribution [49]. Furthermore, heating effect at the LED junction is seen as the contributing reason for the EQE decrease observed in the LED as a consequence of the very high operating voltages. This extreme case, as shown in the LED current – voltage measurements presented in figure 46, is related to highly resistive contacts and/or doped layers. In terms of P_{opt}, the values are in the μW range for the currents injected. The optical power measured was 1 μW at 4 mA then increased to a maximum value of 1.7 μW at 8 mA.

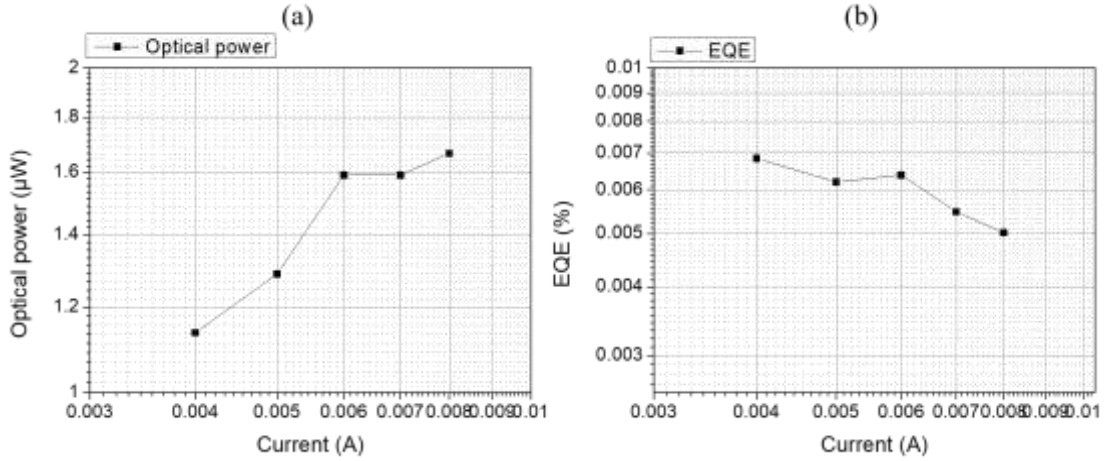

Figure 49. (a) EQE variation as a function of the current (I); (b) P_{opt} variation as a function of I for (Al,Ga)N QD-based LED / h-BN / sapphire characteristics.

IV.4.4. Conclusion

In summary, we successfully carried out the growth of an $Al_{0.3}Ga_{0.7}N$ QD / $Al_{0.7}Ga_{0.3}N$ LED on a 1.5 nm h-BN template grown on sapphire using MBE. One objective was to enhance the crystalline structure of the heterostructure in comparison to QD-based structures grown on 3 nm and 6 nm h-BN templates. The investigation focused on the crystalline properties of the structures through XRD measurements, revealing an improved crystalline quality when compared to the structures grown on 3 nm and 6 nm h-BN templates. Electroluminescence (EL) measurements of the LED indicated a single peak emission in the UV-C range (270 nm) originating from the QDs. Additionally, I-V and TLM measurements highlighted high operating voltages and contact resistances attributed to the contacts themselves, along with a substantial defect density (> 10^{11} cm^{-2}) within the structure. The EQE and P_{opt} measurements showed relatively modest efficiencies, with maximum values of approximately 0.01% and less than 2 µW, respectively. The success of the UV-C emitting LEDs grown on h-BN serves as a promising prototype, demonstrating the feasibility of manufacturing UV-C emitting LEDs on h-BN using MBE. However, further improvements are required in the future, to fully exploit the benefit in growing III-nitrides heterostructures on h-BN.

IV.5. General conclusion

In conclusion, this chapter provided an overview on van der Waals epitaxy of 2D materials, with a specific focus on hexagonal boron nitride (h-BN), and explored the rationale behind the drive to grow III-nitride heterostructures on h-BN substrates. The motivation stemmed from the desire to leverage h-BN's unique properties to enhance the growth of (Al,Ga)N QD-based heterostructures. This study centered on the growth of $Al_yGa_{1-y}N$ QDs / $Al_xGa_{1-x}N$ structures on 3 nm and 6 nm h-BN / sapphire templates, extensively investigating their structural and optical properties through techniques such as X-ray diffraction, transmission electron microscopy, atomic force microscopy, and photoluminescence. The investigation unraveled the impact of h-BN on the heterostructure, revealing an orientational guidance that created two different orientations in the growth plane. The TEM study confirmed the existence of a 30° rotated domain. The UV-C emission from the QDs validated the success of the proposed structure design for both templates. Subsequently, the exploration extended to the domain of exfoliation, where the QDs structure grown on 6 nm h-BN underwent successful exfoliation through scotch-tape. Photoluminescence measurements attested to the persistent UV-C emission from the exfoliated QDs. Transferring the exfoliated structure to an SiO_2 / Si substrate via dry transfer demonstrated a transfer efficiency of 50%, opening avenues for flexible QDs-based UV-C emitting LEDs. Furthermore, the chapter detailed the growth and fabrication of an (Al,Ga)N QDs-based LED on 1.5 nm h-BN / sapphire substrate using MBE. The electroluminescence measurements unveiled UV-C emission at 270 nm. However, the study encountered challenges such as high resistivity in contacts and doped layers, attributed to substantial defects density ($> 10^{11}$ cm^{-2}). These characteristics hindered the increase of current beyond 10 mA due to elevated operating voltages. Although the EQE and optical power values were comparatively weak against conventional LEDs on sapphire, this LED epitomized a proof of concept. It successfully demonstrated the feasibility of growing (Al,Ga)N QDs-based LEDs on h-BN by MBE, emitting in the UV-C range. This achievement also heralded the potential for lift-off attempts for LED exfoliation, laying the groundwork for flexible QDs-based UV-C emitting LEDs. In essence, this chapter underscores the transformative potential of van der Waals epitaxy and its role in advancing optoelectronic devices.

References:

[1] G. Cassabois, P. Valvin, et B. Gil, « Hexagonal boron nitride is an indirect bandgap semiconductor », *Nature Photon*, vol. 10, nº 4, Art. nº 4, avr. 2016, doi: 10.1038/nphoton.2015.277.

[2] S. Zhang, G. Chen, B. Wang, D. Zhang, et H. Yan, « Growth of oriented BN films prepared by electron cyclotron resonance CVD », *Journal of Crystal Growth*, vol. 223, nº 4, p. 545-549, mars 2001, doi: 10.1016/S0022-0248(01)00679-0.

[3] M. J. Molaei, M. Younas, et M. Rezakazemi, « A comprehensive review on recent advances in two-dimensional (2D) hexagonal boron nitride », *ACS Applied Electronic Materials*, vol. 3, nº 12, p. 5165-5187, 2021.

[4] A. Koma, « Van der Waals epitaxy—a new epitaxial growth method for a highly lattice-mismatched system », *Thin Solid Films*, vol. 216, nº 1, p. 72-76, 1992.

[5] K. Watanabe, T. Taniguchi, et H. Kanda, « Direct-bandgap properties and evidence for ultraviolet lasing of hexagonal boron nitride single crystal », *Nature materials*, vol. 3, nº 6, p. 404-409, 2004.

[6] A. K. Geim, « Graphene: status and prospects », *science*, vol. 324, nº 5934, p. 1530-1534, 2009.

[7] X. Tan, S. Yang, et H. Li, « Epitaxy of III-Nitrides Based on Two-Dimensional Materials », *Acta Chimica Sinica*, vol. 75, nº 3, p. 271, 2017.

[8] J. Yu *et al.*, « Van der Waals epitaxy of iii-nitride semiconductors based on 2D materials for flexible applications », *Advanced Materials*, vol. 32, nº 15, p. 1903407, 2020.

[9] H. X. Jiang et J. Y. Lin, « Hexagonal boron nitride for deep ultraviolet photonic devices », *Semiconductor Science and Technology*, vol. 29, nº 8, p. 084003, 2014.

[10] Q. Paduano, M. Snure, D. Weyburne, A. Kiefer, G. Siegel, et J. Hu, « Metalorganic chemical vapor deposition of few-layer sp2 bonded boron nitride films », *Journal of Crystal Growth*, vol. 449, p. 148-155, 2016.

[11] Y. Kobayashi, C.-L. Tsai, et T. Akasaka, « Optical band gap of h-BN epitaxial film grown on c-plane sapphire substrate », *physica status solidi c*, vol. 7, nº 7-8, p. 1906-1908, 2010.

[12] J. Yu *et al.*, « Theoretical study on critical thickness of heteroepitaxial h-BN on hexagonal crystals », *Journal of Crystal Growth*, vol. 467, p. 126-131, 2017.

[13] G. Wang *et al.*, « Decoding the mechanism of the mechanical transfer of a GaN-based heterostructure via an h-BN release layer in a device configuration », *Applied Physics Letters*, vol. 105, nº 12, 2014.

[14] A. Zaiter *et al.*, « Crystalline Quality and Surface Morphology Improvement of Face-to-Face Annealed MBE-Grown AlN on h-BN », *Materials*, vol. 15, nº 23, p. 8602, 2022.

[15] Q. Wu *et al.*, « Growth mechanism of AlN on hexagonal BN/sapphire substrate by metal-organic chemical vapor deposition », *CrystEngComm*, vol. 19, nº 39, p. 5849-5856, 2017, doi: 10.1039/c7ce01064h.

[16] Q. Wu *et al.*, « Exfoliation of AlN film using two-dimensional multilayer hexagonal BN for deep-ultraviolet light-emitting diodes », *Appl. Phys. Express*, vol. 12, nº 1, p. 015505, janv. 2019, doi: 10.7567/1882-0786/aaeede.

[17] T. H. Seo *et al.*, « Boron nitride nanotubes as a heat sinking and stress-relaxation layer for high performance light-emitting diodes », *Nanoscale*, vol. 9, nº 42, p. 16223-16231, 2017.

[18] T. Ayari *et al.*, « Wafer-scale controlled exfoliation of metal organic vapor phase epitaxy grown InGaN/GaN multi quantum well structures using low-tack two-dimensional layered h-BN », *Appl. Phys. Lett.*, vol. 108, nº 17, p. 171106, avr. 2016, doi: 10.1063/1.4948260.

[19] X. Li *et al.*, « Large-area two-dimensional layered hexagonal boron nitride grown on sapphire by metalorganic vapor phase epitaxy », *Crystal Growth and Design*, vol. 16, nº 6, p. 3409-3415, juin 2016, doi: 10.1021/acs.cgd.6b00398.

[20] B. Damilano, J. Brault, et J. Massies, « Formation of GaN quantum dots by molecular beam epitaxy using NH3 as nitrogen source », *Journal of Applied Physics*, vol. 118, nº 2, juill. 2015, doi: 10.1063/1.4923425.
[21] J. Brault *et al.*, « Linear alignment of GaN quantum dots on AlN grown on vicinal SiC substrates », *Journal of Applied Physics*, vol. 93, nº 5, p. 3108-3110, mars 2003, doi: 10.1063/1.1538334.
[22] J. Brault *et al.*, « Investigation of AlyGa1− yN/Al0. 5Ga0. 5N quantum dot properties for the design of ultraviolet emitters », *Japanese Journal of Applied Physics*, vol. 55, nº 5S, p. 05FG06, 2016.
[23] I. Horcas, R. Fernández, J. M. Gómez-Rodríguez, J. Colchero, J. Gómez-Herrero, et A. M. Baro, « WSXM : A software for scanning probe microscopy and a tool for nanotechnology », *Review of Scientific Instruments*, vol. 78, nº 1, p. 013705, janv. 2007, doi: 10.1063/1.2432410.
[24] S. Saha *et al.*, « Comprehensive characterization and analysis of hexagonal boron nitride on sapphire », *AIP Advances*, vol. 11, nº 5, mai 2021, doi: 10.1063/5.0048578.
[25] P. Vuong *et al.*, « Influence of Sapphire Substrate Orientation on the van der Waals Epitaxy of III-Nitrides on 2D Hexagonal Boron Nitride: Implication for Optoelectronic Devices », *ACS Applied Nano Materials*, vol. 5, nº 1, p. 791-800, janv. 2022, doi: 10.1021/acsanm.1c03481.
[26] D. Chugh, S. Adhikari, J. Wong-Leung, M. Lysevych, C. Jagadish, et H. H. Tan, « Improving the Morphology and Crystal Quality of AlN Grown on Two-Dimensional hBN », *Crystal Growth and Design*, vol. 20, nº 3, p. 1811-1819, mars 2020, doi: 10.1021/acs.cgd.9b01543.
[27] S. Sundaram *et al.*, « MOVPE of GaN-based mixed dimensional heterostructures on wafer-scale layered 2D hexagonal boron nitride—A key enabler of III-nitride flexible optoelectronics », *APL Materials*, vol. 9, nº 6, p. 061101, 2021.
[28] J. Brault *et al.*, « Internal quantum efficiencies of AlGaN quantum dots grown by molecular beam epitaxy and emitting in the UVA to UVC ranges », *Journal of Applied Physics*, vol. 126, nº 20, p. 205701, nov. 2019, doi: 10.1063/1.5115593.
[29] S. Matta *et al.*, « Influence of the heterostructure design on the optical properties of GaN and $Al_{0.1}Ga_{0.9}N$ quantum dots for ultraviolet emission », *Journal of Applied Physics*, vol. 122, nº 8, p. 085706, août 2017, doi: 10.1063/1.5000238.
[30] W. Paszkowicz, J. B. Pelka, M. Knapp, T. Szyszko, et S. Podsiadlo, « Lattice parameters and anisotropic thermal expansion of hexagonal boron nitride in the 10–297.5 K temperature range », *Applied Physics A*, vol. 75, p. 431-435, 2002.
[31] J. Brault *et al.*, « Polar and semipolar GaN/Al0. 5Ga0. 5N nanostructures for UV light emitters », *Semiconductor Science and Technology*, vol. 29, nº 8, p. 084001, 2014.
[32] S. Matta *et al.*, « Properties of AlN layers grown on c-sapphire substrate using ammonia assisted MBE », *Journal of Crystal Growth*, vol. 499, p. 40-46, 2018.
[33] S. Matta *et al.*, « Photoluminescence properties of (Al, Ga) N nanostructures grown on Al0. 5Ga0. 5N (0001) », *Superlattices and Microstructures*, vol. 114, p. 161-168, 2018.
[34] J. Brault *et al.*, « UVA and UVB light emitting diodes with $Al_{y}Ga_{1-y}N$ quantum dot active regions covering the 305–335 nm range », *Semiconductor Science and Technology*, vol. 33, nº 7, p. 075007, juill. 2018, doi: 10.1088/1361-6641/aac3bf.
[35] J. Brault *et al.*, « UVB LEDs grown by molecular beam epitaxy using AlGaN quantum dots », *Crystals*, vol. 10, nº 12, p. 1097, 2020.
[36] M. D. Abràmoff, P. J. Magalhães, et S. J. Ram, « Image processing with ImageJ », *Biophotonics international*, vol. 11, nº 7, p. 36-42, 2004.
[37] P. Blake *et al.*, « Making graphene visible », *Applied physics letters*, vol. 91, nº 6, 2007.

[38] A. Yariv et P. Yeh, « Optical waves in crystal propagation and control of laser radiation », janv. 1983, Consulté le: 22 septembre 2023. [En ligne]. Disponible sur: https://www.osti.gov/biblio/5951989
[39] C. Elias *et al.*, « Flat bands and giant light-matter interaction in hexagonal boron nitride », *Physical Review Letters*, vol. 127, nº 13, p. 137401, 2021.
[40] L. V. Rodríguez-de Marcos, J. I. Larruquert, J. A. Méndez, et J. A. Aznárez, « Self-consistent optical constants of SiO 2 and Ta 2 O 5 films », *Optical Materials Express*, vol. 6, nº 11, p. 3622-3637, 2016.
[41] D. T. Pierce et W. E. Spicer, « Electronic structure of amorphous Si from photoemission and optical studies », *Physical Review B*, vol. 5, nº 8, p. 3017, 1972.
[42] Ü. Özgür, G. Webb-Wood, H. O. Everitt, F. Yun, et H. Morkoç, « Systematic measurement of Al x Ga 1− x N refractive indices », *Applied Physics Letters*, vol. 79, nº 25, p. 4103-4105, 2001.
[43] M. Snure, G. Siegel, D. C. Look, et Q. Paduano, « GaN and AlGaN/GaN heterostructures grown on two dimensional BN templates », *Journal of Crystal Growth*, vol. 464, p. 168-174, avr. 2017, doi: 10.1016/j.jcrysgro.2016.11.088.
[44] C. G. Dunn et E. F. Kogh, « Comparison of dislocation densities of primary and secondary recrystallization grains of Si-Fe », *Acta Metallurgica*, vol. 5, nº 10, p. 548-554, oct. 1957, doi: 10.1016/0001-6160(57)90122-0.
[45] M. Nemoz, R. Dagher, S. Matta, A. Michon, P. Vennéguès, et J. Brault, « Dislocation densities reduction in MBE-grown AlN thin films by high-temperature annealing », *Journal of Crystal Growth*, vol. 461, p. 10-15, mars 2017, doi: 10.1016/j.jcrysgro.2016.12.089.
[46] D. M. Follstaedt, N. A. Missert, D. D. Koleske, C. C. Mitchell, et K. C. Cross, « Plan-view image contrast of dislocations in GaN », *Applied Physics Letters*, vol. 83, nº 23, p. 4797-4799, déc. 2003, doi: 10.1063/1.1632540.
[47] Y.-H. Liang et E. Towe, « Progress in efficient doping of high aluminum-containing group III-nitrides », *Applied Physics Reviews*, vol. 5, nº 1, 2018.
[48] S. W. Lee *et al.*, « Origin of forward leakage current in GaN-based light-emitting devices », *Applied physics letters*, vol. 89, nº 13, 2006.
[49] J. Piprek, « How to decide between competing efficiency droop models for GaN-based light-emitting diodes », *Applied Physics Letters*, vol. 107, nº 3, 2015.

General conclusions and perspectives

The main objective of this PhD thesis was to explore the epitaxial growth of (Al, Ga)N using molecular beam epitaxy (MBE) and to investigate innovative strategies for enhancing the quality of aluminum nitride (AlN) templates, which play a crucial role as buffer layers in efficient light-emitting diodes (LEDs). The research also aimed to examine the feasibility of growing (Al, Ga)N quantum dots (QDs) on hexagonal boron nitride (h-BN) through MBE, offering a new avenue for the development of flexible deep ultraviolet (UV-C) emitters, particularly UV LEDs.

The initial segment of our study involved the implementation of a post-growth face-to-face high temperature annealing technique to enhance the crystalline and morphological qualities of AlN templates. The experimentation began by examining the impact of annealing temperature and duration under different atmospheres: nitrogen (N_2) and a combination of 50 % nitrogen (N_2) with 50% hydrogen (H_2). Our goal was to develop an effective annealing recipe that would ensure optimal thermal conditions for the templates. Ultimately, a combination of 30 minutes under N_2 followed by 15 minutes under N_2 + H_2, totaling 45 minutes, yielded the best results. This treatment led to significant improvements in surface morphology, transforming it from a rough grain-dominated surface to a smooth atomic-step arrangement. Additionally, crystalline quality advancements were confirmed through X-ray diffraction (XRD) measurements on both symmetric and skew symmetric planes. Transmission electron microscopy (TEM) studies also revealed a decrease in dislocation density and the elimination of stacking faults due to the annealing process. However, the annealing process gave rise to polarity inversion domain boundaries (IDBs) at the sapphire-AlN interface, attributed to oxygen diffusion from the sapphire substrate. These IDBs displayed an Al-polar zone above and an N-polar zone below. Subsequent annealings under 50% N_2 + 50% H_2 at 1550°C further reduced edge dislocation densities while shifting the IDB in the AlN layer closer to the surface, approximately 70 nm below, likely due to the ongoing oxygen diffusion during annealing. Furthermore, our study included the pioneering investigation of AlN growth on h-BN through MBE. We conducted MBE fabrication of 50 nm and 100 nm AlN layers on 3 nm h-BN/sapphire templates, examining the effects of post-growth face-to-face annealing on surface morphology and crystalline quality. Annealing conditions were varied in terms of temperature (ranging from 1450 to 1650°C) and duration. The atomic force microscopy (AFM)-measured root mean square (RMS) roughness indicated a substantial decrease after the initial two annealing steps at 1450 and 1550°C. Notably, modifications at the AlN surface included a reduction in initially

present 3D island structures and overall surface smoothing, reflected in a decline of RMS roughness from 5.2 to 2.1 nm. However, a noticeable increase in RMS roughness was observed after the third and fourth annealing steps at 1650°C. Crystalline quality improvements were evident from omega scan full-width half-maximum (FWHM) measurements for (0 0 0 2) and (1 0 −1 1) reflections, demonstrating a decrease with rising annealing temperature. The investigation of threading dislocation densities (TDDs), both edge and mixed types, showed reduction with each successive annealing step. TEM analysis after the full annealing cycle revealed unexpected boron (B) diffusion from the sapphire interface through the AlN layer. In certain regions, h-BN diffusion extended to the surface, recrystallizing atop the AlN layer. Additionally, h-BN presence within the sapphire substrate along the interface was identified. These unforeseen diffusion behaviors underscore the need for precise control over annealing conditions to prevent h-BN thermal instability. Lastly, we regrew an AlN layer through MBE on the thermally annealed 100 nm thick layer, resulting in a step-bunching morphology with broad terraces. Enhanced structural quality was evident, marked by reduced mixed and edge TDDs compared to the initial AlN layer.

Subsequently, we employed the annealed AlN templates as substrates to enhance the performance of UV LEDs grown through metal organic chemical vapor deposition (MOCVD), avoiding direct growth on sapphire substrates. A comparison was made with previous studies conducted at CRHEA. The LED structures (UVB-1, UVB-2, and UVB-3) were grown in series, with variations in the Cp_2Mg flow as the distinguishing factor to investigate its impact on LED power efficiency and electrical characteristics. Measured against the current, the light output power and external quantum efficiency (EQE) were determined for all three LEDs. At a current of 20 mA, UVB-1 exhibited a light output power of 0.03 mW, while UVB-2 and UVB-3 displayed 0.23 mW and 0.08 mW, respectively. Correspondingly, the external quantum efficiencies were 0.04%, 0.28%, and 0.11% for UVB-1, UVB-2, and UVB-3. Our findings highlighted the vital role of Mg doping concentration choice in shaping the LED's electrical and optical efficiencies. The LED with the lowest Mg concentration (80 cc) exhibited poor electrical and optical performance, suggesting inadequate hole injection into the active region and subsequent diminished carrier recombination and light emission. Conversely, the LED with the highest Mg concentration (240 cc) demonstrated improved but suboptimal performance, possibly due to unfavorable outcomes tied to excessive Mg concentrations, such as the creation of defects or non-uniform doping profiles. The LED with an intermediate Mg concentration of 160 cc exhibited optimal performance, indicating a balanced provision of efficient hole

injection, reduced resistivity, and enhanced carrier recombination in the active region. Overall, our efforts led to significantly higher EQE values, notably seen in the UVB-2 LED, which recorded an EQE value ten times greater than the highest EQE achieved in previous work involving tunnel junction (TJ) UV LEDs on AlN MOCVD. The improvement can be attributed primarily to enhanced crystalline quality, with the best sample exhibiting dislocation density of $2 – 3 \times 10^9$ cm^{-2}. These outcomes suggest that incorporating tunnel junctions on annealed AlN templates holds potential for further augmenting EQE values of future UV LEDs. This approach has the potential to surpass limitations encountered in prior AlN MOCVD growth, potentially reaching even higher levels of efficiency.

We then directed our attention to exploring the potential of $Al_yGa_{1-y}N$ QDs grown on $Al_{0.7}Ga_{0.3}N$ (0 0 0 1) templates as active regions for deep UV LEDs. Our investigation encompassed the performance of $Al_yGa_{1-y}N$ QD-based UV LEDs spanning a wide wavelength range, from 340 nm to 265 nm. We correlated these results with the QD structural and optical characteristics. Notably, substantial differences emerged between the electroluminescence (EL) and photoluminescence (PL) properties, attributed to variations in QD composition and size (height) inhomogeneities within LED active regions due to the utilization of multiple QD planes, unlike the single plane used in reference PL measurements. A comprehensive analysis of the EQE and optical power as a function of current density (J) unveiled a decline in values at higher J. This reduction was primarily associated with decreased injection efficiency and a concurrent heating effect. Furthermore, a distinct correlation emerged between the EL wavelength and J, attributed to varied injection into different QD populations, reflecting a preference for deeper localization potentials (linked to lower Al concentration and/or larger QD sizes) at lower J.

In the subsequent phase, our focus shifted to the growth of TJ UV LEDs using MBE, aiming to augment non-equilibrium hole injection and overall injection efficiency. The resultant enhanced electrical and optical performance was compared to the standard LEDs manufactured in the earlier phase. Incorporating TJs notably led to a remarkable enhancement in optical power. For instance, at a current density of 10 $A.cm^{-2}$, the optical power for standard LEDs reached 30 µW, whereas for TJ LEDs, it surged significantly to 240 µW, marking an eightfold increase. This enhancement can also be attributed to the improved transparency of the TJ-based LED due to the removal of the semitransparent Ni/Au electrode.

Furthermore, a substantial increase in EQE for TJ UV LEDs was observed compared to standard UV LEDs. The EQE for standard UV LEDs peaked around 0.08%, while for TJ UV LEDs, it reached approximately 0.65%, marking an eightfold increase. These findings underscored a significant enhancement in electrical injection efficiency attributable to the presence of the TJ.

In the final segment of this thesis, $Al_{0.3}Ga_{0.7}N$ QD-based structures emitting in the UV-C range were fabricated on h-BN/sapphire templates via MBE, utilizing two different h-BN thicknesses: 3 nm and 6 nm. Structural analysis of $Al_{0.7}Ga_{0.3}N$ layers indicated the influence of h-BN layers on subsequent structures, manifesting as orientation guidance that generated two distinct orientations within the growth plane. This highlighted the pivotal role of growing high-quality crystalline h-BN layers. Optical assessments revealed UV-C emission from the QDs in the form of emissions with a peak intensity ranging between 275 nm (4.5 eV) and 280 nm (4.43 eV). Moreover, the integrated photoluminescence intensity ratio (I (300K) / I (12K)) of the QD emission peak, between room temperature and low temperature, was determined to be approximately 10%. Subsequently, we delved into investigating the mechanical exfoliation process using scotch tape on the (Al, Ga)N QD structure grown on 6 nm h-BN/sapphire, exploring the structural and optical attributes of the QDs post-exfoliation. Photoluminescence measurements confirmed the UV-C emission from the exfoliated QDs. Transferring the exfoliated structure to a SiO2/Si substrate through dry transfer exhibited a transfer efficiency of 50%, presenting prospects for flexible QDs-based UV-C-emitting LEDs. Furthermore, our study sought to broaden its horizon by aiming to grow (Al, Ga)N QD-based LEDs on a 1.5 nm h-BN layer that emitted in the UV-C range. Opting for a thinner h-BN layer aimed to enhance the quality of (Al, Ga)N heterostructures created through MBE. Electroluminescence measurements unveiled UV-C emission at 270 nm. However, challenges arose, including high resistivity in contacts and layers due to significant defect density ($> 10^{11}$ cm^{-2}), limiting current increase beyond 10 mA due to elevated operating voltages. Although the EQE and optical power values were relatively low compared to conventional LEDs on sapphire, this LED served as a proof of concept. It effectively demonstrated the feasibility of MBE-grown (Al, Ga)N QDs-based LEDs on h-BN, emitting in the UV-C range.

This comprehensive study, encompassing a diverse range of strategies to enhance the quality of (Al, Ga)N heterostructures and (Al, Ga)N-based UV LEDs, presents numerous avenues for building upon the achieved results and achieving significant advancements. The optimized post-growth annealing recipe we developed stands as a pivotal method for attaining

buffer layers with low defect densities ($<10^9$ cm^{-2}). When coupled with TJ UV LEDs, it has the potential to collaboratively enhance the overall opto-electrical performance of the LEDs. Additionally, the growth on 2D materials like h-BN presents ample opportunities to refine the MBE growth conditions for (Al, Ga)N on h-BN. While this study has identified the need for further enhancements to achieve quality levels approaching or surpassing standard UV LEDs, the growth on h-BN serves as a significant gateway for transferring structures to more suitable substrates, with the potential to further elevate LED performances.